

**Development and laboratory characterization of a sampling
system for airborne measurements of peroxy radicals
using chemical amplification**

Vom Fachbereich für Physik und Elektrotechnik
der Universität Bremen

zur Erlangung des akademischen Grades eines

Doktor der Naturwissenschaften (Dr. rer. nat.)

genehmigte Dissertation

von

Anna Chrobry

1. Gutachter:	Prof. Dr. J. P. Burrows
2. Gutachter:	Prof. Dr. O. Schrems
1. Prüfer:	Prof. Dr. M. Rein
2. Prüfer:	Prof. Dr. T. Wehling
Eingereicht am:	14.03.2013
Tag des Promotionskolloquiums:	31.05.2013

„Co my wiemy, to tylko kropelka. Czego nie wiemy, to cały ocean.”

/Isaac Newton/

Abstract

Content

1. Introduction	1
1.1. Motivation and aims of the study	1
1.2. Structure of the work	4
2. Fundamentals	5
2.1. Peroxy radicals - role, sources and sinks in the atmosphere	5
2.2. Measurement techniques for airborne measurements of peroxy radicals	9
2.2.1. Laser Induced Fluorescence (LIF)	9
2.2.2. Peroxy radical Chemical Ionization Mass Spectrometry (PerCIMS).....	10
2.2.3. Peroxy Radical Chemical Amplification (PeRCA)	12
2.2.3.1. Critical factors affecting the chain length	14
2.3. Basic fluid mechanics	17
2.3.1. Hagen-Poiseuille flow, hydraulic resistance	17
2.3.2. Bernoulli's Equation	19
2.3.3. Flow through nozzle	20
2.4. Objectives of experimental applications	20
2.5. Modeling studies - description of a chemical box model	23
3. Experimental	28
3.1. Sampling set-ups for airborne measurements	28
3.1.1. HALO inlet adapted to the HALO aircraft	31
3.1.2. DUALER 2 inlet	35
3.1.3. Different inlet materials and coatings	38
3.1.4. Operation conditions of the sampling set-ups	39
3.2. Laboratory set-ups employed for the experimental work	40
3.2.1. DUALER rack	40
3.2.2. Pressure chamber and radical source	42
3.3. HALO set-up	47
3.4. Calibration procedures for the PeRCA technique	51
3.4.1. NO ₂ calibration	52
3.4.2. Chain length determination	53
3.4.3. Assignment of the uncertainties	56
3.5. Data acquisition systems and software	58

4. Results and discussion	60
4.1. Hydraulic resistance throughout the measurement set-up	60
4.1.1. Lid sampling orifice	64
4.1.2. Reactor entry	70
4.1.3. Scrubbers	73
4.1.4. Detectors	76
4.1.5. Other components (FC valve, PR valve, tubing etc.)	78
4.2. Peroxy radical losses in the sampling system	79
4.2.1. Sampling orifice of the pre-reactor nozzle	79
4.2.1.1. Pre-reactor nozzle of the DUALER 2 inlet	85
4.2.2. Reactor entry	89
4.2.2.1. Interference between reactors, Teflon insert geometry	89
4.2.2.2. Teflon inserts	93
4.2.3. Reactor walls	105
4.3. Application of the laboratory results to aircraft measurements: OMO (Oxidation Mechanism Observations) mission	119
4.4. Radical speciation	120
4.4.1. Modeling studies for ground based measurements	122
4.4.1.1. CH_3O_2 as an example of organic peroxy radical	122
4.4.1.2. Other organic peroxy radicals	126
4.4.2. Comparison with the experimental results	131
4.4.3. Applications for airborne measurements	136
5. Summary and conclusions	141
Appendix	150
Bibliography	157
Acknowledgements	163

Abstract

Hydroxyl- and organylperoxy radicals, HO₂ and RO₂ (R - organic chain), are key intermediates playing a crucial role in the photo-oxidation processes of volatile organic compounds in the troposphere and in the formation and depletion of the tropospheric ozone.

This doctoral thesis presents the outcome of laboratory studies carried out to optimize the sampling conditions and the inlet for airborne measurements of peroxy radicals with the PeRCA (Peroxy Radical Chemical Amplification) technique. The first aspect of the investigation is related to the sampling efficiency of these radicals which partly depends on the flow resistance encountered by the sampling gas through the set-up components. Based on the experimental data, the relative resistances of the components were quantified. The results show that the insufficient amount of air sampled through the reactor is not related primarily to the resistance of the sampling orifice of the inlet but mainly to the resistance of the components behind the reactor.

The second focus concerns a study of heterogeneous losses of peroxy radicals on the instrument surfaces to reduce the losses. It was observed that there was a reduction of the radical losses with decrease of the area to volume ratio of the sampling surface and with decrease of the radical retention time within the surface. In contrast to other literature values, the determined radical loss coefficients for HO₂ and CH₃O₂ are alike. The determined radical removal on surfaces coated with different materials: quartz and Teflon is similar.

Furthermore, as PeRCA measures the total sum of radicals ($[RO_2^* = HO_2 + \Sigma RO_2]$) the capabilities of the technique for the separate measurement of HO₂ and RO₂ radicals were investigated. This is crucial for the study of the processes affecting the oxidative capacity of the atmosphere. The proposed speciation is based on the partial removal of RO₂ by the chemical reaction with NO. As the removal efficiency is not equal for all RO₂, the quantitative measurements of HO₂ and RO₂ concentrations are possible for the radical mixture characterized by similar removal efficiency or with one dominant organic radical. Such conditions are expected in the upper troposphere where CH₃O₂ is likely the main RO₂. Thereby, CH₃O₂ can be discriminated from HO₂ through employment of varying NO mixing ratios in the PeRCA reactor which is a potential improvement for the deployment of PeRCA for the airborne measurements.

Based on the findings of this study, recommendations for the optimal set-up and the measurement conditions on board of the HALO aircraft for determination of abundance of peroxy radicals are provided.

1. Introduction

1.1 Motivation and aims of the study

Hydroperoxy- (HO_2) and organylperoxy (RO_2 , R - organic chain) radicals are short lived species relevant for the photochemical formation of oxidizing agents like ozone, peroxides and organic nitrates. They initiate the removal processes of most oxidisable trace gases emitted into the atmosphere. These radicals originate mainly from the oxidation of CO and hydrocarbons by OH radicals, which respectively leads to the production of HO_2 and RO_2 . In air with high NO_x ($\text{NO} + \text{NO}_2$) concentration peroxy radicals are converted into NO_2 in the reaction with NO. The produced NO_2 can be photolysed to create tropospheric ozone that is not only harmful for human health but it is also one of the greenhouse gases leading to global warming. Thus, the determination of HO_2 and RO_2 concentration is essential for gaining insight in the tropospheric processes involving ozone, NO_x , VOCs (volatile organic compounds) and in the partitioning between OH, HO_2 and RO_2 in clean and polluted areas.

For the measurement of peroxy radicals indirect techniques are employed utilizing the conversion of the radicals into other chemical species that can be detected and quantified more accurately, e.g., NO_2 in case of the PeRCA (**P**eroxy **R**adical **C**hemical **A**mplification) technique. PeRCA was first developed by Stedman and Cantrell in the early 1980s (Cantrell et al., 1982, 1984) and has been, ever since, successfully deployed for a number of measurement on different platforms in polluted and remote areas (Cantrell et al., 1996; Green et al., 2006; Andrés-Hernández et al., 2001; Burkert et al., 2001 a and b; Emmerson et al., 2009; Parker et al., 2009; Sommariva et al., 2011; Whalley et al., 2011). Over several years of the extensive employment of ground based measurements of PeRCA many critical factors have been recognized and addressed by different research groups, like the inlet geometry to reduce the radical losses on the instrument surfaces, and the effect of relative humidity on the radical conversion in the PeRCA reactor.

In recent years, the PeRCA technique has been deployed for airborne measurements with aircrafts in order to obtain information about the vertical distribution of peroxy radicals in the troposphere as it allows the investigation of the regions that have not been reachable so far. Conventionally, the PeRCA instrument consists of a reactor and a detector. However, for airborne measurements a double channel instrument, comprising two identical reactors connected to two detectors, is used. With such a configuration, enhancement of the sensitivity and accuracy is achieved in the conditions of rapidly changing background concentrations

(mainly O₃), which are related to the vertical and forward motion of the airborne platform (Cantrell et al, 1996; Green et al., 2003). The airborne measurements by PeRCA are still in a development stage and there is much that is still required to improve the instruments for measurement of the radicals.

Concerning the partitioning of the radicals, PeRCA measures the total sum of peroxy radicals ($RO_2^* = HO_2 + \sum RO_2$) and it is important to explore the possibilities of this technique for the speciation of the peroxy radicals most frequently present in the troposphere. At present, separate measurements of HO₂ and RO₂ by using Laser Induced Fluorescence (LIF) (Fuchs et al., 2008, 2011) and Peroxy radical Chemical Ionization Mass Spectrometry (PerCIMS) (Edwards et al., 2003; Hanke et al., 2003; Hornbook et al., 2011) have been reported. Recent developments in PeRCA (Miyazaki et al., 2010) have dealt with the separate detection of the organic peroxy radicals to HO₂ under laboratory conditions.

In general, the radical separation can be achieved by:

- (i) Suppression of RO₂ conversion into HO₂ by changing concentration of the reagents;
- (ii) Removal of either RO₂ or HO₂ by the chemical reaction with the species added in a pre-inlet;
- (iii) Removal of HO₂ by the heterogeneous losses on the surface prior to the radical introduction to amplification and conversion area in a reactor.

Option (i) has been already used by Edwards et al., 2003 and Hornbook et al., 2011 for PerCIMS employing the removal of organic peroxy radicals by the chemical reaction with NO. Option (ii) would be a challenging one, owing to the similar chemistry displayed by both organic and inorganic peroxy radicals (Lightfoot et al., 1992). Option (iii) has been exploited by Miyazaki et al., 2010 using the removal of HO₂ on the surface of a pre-inlet filled with glass beads taking advantage of higher wall losses of HO₂ relative to RO₂ (Mihele et al., 1999). However, such a set-up would be difficult to implement in airborne measurements.

The sampling inlet developed and characterized within this work will be employed to measure peroxy radicals with the PeRCA technique onboard HALO aircraft (The **H**igh Altitude and **L**ong Range Research Aircraft) as a measurement platform by the Institute of Environmental Physics of the University of Bremen (IUP-UB). The main focus of OMO (**O**xidation **M**echanism **O**bservations) mission scheduled for summer 2013 is to study oxidation mechanisms and radical chemistry in the free troposphere for which the measurement data is very scarce. With this objective, the vertical profiles of peroxy radicals and their precursors, partially convected from the boundary layer, will be taken as stacked

flights at different altitude levels. In addition, the radical composition in the upper troposphere will be characterized.

In that context, in this work I focused on the optimization of the inlet design and the sampling conditions for the airborne measurements using the PeRCA technique. A further objective is the assessment of the radical speciation by investigating the removal efficiency of HO₂ radicals in the selected reactor.

The efficiency of sampling the radicals depends on the set-up construction. The flow resistance encountered by the sampling gas through the set-up using the PeRCA instrument and the main resistors shall be defined and identified. To account for the potential changes in the radical sampling and detecting conditions during the flights, the pressure of the inlet can be kept constant and below the external pressure. If not, the flow through the reactor and the inlet pressure shall be characterized in the laboratory experiments for all pressure conditions expected during the flights.

Another critical aspect concerns the heterogeneous losses of peroxy radicals, which is an inevitable process owing to their high reactivity, on the instrument surfaces prior to the conversion into NO₂ in the reactor. Thus, there is a need to characterize the removal processes on the surfaces of the pre-reactor nozzle and the entry to reduce the losses and to develop the inlet optimum configuration. Previous work has shown that coating the reactor surfaces with Teflon reduces these losses and increases the sensitivity of the PeRCA technique (Ashbourn et al., 1998; Mihele et. al., 1999; Miyazaki et al., 2010).

In addition, the conduct of numerical simulations serves as a useful tool to study the effect of reagent mixing ratios, pressure etc. on the chemical and physical processes in the PeRCA reactor. It allows prediction of the conversion and amplification efficiency before performing laboratory experiments and is an aid to interpretation of the obtained measurement results, later.

After taking into account all the critical aspects which have been described above, the following is my summary of the objectives of the present doctoral thesis:

- Experimental characterization of the flow resistance in an existing PeRCA set-up by using a pressure chamber so as to optimise the flow conditions during the airborne measurement of peroxy radicals.
- Investigation of the loss processes of radicals on different materials, by the laboratory studies using different inlet surfaces and geometries, and radical composition, in order to

select the best physical conditions for the airborne sampling and conversion of peroxy radicals.

- Investigation of the effect of wall losses and pressure conditions on the total amplification and conversion of peroxy radicals by modeling studies comprising the development of a box model based on the Kintecus V4 compiler.
- Design and characterization of an adequate inlet for the airborne measurement of peroxy radicals on board the HALO aircraft, on the basis of the information obtained in the investigation above described.
- Investigation of the capability of the PeRCA technique for the speciated measurement of the atmospheric HO₂ and RO₂ radicals.
- Provision of the recommendations for the optimal set-up and measurement conditions on board of the HALO based upon the interpretation of the results obtained.

1.2 Structure of the work

The structure of this thesis is as follows:

Chapter 2 introduces the fundamental concepts relevant for this work, including peroxy radicals and their measurements techniques with PeRCA used in this study, basic fluid mechanics, and description of the numerical model used to simulate the chemical reactions in the PeRCA reactor.

Chapter 3 details the experimental set-ups employed in this study, data acquisition systems and software, and the calibration procedures for the PeRCA technique.

Chapter 4 presents the results of the laboratory experiments and the modeling studies.

In Chapter 5 the findings obtained in this research are summarized and discussed.

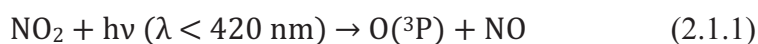
2. Fundamentals

As stated in the introduction chapter the development and characterization of the sampling system and the sampling conditions for the measurement of the peroxy radical chemistry in the upper troposphere is a main objective of the present work. In this context, the chemistry of peroxy radicals in the troposphere is briefly summarized in this chapter. More detailed information is provided in the consulting books: Richard P. Wayne, 2000; Barbara J. Finlayson-Pitts, 2000; Seinfeld and Pandis, 1997; Egbert Boeker, 1994. In addition, the experimental techniques for measurement of peroxy radicals are described. Then it is given brief information about fluid mechanics supporting the studies of the hydraulic resistance in the measurement set-up. In the next section the objectives of experimental applications in the measurement campaigns are presented. The last section of this chapter describes the chemical model used for simulating the chemical reactions in the PerCA reactor.

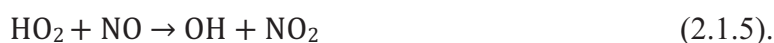
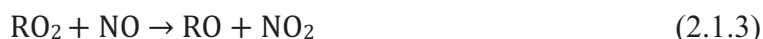
2.1 Peroxy radicals - role, sources and sinks in the atmosphere

Since the pioneering work of Weinstock (1969) and Levy (1971), photochemically formed HO_x radicals (hydrogen radicals: OH+HO₂) have been recognized as the driving force for most of the chemical processes in the troposphere. In particular, peroxy radicals (HO₂ and its organic homologues RO₂) play a key role in the photochemical formation of oxidizing agents: ozone, peroxides and organic nitrates and initiate the degradation and thus the removal of most oxidisable trace gases emitted into the atmosphere.

NO₂ photolysis is the only way of producing ozone in the troposphere:



At high NO_x=NO+NO₂ levels the reaction of peroxy radicals via the oxidation of NO to NO₂ enhances the ozone production:



Where: RO₂ and RO represent organic peroxy and oxy radicals, respectively.

In contrast, at low concentrations of NO_x the ozone loss occurs through:



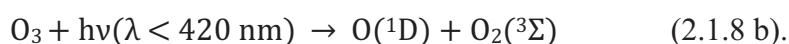
Sources of peroxy radicals

Production of peroxy radicals takes place from the oxidation of carbon monoxide (CO) and volatile organic compounds (VOCs) by hydroxyl radicals (OH), nitrate radicals (NO₃), halogen atoms and ozone (O₃). Depending on the prevailing NO concentration, O₃ and other photooxidants (e.g., peroxides, PAN and other organic nitrates) are formed in these mechanisms. All these processes are presented in detail in the following.

Several primary OH formation mechanisms are known. In a global scale the most important process producing OH is initiated by UV-B photolysis of O₃ to form electronically excited oxygen atoms:



Additionally, some contribution comes from the channel:



The oxygen atoms in excitation state: $\text{O}(^1\text{D})$ from (2.1.8) can be deactivated by a collision with N₂, O₂, or H₂O (i.e., any molecule 'M'):



However, a certain fraction of the excited oxygen atoms will react according to:



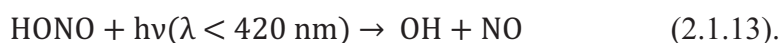
Then hydroxyl radicals react with most oxidisable gases in the atmosphere, like CO:



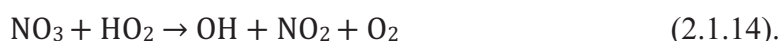
In the atmosphere, the hydrogen atoms immediately form hydroperoxy radicals, HO₂:



Photolysis of nitrous acid, HONO, yields OH:



The reaction of NO₃ with HO₂ can provide a nocturnal source of OH:



Further important reaction of OH producing HO₂ is the oxidation of formaldehyde (and higher aldehydes):



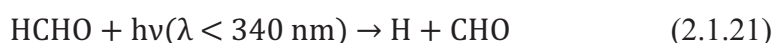
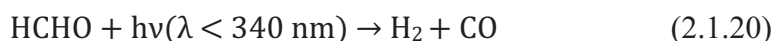
Another source of HO₂ is the reaction of H₂O₂ with OH:



RO₂ are formed as products of the degradation of VOCs, for example methane:



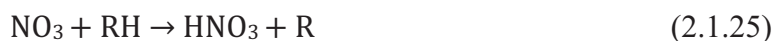
In addition, from the products of the photolysis of aldehydes HO₂ is formed. This process is particularly significant in urban areas, where the oxidation of VOC and direct emissions lead to high aldehyde levels.



The subsequent products of the oxidation and the photolysis of HCHO react as follows:

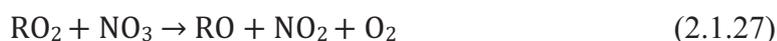


In a number of non-photochemical mechanisms HO₂ radicals are also formed, such as the reaction of NO₃ radicals with certain organic species, like olefins, phenols, or DMS (dimethyl sulfide) (e.g., Platt et al., 1990, 2002; Geyer et al., 2003, 2004):



VOCs are oxidized by OH formed in the reaction e.g., 2.1.14 and peroxy radicals are produced at night.

Following Wayne (2000) a generic nitrooxyalkyl peroxy radical RO₂ reacting with NO₃ can be a source of HO₂:

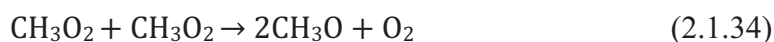
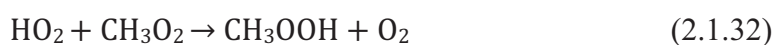


Another source of peroxy radicals is ozonolysis (the reaction of ozone with alkenes). In the remote environment the biogenic emission of VOC is an additional source of peroxy radicals via the oxidation of alkenes like isoprene.

Sinks of peroxy radicals

The following removal reactions for HO₂ and CH₃O₂ play a role in the troposphere. Their significance depends on the level of NO_x:





The reactions (2.1.5) and (2.1.6) reduce HO₂ radicals to OH. The reactions (2.1.30), (2.1.31), (2.1.32) can be considered as terminating steps for peroxy radicals as H₂O₂ and CH₃OOH can dissolve in cloud droplets and be removed by rain. However, the photolysis or the reaction with OH may generate the radicals:

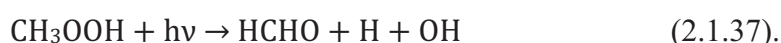


Fig. 2.1.1 shows the chemistry of the troposphere where the processes of OH, HO₂ and RO₂ generation and destruction are emphasized.

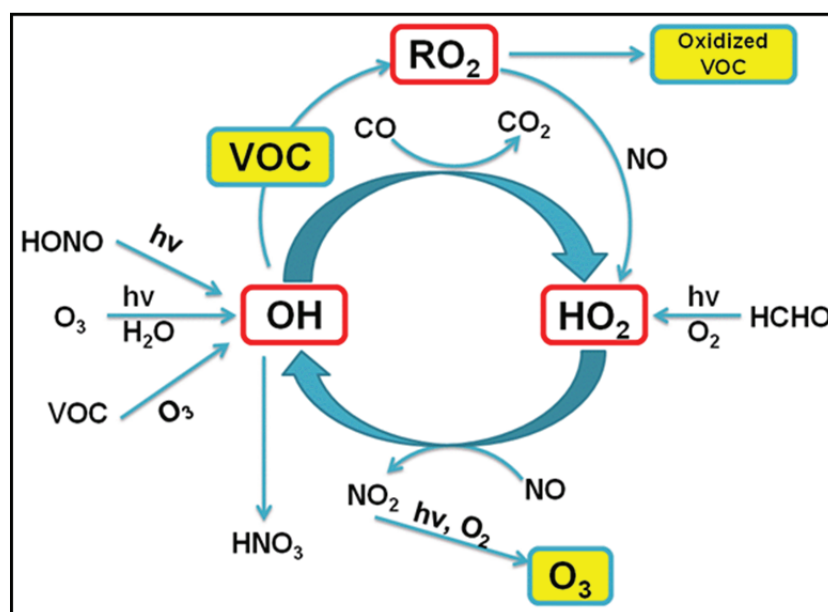


Fig. 2.1.1 Simplified schematic of tropospheric photochemistry
(Source: <http://www2.fz-juelich.de/icg/icg-2/groups/lif/>).

Peroxy radical levels have been observed to increase with altitude to peak concentrations between 2 and 5 km (lower middle troposphere) even up to 80 pptv and to decrease at higher altitudes (Tan et al., 2001; Cantrell et al., 2003 a). The HO_x = HO₂ + OH profile in the troposphere depends strongly on the behavior of NO_x, ozone and CO, solar radiation and radical precursors including water vapour.

2.2 Measurement techniques for airborne measurements of peroxy radicals

In general, atmospheric measurements of peroxy radicals are a challenging task owing to their high reactivity and low concentrations. Therefore, the measurement instruments must have high detection sensitivity. In addition, reliable determinations of the radical abundances are further complicated by the fact that the short-lived radicals can be lost by the surface reactions in the inlet system of the instruments. Consequently, indirect techniques are generally used, i.e., utilizing the conversion of peroxy radicals into other chemical species that can be detected and quantified more accurately. The indirect measurement techniques successfully employed on airborne platforms are the Laser Induced Fluorescence (LIF), the Chemical Ionisation Mass Spectroscopy (CIMS) and the Peroxy Radical Chemical Amplification Technique (PeRCA). The only direct technique, the Matrix Isolation-Electron Spin Resonance (MIESR), is not applicable for aircraft measurements in particular because of too long sampling time over 20-30 min. The techniques used for airborne measurements will be presented in the following sections.

2.2.1 Laser Induced Fluorescence (LIF)

The techniques termed interchangeably as LIF (Laser Induced Fluorescence) and FAGE (Fluorescence Assay by Gas Expansion) are essentially the same technique and can be used to measure concentrations of OH and HO₂ both from the ground and on board aircraft. LIF is a spectroscopic technique, employing laser excitation at a particular wavelength to select a particular transition of a target molecule and monitoring the fluorescence signal. In case of FAGE air is expanded through a critical orifice into a low-pressure fluorescence cell (Hard et al., 1984; Hofzumahaus et al., 1996).

HO₂ cannot be detected directly through LIF, therefore it is converted by NO to form OH (Reaction 2.1.5) which is afterward detected by LIF. The excitation of OH occurs with a laser beam at 308 nm and the fluorescence signal of excited OH molecules from their ground state into the first electronically excited state is measured by gated photon counting using a time delay to discriminate between the OH fluorescence extremely weak long-lived ($\tau_{fluorescence} \approx 150$ ns at 3.5 hPa) signal and intensive instantaneous laser light (around 20 ns duration). The detection limits below 10^5 molecule cm⁻³ can be achieved for averaged measurement periods of 1-2 min (Lee, 2000).

In 2011 Fuchs et al., reported that a large fraction of RO₂ radicals from alkenes such as isoprene and aromatics are also detected for the conditions, at which the LIF instrument

was operated during the field campaigns in the past for HO₂ measurements. RO₂ radicals can be converted to OH via a similar radical reaction sequence including the reaction with NO, so that they create potential interferences for HO₂ measurements. Thus, the previous measurements of HO₂ concentrations with this instrument were biased in the presence of high RO₂ radical concentrations from isoprene, alkenes or aromatics radicals, but were not affected by the interferences in remote clean environment where no significant emissions of biogenic VOCs and the OH chemistry was controlled mainly by small alkanes.

Recently the LIF technique has been modified as ROxLIF to allow a speciation of HO₂ from RO₂ (Fuchs et al., 2008, 2011). A two-stage chemical conversion of RO_x= RO₂+ RO+HO₂+OH into OH has been introduced at low pressure of 25 hPa at ‘RO_x mode’, firstly into HO₂ by doping air with CO and NO, following by HO₂ into OH with NO at 3.5 hPa and OH detection by the fluorescence. At ‘HO_x mode’ CO is added to ensure HO_x= HO₂+OH become HO₂, some RO₂ also undergo the conversion into HO₂, then HO₂ is converted into OH at 3.5 hPa. From the difference between the mode signals RO₂ and HO₂ abundance can be calculated. However, the interference presented above can occur also at ‘HO_x mode’ in the detection cell. Significant suppression of the interferences can be obtained (below 20% relative to the HO₂ detection sensitivity) by a reduction of the reaction time and/or the NO concentration in the detection cell. It leads to a decrease of the HO₂ detection sensitivity by a factor of four which is however sufficient for atmospheric HO₂ concentration measurements for a wide range of conditions.

The ROxLIF technique is very sensitive with the detection limit signal-to-noise ratio equal to 2 of around 0.1 pptv of HO₂ or RO₂ at a time resolution of 1 min.

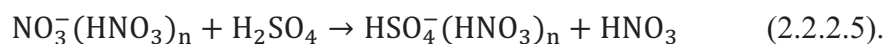
2.2.2 Peroxy radical Chemical Ionization Mass Spectrometry (PerCIMS)

Peroxy radicals are measured using the technique of amplifying chemical conversion and amplification to sulfuric acid and detection of sulfuric acid by Ion Molecule Reaction Mass Spectrometry: IMRMS (Reiner et al., 1997, 1998, 1999). The technique is termed either PerCIMS (Peroxy radical Chemical Ionization Mass Spectrometry) (Cantrell et al., 2003, Edwards et. al., 2003) or ROxMas (ROx Chemical Conversion/Chemical ionisation Mass spectrometry) (Hanke et al., 2002) depending on the group implementing the technique. The following reactions of the chemical conversion of HO₂ into H₂SO₄ take place:





The concentration of H_2SO_4 can be obtained from the measured ratio of the $\text{HSO}_4^- (\text{HNO}_3)_n$ product ions and the $\text{NO}_3^- (\text{HNO}_3)_n$ reactant ions created by the gas phase ion molecule reaction:



PerCIMS serves as sensitive and selective measurements of atmospheric peroxy radicals with a high time resolution (Hanke et al., 2002; Reiner et al., 1997, 1998, 1999). A detection limit of 0.5 pptv for the ground based measurements of the sum of radicals $[\text{RO}_2^*]$, (i. e., $[\text{RO}_2^* = \text{HO}_2 + \Sigma\text{RO}_2]$) may be achieved at a frequency of 1 min (Hanke et al., 2002). The absolute accuracy of the measurements is estimated to be about 35-40%, with a precision of 5-15%.

Hornbrook et al., in 2011 reported an improved PerCIMS technique for the separate measurement of HO_2 and RO_2 , which can be employed to both ground based and aircraft platforms. Time resolution of one minute was obtained which is sufficient to analyze measured $[\text{HO}_2]/[\text{HO}_2+\text{RO}_2]$ ratios on the timescales relevant for the tropospheric photochemistry. The instrument works in two operation modes:

- ‘ HO_2+RO_2 mode’ in the first 30 s, at low $[\text{NO}]/[\text{O}_2]=2.53*10^{-5}$ RO_2 which are converted into HO_2 radicals are detected at close to 100% efficiency together with HO_2 radicals. Sampled air is diluted by half with O_2 so the conversion is more effective:



- ‘ HO_2 mode’ in the second 30s, at high $[\text{NO}]/[\text{O}_2]=6.80*10^{-4}$ HO_2 is measured and most of RO_2 radicals are measured with low efficiency, around 15%. Air is diluted by half with N_2 and RO are more likely to form stable alkyl nitrate and not undergo conversion into HO_2 :



The speciation is based on the low efficiency conversion of RO_2 such as CH_3O_2 , $\text{CH}_3\text{CH}_2\text{O}_2$ and other simple organic peroxy radicals, which are most likely to be present in the atmosphere. Underestimation of the RO_2 concentration ($[\text{RO}_2]$) and overestimation of $[\text{HO}_2]$ owing to the conversion in the inlet in the ‘ HO_2 mode’ may take place at the conditions when unsaturated hydrocarbons are present in high concentrations. Therefore, the $[\text{HO}_2]$ uncertainty will be larger in these regions.

2.2.3 Peroxy Radical Chemical Amplification (PeRCA)

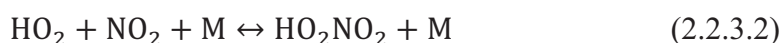
With the PeRCA technique the total sum of peroxy (i.e., hydroperoxy HO₂ and organylperoxy RO₂, R-organic chain), and oxy (i.e. OH and RO) radicals is measured. As the concentration of HO₂ significantly exceeds the concentration of OH ([HO₂]»[OH]) and the concentration of ΣRO₂ significantly exceeds the concentration of ΣRO ([ΣRO₂]»[ΣRO]) in the troposphere, the obtained radicals concentrations can be considered in a good approximation of [RO₂^{*}].

The PeRCA technique utilizes RO₂^{*} conversion with NO and CO into NO₂ and CO₂ in the reactor. Thus, the chain reaction is taking place with the amplification factor called Chain Length (*CL*) defined as an average number of NO₂ molecules formed per initial peroxy radical. For HO₂ the chain reaction is the following:



Where: ‘M’ refers to any third collision partner, e.g., mainly N₂ or O₂.

In practice, the chain length is limited by the radical termination reactions including OH with NO and NO₂, the radical-radical reactions and the RO₂^{*} loss on the walls of the sampling system:



Organic radicals RO₂ are converted by the reaction with NO to HO₂:



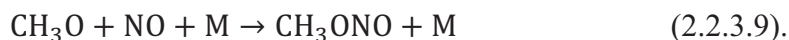
Alkyl nitrates RONO₂ are also formed:



In case of CH₃O₂:



Then HO₂ is amplified by the reactions (2.1.5), (2.1.11-12). Additionally, the production of alkyl nitrites RONO is taking place by the reaction:



HO₂ is involved directly in the chain reaction, whereas RO₂ are converted to HO₂ via the reaction with NO and O₂ with an efficiency depending on the structures of RO₂ and the intermediate RO (alkoxy) radicals. Thus, the sensitivity for organic radicals varies between 0.85 and 0.93 of that HO₂ (Cantrell et al., 1993; Jenkin et al., 1997).

The PerCA reaction chemistry is shown in Fig. 2.2.3.1.

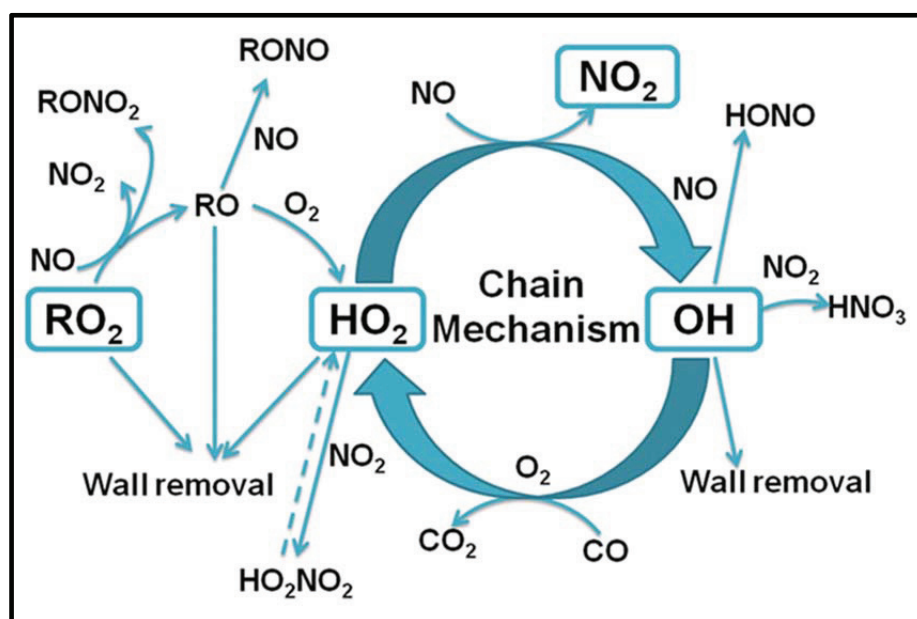


Fig. 2.2.3.1 The amplification cycle and the main loss reactions of PerCA (adapted from Sadanaga et al., 2004).

In order to discriminate the NO₂ present in ambient air from the NO₂ produced from the amplified conversion of the radicals, the NO₂ signal is modulated during the operation of the PerCA instrument. It is achieved by alternate adding to the top addition point of the reactor to the flow of ambient air (Hastie et al., 1991):

- NO+N₂ in the ‘background mode’ (to measured NO₂ contributes NO₂ from the conversion of the trace gases in the reaction with NO, plus NO₂ present in ambient air),
- NO+CO in the ‘amplification mode’ (to the total NO₂ contributes NO₂ from the conversion of peroxy radicals and background trace gases as in the ‘background mode’).

In such a way the amount of peroxy radicals in air can be determined from the difference between amplification and background signals ($[\Delta\text{NO}_2]$) provided that the CL is determined in the laboratory:

$$[\text{RO}_2^*] = \frac{[\text{NO}_2]_{\text{amplification}} - [\text{NO}_2]_{\text{background}}}{\text{CL}} = \frac{[\Delta\text{NO}_2]}{\text{CL}} \quad (2.2.3.10).$$

Clemitchaw et al., 1997 reported the *CL* value around 250 in the presence of 3.0 ppmv NO and 7.0% CO for the quartz reactor. The *CL* can be estimated from the formula provided by Hastie et al., 1991, if the reagent concentrations and the reaction rate coefficients are known:

$$\frac{1}{CL} \approx \frac{\sum \text{HO}_2 \text{ removal processes}}{\sum \text{HO}_2 \text{ propagating processes}} + \frac{\sum \text{OH removal processes}}{\sum \text{OH propagating processes}} \quad (2.2.3.11).$$

If taking into account the main removal and propagating processes, it leads to:

$$\frac{1}{CL} \approx \frac{k_{w\text{HO}_2} * [\text{HO}_2]}{k_{\text{HO}_2+\text{NO}} * [\text{NO}] * [\text{HO}_2]} + \frac{k_{\text{HONO}} * [\text{NO}] * [\text{OH}]}{k_{\text{CO+OH}} * [\text{CO}] * [\text{OH}]} \quad (2.2.3.12).$$

Recently the PeRCA instrument has been modified and the speciation between RO₂ and HO₂ has been attempted (Miyazaki et al., 2010) for ground based measurements. The air passes through a pre-inlet filled with the material (among investigated were glass, Teflon (PFA, PTFE)) where HO₂ undergoes higher heterogeneous losses in comparison to CH₃O₂ prior to the introduction into the reactor. Glass showed the best qualities for the radical loss as its removal properties do not depend on humidity. For glass beads 90% of HO₂ was removed at dried conditions, at RH=100% 85%, whereas the loss of CH₃O₂+CH₃C(O)O₂ radicals was 15% at the whole range of tested RH. A decrease of the removal efficiency with decreased radical concentration for HO₂ was observed. On the other hand, the stable loss of 15% for CH₃O₂+CH₃C(O)O₂ was obtained. For ambient measurements higher removal efficiency at lower HO₂ concentrations can be achieved by increasing the length of a removal cell and thus increasing its volume to surface ratio and residence time. The utility of the instrument was tested during summer in Tokyo in Japan. However, more research is necessary to characterize losses of different RO₂ radicals.

2.2.3.1 Critical factors affecting the chain length

The following factors have influence on the actual number of NO₂ molecules produced per radical, i.e. the *CL* value:

- concentration of the reactants CO and NO as the competing processes between the amplification reactions (Eq. 2.1.5, 2.1.11-12) and the chemical reaction losses (Eq. 2.2.2.3, 2.2.3.1-4) take place,
- reactor volume, i.e., sample residence time,
- reactor material and shape, i.e., heterogeneous losses at the inlet surfaces (Eq. 2.2.3.5),
- relative humidity.

CO and NO dependence

In case of CO, the *CL* value increases monotonously with CO concentration up to 10% (Ashbourn et al., 1998; Sadanaga et al., 2004), see Fig. 2.2.3.3 a. As CO increases, the rate of the reaction of chain propagation: OH+CO increases in respect to the terminating reaction OH+NO (2.2.2.2) and thereby the chain reaction is promoted. In case of the NO dependence, the *CL* has maximum value between 3-6 ppmv (shown in Fig. 2.2.3.3 b). This is because the chain termination reaction OH+NO (2.2.2.2) becomes more effective at higher NO concentrations.

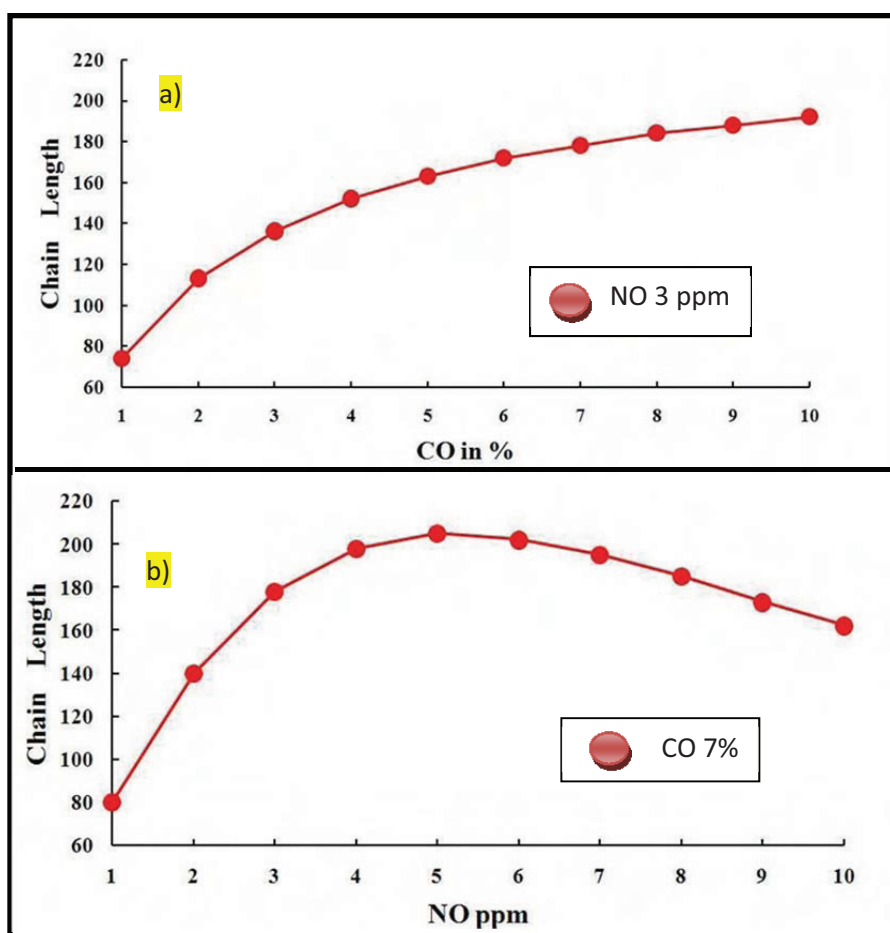


Fig. 2.2.3.3 The simulated *CL* dependence on a) CO and b) NO concentrations and 50 pptv CH_3O_2 initial mixing ratio (adapted from Kartal D., 2009).

Radical wall losses

The following features affect wall losses of peroxy radicals in a reactor: the geometry, surface to volume ratio, material of the reactor and the radical type. Therefore, the influence of those has to be determined for each particular set-up.

Removal of the radicals on the walls of the sampling system can be characterized by the wall loss rate coefficient $k_w \text{ s}^{-1}$. In general, the flow tubes can be employed to determine this parameter (Howard, 1979). The radical concentration is measured as a function of the

downstream distance from the inlet of the tube l with a cross section area A . The flow Q and the volume of the tube V are used to convert distance l into time:

$$t = \frac{V}{Q} = \frac{A \cdot l}{Q} \quad (2.2.3.13).$$

The results are fitted using least square method to obtain first order rate constant. When k_w is known, the radical concentration after time t ($[RO_2(t)^*]$) can be then calculated from the initial concentration $[RO_2^{*0}]$ as a first order reaction:

$$[RO_2(t)^*] = [RO_2^{*0}] \cdot \exp(-k_w \cdot t) \quad (2.2.3.14).$$

It was determined experimentally the rate coefficients of $k_{wHO_2}=0.175 \pm 0.007 \text{ s}^{-1}$ for the PYREX tube (inner diameter of ID=75 mm, length of L=30 cm) by Mozurkewich et al., 1987, and $k_{wHO_2}=2.0 \text{ s}^{-1}$ for the quartz tube (ID=2.6 cm, L=50cm) by Qi et al., 2006.

The wall losses in the sampling system depend additionally on the composition and nature of sampled RO_2^* . In general, the radicals with higher chain R have lower wall loss rates (Volz-Thomas A. et al., 1998). In 1999, Mihele et al. reported different wall loss coefficients: $k_{wHO_2}=2.8 \pm 0.2 \text{ s}^{-1}$ and $k_{w50\%CH_3O_2+50\%C_2H_5O_2}=0.8 \pm 0.1 \text{ s}^{-1}$ for 1/4" PFA tube employed as a PeRCA reactor. The ratio $k_{wHO_2}/k_{w50\%CH_3O_2+50\%C_2H_5O_2} \approx 3$ is probably due to lower polarity of the RO_2 radicals.

The wall loss rate coefficient for the heterogeneous reaction of the radicals on the inlet walls is proportional to the surface/volume (S/V) ratio (Murphy et. al., 1987):

$$k_w \sim \left(\frac{S}{V}\right) \quad (2.2.3.15).$$

In case of a cylindrical reactor with a diameter d : $\frac{S}{V} = \frac{4}{d}$.

The wall loss rate can be estimated by using a set of equations by Hayman, 1997:

$$k_w = 1.85 \left(\frac{v^{1/3} D^{2/3}}{d^{1/3} L^{1/3}} \right) \left(\frac{S}{V} \right) \quad (2.2.3.16).$$

Where: S is surface area [cm^2], V volume [cm^3], L length [cm], d diameter [cm] of the flow tube, v velocity [cm/s] of the gas, D diffusion coefficient [cm^2/s]. This empirical correlation is in general valid for $75 < Re < 7000$, $600 < Sc < 12000$, $0.05 < d/L < 20$ which puts it in the laminar flow regime (Selman et al., 1978). The Reynolds number is defined as:

$$Re = \frac{\rho \cdot V_0 \cdot h}{\eta} \quad (2.3.1.17).$$

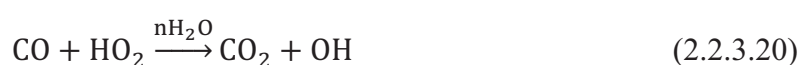
Where: ρ is fluid density [kg/m^3], V_0 fluid velocity [m/s], h characteristic linear dimension [m], η fluid viscosity [$\text{kg/m} \cdot \text{s}$]. And the Schmidt number:

$$Sc = \frac{\eta}{\rho D} \quad (2.2.3.18).$$

Where: ρ is fluid density [kg/m^3], η fluid viscosity [kg/m*s], D diffusion coefficient [m^2/s].

Relative humidity effect

It has also been observed that there is a chain length dependency on the water vapour content in sampled air (Mihele and Hastie, 1998; Mihele et al., 1998; Reichert et al., 2003), i.e., a CL decrease with increasing relative humidity RH. The mechanism of this dependency has not yet been fully understood, but some possible explanations are based on the reactions involving HO_2 - $n\text{H}_2\text{O}$ dimers and CO or NO, leading to CO_2 and OH or HNO_3 (Reichert et al., 2003):



In Section (3.1) the approaches to account for RH variations during airborne measurements which affect the CL are presented.

2.3 Basic fluid mechanics

The Navier-Stokes equation describes incompressible, viscous flow of a fluid:

$$\rho \left(\frac{\partial \vec{v}}{\partial t} + (\vec{v} \cdot \nabla) \vec{v} \right) = -\nabla p + \mu \nabla^2 \vec{v} + \rho \vec{g} \quad (2.3.1).$$

Where: ρ - density (assumed constant throughout the fluid), \vec{v} - fluid velocity, p - pressure, μ - viscosity (assumed constant throughout the fluid), \vec{g} - the body force caused by gravity.

2.3.1 Hagen-Poiseuille flow, hydraulic resistance

The Poiseuille flow or Hagen-Poiseuille flow is an analytical solution to the Navier-Stokes equation for the pressure-driven, steady-state flows in channels. In such a flow the incompressible fluid is driven through a long, straight, and rigid channel by imposing a pressure difference between the two ends of the channel.

The Hagen-Poiseuille law states that a constant pressure drop Δp results in a constant flow rate Q :

$$\Delta p = R_{\text{hyd}} * Q = \frac{1}{H_{\text{hyd}}} * Q \quad (2.3.1.1).$$

Where: R_{hyd} and H_{hyd} are the proportionality factors known as the hydraulic resistance and conductance, respectively. The Hagen-Poiseuille law (Eq. 2.3.1.1) is analogous to the Ohm's

law, $\Delta V = R * I$, relating the electrical current I through a wire with the electrical resistance R of the wire and the electrical potential drop ΔV along the wire.

The SI units used in the Hagen-Poiseuille law are:

$$[Q] = \frac{\text{m}^3}{\text{s}}, [\Delta p] = \text{Pa} = \frac{\text{N}}{\text{m}^2} = \frac{\text{kg}}{\text{m*s}^2}, [R_{\text{hyd}}] = \frac{\text{Pa*s}}{\text{m}^3} = \frac{\text{kg}}{\text{m*s}^4}.$$

Table 2.3.1.1 summarizes the hydraulic resistance R_{hyd} for different cross sections of channel (formulas taken from Theoretical microfluidics, Henrik Bruus, 2008).

Shape	R_{hyd} expression	Eq.
circle 	$\frac{8\eta L}{\Pi r^4}$	2.3.1.2
annulus 	$\frac{2\eta L}{\Pi} * \frac{1}{\frac{a^4}{4} - \frac{r^2 a^2}{2} + \frac{r^4}{4}}$	2.3.1.3

Table 2.3.1.1 The hydraulic resistance for straight channels with different cross sectional shapes.

Hydraulic resistance of two connected straight channels

When two straight channels of different dimensions are connected to create one long channel the translation invariance will in general be broken (the non-linear term in the Navier-Stokes equation $(\vec{v} \cdot \nabla)\vec{v}$ does not vanish) and thus the expressions for the ideal Poiseuille flow is no longer valid. However, it is expected that the ideal approximation is correct if the Reynolds number Re of the flow is sufficiently low $Re \rightarrow 0$:

$$Re = \frac{\rho * V_0 * h}{\eta} \quad (2.2.3.17).$$

Two straight channels in series

Considering series of two hydraulic resistors as shown in Fig. 2.3.1.1 a and assuming the validity of the Hagen-Poiseuille law for each of the resistors after they are connected and using the additivity of the pressure drop along the series, i.e., $\Delta p = \Delta p_1 + \Delta p_2$, the law of additivity of the hydraulic resistors in series can be derived:

$$R = R_1 + R_2 \quad (2.3.1.4).$$

Bearing in mind the discussion above the additivity law is only valid for low Reynolds numbers $Re \rightarrow 0$ and for long and narrow channels.

Two straight channels in parallel

Considering two hydraulic resistors connected in parallel presented in Fig. 2.3.1.1 b and assuming the validity of the Hagen-Poiseuille law for each of the resistors and using the

conservation of flow rate, i.e., $Q = Q_1 + Q_2$, it can be shown the law of additivity of the inverse hydraulic resistances in a parallel coupling:

$$R = \left(\frac{1}{R_1} + \frac{1}{R_2} \right)^{-1} \quad (2.3.1.5).$$

Similar to channels in series the inverse-additive law is only valid for low Reynolds numbers $Re \rightarrow 0$ and for long and narrow channels far apart.

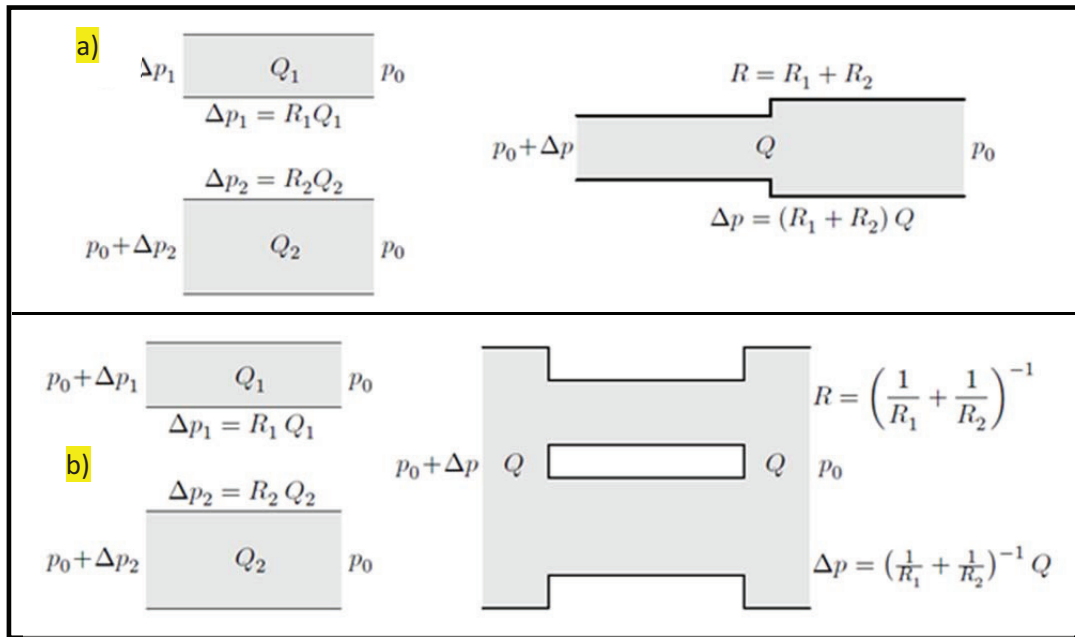


Fig. 2.3.1.1 The resistance of two channels with hydraulic resistance R_1 and R_2 connected a) in series b) in parallel. (Illustration adapted from Theoretical microfluidics, Henrik Bruus, 2008).

2.3.2 Bernoulli's Equation

The Bernoulli's equation (derivation from the Navier-Stokes equation provided in Clark M., 2002) relates the variation of speed and variation of pressure along a streamline for incompressible fluid and inviscid steady flow:

$$\frac{1}{2} \rho v^2 + p + gz = \text{const} \quad (2.3.2.1).$$

One of the consequences of the equation is an increase of velocity of the fluid through a narrower opening (see Fig. 2.3.2.1) which is an important consideration in a design of the openings in the radical sampling system.

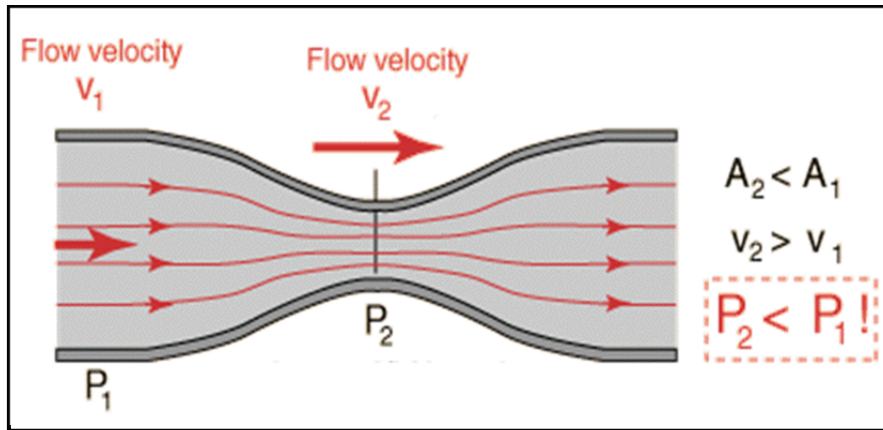


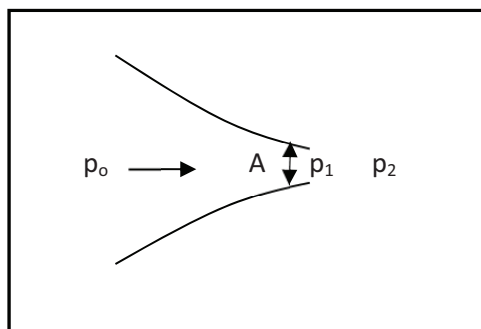
Fig. 2.3.2.1 Illustration of the Bernoulli's equation application (Illustration adapted from <http://hyperphysics.phy-astr.gsu.edu/hbase/pber.html#beq>).

2.3.3 Flow through nozzle

To determine the flow rate through a nozzle from the upstream p_0 (the nozzle from a large chamber where gas velocity is effectively zero referred with subscript 0) to external pressure p_2 (see Fig. 2.3.3.1) firstly p° the critical pressure is calculated:

$$\frac{p^\circ}{p_0} = \left(\frac{2}{k+1} \right)^{k/(k-1)} \quad (2.3.3.1).$$

Where: k is adiabatic index, for air 1.4. If $p_2 > p^\circ$ then the flow through the orifice is unchoked and is a function of p_0 and p_2 (Green and Perry, 2007). For $p_2 \leq p^\circ$ the flow is only a function of p_0 .



2.3.3.1 Isentropic flow through a nozzle of area A .

2.4 Objectives of experimental applications

The objective of the present work was the development of the sampling system (the HALO inlet) as a part of the PerCEAS instrument (presented in Section 3.3) for the airborne measurement of peroxy radicals with the HALO aircraft (The High Altitude and Long Range Research Aircraft) within the OMO campaign (Oxidation Mechanism Observations). In the following section the aircraft (see Fig. 2.4.1) and the campaign will be presented. In addition,

a ground based measurement campaign: PARADE within which the PerCEAS instrument was employed will also be described.



Fig. 2.4.1 Flight of the HALO over the DLR in Oberpfaffenhofen (Source: http://www.halo.dlr.de/aircraft/schemes/HALO_over_OP.jpg).

The HALO aircraft

The HALO project was based on an initiative of the German atmospheric science community and is operated by the DLR (Deutsches Zentrum für Luft- und Raumfahrt) and MPG (Max-Planck-Gesellschaft). The concept of the HALO is to provide an optimal platform for atmospheric science and Earth observation, a well-equipped flying laboratory that allows the scientists onboard to completely focus on their experiment.

The HALO was based on a Gulfstream G550 jet that was modified from the luxury passenger airplane into a research platform, including adaptation of the aircraft frame, electronics, avionics, and sensor systems. The modifications were prerequisite to meet the essential requirements of the future HALO users to operate any scientific instrumentation and to fulfill scientific objectives:

- range more than 10000 km or more than 10 flight hours for intercontinental experiments and long duration measurements,
- certified altitudes up to 15 km,
- maximum payload of 3 tons,
- a large usable cabin area of 20-30 m² for simultaneous operation of several instruments and scientific personnel from several groups (for multidisciplinary and international projects),
- prospect for quick modifications for a wide variety of applications and for flexible use as research aircraft with different instrument configurations for various research projects.

The main strengths of the HALO aircraft: long range and endurance, high flying altitude and large instrument load capacities are not available in such a combination on another research aircraft in Europe. Thus, the measurements can be carried out in the areas that can currently not be probed by other platforms: the full altitude range of the troposphere and lowermost stratosphere and remote parts of the Earth with a large set of chemical species.

The details concerning the HALO inlet installation through the aircraft fuselage are described in Section 3.1.1 and the PerCEAS deployment onboard of the HALO in Section 3.3.

The OMO campaign

For the OMO mission (Oxidation Mechanism Observations) the HALO aircraft is an ideal platform as it allows performing the accurate measurement of radicals and their precursors which is not achievable with smaller aircraft. The OMO mission objective is to study oxidation mechanisms and radical chemistry in the free troposphere over Europe in summer 2013. For this purpose the vertical profiles of RO_2^* and their precursors which are partially convected from the boundary layer will be additionally taken as stacked flights with 10-20 minute duration at each altitude level. Based on that, it will be determined the rates at which natural and human-made compounds are converted by oxidative processes in the upper troposphere, which influence the lifetime and the global distribution of air pollutants and greenhouse gases, such as the tropospheric ozone. In addition, the radical composition in the upper troposphere and lower stratosphere (UT/LS) will be characterized which is very sensitive to the amount of actinic radiation and mixing processes. This is essential for assessment of the climatic effect of stratospheric changes.

The PARADE campaign

The PARADE (**P**Articles and **R**Adicals: **D**iel observations of the impact of urban and biogenic Emissions) campaign took place at the Taunus Observatory on the summit of the Kleiner Feldberg (nearby Frankfurt) between 8.08 and 9.09.2011. The main objective of the campaign was examination of the effect of biogenic and anthropogenic emissions on radical chemistry (diurnal and nocturnal) by employment of several instruments to measure RO_2^* , HO_x and relevant species: O_3 , H_2O_2 , NO_x , organics, CO. Because of its elevation the station is considered as a remote site for central Germany with a few main roads and some small towns within 5 km. The area around the site is forest and influenced by the significant biosphere emissions within the warm months. However, the station is also impacted by pollution originating in the heavily populated Rhein-Main area (pop. \approx 2 million) with a dense

motorway system and large cities: such as Frankfurt, Wiesbaden, Mainz, and Kleiner Feldberg which is lightly populated and industrial region.

The PerCEAS together with other PerCA instrument of the University of Bremen were successfully installed on the measurement scaffold on the observatory and the HALO inlet position is presented in Fig. 2.4.3 and RO_2^* radicals were measured.

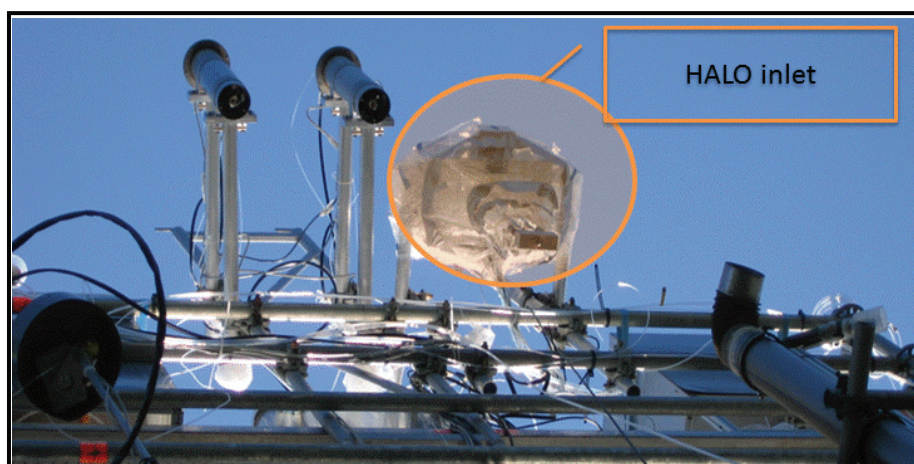


Fig. 2.4.3 The HALO inlet (on the right side) photographed mounted to the scaffold.

2.5 Modeling studies - description of a chemical box model

The aim of the modeling study is to simulate the *CL* for different pressure conditions, wall losses and different concentrations of the reagent gasses (CO and NO) in the PerCA reactor. For this purpose a chemical box model was developed within this work based on the Kintecus V4 compiler described in the following. The previous model developed in Matlab within the PhD work by Kartal D. (2009) requires advanced programming skills of the user. Thus, the Kintecus® has been selected as its big advantage of over other models is short execution time and user friendly interface.

Kintecus® (Ianni, James C., Kintecus, Windows Version 4.00, 2010, www.kintecus.com) is a compiler in MS Excel to simulate the reactions of chemical, biological, nuclear and atmospheric processes. Three input spreadsheet files are used in the model:

- ‘model’,
- ‘species description’,
- ‘parameter description’,
- ‘thermodynamics’ (optional).

In the ‘model spreadsheet’ the reactions (reversible and/or irreversible) and the reaction rates are an input data. The support for special reactions involving third-bodies is build, i.e., the reaction rate coefficient calculated as Troe formula with the JPL coefficients. The heterogeneous chemistry can be also included.

In the ‘species spreadsheet’ the initial value reagents (c) is an input data expressed according to the pressure conditions (p):

$$c = MR * c_{STP} * \frac{p_{STP}}{p} \quad (2.5.1).$$

Where: MR - volume mixing ratio, c_{STP} - reagent concentration at STP conditions [molecule/cm³] and p_{STP} - pressure at STP condition. Based on the sum of reagents, the Kintecus calculates the overall pressure. In addition, concentrations of any species can be hold at a constant level or included as a profile over time.

In the ‘parameter description spreadsheet’ simulation time, units of species concentrations, temperature are set. The Starting Integration Time, Maximum Integration Time and Accuracy fields determine how fast the Kintecus can integrate the model and the error in the final concentrations. The accuracy determines how far out in the decimal place to keep the concentration accurately computed, e.g., a value of 1.0E-9 will keep the first nine digits of the integrated concentration accurately computed. The smaller is the accuracy field, the slower the Kintecus runs the model. The Starting Integration Time (in seconds) determines the starting time step to integrate the model. After the first integration, this will change and grow larger if the accuracy is large and/or the stiffness of the model is low (which follows a decrease in execution time of the program), or grow smaller if the accuracy is very small and/or the stiffness of the model is high (meaning an increase in execution time of the program). The Maximum Integration Time has a few uses in the Kintecus. If a concentration profile on any species is not used and the '-obeymaxint' option is set in the ‘control spreadsheet’, then this field is only used to determine the minimum time after which concentrations will be displayed. If some species are loaded as a concentration profile, e.g., are added or removed after the starting time of a simulation (this feature is used to simulate the radical wall losses in the modified reactor in Section 4.2.3), then this will determine how often the data is retrieved from the concentration profile files.

In the ‘control spreadsheet’ options how the program is run are specified, e.g., which integrator is used.

The differential equations representing the production and loss rates of the reactions can be solved by differencing the equation by numerical solutions. For the Kintecus the

modified Bader-Deufhard method is set as a default and internally implemented in the program so that the user does not need to program it. It is an internally developed method by the Kintecus programmers almost identical to the regular Bader-Deafhard method as shown in Bader, G., and Deuffhard, P., 1983.

The model created within this work simulates the amplification and termination reactions in the PeRCA reactor and provides the concentrations of all reagents and products at constant temperature and different concentrations of NO and CO. The medium for the simulations is considered as a volume V where all the reagents are located. The chemical reactions and the rate constants of the reactions used for the simulations summarized in Table 2.5.1 are taken from the JPL publication 10-06 (Sander et al., 2011). The initial concentration of radicals, NO, CO, O₂ and N₂ are an input data.

Reaction	Low pressure limit		High-pressure limit		Rate constants for bimolecular reactions at 298 K
	k_0	n	k_∞	m	
$\text{CH}_3\text{O}_2 + \text{NO} \rightarrow \text{CH}_3\text{O} + \text{NO}_2$					7.7E-12
$\text{CH}_3\text{O} + \text{O}_2 \rightarrow \text{CH}_2\text{O} + \text{HO}_2$					1.9E-15
$\text{CH}_3\text{O} + \text{NO} \xrightarrow{\text{M}} \text{CH}_3\text{ONO}$	2.3E-29	2.8	3.8E-11	0.6	
$\text{HO}_2 + \text{NO} \rightarrow \text{NO}_2 + \text{OH}$					8E-12
$\text{CO} + \text{OH} \xrightarrow{\text{O}_2} \text{CO}_2 + \text{HO}_2$					$1.5\text{E} - 13 * \frac{0.6 * P}{1013.25}$
$\text{OH} + \text{NO} \xrightarrow{\text{M}} \text{HONO}$	7E-31	2.6	3.6E-11	0.1	
$\text{OH} + \text{NO}_2 \xrightarrow{\text{M}} \text{HNO}_3$	1.8E-30	3	2.8E-11	0	
$\text{HO}_2 \rightarrow \text{HO}_2 \{s\}$					$k_{w\text{HO}_2}$
$\text{CH}_3\text{O}_2 \rightarrow \text{CH}_3\text{O}_2 \{s\}$					$k_{w\text{CH}_3\text{O}_2}$
$\text{OH} + \text{HO}_2 \rightarrow \text{H}_2\text{O} + \text{O}_2$					1.1E-10
$\text{HO}_2 + \text{CH}_3\text{O}_2 \rightarrow \text{CH}_3\text{OOH} + \text{O}_2$					5.2E-12
$\text{OH} + \text{OH} \xrightarrow{\text{M}} \text{H}_2\text{O}_2$	6.9E-31	1	2.6E-11	0	
$\text{OH} + \text{HONO} \rightarrow \text{H}_2\text{O} + \text{NO}_2$					4.5E-12
$\text{OH} + \text{H}_2\text{O}_2 \rightarrow \text{HO}_2 + \text{H}_2\text{O}$					1.8E-12
$\text{HO}_2 + \text{HO}_2 \rightarrow \text{H}_2\text{O}_2 + \text{O}_2$					1.4E-12
$\text{HO}_2 + \text{NO}_2 \xrightarrow{\text{M}} \text{HO}_2\text{NO}_2$	2E-31	3.4	2.9E-12	1.1	
$\text{HO}_2\text{NO}_2 \xrightarrow{\text{M}} \text{HO}_2 + \text{NO}_2$	$k = \frac{k_{\text{HO}_2 + \text{NO}_2}}{2.1\text{E} - 27 * \exp(\frac{10900}{T})}$				

Table 2.5.1 The reactions used to simulate the processes in the PeRCA reactor. The rate coefficients are in cm³ molecule⁻¹s⁻¹ except for the first order heterogeneous wall loss of $k_{w\text{HO}_2}$ and $k_{w\text{CH}_3\text{O}_2}$ and the unimolecular decomposition of H₂O₂ which are in s⁻¹. $k_{w\text{HO}_2}$ and $k_{w\text{CH}_3\text{O}_2}$ value were adjusted to the experimental *CL*.

The termolecular reaction rate coefficients are calculated by the Kintecus program according to the Troe formula (explained in DeMore et al., 1994 in detail):

$$k_f([M], T) = \left(\frac{k_0(T)[M]}{1 + \frac{k_0(T)[M]}{k_\infty(T)}} \right) 0.6 \left\{ 1 + \left(\log_{10} \left[\frac{k_0(T)[M]}{k_\infty(T)} \right] \right)^2 \right\}^{-1} \quad (2.5.2).$$

The reaction $\text{CO} + \text{OH} \xrightarrow{\text{O}_2} \text{CO}_2 + \text{HO}_2$ is a special case as the Kintecus does not provide a direct method to represent these three body reaction. Therefore, the rate coefficient (k) was introduced in the following way to keep mass balance:

$$k = \frac{k_{\text{CO}+\text{OH}+\text{O}_2}}{[\text{O}_2]} \quad (2.5.3).$$

Where: $k_{\text{CO}+\text{OH}+\text{O}_2} = 1.5E - 13 * \left(1 + \frac{0.6 * P}{1013.25} \right)$ and $[\text{O}_2]$ is the concentration of oxygen [molecule/cm³].

The performance of the model was proved by running the simulations and a comparison with a previous study by Clemitshaw et al., 1997 that used the FACSIMILE/CHECKMAT program (Curtis and Sweetenham, (1988)). The same conditions concerning the initial reagent concentrations were used. Initially a discrepancy between the results obtained with the Kintecus model and by Clemitshaw was observed. It was related to the reaction rate coefficient for the reaction (2.2.2.2) $\text{OH} + \text{NO} \xrightarrow{\text{M}} \text{HONO}$ which differs between the JPL Publ., 94-26, 1994 used by Clemitshaw ($k_\infty(300) = (1.5 \pm 1.0)E-11$, $m = 0.5 \pm 0.5$) from the JPL publication 10-06, 2011 ($k_\infty(300) = 3.6E-11$, $m = 0.1$). Thus, for the comparisons the JPL Publ., 94-26, 1994 coefficients for this reaction were used, and then a very good agreement was obtained showed in Fig. 2.5.1. For the simulations in this work the revised coefficients from the JPL publication 10-06 were used.

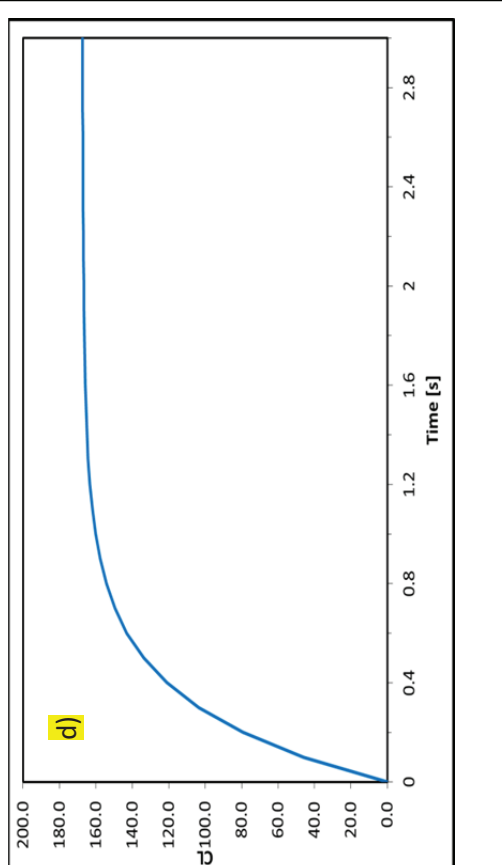
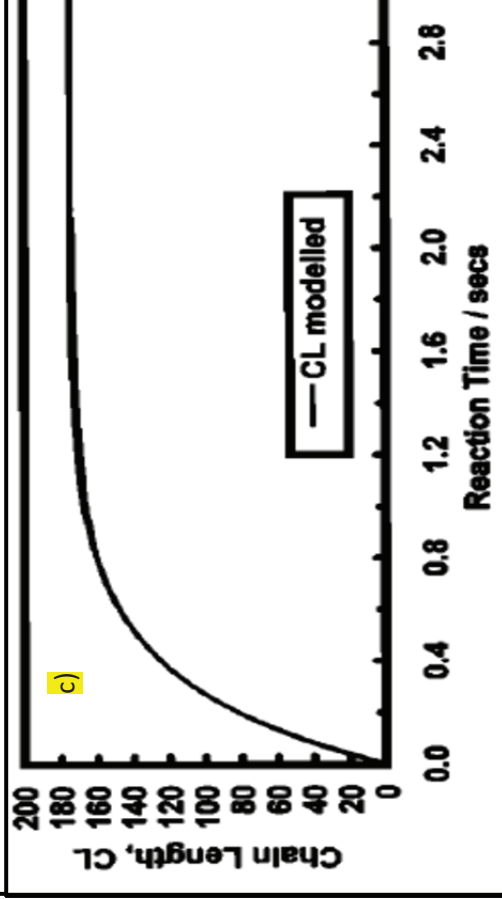
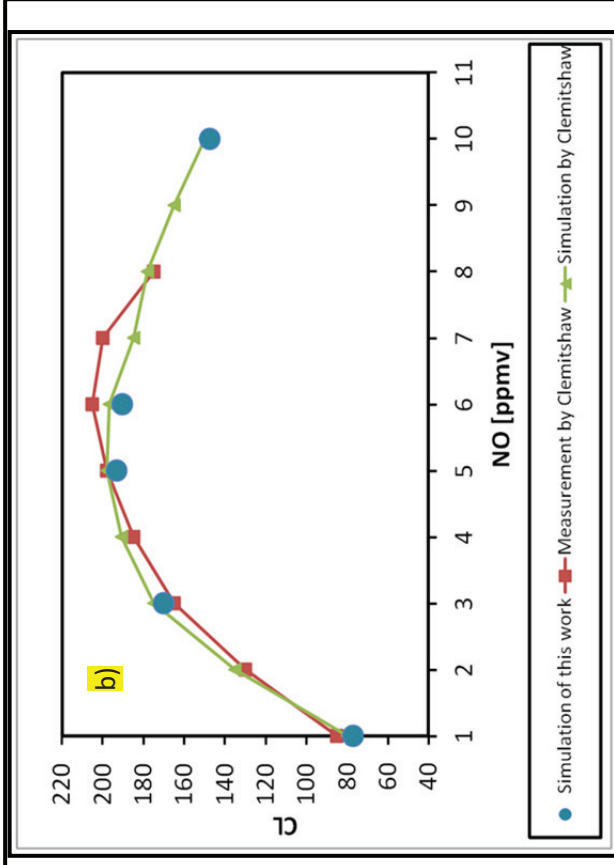
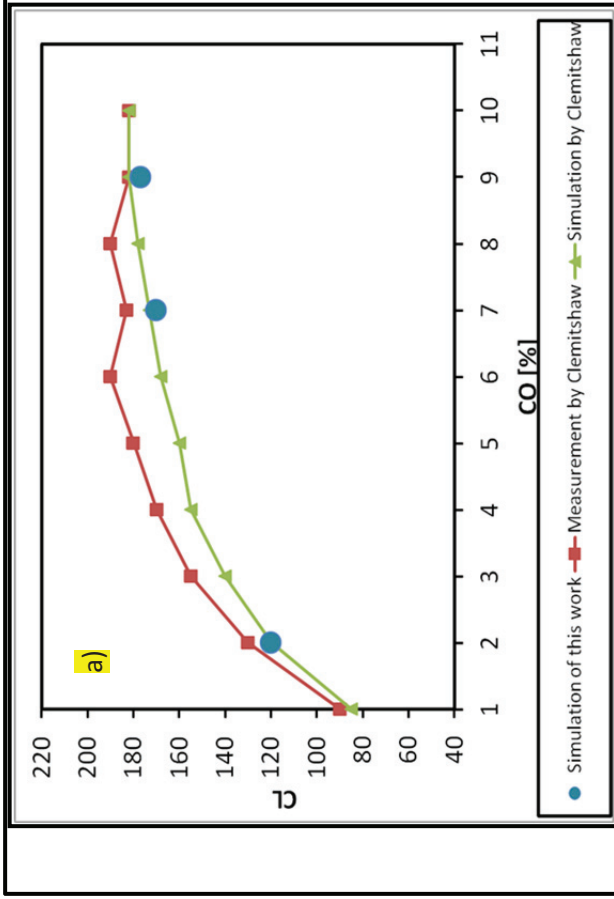


Fig. 2.5.1 a) Variations of the *CL* with CO mixing ratio at 3 ppmv NO b) Variations of the *CL* with NO mixing ratio at 7% CO. Time evolution of *CL* at NO 3 ppmv and CO 7% CH₃O₂ with initial mixing ratio c) Simulation by Clemitshaw et al., 1997, d) Simulation of this work.

3. Experimental

In this chapter the experimental set-ups and the calibration procedures employed to characterize the radical losses and the flow resistance in the PeRCA instrument are described. Special attention is paid to critical aspects and parameters. The analysis of the uncertainties involved in the determination of the chain length is also described. In the last part of the chapter the data acquisition systems and software are presented.

3.1 Sampling set-ups for airborne measurements

In general, a PeRCA measurement system comprises:

- a reactor where the reagent gases NO+CO are added and RO_2^* is converted into NO_2 and CO_2 ,
- a control unit to add the gases and to create the modulated signal (flow controllers, magnet valves),
- a detector to determine the NO_2 concentrations,
- a pump to sample air.

For the airborne platforms the set-up described above has to be modified to meet many safety regulations and also to deal with variations of the conditions during the air sampling like changes of ambient pressure, temperature, RH (relative humidity). The sampling point has to be placed above the boundary layer of the aircraft fuselage to take representative samples. In addition, the conversion of radicals into NO_2 has to take place immediately after the sampling to reduce the radical losses on the instrumental surfaces (Wendisch et al., in preparation, 2013).

Because of the location of the sampler outside the fuselage and its exposition to the free air stream, its shape, size, orientation and position is constrained by the external factors related to the accessibility and the safety regulations, such as reduction of a bird strike effect. A bird strike is a collision between an airborne animal and an aircraft (usually windscreen or engine) most often during take-off or landing, or during low altitude which results in a significant reduction of flight safety and even in a failure of the vehicle.

A reactor with small surface to volume ratio (S/V) and thus lower wall losses is characterized by higher CL value. However, low volume results in shorter modulation time which is preferable for airborne measurements. Different inner materials to manufacture the inlet have

been used such as Teflon or Teflon coated surfaces to reduce the wall losses (Koutrakis, P. et al., 1989; Hastie et. al., 1999; Miyazaki et al., 2010) and to meet the safety requirements.

The valves used for adding of the reactant gases should be mounted nearby the reactors to reduce the time for the signal stabilisation after switching the modes (between the background and signals). In addition, the tubes length should be the same so that the shifts between the signals of detector do not occur which might result in errors in the radical determination.

As mentioned in Section 2.2.3 the background and amplified signals in the reactor are measured consecutively and two backgrounds and one amplification period are averaged to obtain data. For airborne measurements, a dual-channel instrument is employed that consists of two separated reactors coupled with two detectors which concurrently work out of phase. This allows monitoring quickly changing background and results in increasing the sensitivity and accuracy in the radical determination (Green et al., 2006; Brookes et al., 2009; Kartal et al., 2010). To account for the pressure variations during the airborne sampling (involving measurements at different altitudes) which influence the stability of the chain chemistry and the NO_2 detection, two approaches are used:

- Control of the pressure in a reactor at constant value below the external pressure and keeping at constant mass flows of the sampling and addition gases (NO and CO/N_2). It is obtained by introducing a pre-reactor nozzle in front of the reactors, which is continuously kept at a constant pressure value and from which air is sampled to the reactors (Andrés-Hernández, et al., 2009; Kartal et al., 2010). A careful construction of the entry of the reactor is required so that the reactors are separated and do not interfere.
- Applying a pressure dependent correction factor for the CL based on either a laboratory characterisation or the modeling studies of the chain chemistry (Brookes, 2009).

To account for the RH variations during the sampling which affects the CL two approaches are used:

- Applying the RH correction factor determined in the laboratory experiments. However, it has to be carefully introduced in the case of $[\text{NO}_2]$ close to the detection limit, i.e., at low $[\text{RO}_2^*]$. Otherwise the background noise of the luminol detector can be unrealistically amplified (Andrés-Hernández et al., 2010).
- Reducing the RH in the reactor by keeping the reactor temperature higher than the external air,

as $RH = (p_{\text{partial}}^{\text{H}_2\text{O}}/p_{\text{saturation}}^{\text{H}_2\text{O}})$ and $p_{\text{saturation}}^{\text{H}_2\text{O}}$ rises if T_{ambient} is lower than T_{reactor} (Brookes, 2009; Andrés-Hernández et al., 2010). The RH effect on the CL can be diminished if the reactors are kept at a constant pressure below the ambient which is related to a decrease in $p_{\text{partial}}^{\text{H}_2\text{O}}$. However, thermal decomposition of peroxy nitrates like peroxy nitric acid (PNA) can result in the interference if the retention time in the reactor is high enough.

Based on a previous experience of the TROLAS group (Tropospheric Radical Observations and Laser Absorption Spectroscopy of the Institute of Environmental Physics of the University of Bremen (IUP-UB)) with the PerCA instruments on various platforms, two inlets: HALO and DUALER 2 were constructed and manufactured at the mechanical workshop of the University of Bremen within the present work. The sampling systems will be presented in the next sections and compared to the DUALER (DUal channel Airborne peroxy radical chemical amplifier) which was successfully employed for the airborne measurement of peroxy radicals during the AMMA campaign (Andrés-Hernández et al., 2009, Kartal et al., 2010) in the scientific aircraft DLR-Falcon (Deutsches Zentrum für Luft und Raumfahrt). The DUALER instrument: inlet, detectors, rack was developed at the Institute of Environmental Physics of the University of Bremen (IUP-UB). The DUALER inlet is made from stainless steel and is Teflon coated and its main parts are the following:

Pre-reactor nozzle: In this unit the air is sampled through a 1mm nozzle and the pressure is controlled. The reactors and the pressure lines are connected to this component (Fig. 3.1.1).

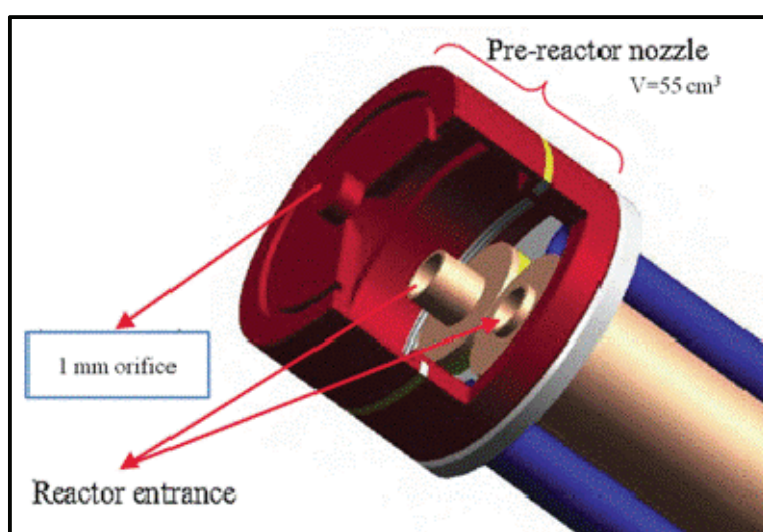


Fig. 3.1.1 The pre-reactor nozzle of the DUALER inlet (Kartal D., PhD thesis, 2009).

Reactors: The DUALER inlet has two identical reactors (with an inner diameter of ID=21 mm, length of L=310 mm). The first addition point comprises 8 orifices of ID=1.5 mm drilled radially at the top of the reactors, the second is a T-connector located at the bottom (see Fig. 3.1.3).

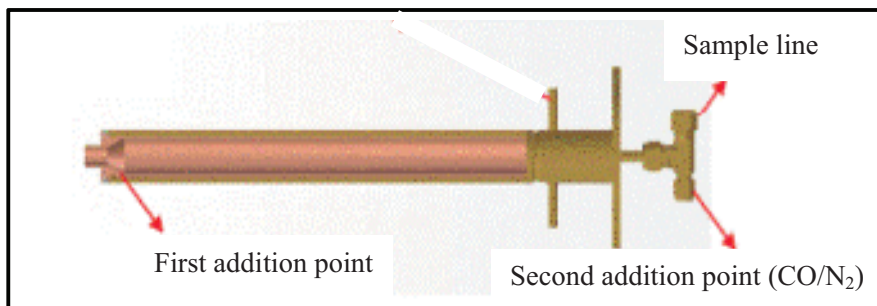
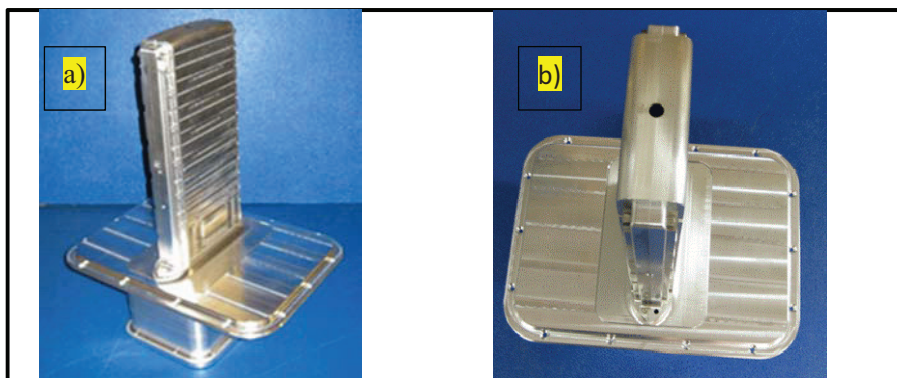


Fig. 3.1.3 A detailed view of DUALER reactor (Kartal D., PhD thesis, 2009).

Section 3.1.1 presents the HALO inlet adapted to the HALO aircraft. In Section 3.1.2 the DUALER 2 inlet to determine the losses of HO₂ and CH₃O₂ radicals on the reactor surfaces is described. Section 3.1.3 presents a glass reactor as a laboratory pre-study for the selective measurement of HO₂ and CH₃O₂. At the end the reactor employed for an investigation of the effect of amorphous silicon as a coating material on the wall losses is described.

3.1.1 HALO inlet adapted to the HALO aircraft

The HALO inlet was designed and constructed as a sampling system for the HALO aircraft to be employed during the OMO campaign. The HALO inlet housing (pylon) to be installed in the HALO aircraft fuselage, which was designed and constructed by Enviscope GmbH, is presented in the Fig. 3.1.1.1 a-c. To reduce the effects of a potential bird strike the housing physical dimensions were constrained to 126x44mm (see Fig. 3.1.1.1 d) which defines the rectangular shape and dimensions of the pre-reactor nozzle.



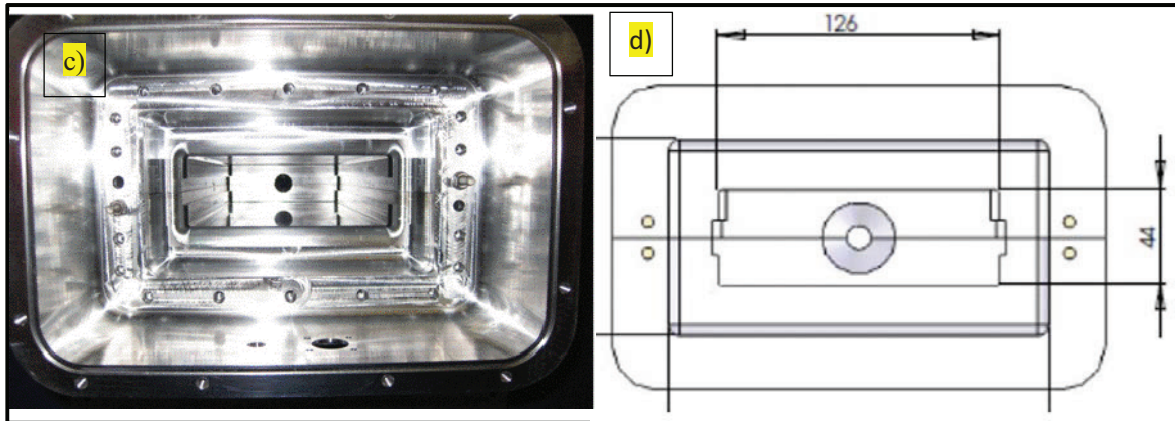


Fig. 3.1.1.1 The HALO inlet housing a) side view b) top view c) interior d) dimensions of the interior.

Another physical constraint was related to the weight of the inlet and its housing which should not exceed 29.9 kg in total according to the specifications of the window aperture of the HALO inlet (see Fig. 3.1.1.2) based on materials of the HALO-Workshop 8-9.10.2007 (Wernsdorfer, T.).

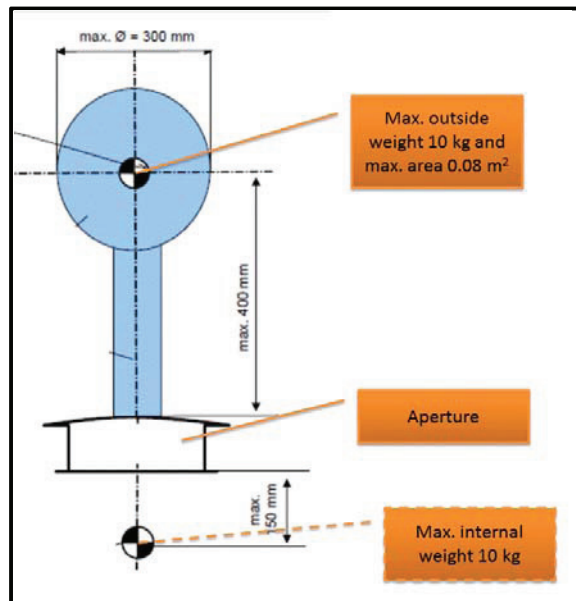


Fig. 3.1.1.2 The aperture weights.

The height of the pylon is around 35 cm so that air is sampled above the boundary layer of the aircraft fuselage (see Fig. 3.1.1.3) which is acceptable according to the simulation with Computational Fluid Dynamics-Software ANSYS CFX 10.0 (Witte K., 2009). A sampling orifice is located around 15 mm to sample air above the pylon boundary layer.

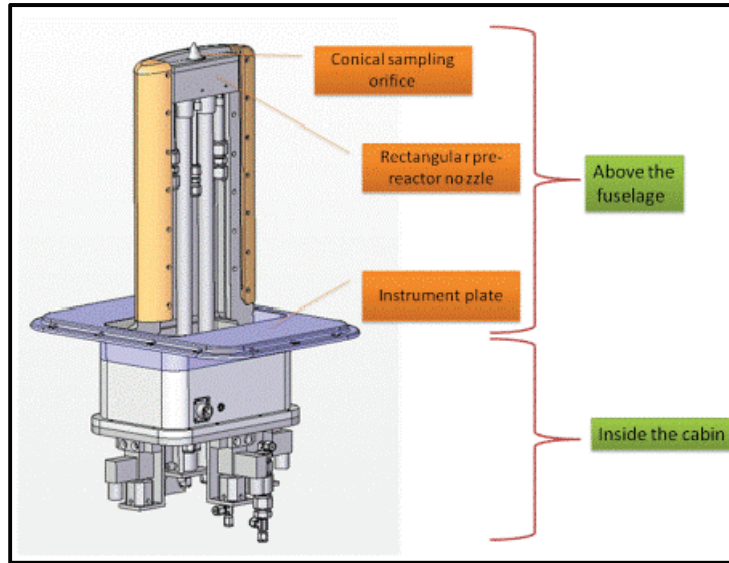


Fig. 3.1.1.3 The HALO inlet installed inside the pylon.

The HALO inlet is made of stainless steel for which all the inner surfaces in contact with the sampled air are coated with Teflon to minimize the wall losses. The main parts of the inlet presented in Fig. 3.1.1.4 are:

Pre-reactor nozzle: Through which the air is sampled and where the pressure of the inlet is regulated. Two reactors and the pressure lines made of 1/2" tubes are fixed to this unit and placed symmetrically. The pre-reactor nozzle consists of two parts presented in Fig. 3.1.1.5 a: a conical entry with a variable orifice of diameter $\varnothing 1, 1.2, 1.5$ mm as a lid which is fixed with 6 screws to a rectangular chamber 125.5 mm long, 43.5 mm wide, 45 mm high. As a sealing element a $\varnothing 2$ mm silicone O-ring is used. Owing to the space constraints a shape of the O-ring gland has been manufactured as presented in Fig. 3.1.1.5 b.

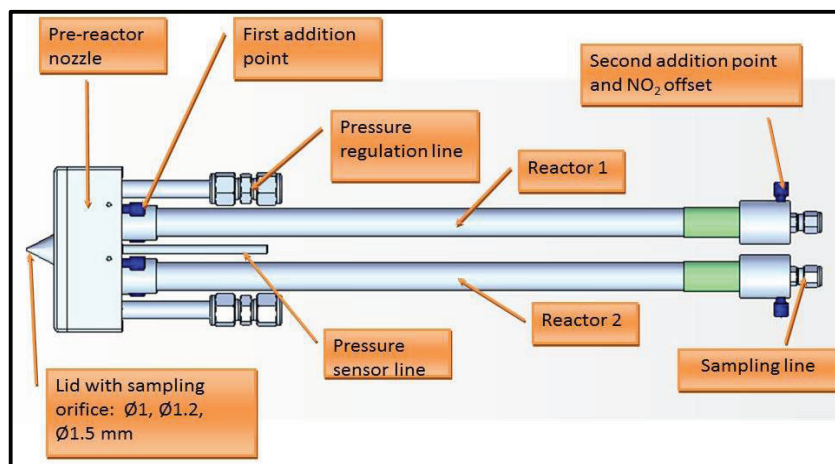


Fig. 3.1.1.4 The components of the HALO inlet.

Reactors: The HALO inlet comprises two identical reactors welded to the pre-reactor nozzle (see Fig. 3.1.1.5a). The reactor entry is a conically shaped opening with a diameter of 10 mm and an opening angle of 54.5°, which expands into a cylinder with a diameter of 17 mm and a length of 47 cm. The entry was designed as a plate that can be easily removed from the main unit. The reagent gases are delivered by 8 ring shaped small orifices with a diameter of Ø1.5 mm. The second addition point is Ø1 mm orifice in the removable element which enables montage in the aircraft.

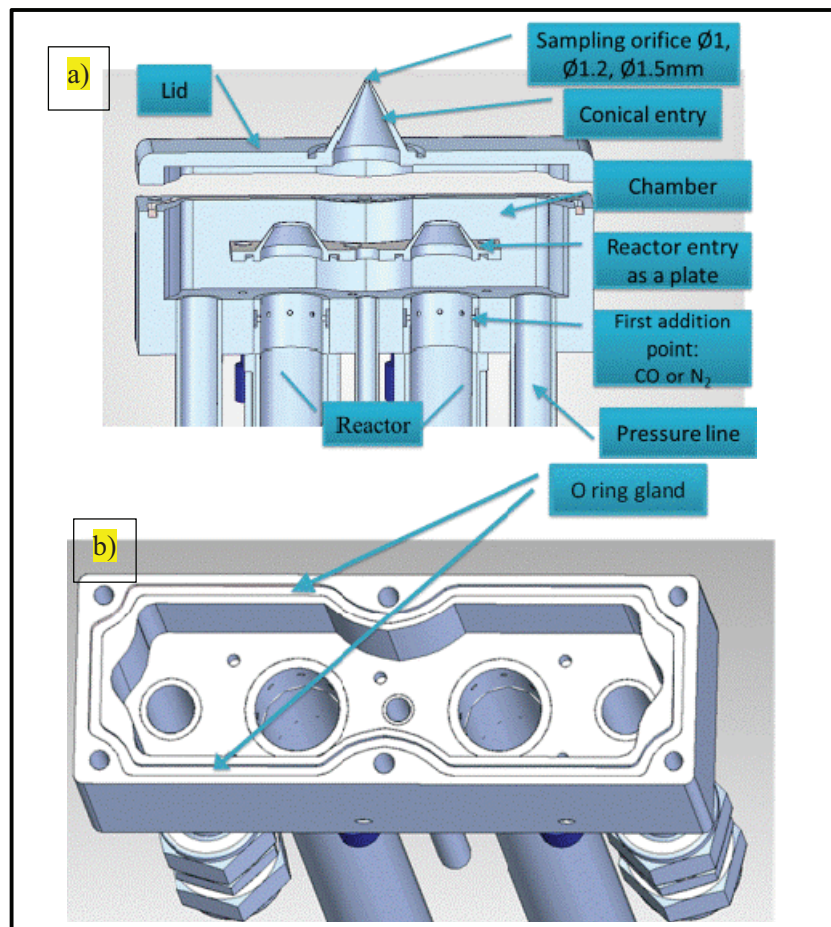


Fig. 3.1.1.5 The components of the pre-reactor nozzle a) a cut view b) O-ring gland.

Magnet valves (MV) and NO scrubber: The addition of CO and N₂ to the first and second addition points of the reactors is operated by 3-way magnet valves (Staiger, Typ QE 622). The NO scrubbers filled with FeSO₄ remove traces of NO₂ in the NO flow that is added continuously to the reactors. Both the magnet valves and the scrubbers are installed on a plate and connected at the bottom of the inlet (see Fig. 3.1.1.6). The plate during the flights will be fixed to the pylon and the aperture window (see Fig. 3.1.1.3).

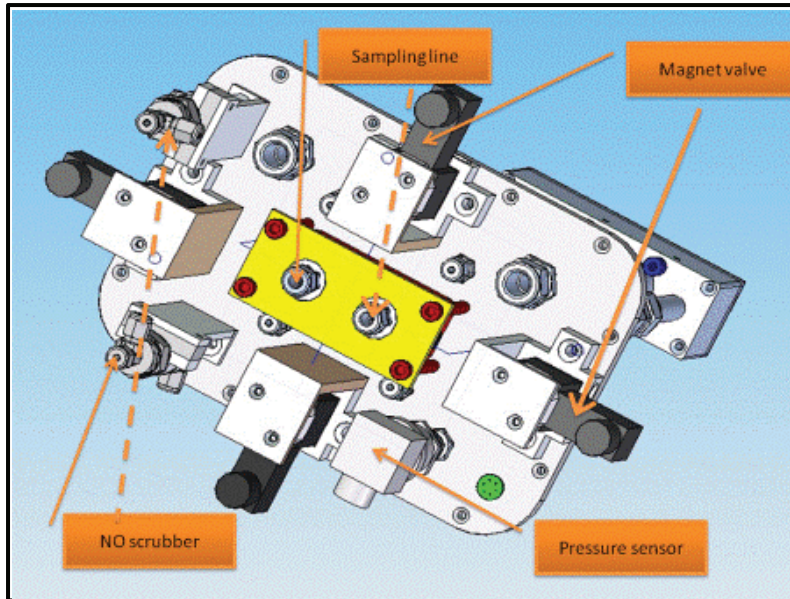


Fig. 3.1.1.6 The plate with the magnet valves and NO scrubbers and pressure sensor.

3.1.2 DUALER 2 inlet

A laboratory pre-study was conducted for characterizing an aircraft inlet for the selective measurement of HO_2 and RO_2 by using a dual channel system: DUALER 2. By using the PeRCA technique the sum of concentration of HO_2 and RO_2 is determined. HO_2 radicals show a greater loss rate in contact with the inlet walls comparing to RO_2 . Based on this property, a modified reactor to measure solely RO_2 was constructed varying the position of the addition point of NO and CO as shown in Fig. 3.1.2.1. Theoretical considerations of the radical removal in the modified reactor are presented in Section 4.2.3.

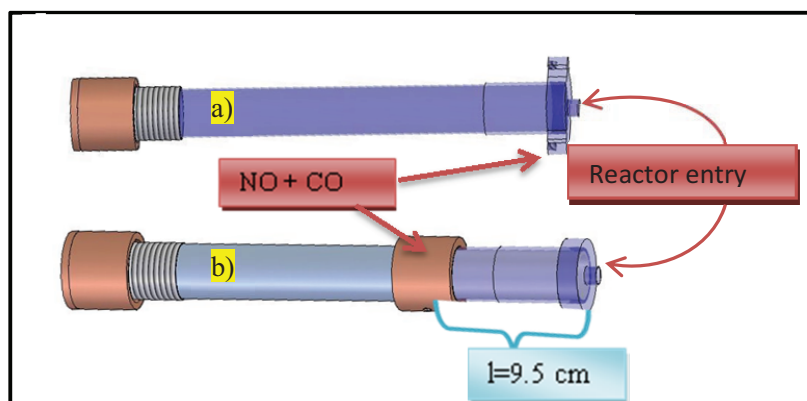


Fig. 3.1.2.1 a) The reference reactor and b) the modified reactor with the first addition point 9.5 cm below the reactor entry.

The DUALER 2, shown in Fig. 3.1.2.2, can be disassembled into its basic components. The reactors are removable and can therefore be integrated into another set-up or replaced by other with a modified length. The second addition point of gases can be dismantled so that a Teflon insert can be placed inside the reactor to reduce its diameter. However, such a system, in contrast to a welded block, is vulnerable to leaks that have to be carefully identified and tightened.

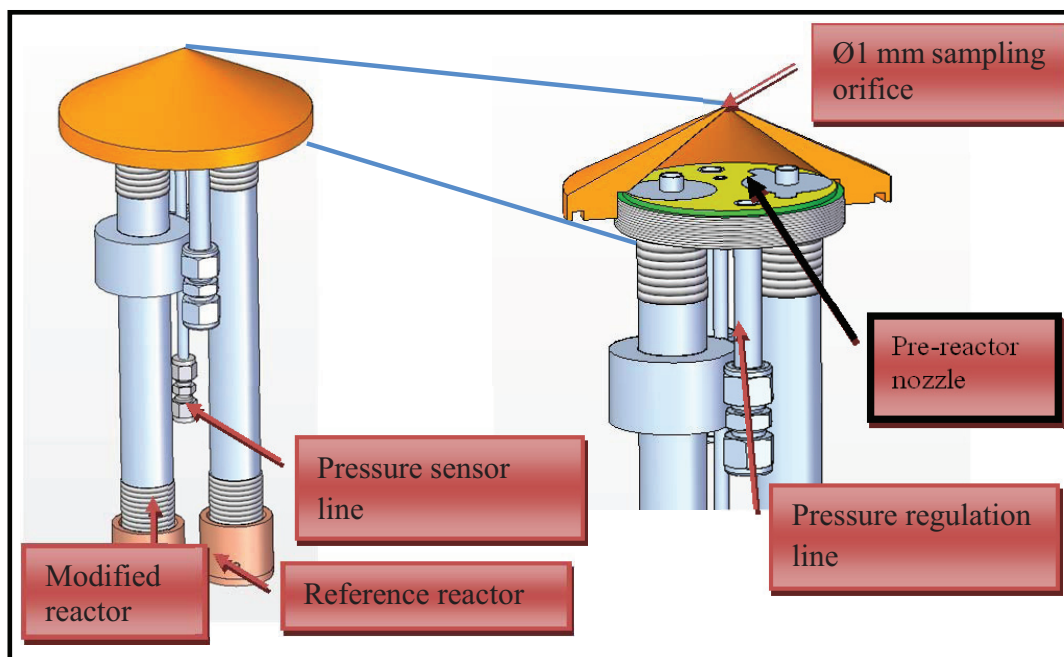


Fig. 3.1.2.2 A scheme of the DUALER 2 inlet and a cross section of the conical pre-reactor nozzle.

Comparison of the sampling systems

The HALO and DUALER 2 inlets are based on the DUALER design (Kartal D., PhD thesis 2009) trying to address and improve the issues identified as problematic in the previous work, which can affect the sampling of the radicals and the operation of the PerCA instrument:

- The pre-reactor nozzles are compared in Table 3.1.2.1. A conical shape of the DUALER 2 and HALO inlets (see Fig. 3.1.1.3 and 3.1.2.2) was selected to minimize the losses on the instrumental surface before the introduction of the radicals into the inlet, in contrast to a flat top of the pre-reactor nozzle of the DUALER (see Fig. 3.1.1) which might enhance this process. The pre-reactor nozzle shapes of the DUALER and DUALER 2 inlets are symmetrical, thus there is not expected enhancement of turbulence resulting from asymmetries in flow conditions during the sampling to the reactors, which might be the case in an asymmetric nozzle of the HALO inlet.

Less effective removal process of the radicals are expected within a bigger sampling orifice ($\text{Ø}1.5$ mm) as the losses are proportional to the surface to volume ratio S/V which is 33% lower for the $\text{Ø}1.5$ mm sampling orifice in comparison to the $\text{Ø}1$ mm of the HALO inlet. Likewise, the same magnitude of wall losses is expected in $\text{Ø}1$ mm orifice of all three inlets. The sampling flow is twice higher in case of the HALO and DUALER 2 inlets than the DUALER. Higher flow is related to lower residence time in the pre-reactor nozzle, thus the radicals have less time to be removed on the walls. On the other hand, higher flow corresponds to higher velocity which may lead to turbulences in the pre-reactor nozzle, and consequently higher losses of the radicals.

Inlet	DUALER by Kartal et al., 2009	HALO (this work)	DUALER 2 (this work)
Shape	cylindrical	rectangular	conical
Orifice diameter [mm]	1	1, 1.2, 1.5	1
Inner dimension [mm]	$\text{Ø}63$	101.5x31.5	$\text{Ø}49$
Height [mm]	20	30	37
Volume [cm^3]	55	95	94

Table 3.1.2.1 Geometrical features of the pre-reactor nozzle of the DUALER, DUALER 2 and HALO inlets.

- The reactors are compared in Table 3.1.2.2. The diameter of the DUALER 2 reactor is 1.4 higher than the DUALER reactor, for the HALO reactor is 24% higher than the DUALER. And thus, on the basis of the S/V ratio, lower losses are expected in case of DUALER 2 reactor and higher radical losses for HALO reactor in comparison to the DUALER.

	Reactor by Kartal et al., 2009 DUALER	HALO (this work)	DUALER 2 (this work)
Entry diameter [mm]	10	10	9
Entry length [mm]	10	10	7
Inner diameter [mm]	21	17	29
Length [mm]	366	500	321
Volume [cm^3]	127	114	206
S/V [$1/\text{cm}$]	1.90	2.35	1.38
Q flow [dm^3/min]	0.5	1	1
t residence time [s]	15.4	6.8	12.4
Reactor material	Stainless steel coated with Teflon		

Table 3.1.2.2 Comparison of the features of the DUALER, HALO, DUALER 2 reactors.

- For the DUALER 2 and HALO inlets as the pressure regulation lines two symmetrically placed ½” tubes are used. The pressure sensor (Druckmessumformer DMP 331, BD SENSORS GmbH) is installed in the line in the pre-reactor nozzle. Therefore, the pressure can be more accurately determined in the pre-reactor nozzle of the DUALER 2 and HALO inlets. In contrast to the DUALER for which the sensor was installed on the rack together with the pressure regulator.

3.1.3 Different inlet materials and coatings

Teflon and silicon coating

Two identical stainless steel reactors but coated with two different materials: Teflon and new material amorphous silicon SilcoNert 2000 were constructed and presented in Fig. 3.1.3.1. The radical wall losses depend on the properties of surface material (Mihele et al., 1999) and it has been shown that coating the reactor surfaces with Teflon reduces the radical wall losses and increases the sensitivity of the PeRCA technique (Ashbourn et al., 1998). Thus, the reactors employed by the TROLAS group of the University of Bremen for airborne measurement of peroxy radicals, e.g., during the AMMA Campaign (Kartal et al., 2010) are made of stainless steel and Teflon coated by a company HST GmbH. The new coating material amorphous silicon SilcoNert 2000 shows advantages as follows: resistance to temperature deformations and reduction of layer porosity and thereby chemicals cannot diffuse inside coating and destroy it and through desorption contaminate the sampled air.

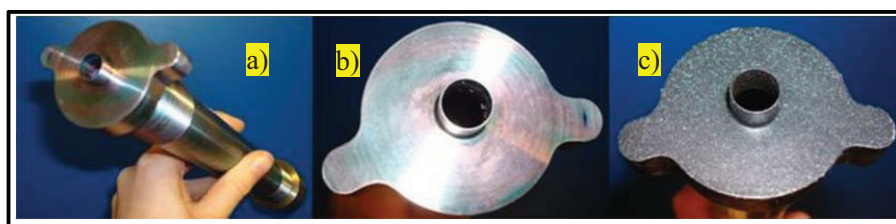


Fig. 3.1.3.1 The stainless steel reactor a) and b) silicon coated and c) Teflon coated.

Glass reactor

The glass reactor (see Fig. 3.1.3.2) was used for a characterization of the dependence of the chain length on NO concentration in the reactor as a laboratory pre-study. It has a diameter of ID= 20 mm and a length of L=220 mm; its entry has a diameter of ID=4 mm and is 25 mm long.

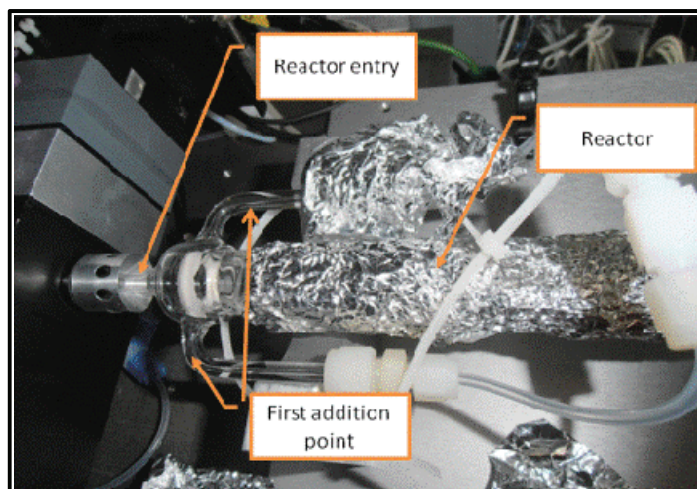


Fig. 3.1.3.2 The glass reactor.

3.1.4 Operation conditions of the sampling set-ups

The pressure at the pre-reactor nozzle of the HALO and DUALER 2 inlets was kept below the external pressure, which was achieved by a regulation with a pressure controller (Bronkhorst, HI-Tec Model F-004AI-IUU-55-V) and a pressure sensor (DMP 331). Each reactor was connected to a mass flow controller (Bronkhorst, F-201DV-RBD-22-K) modified in such a way that it can be operated with a pressure difference $\Delta p=100$ mbar between the input and the output of the device. The sampling flow was kept at 1l/min STP.

To the sampled air NO with CO/N₂ was added to the first addition point of the reactors which can be operated in the same or opposite modes (SG or BG, i.e., signal and background) by three way magnet valves (Staiger, Typ QE 622) switching every 60 or 90 sec the modes. In order to prevent the pressure variations by switching the measurement modes and to keep the mixing ratios constant, the same amount of N₂/CO was added at the second addition point.

To obtain high *CL* the inlet is generally operated with 9% CO and 3 ppmv NO, in case of the glass reactor 3-24 ppmv NO. However, a further increase of NO between 3-6 ppmv though corresponding to an increase of the *CL*, results in a decrease in the absolute sensitivity of the NO₂ luminol detector.

In the laboratory studies the offset of the NO₂ detectors was kept at 40 ppbv to work in a linear range of the detectors.

The flow controllers, the pressure regulator and the magnet valves were operated by the application created in Labview within this work (see Section 3.5).

3.2 Laboratory set-ups employed for the experimental work

In the following sections the set-ups, namely a DUALER rack and a pressure chamber, a HALO rack used for the characterization of inlets (the sampling systems) will be presented.

3.2.1 DUALER rack

The characterization of the HALO and DUALER 2 inlets involved employment of some components of the DUALER rack, i.e., the luminol detectors, the luminol feed, the NO₂ mass flow controllers, the data acquisition DAQ set-up, which is a part of the DUALER instrument (see Section 3.1). The components of the DUALER rack are (see Fig. 3.2.1.1):

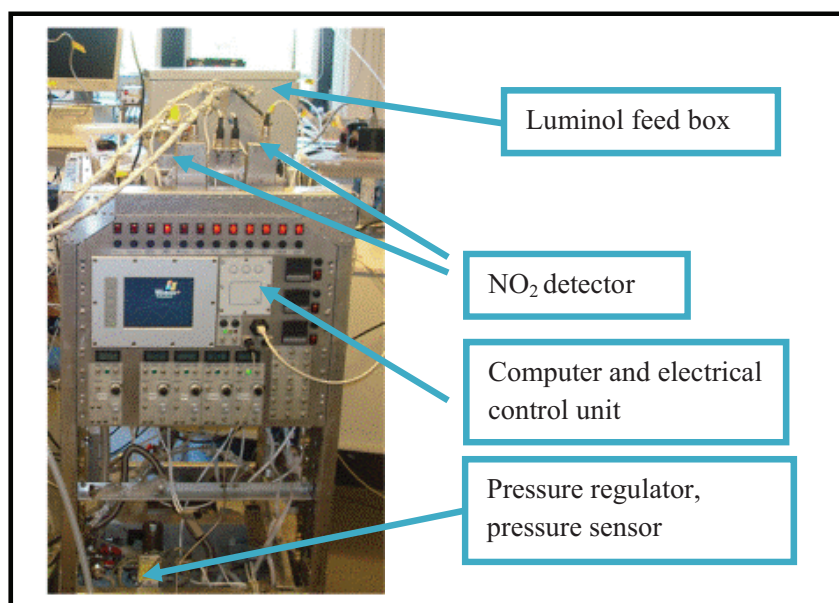


Fig. 3.2.1.1 Components of the DUALER rack employed in this research.

Computer and the electrical control units: The computer is used for data acquisition. The operation of the flow controllers and the data collection of the detector signal are controlled by the data cards (Data Translation, Inc DT 322 Multifunction Data Acquisition Board).

Mass flow controller, scrubbers: The NO₂ mass flow controllers are operated by the computer and the electrical control unit. Both input and output gases are purified using the chemical converters. Charcoal/iodine trap removes iron and nickel carbonyls from CO, FeSO₄ trap removes traces of NO₂ in NO, and both scrubbers are located prior to the mass flow controllers. The exhaust

air contains 9% v/v CO and 3 ppmv NO. Pt/Al pellets placed in 1/2" tube (see Fig. 3.2.1.2) at a temperature $T > 100^\circ\text{C}$ convert CO into CO_2 , whereas NO is removed by adsorption on activated charcoal.

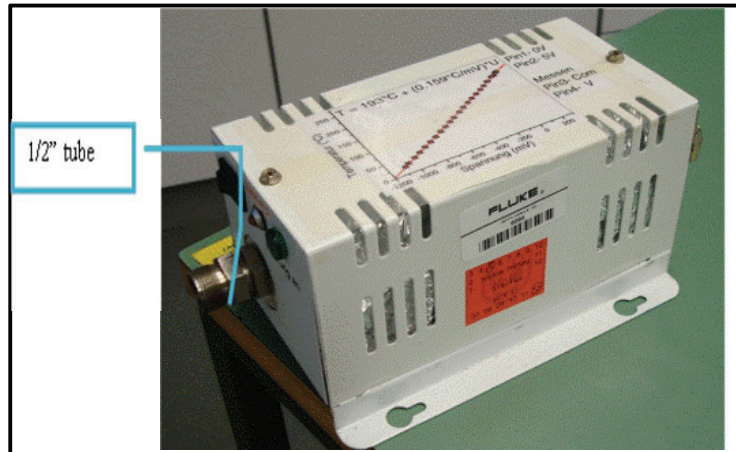


Fig. 3.2.1.2 The 1/2" CO scrubber.

NO₂ detector unit: The NO₂ detection is based on the chemiluminescence reaction of NO₂ with 5×10^{-4} M luminol solution (3-aminophthalhydrazide: $\text{C}_8\text{H}_7\text{N}_3\text{O}_2$) taking place on the surface of a Whatman glass fibre filter. The photons at wavelength range 400-500 nm are detected with a photodiode (Hamamatsu Si-1248) whose signal is amplified and converted to a voltage that is digitized and stored by a data acquisition system (Agilent Vee). The homemade detector (see Fig. 3.2.1.3 a) consists of the detector unit and the luminol box. The inlets and the luminol box with the peristaltic pump for the luminol flow (see Fig 3.2.1.3 b) are operated under the same pressure to prevent instabilities in the detector response due to irregularities in the pressure conditions.

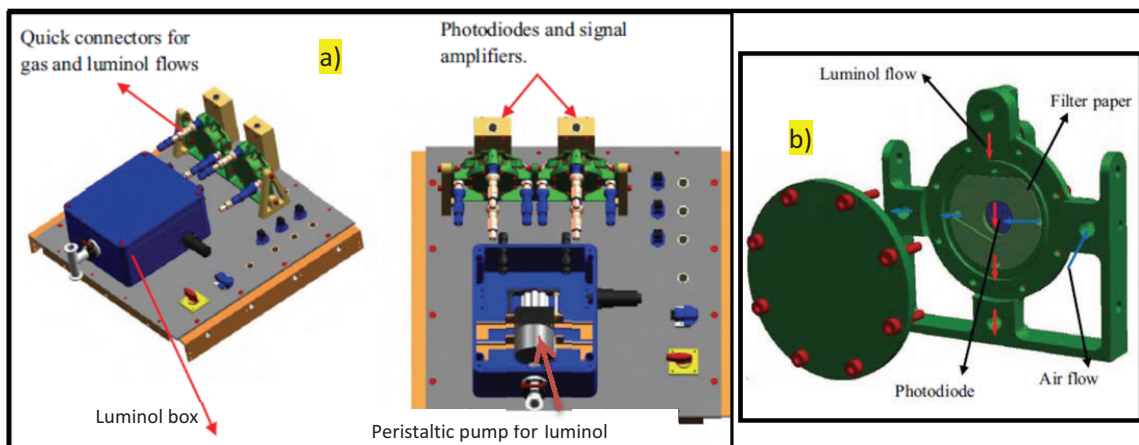


Fig. 3.2.1.3 a) Inner view of the detector b) NO₂ detector unit (Kartal, D., PhD thesis, 2009).

3.2.2 Pressure chamber and radical source

A pressure chamber was employed within this research to simulate the pressure variations close to the flight conditions and with this objective, the HALO inlet was installed in the chamber. The chamber is a metal cylinder with a volume of 0.2 m³ with an inner diameter of 49.5 cm and a length of 105 cm. The closure lids are constructed from a 25mm thick Plexiglas. The feed-throughs for data cables, gas lines, and electrical connections to the power suppliers of the instruments installed outside the chamber are fixed on the flanges welded along the chamber (see Fig. 3.2.2.1). A vacuum pump evacuates the pressure chamber whose pressure is regulated by a MKS pressure regulator (Model 640A13TS1K62K), the absolute value of the pressure in the chamber is measured with a MKS barometer (Model 122BAX-01000DBS).

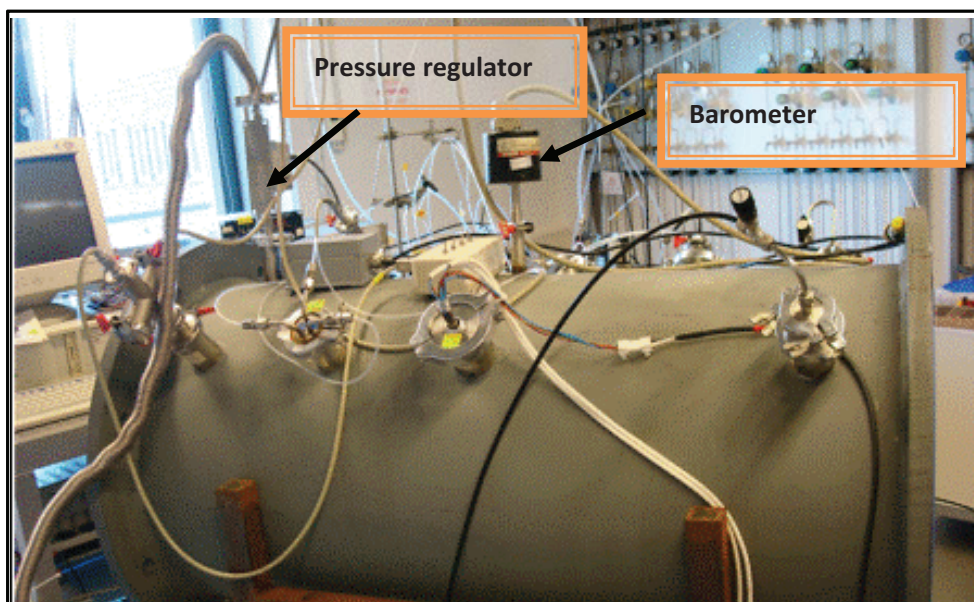


Fig. 3.2.2.1 The pressure chamber.

The radical source used for the calibrations is located inside the chamber. The radicals are generated by the photolysis of water at 184.9 nm in the presence of oxygen (Shultz et al., 1995). The synthetic air is humidified in a glass unit with a peristaltic pump (Fig. 3.2.2.2). Different water flows and thus different water mixing ratios in the calibration air are created by alternating the pump velocity. The water content in the sampled air is calculated from the dew point temperature of the sampled gas measured by a dew point sensor (Vaisala DMP 248) installed inside the chamber.

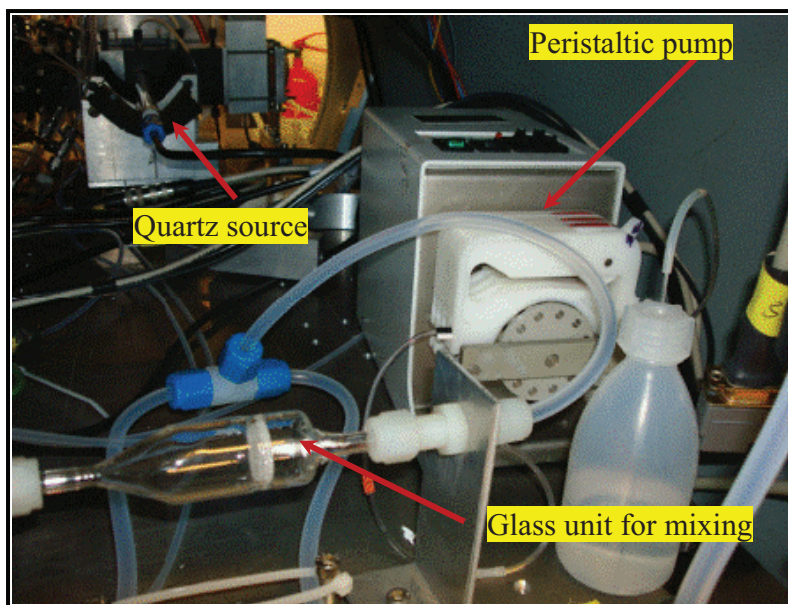


Fig. 3.2.2.2 The humidifier unit of the radical source.

Then the humidified air undergoes photolysis in the photolysis zone where the radical production occurs (see Section 3.4.2). Prior to the introduction to the photolysis zone CO is mixed with the calibration air so that OH, which is the photolysis product of water, is converted into HO₂ (see Section 3.4.2). The IUP-UB calibration source, described in detail elsewhere (Reichert et al., 2003), consists of the following components (shown in Fig. 3.2.2.3):

Hg-Lamp (Pen-Ray lamp): The 184.9 nm emission line of the mercury vapour is used for the photolysis of H₂O and O₂ (see Section 3.4.2). The lamp installed in a block is kept at constant temperature around 40°C to avoid unstable lamp profile resulting from the temperature changes of air. The lamp spectrum depends on the age and the operation conditions (Hofzumahaus et al., 1997).

Shutter: This unit allows cutting off the lamp light without switching off the lamp.

Cylindrical Lens: This unit is used to create a parallel beam of light from the lamp through the absorption and the photolysis cells.

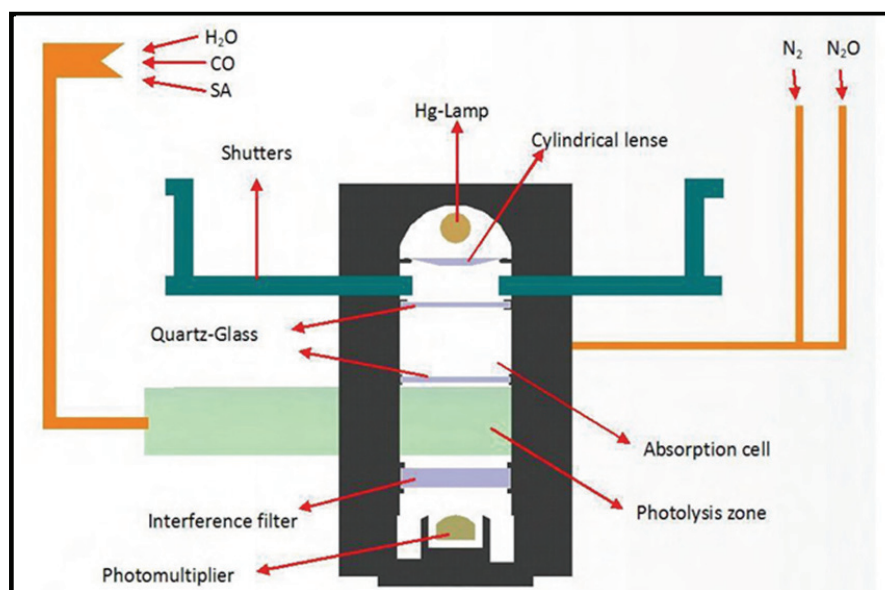


Fig. 3.2.2.3 Schematic diagram of the IUP radical source (Kartal, D., PhD thesis, 2009).

Absorption cell: The absorption zone is the zone between the Hg lamp and the photolysis zone and consists of two quartz discs in a distance of 23 mm having 85% transmission for 184.9 nm light. The intensity of the light is changed by using a gas filter, i.e., varying the N_2O/N_2 ratio as N_2O has around 184.9 nm a fairly constant absorption coefficient ($14.05 \times 10^{-20} \text{ cm}^2 \text{ molecule}^{-1}$ at 25 °C (Cantrell et al., 1997)). Different radical mixing ratios are produced by modifying the light intensity at the absorption cell at constant mixing ratio of water in the calibration air.

Photolysis zone: The photolysis zone defined as the region where the UV radiation from the Hg lamp photolyzes the H_2O and O_2 is a cylindrical quartz tube with an inner diameter of 15 or 16 mm and a length of 20 cm.

Interference Filter: This filter allows the specific transmission for the wavelength of interest 184.9 nm. The peak wavelength for the filter is 184.9 ± 2.5 nm with the transmittance 12.5%.

Photomultiplier: The light is detected by a photomultiplier Hamamatsu 1259 with the MgF_2 window enabling a spectral response between 115 and 195 nm.

Purging system: All the optical paths in the source are purged with N_2 to prevent the potential interferences of the ambient air during the calibration.

The original IUP-UB radical source, shown in Fig. 3.2.2.4 a, has been modified so the HALO inlet and its adapter could be be installed in the pressure chamber by (shown in Fig. 3.2.2.4 b):

- exchange of the shutter,
- repositioning of the PMT,
- removal of one interference filter thus an increase of the light intensity and a reduction of the PMT supply voltage.

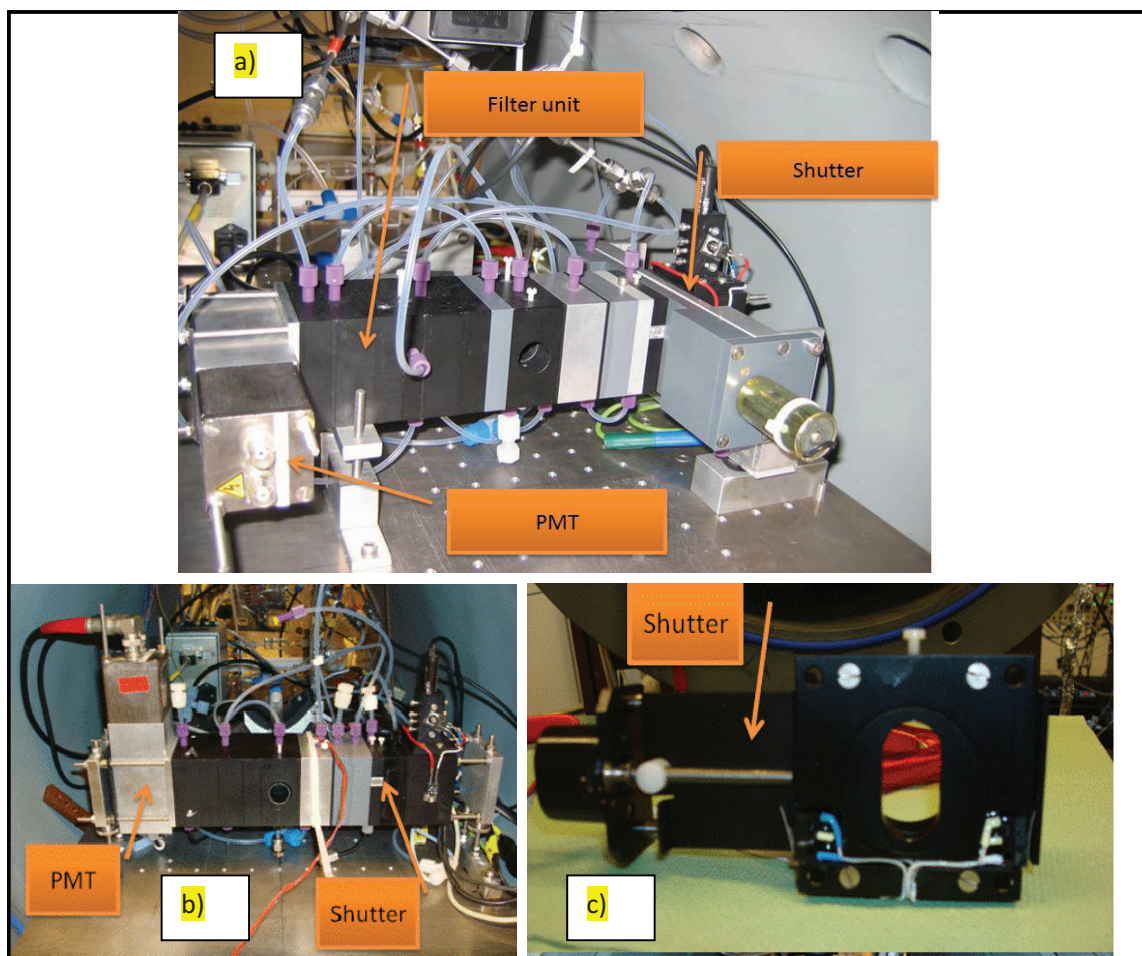


Fig. 3.2.2.4 a) The original IUP radical source, b) the modified source, c) the new shutter.

The hysteresis of the PMT signal was observed (see Fig. 3.2.2.5). A photomultiplier tube exhibits a slightly unstable output as an overshoot for several seconds after the light was input before a stable level is reached. The hysteresis is mainly caused by the electrons deviating from their trajectories and electrostatically charging the dynode support section and the glass bulb (Source: Photomultiplier tubes, HAMAMATSU).

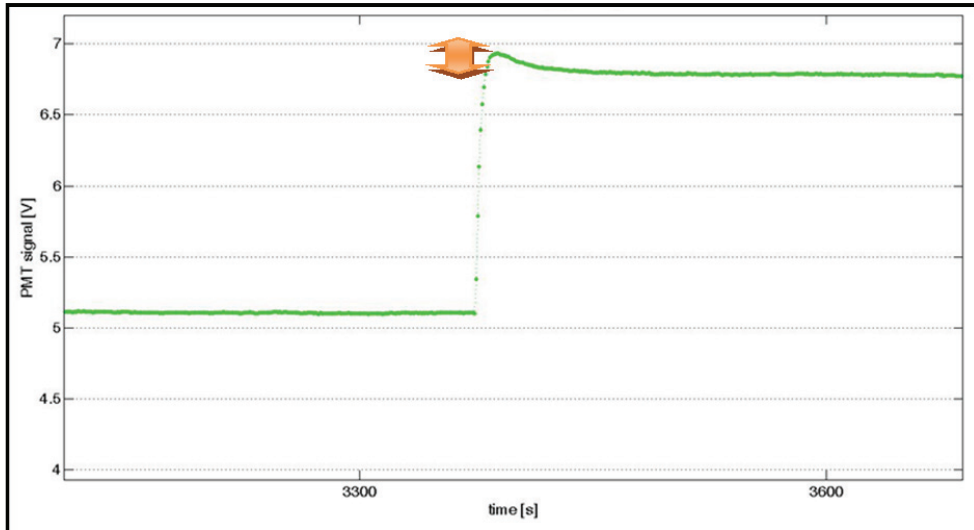


Fig. 3.2.2.5 The hysteresis as an overshoot (orange arrow).

To account for a longer stability time, the PMT signal collection after changing the light conditions was extended in the O_2 cross section and the HO_2 calibration programs and then first 90 s of the PMT signal was removed so a steady signal is obtained (presented in Fig. 3.2.2.6).

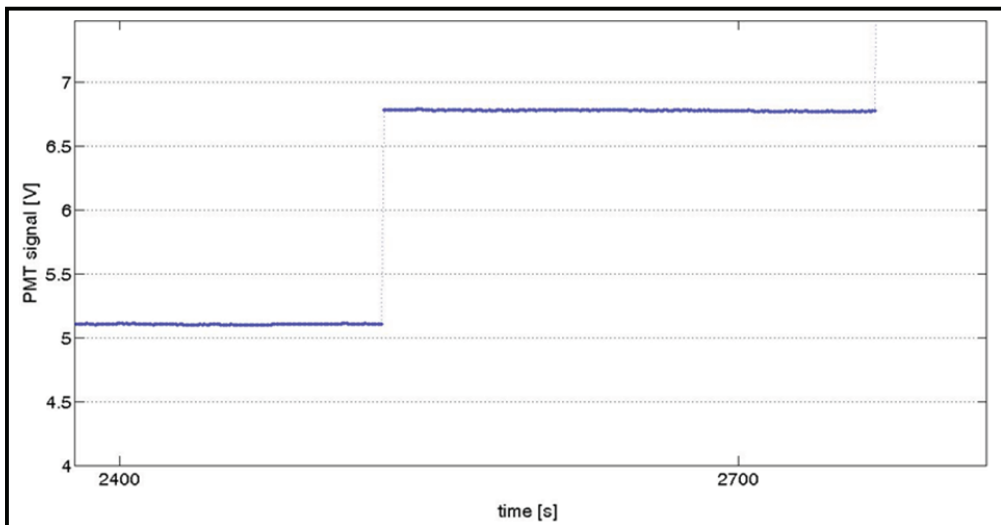


Fig. 3.2.2.6 The PMT signal filtered from the hysteresis.

The sampling systems: HALO and DUALER 2, described in Section 3.1, were installed in the pressure chamber with the special adapters fixed to the Plexiglass closure lids (presented in Fig. 3.2.2.7). The radical source position was adjusted to assure that the air is sampled from the middle of the source, i.e., a position of the sampling remains the same which guaranties the reproducibility of the radical mixing ratios introduced into the inlet.

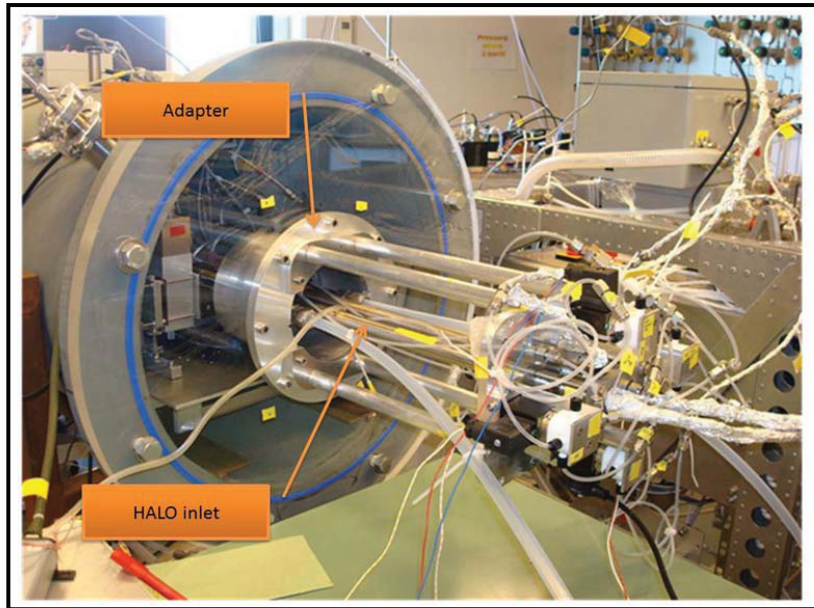


Fig. 3.2.2.7 The HALO inlet installed to the pressure chamber for calibration purposes.

3.3 HALO set-up

The HALO instrument: PerCEAS (Peroxy radical Cavity Enhanced Absorption Spectrometers) will consist of the HALO inlet and the HALO rack which is the operation unit of the system. The certification for deployment of the PerCEAS in the OMO mission was started in the collaboration with Enviscope GmbH to show that the HALO safety requirements are fulfilled. The main parts of the HALO rack are schematically represented in Fig. 3.3.1:

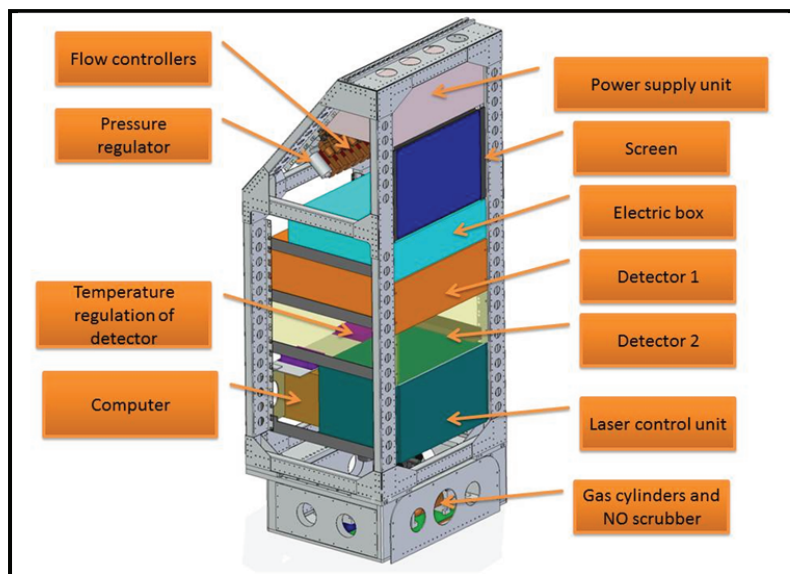


Fig. 3.3.1 Components of the PerCEAS rack.

Computer: The computer is responsible for data acquisition. The operation of the flow controllers and the data collection of the detector signal are controlled by data acquisition cards.

Electrical control units: The power suppliers for the temperature sensor, the relative humidity sensor, the magnet valves and the mass flow controllers, the laser and its control unit are all installed in this unit.

CEAS detector (Cavity Enhanced Absorption Spectroscopy), laser control unit:

The NO₂ detection is based on laser absorption spectroscopy - CEAS. The detector shown in Fig. 3.3.2 is homemade. The finesse cavity is made of cast plate aluminium and has a volume of 280 cm³. As a laser the extended cavity diode laser (ECDL) at 409 nm is used and it is controlled by a control unit comprising the laser current controller, the laser temperature controller, and the piezo controller. The light detector is a photodiode, Femto Messtechnik GmbH, HCA-S, 10 MHz bandwidth, 10⁴ V/W. The high-reflectance mirrors in the cell have a minimum reflectance of 99.995%, the transmission is approximately 0.002%. The sampled air is introduced to the cell with two inlets and is removed by one outlet located in the center of the cell. The temperature of the detector case is controlled by the temperature regulator.

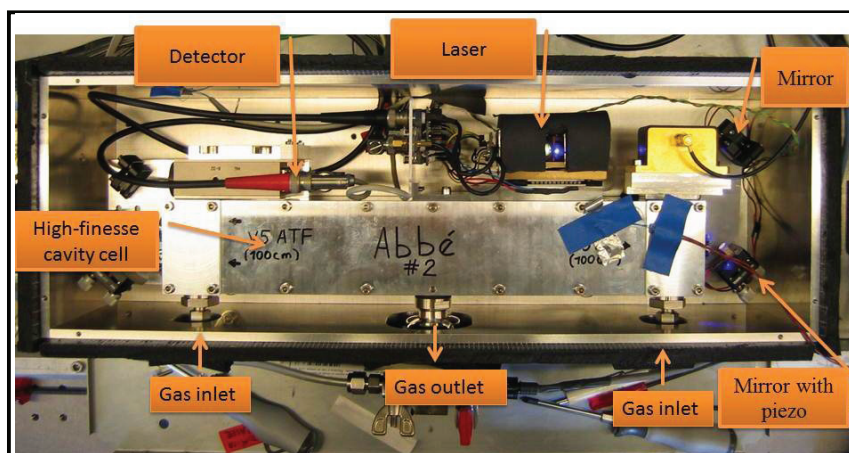


Fig. 3.3.2 The CEAS NO₂ detector.

Gas cylinders, mass flow controller, scrubbers: The gas cylinders planned to be used during the flights will be connected to the mass flow controllers operated by the computer and the electrical control unit. The NO and NO₂ cylinders will be placed in the HALO rack on the drawer (see Fig. 3.3.3 a).

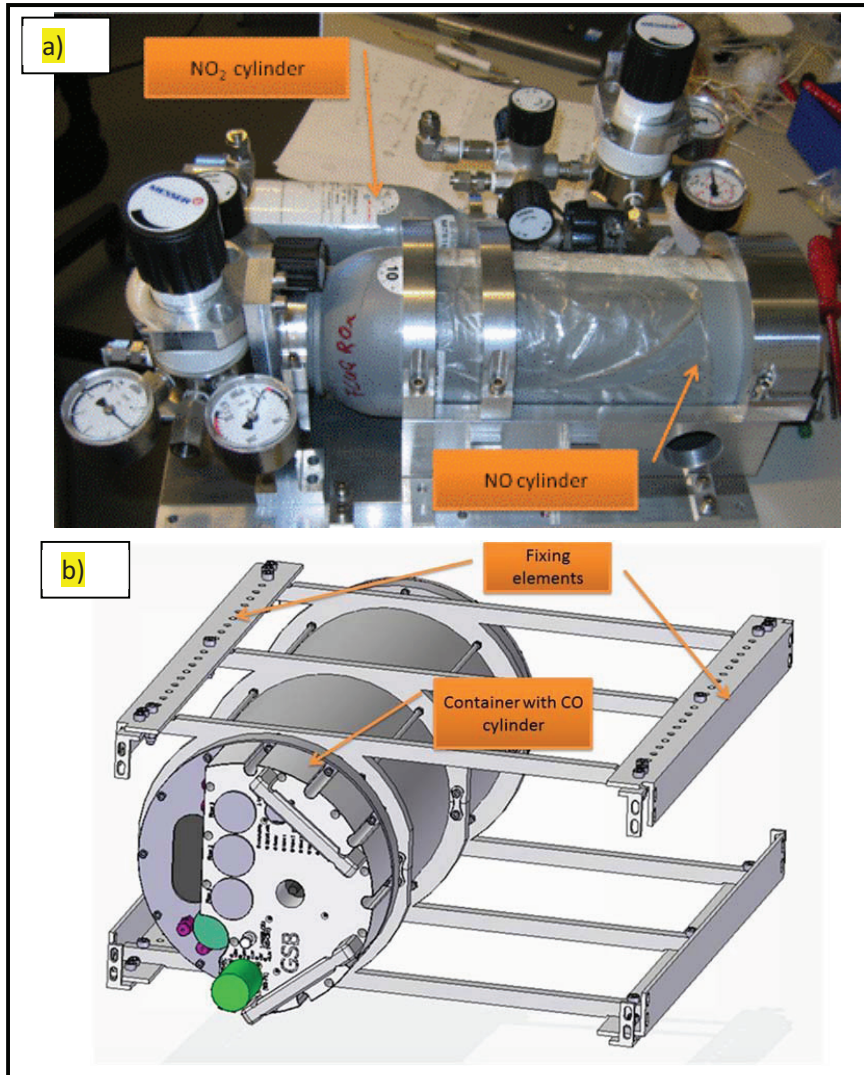


Fig. 3.3.3 The gas cylinders and its fixing elements a) NO and NO₂ b) CO.

Additionally, there is the NO scrubber between the NO flow controllers and the NO gas cylinder containing FeSO₄ to remove the NO₂ traces from NO. The CO gas cylinder, the CO scrubber will be placed in another rack next to the HALO rack in a special pressure-resistant container (see Fig. 3.3.3 b). The CO scrubber is located prior to the CO flow controllers containing charcoal/ iodine to remove iron and nickel carbonyls from CO.

Vacuum pump, scrubbers: These units are placed in a special rack for the vacuum pumps, shown in Fig. 3.3.4, placed in the rear part of the HALO aircraft.

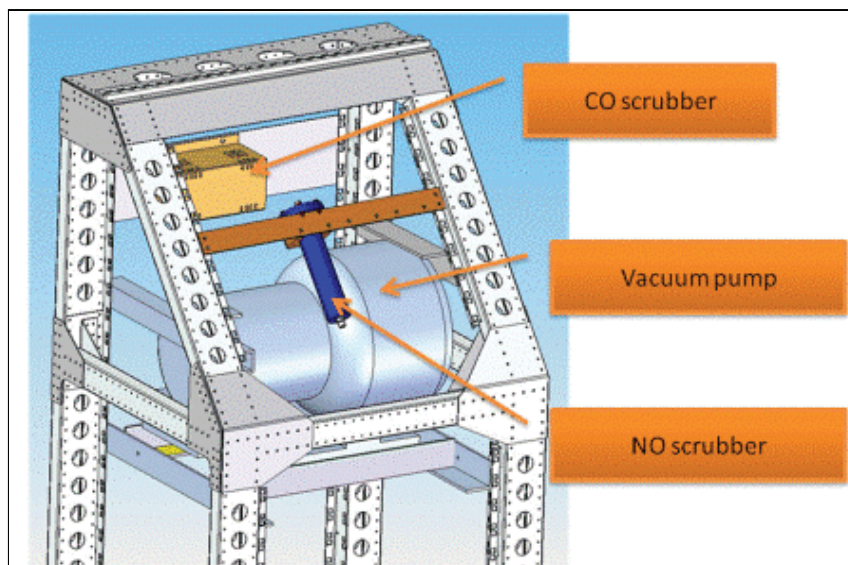


Fig. 3.3.4 The pump and the scrubbers fixed at the pump rack.

A vacuum pump (SCROLLVAC SC 30D) connected to the pressure controller is used to regulate the pressure of the HALO inlet and to sample the required air through the system. As in the DUALER rack, CO gas in the exhaust line is converted into CO₂ by means of a catalytic reaction taking place in the scrubber installed before the vacuum pump. A new CO scrubber (see Fig. 3.3.5 a) was constructed based on using a KF-25 stainless steel tube containing Pt/Al pellets heated to temperature above 100°C to initiate the conversion of CO into CO₂. At the ends of the scrubber there is placed a dense grid to prevent the pellets to be sucked from the tube. The NO_x scrubber is a 40 mm diameter tube filled with charcoal powder which adsorbs NO_x (see Fig. 3.3.5 b).

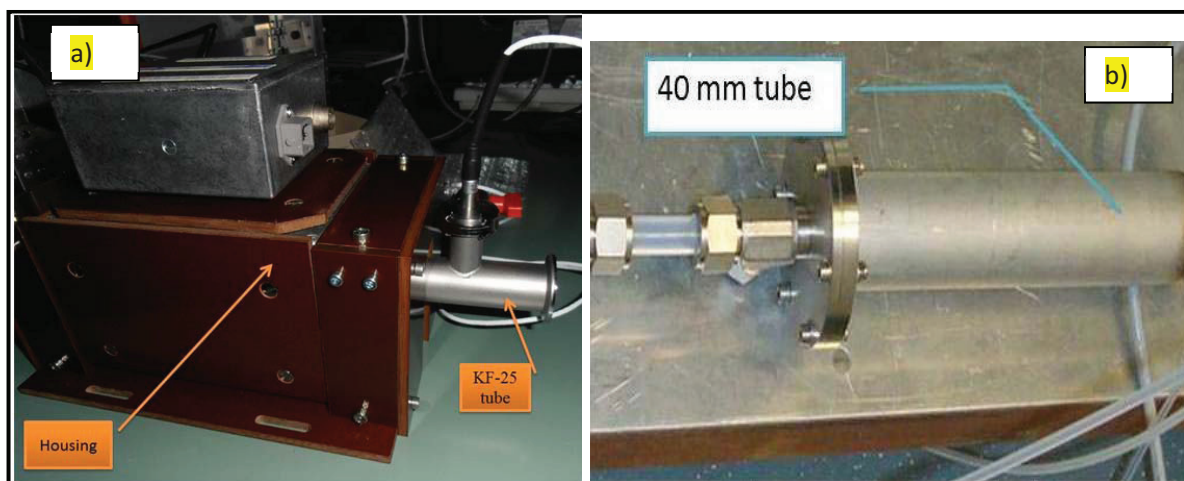


Fig. 3.3.5 The scrubbers in the exhaust line b) Tube KF-25 flanged for new CO scrubber c) NO_x scrubber.

The HALO instrument: the inlet (shown in Fig. 3.3.6a, b), the HALO rack with the gas cylinders drawer (shown in Fig. 3.3.7c), the pump on the pump rack were installed in the HALO aircraft in August 2009 as a pre-mounting test before the OMO campaign. In addition, the length of electric cables, gas tubes were determined and their fixing elements to the aircraft walls were defined.

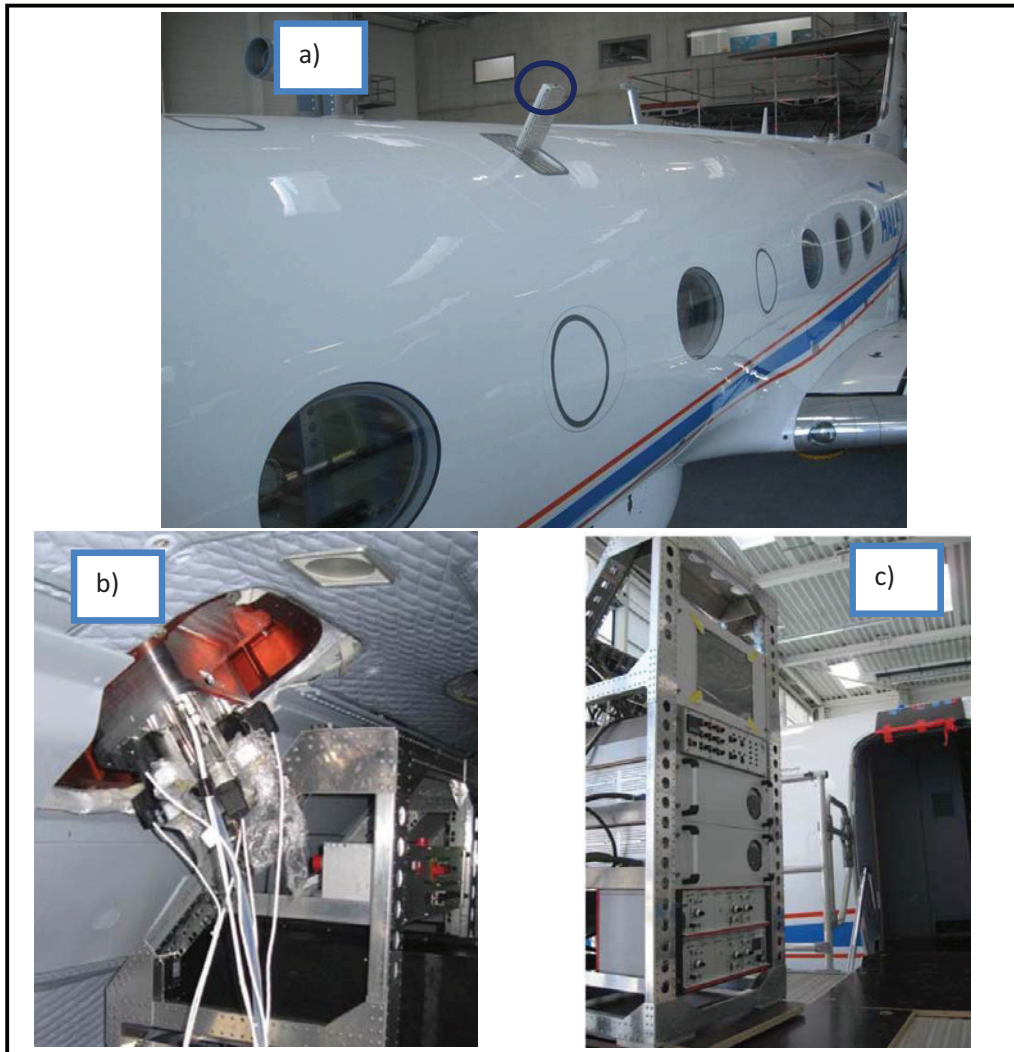


Fig. 3.3.6 The HALO inlet installed in the HALO aircraft a) the pylon and a sampling point marked as a blue circle b) view inside the cabin c) the HALO rack before an installation in the HALO aircraft.

3.4 Calibration procedures for the PerCA technique

The PerCA technique is not a direct method for the measurement of peroxy radicals, thus a calibration of the measurement instrument at the conditions expected during the flights comprises a series of steps:

- Response of the detector to known NO₂ mixing ratios called ‘NO₂ calibration’, described in Section 3.4.1,
- Determination of the chain length – a conversion factor of HO₂ into NO₂ called ‘HO₂ calibration’, described in Section 3.4.2.

3.4.1 NO₂ calibration

Regular calibrations of the luminol detector consists in adding different NO₂ flows from the gas cylinder (around 10 ppmv NO₂) mixed with synthetic air (SA) to create known NO₂ mixing ratios and then measuring the detector response. The response is quadratic as 2 molecules of NO₂ are believed to participate in the chemiluminescent reaction with the luminol in the absence of NO (Wendel et al., 1983; Cantrell et al., 1993 a). The response is linear to a very good approximation above 3-5 ppbv in absence of NO (Kelly et al., 1990; Clemitshaw et al., 1997). Thus, the aim of this calibration is to determine parameters ‘*a*’ and ‘*b*’ with the linear least square fit method:

$$[NO_2] = a * V + b \quad (3.4.1.1).$$

Where: ‘*1/a*’ is a sensitivity [V/ppbv], *b* an offset [ppbv], *V* the detector response in volts, [*NO*₂] the NO₂ mixing ratio in ppbv.

The sensitivity of the detector is reduced by a factor of approximately 2 in the presence of 3 ppmv NO and becomes non-linear below about 25 ppbv NO₂ (Hastie et al., 1991; Clemitshaw et al., 1997). A NO₂ offset of 40 ppbv is added so that the luminol detector works in the linear regime. There has not been observed any effect of CO to the detection response up to 10%. The exemplary NO₂ calibration of the detectors is presented in Fig. 3.4.1.1.

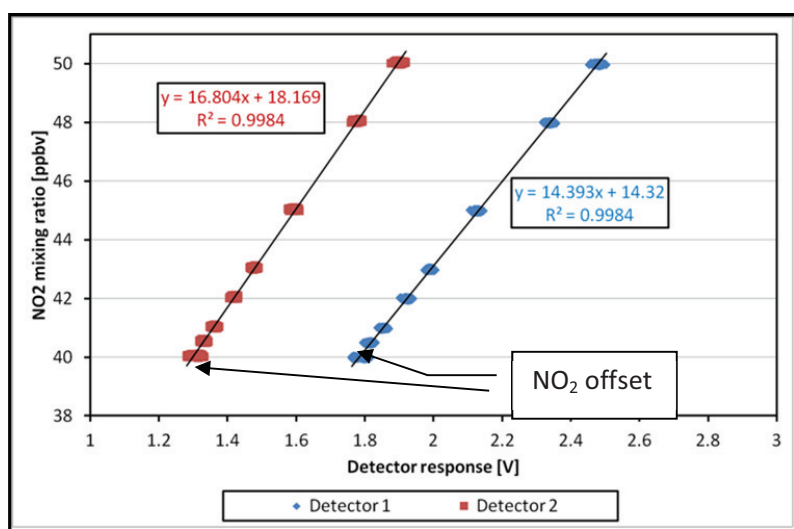


Fig. 3.4.1.1 The NO₂ detector response of the instrument with two detectors.

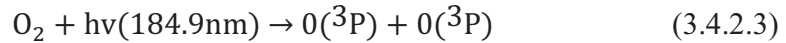
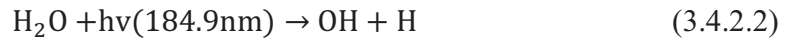
3.4.2 Chain length determination

The chain length has to be determined for each reactor as it depends on the conditions during the measurements and the geometry of the reactor and is calculated from the following formula:

$$CL = \frac{[\Delta NO_2]}{[HO_2]} \quad (3.4.2.1).$$

Where: $[\Delta NO_2] = [NO_{2am}] - [NO_{2bg}]$ is calculated as a difference between the NO_2 produced in the amplification and background and mode corresponding to the known amount of HO_2 ($[HO_2]$).

Different mixing ratios of the radicals are produced by the photolysis of water at 184.9 nm (Shultz et al., 1995) in the radical source by changing the intensity of the light as the humidified calibration air flows through the quartz tube of the radical source. A low pressure Hg lamp emits UV radiation which is used to photolyze water and oxygen and produce radicals and ozone:



CO is added to the mixture to convert OH into HO_2 :



In addition, alkanes can be added instead of CO to produce a mixture of organic and hydroxyradicals:



The continuity equations for the above processes are:

$$\frac{\partial HO_2}{\partial t} = \eta_{HO_2} * \Theta^{184.9nm} * \sigma_{H_2O}^{184.9nm} * [H_2O] \quad (3.4.2.4)$$

$$\frac{\partial O_3}{\partial t} = \eta_{O_3} * \Theta^{184.9nm} * \sigma_{O_2}^{184.9nm} * [O_2] \quad (3.4.2.5).$$

$\Theta^{184.9nm}$ the photon flux at 184.9 nm is the same for the equations (3.4.2.4) and (3.4.2.5). The formation yields are for ozone $\eta_{O_3} = 2$ and for HO_2 $\eta_{HO_2} = 2$ as OH is converted into HO_2 in the reaction 2.1.11-12. As $HO_2(t = 0) = 0$ and $O_3(t = 0) = 0$ integrating the above equations leads to:

$$[\text{HO}_2] = \frac{\sigma_{\text{H}_2\text{O}} * [\text{H}_2\text{O}] * [\text{O}_3]}{\sigma_{\text{O}_2} * [\text{O}_2]} \quad (3.4.2.6).$$

The absorption cross section for H₂O at 184.9 nm reported in the literature $\sigma_{\text{H}_2\text{O}} = 7.14 * 10^{-20}$ cm² molecule⁻¹ (Cantrell et al., 1997; Hofzumahaus et al., 1997) was used. The water mixing ratio [H₂O] is calculated from the dew point temperature measured by the dew point sensor. The O₂ abundance is taken according to the composition of the gas cylinder provided for the synthetic air. The O₂ absorption cross section and the O₃ mixing ratio are measured at each calibration condition.

O₃ calibration

Different HO₂ mixing ratios required for the calibration are produced by changing the intensity of the light. Generated O₃ is too small to be measured directly after its conversion into NO₂ and detection as NO₂ in reference to the background signal (0.2-0.7 ppbv). The ozone mixing ratio is thus determined by measuring the light emitted through the source as the O₃ amount and the Hg lamp intensity shows a linear relationship. Therefore, the ratio of the produced O₃ to the maximum ozone mixing ratio ($O_{3\text{max}}$) equals to the ratio of the light intensity and the light intensity detected at the maximum production of ozone (I_{max}). Consequently, at each HO₂ calibration point the $O_{3\text{detected}}$ mixing ratios can be calculated from:

$$[\text{O}_{3\text{detected}}] = [\text{O}_{3\text{max}}] * \frac{I_{\text{detected}}}{I_{\text{max}}} \quad (3.4.2.7).$$

Determination of the effective absorption cross section of oxygen

The O₂ absorption cross section in the Schumann-Runge bands shows highly structured features around the Hg lamp line: 184.9 nm (Yoshino et al., 1983; Lanzendorf et al., 1997), see Fig. 3.4.2.2. The light emission profile coming from the Hg lamp changes by passing through the oxygen column (Schultz et al., 1997) and depends upon the lamp conditions (operation conditions, temperature, age and position of the lamp). Therefore, the effective absorption cross section of O₂ will be different for different experimental set-ups and has to be determined for each set-up (Hofzumahaus et al., 1997).

For the determination of the O₂ effective absorption cross section different oxygen column are produced by mixing N₂ and synthetic air in the photolysis zone. The apparent absorption cross section was measured for a given oxygen column (x) and calculated using the Beer-Lambert law:

$$\sigma_{\text{O}_2,\text{app}}^*(x) = \frac{1}{x} \ln \left(\frac{I_0}{I(x)} \right) \quad (3.4.2.8).$$

Where: $I(x)$ and I_0 is the intensity of the lamp radiation after passing through the photolysis zone with an absorbing oxygen column (x) and with N_2 , respectively. The apparent $\sigma_{O_2,app}^*(x)$ absorption cross section results from the integration of the effective absorption cross section through an oxygen column (x).

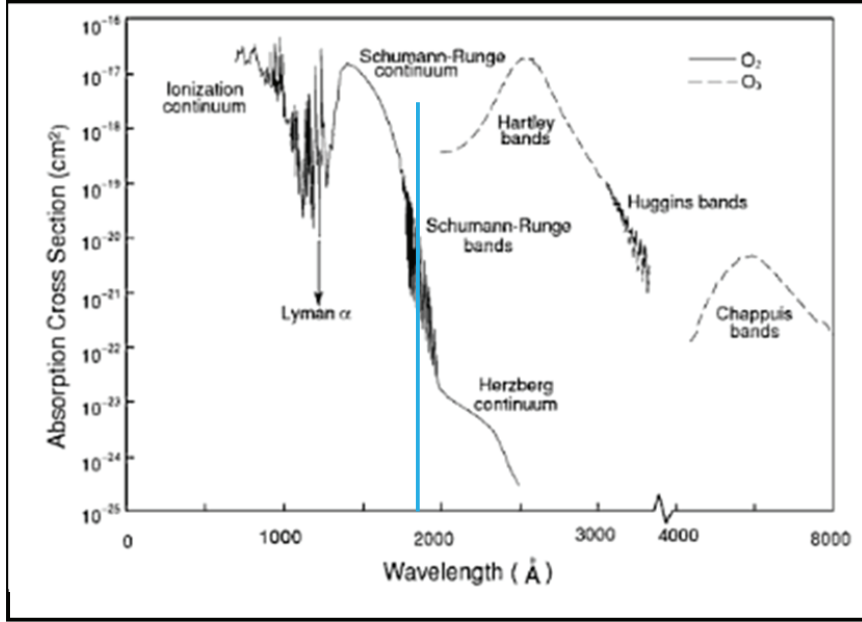


Fig. 3.4.2.2 The absorption cross section of ozone and molecular oxygen in the ultraviolet spectral region (information taken from ‘An introduction to atmospheric radiation’, Kuo-Nan Liou. Data taken from Brasseur and Solomon (1986), Vigroux (1953), and Griggs (1968)). The absorption features around 184.9 nm are highlighted in blue.

The effective cross section required for the HO_2 calibration is given as a slope of the Beer-Lambert law at a given oxygen column x :

$$\sigma_{O_2,eff}(x) = \frac{d}{dx} \left[\ln \left(\frac{I_0}{I(x)} \right) \right] = - \frac{d[\ln I(x)]}{dx} = \frac{d[x \cdot \sigma_{O_2,app}^*(x)]}{dx} \quad (3.4.2.9)$$

$$\sigma_{O_2,eff}(x) = \sigma_{O_2,app}^*(x) + x \left[\frac{d\sigma_{O_2,app}^*(x)}{dx} \right] \quad (3.4.2.10).$$

The exemplary dependence of $\sigma_{O_2,app}^*(x)$ and $\sigma_{O_2,eff}(x)$ from the oxygen column measured within this work at 1013 mbar is shown in Fig. 3.4.2.3.

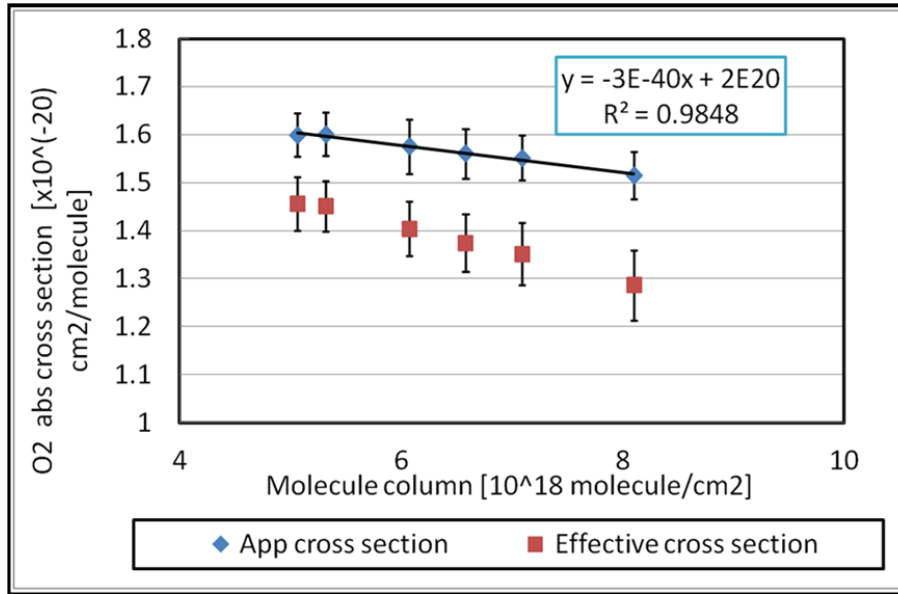


Fig. 3.4.2.3 Variations of the O₂ absorption cross section with oxygen column at 184.9 nm measured for the IUP-UB source at 1013 mbar.

3.4.3 Assignment of the uncertainties

The radicals mixing ratios measured with the PerCA technique are calculated from the formula:

$$[RO_2^*] = \frac{[NO_2]_{\text{amplification}} - [NO_2]_{\text{background}}}{CL} = \frac{[\Delta NO_2]}{CL} \quad (2.2.3.10).$$

$[\Delta NO_2]$ is the difference between the amplification and background response of the detector as a mixing ratio and CL is the chain length obtained in the laboratory calibrations. Thus, the uncertainty in the radical determination depends on the uncertainty of the CL determination: ΔCL and on the uncertainty of $[\Delta NO_2]$ ($\Delta[\Delta NO_2]$), calculated from the error propagation law:

$$\Delta RO_2^* = \sqrt{\left(\frac{1}{CL} * \Delta[\Delta NO_2]\right)^2 + \left(\frac{[\Delta NO_2]}{CL} * \Delta CL\right)^2} \quad (3.4.3.1).$$

In the following section all relative uncertainties are expressed in percentage.

The CL is calculated from:

$$CL = \frac{[\Delta NO_2]}{[HO_2]} \quad (3.4.2.1)$$

and the uncertainty of the CL (ΔCL) depends on the error of the NO₂ detector response and the uncertainty of the HO₂ production procedure. Thus, the relative uncertainty $\frac{\Delta CL}{CL}$ calculated from the error propagation law is:

$$\frac{\Delta CL}{CL} = \sqrt{\left(\frac{\Delta[\Delta NO_2]}{[\Delta NO_2]}\right)^2 + \left(\frac{\Delta[HO_2]}{[HO_2]}\right)^2} \quad (3.4.3.2).$$

Concerning the $\Delta[NO_2]$ uncertainty ($\Delta(\Delta[NO_2])$), it depends on the uncertainty of the detector sensitivity $\Delta\left(\frac{1}{a}\right)$ and the uncertainty in the difference $\Delta V = V_{sg} - V_{bg}$ the between signal and background mode ($\Delta(\Delta V)$). As the parameters 'a' and 'b' are determined in the NO_2 calibration, then ΔNO_2 can be calculated from a detector response V in volts:

$$[NO_2] = a * V_{\text{signal}} + b - a * V_{\text{background}} - b = a * \Delta V \quad (3.4.3.3).$$

Thus,

$$\frac{\Delta([\Delta NO_2])}{\Delta[NO_2]} = \sqrt{\left(\frac{\Delta(\Delta V)}{\Delta V}\right)^2 + \left(\frac{\Delta a}{a}\right)^2} \quad (3.4.3.4).$$

$\Delta(\Delta V)$ is a calculated as the standard deviation of the detector response as a voltage and the $\frac{\Delta(\Delta V)}{\Delta V}$ is around 6%. In case of the characterization of the modified reactor (see Section 4.2.3) $\frac{\Delta(\Delta V)}{\Delta V}$ was twice higher. To Δa , calculated with the least square fit method, contribute the error of the detector response as a voltage, the uncertainty of the NO_2 concentration of the calibration gas cylinder (around 2%), the uncertainty of the flows used to produce different NO_2 mixing ratios within the calibration. $\frac{\Delta a}{a}$ is around 2% and the stability of the NO_2 offset response during the calibration affects the ratio significantly. In summary, $\frac{\Delta([\Delta NO_2])}{\Delta[NO_2]}$ varies within 6.5% according to the obtained uncertainties $\frac{\Delta(\Delta V)}{\Delta V}$ and $\frac{\Delta a}{a}$.

Based on the Eq. 3.4.2.6, to the relative uncertainty $\frac{\Delta[HO_2]}{[HO_2]}$ contribute the uncertainties of the water mixing ratio in the sampled air, the determination of the oxygen effective absorption cross section and of the ozone mixing ratios:

$$\frac{\Delta[HO_2]}{[HO_2]} = \sqrt{\left(\frac{\Delta\sigma_{O_2}^{189.4 \text{ nm}}}{\sigma_{O_2}^{189.4 \text{ nm}}}\right)^2 + \left(\frac{\Delta\sigma_{H_2O}^{189.4 \text{ nm}}}{\sigma_{H_2O}^{189.4 \text{ nm}}}\right)^2 + \left(\frac{\Delta[H_2O]}{[H_2O]}\right)^2 + \left(\frac{\Delta[O_3]}{[O_3]}\right)^2} \quad (3.4.3.5).$$

The accuracy of the dew point sensor is 2 °C for the range of -50...+80 °C in the interval that the calibrations are performed. Based on this value, for the water mixing ratios calculated from the dew point temperature $\frac{\Delta[H_2O]}{[H_2O]}$ is 5-6%.

The contribution of all the error sources leads to $\frac{\Delta\sigma_{O_2}^{189.4\text{ nm}}}{\sigma_{O_2}^{189.4\text{ nm}}}$ around 6% for the O₂ effective absorption cross section for the set-up employed in this work.

The uncertainty of the ozone determination depends on: the NO₂ detection, the conditions of the Hg lamp operation and the instrumental error of the photomultiplier. Thus, the error of propagation based on Eq. (3.4.2.7) is:

$$\begin{aligned} \frac{\Delta[O_3]}{[O_3]} &= \sqrt{\left(\frac{\Delta[O_{\max}]}{[O_{\max}]}\right)^2 + \left(\frac{\Delta I_{\max}}{I_{\max}}\right)^2 + \left(\frac{\Delta I}{I}\right)^2} = \\ &= \sqrt{\left(\frac{\Delta a}{a}\right)^2 + \left(\frac{\Delta(\Delta V_{[O_3\max]})}{\Delta V_{[O_3\max]}}\right)^2 + \left(\frac{\Delta I_{\max}}{I_{\max}}\right)^2 + \left(\frac{\Delta I}{I}\right)^2} \quad (3.4.3.6). \end{aligned}$$

Where: $[O_{3\max}]$ is calculated as $a * \Delta V_{[O_3\max]}$, $\Delta V_{[O_3\max]}$ is a difference between the detector response at maximum ozone and no ozone production. All the relative uncertainties lead to $\frac{\Delta[O_3]}{[O_3]}$ around 7%.

The absorption cross section for H₂O at 184.9 nm reported in the literature was used $\sigma_{H_2O} = 7.14 * 10^{-20} \pm 0.1 * 10^{-20} \text{ cm}^2 \text{ molecule}^{-1}$ (Cantrell et al., 1997; Hofzumahaus et al., 1997), thus $\frac{\Delta\sigma_{H_2O}^{189.4\text{ nm}}}{\sigma_{H_2O}^{189.4\text{ nm}}}$ is 1.4%.

Taking into account all the contributions $\frac{\Delta[HO_2]}{[HO_2]}$ is around 10% for the $[HO_2]$ determination.

Consequently, the relative uncertainty $\frac{\Delta CL}{CL}$ varies between 10-25% for the amplification factors determined within this work.

3.5 Data acquisition systems and software

The pressure regulator and the flow controllers (digital BRONKHORST HIGH-TECH B.V. products) and computer are interconnected by FLOW-BUS a 3-wire, RS485-based fieldbus communication system for the parameter value exchange. The FLOW-BUS cables allow handling power supply and communication with the same cable.

In this system each digital instrument is equipped with a micro-controller for its own dedicated task but also for exchanging information with other devices connected to the same FLOW-BUS system. The microcontroller allows several processes being run simultaneously:

- Reading analog input signal (e.g., flow),
- Digital signal processing,
- Driving the valve,
- Setting analog output signal.

Communication between the computer and all the devices connected to the FLOW-BUS can take place simultaneously. These two features are in contrast to communication RS232-based where at one time only one device can be controlled and either reading or setting is possible.

The communication of the FLOW-BUS system with the computer was performed by the FLOW-BUS DDE server as it allows data exchange with Microsoft Windows applications. Reading/changing parameter values via FLOWDDE is performed by a different interface to the instrument and within this work an application in LabView was generated to control the flow controllers and the pressure regulator, presented in Appendix 1.

4. Results and discussion

In the following chapter the findings obtained within this doctoral work are presented and discussed. The chapter has been divided into four parts:

Section 4.1 presents the results of the experiments performed to determine the hydraulic resistance in the PerCEAS instrument using the HALO inlet. The main objective of this investigation is the identification and quantification of the contribution of the main elements in the set-up imposing a restriction against the sampling flow, e.g., pre-reactor nozzle orifice, mass flow controllers, gas scrubbers etc. The Hagen-Poiseuille law will be used for the interpretation of the experimental results.

Section 4.2 includes the results of the experiments to identify the radical removal processes in the HALO and DUALER 2 inlets. The losses of the radicals on the sampling surfaces of the pre-reactor nozzle and the reactor entry are determined. The effect of different coating materials (Teflon and amorphous silicon) on the radical removal is investigated.

In Section 4.3 the applications of the laboratory experiment results with the HALO inlet to the OMO campaign are summarized.

Section 4.4 focuses on the modified PerCA technique to speciate HO₂ and RO₂ from RO₂^{*}. The simulation results and experimental findings are presented together with implications for the standard PerCA measurements.

4.1 Hydraulic resistance throughout the measurement set-up

As stated in the introduction, one of the objectives of the present work was the investigation of the hydraulic resistance encountered by the sampling gas through the set-up using the HALO inlet. In order to fulfill this objective, the performance of the set-up under the expected flight conditions was investigated by using the pressure chamber whose pressure was regulated between 200-1013 mbar. Measuring onboard the HALO aircraft within the OMO mission implies changes in the pressure conditions during the air sampling by taking vertical profiles up to altitudes around 12 km, i.e., the variations in the ambient pressure between 200 and

900 mbar approximately. To account for the changes in the radical sampling and detecting conditions, the pressure of the pre-reactor nozzle is kept constant and below the pressure of the sampled air, i.e., around 100 mbar, while high sampling flows are favoured to minimize the radical losses in the pre-reactor nozzle.

In Fig. 4.1.1 the general set-up described in detail in Sections 3.1 and 3.2 is depicted. All the reaction gases were added as 1000 ml/min of the total air flow was sampled, i.e., 90 ml/min of N₂/CO + 5 ml/min of NO to the first addition point and 90 ml/min of N₂/CO to the second addition point. The capability of the pump to control pressure and flows through the channel, i.e., comprising a reactor, a detector, a flow controller including the tubing between them, depends on the physical restrictions of the measurement system and can consequently be used as a tool to quantify the contribution of different units of the set-up to the general hydraulic resistance to the air flow.

Eq. (2.3.1.2) states that the pressure drop owing to passage through a circular barrier is proportional to $1/r^4$:

$$\Delta p = R_{hyd} * Q = \frac{8\eta L}{\pi r^4} * Q \quad (2.3.1.2).$$

Where: r is radius [m], L length [m], η viscosity [kg m⁻¹s⁻¹], Q volumetric flow rate [m³/s], R_{hyd} hydraulic resistance $\left[\frac{Pa*s}{m^3} = \frac{kg}{m*s^4}\right]$. Consequently, the following barriers in the set-up were defined:

- Fixed orifices, like orifices of the lid and the reactor shown in Fig. 4.1.2

The amount of air through the pre-reactor nozzle depends on the sampling orifice and the pressure gradient $\Delta p = p_{external} - p_{inlet}$ (at the conditions $p_{inlet} > p^o$, p^o is the critical pressure. see Section 2.3.3). Therefore, three lids with different sampling orifices with diameters of Ø1, Ø1.2 and Ø1.5 mm and different reactor entries were used to examine their influence on the flows through the reactor and the pressure in the pre-reactor nozzle.

- Adjustable orifices, i.e., valves in the pressure regulator and the sampling flow controllers

The valve position of the sampling flow controllers (FC) and the pressure regulator (PR) were monitored to identify the conditions when the maximum flow through the valve is reached (valve in fully open position). Similarly, it is expected that the pressure regulator valve closes at low $\Delta p = p_{external} - p_{inlet}$. It should be noted that the maximum valve position,

i.e., valve fully open, corresponds to 66.67%, and the minimum position, i.e., valve closed, corresponds to 0%.

- Gas scrubbers like CO and NO_x scrubbers with the resistance depending on the content, and grid, and geometry (length, cross section area).
- Tubing for the sampling and pressure regulation, gas fittings, safety valves

To reduce the resistance wherever possible in the set-up instead of PFA tube with an outer diameter of OD ¼” or ½”, the tubes with a bigger diameter, such as KF-60, were used. The tubing length was minimized but kept within the dimensions similar to the length that will be used in the final PerCEAS instrument. In addition, wherever possible ½” instead of ¼” Swagelok fittings and unions (crosses or tees where the lines were combined) within the sampling lines were implemented. However, due to a design of the flow controller and the luminol detector ¼” fittings could not be entirely eliminated.

Table 4.1.1 provides a summary of the conditions during the investigation of the hydraulic resistance in the PerCA set-up.

\varnothing_1	p_1	p_2
1	200	1000, 500, 300
1.2		
1.5	100	1000, 500, 200

Table 4.1.1 Summary of the conditions for the investigation: \varnothing_1 - orifice of the lid entry [mm], p_1 - pressure of the pre-reactor nozzle [mbar], p_2 - external pressure in the pressure chamber [mbar].

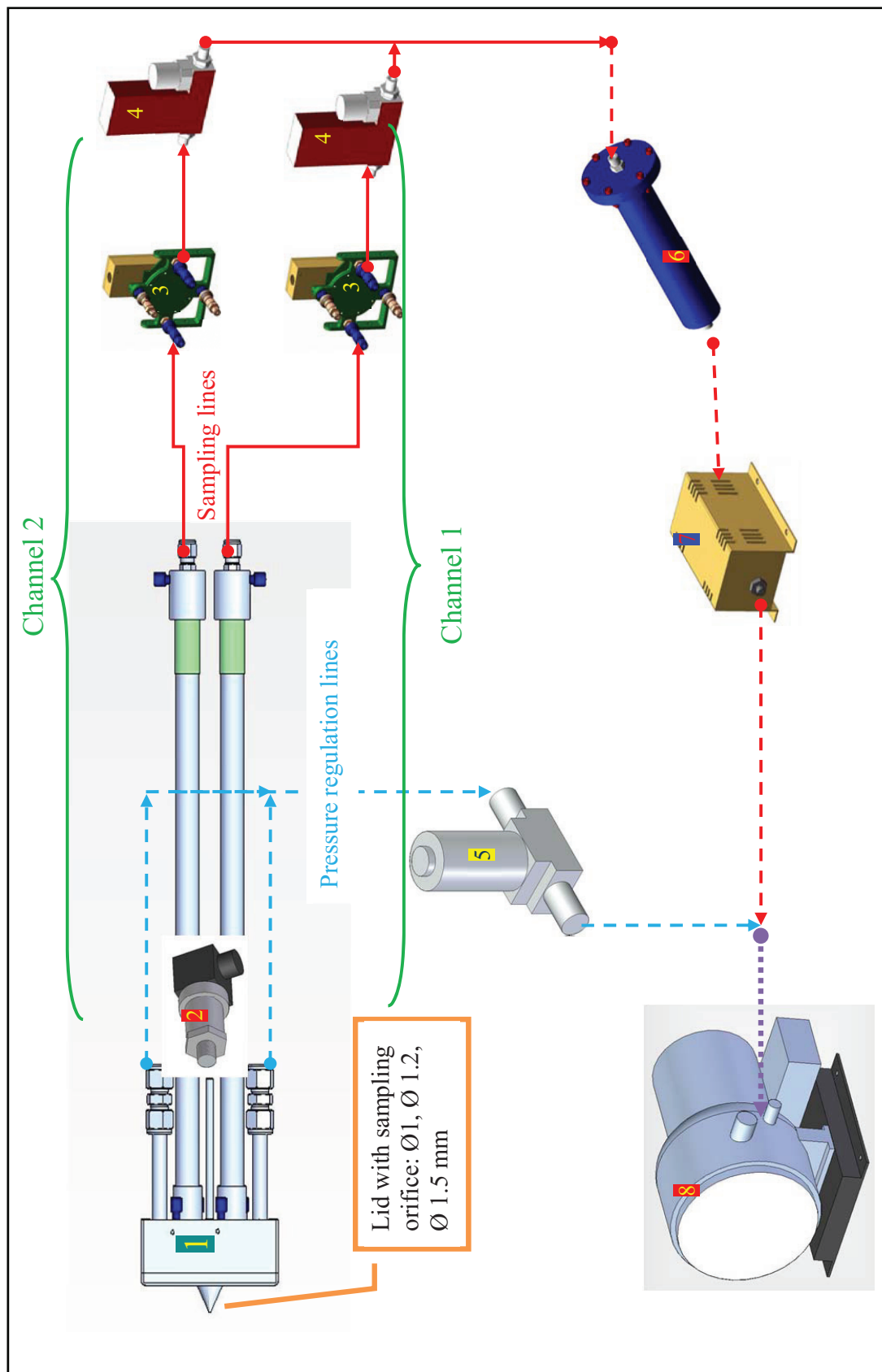


Fig. 4.1.1 Schematic diagram of the main components of the set-up: 1 - HALO inlet, 2 - pressure sensor, 3 - NO₂ detector and luminol trap, 4 - mass flow controller, 5 - pressure regulator, 6 - NO_x scrubber, 7 - CO scrubber, 8 - vacuum pump. In red are sampling lines, in blue pressure regulation lines and in violet KF60 tubing. Solid line refers to 1/4" and dashed line to 1/2" diameter tubings. Channel consists of a reactor, a detector, a flow controller including the tubing between them.

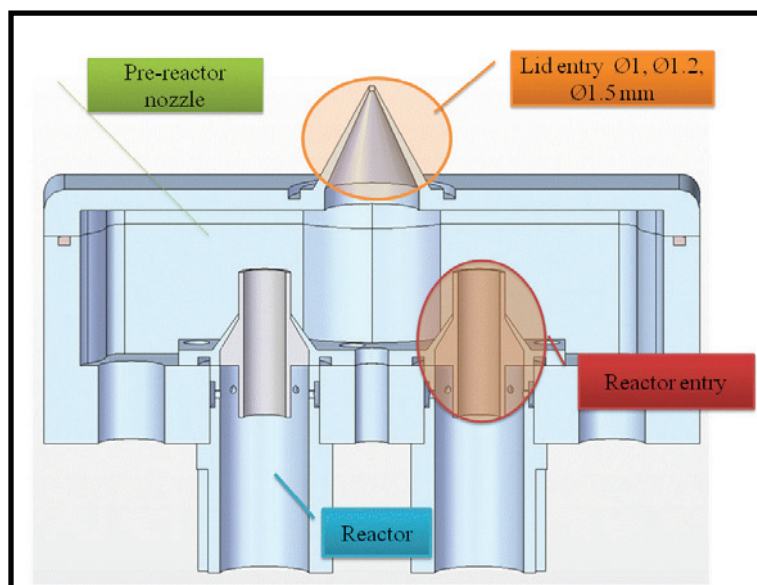


Fig. 4.1.2 Components of the HALO inlet.

4.1.1 Lid sampling orifice

The first step of the investigation consisted in the determination of the effect of the lid sampling orifice (diameters of $\text{Ø}1$, $\text{Ø}1.2$ and $\text{Ø}1.5$ mm) on the sampling flow through the reactor and on the pressure regulation. It is predicted lower amount of air introduced through a smaller orifice (Green and Perry, 2007). These experiments were carried out with two CO scrubbers filled with active charcoal: with a $\frac{1}{2}$ " tube and with a KF-25 tube.

At first, $\text{Ø}1$ and $\text{Ø}1.5$ mm lid entry were investigated and using Eq. (2.3.1.2) the resistance of the $\text{Ø}1.5$ mm orifice is estimated to be 5 times higher than in case of the $\text{Ø}1$ mm. For this study different reactor entries were used as Teflon inserts (see Fig. 4.1.2). The dimensions and shape of the Teflon inserts were optimized to minimize the radical losses and to prevent that the reactors interfere each other, so that air is sampled only from the pre-reactor nozzle (showed in detail in Section 4.2.2). The experiments with the $\text{Ø}1.5$ mm entry lid were performed with the insert 4 mm longer than with the $\text{Ø}1$ mm lid. On the basis of Eq. (2.3.1.2) this $\Delta l=4$ mm corresponds to 16% higher hydraulic resistance for a longer insert and it is not expected to play a significant role as a constraint in reference to 5 times higher resistance of the $\text{Ø}1$ orifice than the $\text{Ø}1.5$ mm. Thus, as an approximation it can be assumed that the entries are equivalent. The experiments were performed with the $\frac{1}{2}$ " CO scrubber.

In Table 4.1.1.1 the results with the lid of $\text{Ø}1$ mm orifice are summarized.

Teflon insert	Scrubbers	p_{1s}	Q_r	p_2	Results
3 rd , 8 mm orifice, 21 mm length	1/2" CO scrubber, NO _x scrubber	200	1000	~1013, 502, 406	<ul style="list-style-type: none"> • $Q_{1,2}=Q_r$ • $p_1=p_{1s}$
				316	<ul style="list-style-type: none"> • $p_1 < p_{1s}$ • $p_1 = \sim 155$ • $V_{PR} = 0\%$ • $Q_{1,2} < Q_r$ • $Q_1 = \sim 900$ • $Q_2 = \sim 937$ • $V_{FC1,2} = 66.67\%$
		100	1000	~1013, 525, 412, 207	<ul style="list-style-type: none"> • $p_1 = p_{1s}$ • $Q_{1,2} < Q_r$ • $Q_{1,2} < 450$ • $V_{FC1,2} = 66.67\%$

Table 4.1.1.1 The results of the investigations with the lid with the $\varnothing 1$ mm orifice, p_{1s} - set pressure of the pre-reactor nozzle [mbar], p_1 - obtained pressure in the pre-reactor nozzle [mbar], Q_r - set flow through the reactor [ml/min], Q_i - obtained flow in the channel 1 or 2 [ml/min], p_2 - chamber pressure [mbar], V_{PR} - position of the pressure regulator valve, $V_{FC1,2}$ - position of the flow controller in the channel 1 or 2.

- Set 200 mbar in the pre-reactor nozzle ($p_1=200$ mbar) was obtained when ambient pressure (p_2) was above 406 mbar. At p_2 below 300 mbar, the pressure 200 mbar in the pre-reactor nozzle could not be achieved, it was 45 mbar lower ($p_1=\sim 155$ mbar) and the pressure regulator valve was in a fully closed position.
- The sampling flow of $Q=1000$ ml/min was achieved at the pressure of the pre-reactor nozzle 200 mbar when p_2 was above 406 mbar.
- $P_1=100$ mbar was controlled in the pre-reactor nozzle at all external pressures.
- At $p_1=100$ mbar the flow of $Q=1000$ ml/min was not obtained, Q remained below 450 ml/min.
- Interestingly, when the difference between the pressure in the chamber (p_2) and in the inlet (p_1) decreased, the flow through the reactor increased (see Fig. 4.1.1.2). The opposite was expected. As p_1 is always below the critical pressure (189 mbar for $p_2=100$ mbar on the basis of Eq. 2.3.3.1) the mass flow is proportional to the external pressure p_2 (Green and Perry, 2007). Thus, at lower external pressure (p_2) lower air flow through the sampling orifice was expected and then less available air in the pre-reactor nozzle. As a consequence, less air through the reactor was predicted to be sampled.

The flow through the channel 2 is higher than through the channel 1 with a fully open FC valve which demonstrates that the resistance of the channel 2 is lower. This can be related to slightly different physical properties of the FC valve, such as size of the valve orifice, despite that the flow controllers are identically designed and manufactured.

Furthermore, the minimum pressure in the pre-reactor nozzle enabling a flow of 1000ml/min through the reactor is 160 mbar, with the minimum gradient pressure $\Delta p_{min}=130$ mbar between the chamber pressure $p_2=290$ mbar and the pre-reactor nozzle pressure $p_1=160$ mbar.

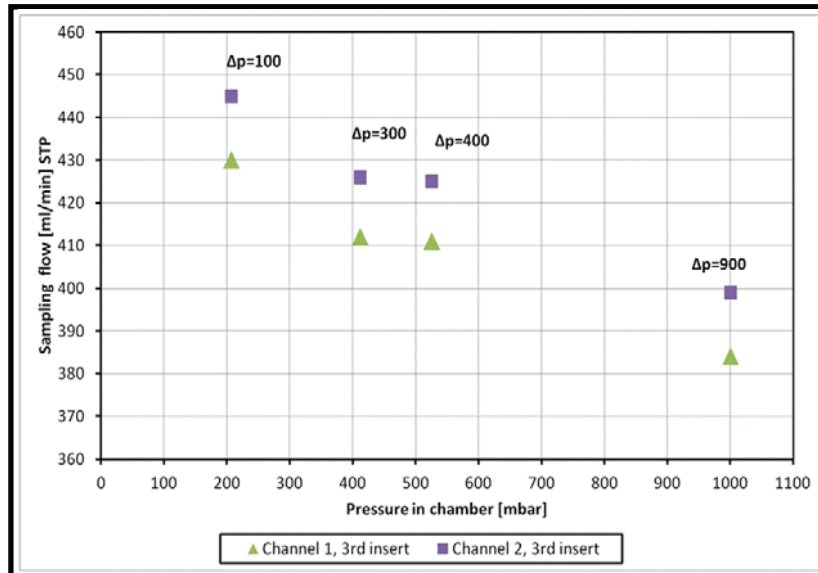


Fig. 4.1.1.2 Variations of the sampling flow with $\Delta p=p_2-p_1$, p_1 - pressure obtained in the pre-reactor nozzle [mbar], p_2 - chamber pressure [mbar].

The low flows and the pressure obtained with the $\varnothing 1$ mm orifice can be attributed to the flow resistance of the orifice, i.e., the opening is too small to allow a sufficient amount of air to pass through it. Therefore, similar experiments were performed with the lid with the 1.5 mm diameter orifice. In Table 4.1.1.2 the experimental results are summarized.

Teflon insert	Scrubbers	p_{1s}	Q_r	p_2	Results
2 nd , 8 mm orifice	½" CO scrubber, NO _x scrubber	200	1000	~1013, 508, 310	<ul style="list-style-type: none"> • $Q_{1,2}=Q_r$ • $p_1=p_{1s}$
		100	1000	~1013	<ul style="list-style-type: none"> • $p_1 > p_{1s}$ • $p_{1s} = 200$ • $V_{PR} = 66.67\%$ • $Q_{1,2}=Q_r$
				508	<ul style="list-style-type: none"> • $p_1 > p_{1s}$ • $p_{1s} = 106$ • $V_{PR} = 66.67\%$ • $Q_{1,2} < Q_r$ • $Q_{1,2} < 490$ • $V_{FC1,2} = 66.67\%$

Teflon insert	Scrubbers	p_{1s}	Q_r	p_2	Results
2 nd , 8 mm orifice	½" CO scrubber, NO _x scrubber	100	1000	200	<ul style="list-style-type: none"> • $p_1 = p_{1s}$ • $Q_{1,2} < Q_r$ • $Q_{1,2} < 460$ • $V_{FC1,2} = 66.67\%$

Table 4.1.1.2 The results of the investigations with the lid with Ø1.5 mm orifice, p_{1s} - set pressure of the pre-reactor nozzle [mbar], p_1 - obtained pressure in the pre-reactor nozzle [mbar], Q_r - set flow through the reactor [ml/min], Q_i - obtained flow in the channel 1 or 2 [ml/min], p_2 - chamber pressure [mbar], V_{PR} - position of the pressure regulator valve, $V_{FC1,2}$ - position of the flow controller in the channel 1 or 2.

- In contrast to the Ø1 mm, for the Ø1.5 mm orifice the pre-reactor nozzle can be regulated at 200 mbar and the flow of $Q=1000$ ml/ min can be obtained at all external pressure levels of the sampling air.
- The pre-reactor nozzle pressure 100 mbar ($p_I=100$ mbar) was not obtained when the sampled air was above 500 mbar, and the valve of the pressure regulator was fully open.
- With $p_I=100$ mbar the flow 1000 ml/min was not reached, but remained below 490 ml/min.
- $P_I=160$ mbar was measured in the pre-reactor nozzle for 1000 ml/min flow through the channel and around 200 mbar external pressure (in the pressure chamber).

In summary, the minimum pressure difference $\Delta p_{min} = p_2 - p_1$ required to obtain 1000 ml/min flow is summarized in Table 4.1.1.3 below, when p_I is above 160 mbar.

\varnothing_1	$\Delta p_{min} = p_2 - p_1$
1	> 130
1.5	> 40

Table 4.1.1.3 Pressure gradient $\Delta p = p_2 - p_1$ required to obtain 1000 ml/min flow through each channel, \varnothing_1 - sampling orifice of the lid [mm], p_I - pressure of the pre-reactor nozzle [mbar], p_2 - chamber pressure [mbar].

Based on Eq. (2.3.1.2) and assuming the same total flow through both sampling orifices (Q), the resistance of the orifice Ø1 mm ($R_{\varnothing 1mm}$) is around three times higher than the Ø1.5 mm ($R_{\varnothing 1.5mm}$), as:

$$\Delta p_{\varnothing 1mm} = 130 = R_{\varnothing 1mm} * Q \quad (4.1.1)$$

$$\Delta p_{\varnothing 1.5mm} = 40 = R_{\varnothing 1.5mm} * Q \quad (4.1.2).$$

Contrary to expectations, employment of the Ø1.5 mm orifice does not lead to sufficient reduction of the resistance and an increase of the sampling flow through the channel when the pre-reactor nozzle is at 100 mbar. In addition, the Ø1.5 mm orifice allows passing too much air to the pre-reactor nozzle and consequently the regulation of the pressure in this component of the set-up could not be performed.

Further experiments were carried out with the Ø1.2 and Ø1.5 mm orifices. As the reactor entries were used the inserts 4th with a 4 mm orifice and a conical cross section characterized by the lowest radical losses (see Section 4.2.2). The modified CO scrubber made of KF-25 tube was used to reduce the hydraulic resistance in the set-up.

The results of the experiments carried out with the biggest orifice Ø1.5 mm are presented in Table 4.1.1.4.

Teflon insert	Scrubbers	p_{1s}	Q_r	p_2	Results
4 th , 4 mm orifice, 14.2 mm length	KF-25 CO scrubber, NO _x scrubber	200	1000	~1013	<ul style="list-style-type: none"> • $p_1 > p_{1s}$, • $p_1 = 209$ • $V_{PR} = 66.67\%$ • $Q_{1,2} = Q_r$
				515, 319	<ul style="list-style-type: none"> • $Q_{1,2} = Q_r$ • $p_1 = p_{1s}$
		100	1000	~1013	<ul style="list-style-type: none"> • $p_1 > p_{1s}$ • $p_1 = 209$ • $V_{PR} = 66.67\%$ • $Q_{1,2} = Q_r$
				515	<ul style="list-style-type: none"> • $p_1 > p_{1s}$ • $p_1 = 109$ • $V_{PR} = 66.67\%$ • $Q_{1,2} < Q_r$ • $Q_{1,2} < 680$ • $V_{FC1,2} = 66.67\%$
		145	1000	319, 222	<ul style="list-style-type: none"> • $p_1 = p_{1s}$ • $Q_{1,2} < Q_r$ • $Q_{1,2} < 630$ • $V_{FC1,2} = 66.67\%$
				222	<ul style="list-style-type: none"> • $Q_{1,2} = Q_r$ • $p_1 = p_{1s}$

Table 4.1.1.4 The results of the investigations with the lid with the Ø1.5 mm orifice, p_{1s} - set pressure of the pre-reactor nozzle [mbar], p_1 - obtained pressure in the pre-reactor nozzle [mbar], Q_r - set flow through the reactor [ml/min], Q_i - obtained flow in the channel 1 or 2 [ml/min], p_2 - chamber pressure [mbar], V_{PR} - position of the pressure regulator valve, $V_{FC1,2}$ - position of the flow controller in the channel 1 or 2.

- The pressure in the pre-reactor nozzle was successfully regulated at 200 mbar ($p_1 = 200$ mbar) when the sampled air remained below 515 mbar. In case of the external pressure $p_2 \sim 1013$ mbar p_1 was slightly higher than 200 ($p_1 = 209$ mbar) with a fully open valve of the pressure regulator.
- The sampling flow of $Q = 1000$ ml/min was achievable at all external pressures of the sampled air with $p_1 = 200$ mbar.

- $p_1=100$ mbar in the pre-reactor nozzle was reached when the external air was below 319 mbar.
- At $p_1=100$ mbar in the pre-reactor nozzle the sampling flow (Q) did not reach 1000 ml/min but remained below 630 ml/min.
- In order to obtain a sampling flow of $Q=1000$ ml/min at the ambient pressure $p_2=200$ mbar, p_1 had to be kept at 145 mbar, i.e., a slightly lower value than the 160 mbar obtained when using the ½” CO scrubber under the same conditions. This confirms the importance of the scrubber resistance in the set-up.

These results confirmed that the Ø1.5 mm orifice allows passing too much air and thus the pressure in the pre-reactor nozzle cannot be controlled below 200 mbar for the external pressures above 320 mbar.

Finally the Ø1.2 mm orifice was investigated and the results are shown in Table 4.1.1.5.

Teflon insert	Scrubbers	p_{1s}	Q_r	p_2	Results
4 th , 4 mm orifice	KF-25 CO scrubber, NO _x scrubber	200	1000	~1013, 515, 315	<ul style="list-style-type: none"> • $Q_{1,2}=Q_r$ • $p_1=p_{1s}$
		100	1000	~1013	<ul style="list-style-type: none"> • $p_1 > p_{1s}$ • $p_1=144$ • $V_{PR}=66.67\%$ • $Q_{1,2} < Q_r$ • $Q_{1,2} < 980$ • $V_{FC1,2}=66.67\%$
				515, 315, 221	<ul style="list-style-type: none"> • $p_1=p_{1s}$ • $Q_{1,2} < Q_r$ • $Q_{1,2} < 640$ • $V_{FC1,2}=66.67\%$

Table 4.1.1.5 Results of the investigations with the lid with the Ø1.2 mm orifice: p_{1s} - set pressure of the pre-reactor nozzle [mbar], p_1 - obtained pressure in the pre-reactor nozzle [mbar], Q_r - set flow through the reactor [ml/min], Q_i - obtained flow in the channel 1 or 2 [ml/min], p_2 - chamber pressure [mbar], V_{PR} - position of the pressure regulator valve, $V_{FC1,2}$ - position of the flow controller in the channel 1 or 2.

- In contrast to the Ø1.5 mm orifice, for the Ø1.2 mm the pressure at 200 mbar can be kept in the pre-reactor nozzle at all levels of the external pressure.
- The flow 1000 ml/min ($Q=1000$ ml/min) was obtained for all external pressures when the pre-reactor nozzle was kept at 200 mbar.
- The pressure in the pre-reactor nozzle cannot be regulated at 100 mbar ($p_1=144$ mbar) when the external pressure is around 1000 mbar.

- The sampling of flow $Q=1000$ ml/min cannot be obtained at the pre-reactor nozzle regulated at 100 mbar; the flow remained below 640 ml/min.

The data presented in this section clearly indicate that it is not the resistance of the lid sampling orifice that prevents a sufficient amount of air to be sampled through the reactor. Thus, an increase of diameter of the lid orifice not only will not provide higher sampling flow (1000 ml/min) but will also lead to difficulties in the pressure regulation. Therefore, it can be concluded that the bottle neck is not this orifice but other components of the set-up behind it which create the hydraulic resistance (i.e., tubes, gas scrubbers). Next experiments, described in the following section, were performed to investigate the resistance of the reactor entry.

4.1.2 Reactor entry

A set of the experiments was carried out with different entries of the reactor. The orifice of the reactor entry might create a significant resistance in the set-up and be a limiting factor to obtain 1000 ml/min flow. Therefore, the experiments were additionally performed with the open reactors of a diameter of $\varnothing 17$ mm (see Fig. 4.1.2.1). The biggest available lid orifice of $\varnothing 1.5$ mm was selected to reduce the opposition to the flow and maximally increase the amount of air in the pre-reactor nozzle.

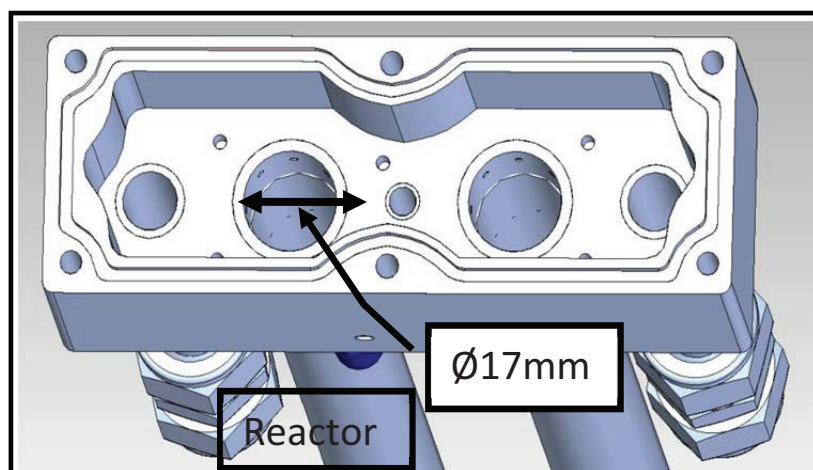


Fig. 4.1.1.2 Schematic diagram of the inlet: pre-reactor nozzle interior and open reactors.

Table 4.1.2.1 summarizes the obtained results.

Scrubbers	p_{1s}	Q_r	p_2	Results
½" CO scrubber, NO _x scrubber	200	1000	~1013, 491, 300	<ul style="list-style-type: none"> • $Q_{1,2}=Q_r$ • $p_1=p_{1s}$

Scrubbers	p_{1s}	Q_r	p_2	Results
1/2" CO scrubber, NO _x scrubber	100	1000	~1013	<ul style="list-style-type: none"> • $p_1 > p_{1s}$ • $p_1 = 200$ • $V_{PR} = 66.67\%$ • $Q_{1,2} = Q_r$
			500	<ul style="list-style-type: none"> • $p_1 > p_{1s}$ • $p_1 = 107$ • $V_{PR} = 66.67\%$ • $Q_{1,2} < Q_r$ • $Q_{1,2} < 500$ • $V_{FC1,2} = 66.67\%$
			200	<ul style="list-style-type: none"> • $p_1 = p_{1s}$ • $Q_{1,2} < Q_r$ • $Q_{1,2} < 460$ • $V_{FC1,2} = 66.67\%$

Table 4.1.2.1 The results of the investigations with the lid with the $\varnothing 1.5$ mm orifice and open reactors: p_{1s} - set pressure of the pre-reactor nozzle [mbar], p_1 - obtained pressure in the pre-reactor nozzle [mbar], Q_r - set flow through the reactor [ml/min], Q_i - obtained flow in the channel 1 or 2 [ml/min], p_2 - chamber pressure [mbar], V_{PR} - position of the pressure regulator valve, $V_{FC1/2}$ - position of the flow controller in the channel 1 or 2.

- The pre-reactor nozzle pressure was successfully controlled at $p_1=200$ mbar and the flow of $Q=1000$ ml/ min was achieved at all the levels of the external pressure, similarly to the previous study with the reactor entry of an 8 mm diameter.
- $P_j=100$ mbar in the pre-reactor nozzle was kept when the sampled air pressure was below 200 mbar.
- At $p_1=100$ mbar the sampling flow (Q) remained below 500 ml/min and it did not improve significantly in comparison to 8 mm orifice entry (Q below 460 ml/min).
- The minimum inlet pressure of the pre-reactor nozzle remained above 160 mbar for the 1000 ml/min sampling flow (for comparison see Table 4.1.1.3).

The similar results concerning the pressure regulation and the flows through the reactor were obtained with a smaller reactor entry orifice: 8mm (see Table 4.1.1.2). Thus, increasing of the reactor opening does not lead to any increase of the sampling flow. Therefore, it can be interpreted that the reactor entry is not the constraint that prevents to measure the flow of $Q=1000$ ml/min through the reactor.

As will be shown in Section 4.2.2 a careful design of the reactor entry is required to reduce the radical losses. The effect of the reactor entry on the resistance to the air flow was determined based on comparison of a smaller orifice with a 4 mm inner diameter (insert 4th) characterized by the lowest radical losses and the 8 mm orifice (insert 3rd). 8 times higher resistance is expected through the smaller insert 4th on the basis of Eq. 2.3.1.2. On the other

hand, the 3rd insert is 7 mm longer than the 4th, thus the overall resistance of the latter insert is expected to be 11 times higher. In Table 4.1.2.2 the results with the lid of the Ø1 mm orifice and the ½” CO scrubber are summarized.

Teflon insert	p_{1s}	Q_r	p_2	Results
4 th , 4 mm orifice, 14.2 mm length	200	1000	~1013, 508, 436	<ul style="list-style-type: none"> • $Q_{1,2}=Q_r$ • $p_1=p_{1s}$
			357	<ul style="list-style-type: none"> • $p_1 < p_{1s}$ • $p_1 = \sim 172$ • $V_{PR} = 0\%$ • $Q_{1,2} < Q_r$ • $Q_1 = \sim 964$ • $V_{FC1} = 66.67\%$ • $Q_2 = \sim 1011$ • $V_{FC2} = 52\%$
3 rd , 8 mm orifice, 21 mm length	200	1000	~1013, 502, 406	<ul style="list-style-type: none"> • $Q_{1,2}=Q_r$ • $p_1=p_{1s}$
			316	<ul style="list-style-type: none"> • $p_1 < p_{1s}$ • $p_1 = \sim 155$ • $V_{PR} = 0\%$ • $Q_{1,2} < Q_r$ • $Q_1 = \sim 900$ • $Q_2 = \sim 937$ • $V_{FC1,2} = 66.67\%$
4 th , 4 mm orifice, 14.2 mm length	100	1000	~1013, 516, 447, 255	<ul style="list-style-type: none"> • $p_1=p_{1s}$ • $Q_{1,2} < Q_r$ • $Q_{1,2} < 425$ • $V_{FC1,2} = 66.67\%$
3 rd , 8 mm orifice, 21 mm length	100	1000	~1013, 525, 412, 207	<ul style="list-style-type: none"> • $p_1=p_{1s}$ • $Q_{1,2} < Q_r$ • $Q_{1,2} < 445$ • $V_{FC1,2} = 66.67\%$

Table 4.1.2.2 The results of the investigations with the lid with the Ø1 mm orifice: p_{1s} - set pressure of the pre-reactor nozzle [mbar], p_1 - obtained pressure in the pre-reactor nozzle [mbar], Q_r - set flow through the reactor [ml/min], Q_i - obtained flow in the channel 1 or 2 [ml/min], p_2 - chamber pressure [mbar], V_{PR} - position of the pressure regulator valve, $V_{FC1/2}$ - position of the flow controller in the channel 1 or 2.

- For both inserts 3rd and 4th the pre-reactor nozzle can be regulated at $p_1=200$ mbar and the flow of $Q=1000$ ml/min can be obtained at the external pressure p_2 above 300 mbar.
- For both inserts the pressure can be successfully regulated at $p_1=100$ mbar and the obtained flow is below 500 ml/min.

The results obtained in this section demonstrate that the reactor entry is not the element that creates the resistance and prevents to obtain the 1000 ml/min sampling flow when the pre-reactor nozzle is regulated at 100 mbar. Therefore, other elements of the set-up were investigated.

4.1.3 Scrubbers

The CO and NO_x gas scrubbers are described in detail in Section 3.3. Two important factors play a role in the resistance of the scrubber: tube diameter and its content. The CO scrubber is a ½” tube filled with cylindrical pellets of platinum, whereas the NO_x scrubber is a 40 mm wide tube filled with charcoal powder. On the basis of Eq. (2.3.1.2) it is expected that the CO scrubber causes a bigger resistance owing to a smaller diameter than the NO_x scrubber. On the other hand, low porosity of the charcoal may result in high flow resistance of the NO_x scrubber. In addition, the grids installed at the inlet and the outlet of the scrubbers to prevent the content from being sucked out by the pump create a physical barrier.

Fig. 4.1.3.1 presents the set-up to measure the pressure difference between the inlet and the outlet of the flow controller (Δp) by means of the pressure gauges (MKS, Baratron 122BAX-01000DBS, Type 122B) placed in the channel 2. The study was carried out with sampled air at 1013 mbar with the Ø1 mm orifice and the 10 mm reactor entry with the following set points: the pressure in the pre-reactor nozzle 100 mbar and sampling flow through reactor 1000 ml/min.

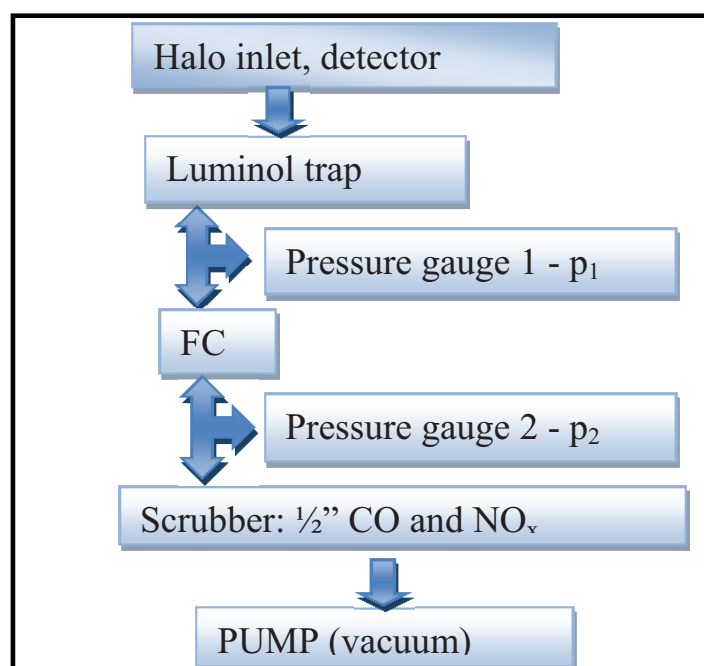


Fig. 4.1.3.1 The set-up used for the determination of the scrubber resistance.

The results obtained with and without the scrubbers are summarized in Table 4.1.3.1.

NO _x scrubber	CO scrubber	p	p ₁	p ₂	Δp=p ₁ -p ₂	Q ₁	Q ₂
+	+	~99	96	81.6	14	414	443
-	-	~99	81.7	0.05	82	781	832
+	-	~99	88.7	66.1	23	614	652
-	+	~99	98.1	77.9	20	488	520

Table 4.1.3.1 The results of the investigation of the scrubber hydraulic resistance: p - pressure obtained in the pre-reactor nozzle [mbar], p_1 - pressure obtained in front of the inlet of the sampling flow controller [mbar], p_2 - pressure obtained behind the sampling flow controller [mbar], Q_i - flow obtained in the channel 1 or 2 [ml/min].

In all the cases the pressure in the pre-reactor nozzle was successfully regulated at 100 mbar. Valves of the flow controllers were maximally open (66.67%) allowing the maximum air passage but the flow was below 1000 ml/min. The lowest $\Delta p=20$ mbar was achieved when both scrubbers were placed which also corresponds to the lowest flows below 450 ml/min. Without the scrubbers the flow through the reactor is twice higher but the flow of 1000 ml/min is, however, not achievable. The sampling flows obtained with the CO scrubber were lower than with the NO_x scrubber, although both FC valves were at a fully open position. This is related to lower Δp between the inlet and the outlet of the flow controller in case of the set-up with the CO scrubber. Thus, the results show that the CO scrubber has higher hydraulic resistance. Further improvements of the system consist in a modification of the CO scrubber that plays a main role as opposition to the air flow in the set-up.

The ½" CO scrubber tube was exchanged with a double diameter KF-25 tube of comparable length which leads to a reduction of the flow resistance 37 times according to Eq. (2.3.1.2). To gain more information about the modified set-up, the pressure in the pre-reactor nozzle to obtain 1000 ml/min through the reactor with and without the scrubbers was measured and based on that the pressure drop the relative resistance due to the scrubbers was determined. In the reactor entry the 4th Teflon insert (4mm orifice) which shows the lowest radical losses was placed and as a lid entry the Ø1.5 mm orifice was used. This study was carried out at the most extreme sampling conditions, i.e., when difference of pressure between the pre-reactor nozzle and ambient air was around 100 mbar and the corresponding flow through orifice is low. The obtained results are summarized in Table 4.1.3.2.

Orifice \varnothing	KF-25 CO scrubber, NO _x scrubber	p_{1s}	Q_r	p_2	Results
1.5	+	145	1000	222	<ul style="list-style-type: none"> • $Q_{1,2}=Q_r$ • $p_1=p_{1s}$
	-	130			<ul style="list-style-type: none"> • $Q_{1,2}=Q_r$ • $p_1=p_{1s}$

Table 4.1.3.2 The results of the investigations with the lid with the $\varnothing 1.5$ mm orifice with or without scrubbers: p_{1s} - set pressure of the pre-reactor nozzle [mbar], p_1 - pressure obtained in the pre-reactor nozzle [mbar], Q_r - set flow through the reactor [ml/min], Q_i - flow obtained in the channel 1 or 2 [ml/min], p_2 - chamber pressure [mbar].

As the required pressure difference between the inlet and the outlet of the flow controller to obtain 1l/min flow must be $\Delta p=100$ mbar according to the specification by Bronkhorst, it can be concluded that the pressure drop between the pre-reactor nozzle and the inlet of the sampling flow controller is 30 mbar (see Fig. 4.1.3.2). Consequently, the pressure drop due to the scrubbers is 15 mbar (see Fig. 4.1.3.2). By a modification of the CO scrubber, a reduction of the minimum pressure in the pre-reactor nozzle for the 1000 ml/min flow through the channel from 160 mbar to 145 mbar was achieved (see Section 4.1.1). Thus, the pressure drop related to the NO and $\frac{1}{2}$ " CO scrubbers is 30 mbar and the resistance of the NO+ $\frac{1}{2}$ "CO scrubbers was reduced by half in comparison to NO+KF-25 CO scrubbers.

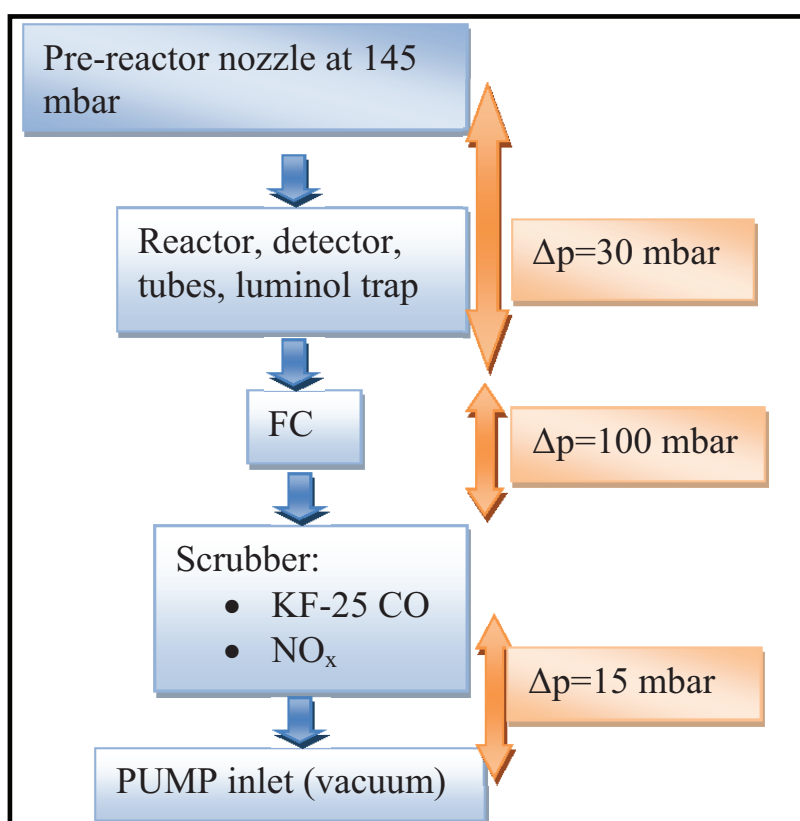


Fig. 4.1.3.2 Determination of the pressure drop through the set-up components.

The relative resistances of the components were quantified based on the pressure drop within the set-up in reference to the total pressure difference between the pre-reactor nozzle and the pump inlet ($\Delta p=145$ mbar):

- Reactor, detector, tubes, luminol trap $30/145*100\%=21\%$,
- Flow controller $100/145*100\%=69\%$,
- Scrubbers $15/145*100\%=10\%$.

4.1.4 Detectors

All the experiments to characterize the hydraulic resistance in the PeRCA set-up were performed with the luminol detector which was used for the characterization of the HALO reactors as a NO_2 detector. However, instead of this device a new CEAS (Cavity Enhanced Absorption Spectroscopy) detector will be employed during the OMO campaign. Therefore, a comparison of the flow resistance of the detectors was performed. In the channel 2 (see Fig. 4.1.1) the luminol detector was replaced by the new CEAS detector, the $\text{Ø}1.2$ mm entry orifice and the 4th insert as a reactor entry were used.

The luminol detector is expected to show higher hydraulic resistance because it includes a glass fibre filter of a thickness of 1 mm through which air has to pass (see Fig. 4.1.4.1 a). The CEAS, on the other hand, consists of a rectangular cell of a 280 cm^3 volume with no physical barriers inside that might create an opposition to the flow (see Fig. 4.1.4.1 b).

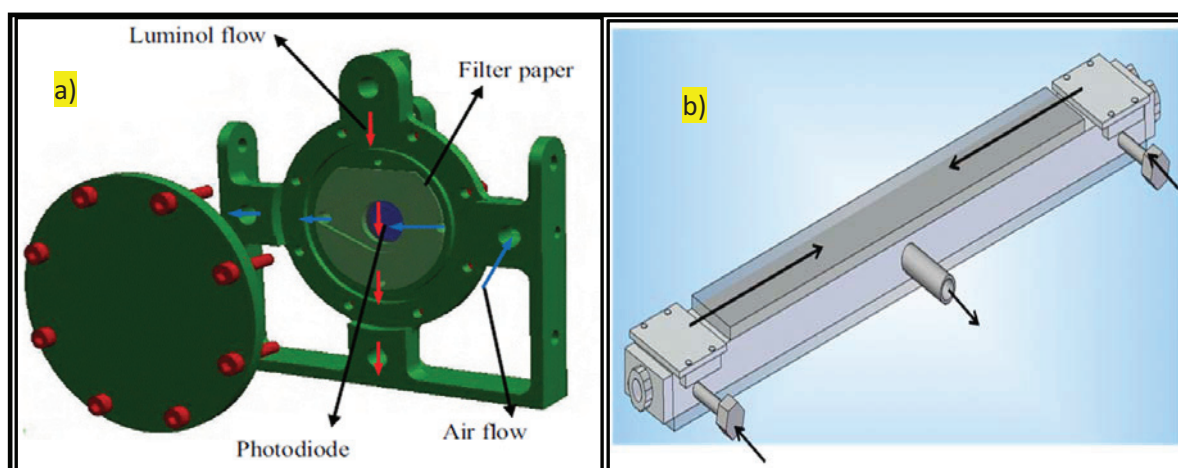


Fig.4.1.4.1 A schematic diagram of the NO_2 detectors a) luminol detector (Kartal D., PhD thesis 2009) b) CEAS detector.

The outcome is summarized in Table 4.1.4.1.

Orifice Ø	Scrubbers	p_{1s}	Q_r	p_2	Results
1.2	KF-25 CO scrubber, NO _x scrubber	200	1000	~1013, 515, 315	<ul style="list-style-type: none"> • $Q_{1,2}=Q_r$ • $p_1=p_{1s}$
		100	1000	~1013	<ul style="list-style-type: none"> • $p_1 > p_{1s}$ • $p_1=150$ • $V_{PR}=66.67\%$ • $O_{1,2}=Q_r$
				515, 315, 221	<ul style="list-style-type: none"> • $p_1=p_{1s}$ • $O_{1,2} < Q_r$ • $Q_1 < 550$ • $Q_2 < 830$ • $V_{FC1,2}=66.67\%$
		145	1000	221	<ul style="list-style-type: none"> • $Q_{1,2}=Q_r$ • $p_1=p_{1s}$

Table 4.1.4.1 The results of the comparison of the detector resistance: p_{1s} - set pressure of the pre-reactor nozzle [mbar], p_1 - obtained pressure in the pre-reactor nozzle [mbar], Q_r - set flow through the reactor [ml/min], Q_i - obtained flow in the channel 1 or 2 [ml/min], p_2 - chamber pressure [mbar], V_{PR} - position of the pressure regulator valve, $V_{FC1/2}$ - position of the flow controller in the channel 1 (luminol detector) or 2 (CEAS detector).

- The pressure in the pre-reactor nozzle can be controlled at 200 mbar and the 1000 ml/min flow can be achieved through both channels at all external p_2 pressures.
- The regulation at 100 mbar can be performed when the sampling air pressure p_2 is below 515 mbar.
- The pressure could not be controlled at $p_1=100$ mbar when $p_2 \approx 1013$ mbar (then $p_1=150$ mbar). The sampling flow of $Q=1000$ ml/min was achieved. It also supports the previous determination that the pressure in the pre-reactor nozzle to obtain 1000 ml/min should be higher than 145 mbar.

Similar results were obtained with the luminol detector in both channels (see Table 4.1.1.5).

The most striking feature is around 300 ml/min higher flow of through the channel 2 (with the CEAS detector) than the channel 1 (with the luminol detector) when the valves of the flow controller are fully open and do not regulate the flow conditions. This results from the asymmetry of the system and proves that the new detector has lower hydraulic resistance than the luminol detector. The difference in flow Q_2-Q_1 between the identical channels (both with the luminol detector) was also observed but at lower extent, i.e., around 180 ml/min (see Fig. 4.1.1.2).

In summary, the results indicate that the detector CEAS is not expected to play a significantly different role as a flow resistor in the PerCEAS instrument in comparison to the luminol detector. Therefore, the introduction of the new detector into the set-up will not

change the hydraulic properties of the instrument and the characterization carried out with the luminol detector is also valid for the OMO campaign.

4.1.5 Other components (FC valve, PR valve, tubing etc.)

The pressure regulator (PR) valve is an adjustable orifice in the set-up. The PR valve was in fully open position and it acted as a flow resistor in case of the experiments with the Ø1.5 mm entry when the pressure in the pre-reactor nozzle could not be regulated at 100 mbar at the external pressure higher than 500 mbar (see Table 4.1.5.1).

p_{1s}	Q_r	p_2	Results	
			½" CO scrubber, NO _x scrubber, Teflon insert 2 nd (8 mm orifice)	KF-25 CO scrubber, NO _x scrubber, Teflon insert 4 th (4 mm orifice)
100	1000	~1013	<ul style="list-style-type: none"> • $p_1 > p_{1s}$ • $p_1 = 200$ • $V_{PR} = 66.67\%$ 	<ul style="list-style-type: none"> • $p_1 > p_{1s}$ • $p_1 = 209$ • $V_{PR} = 66.67\%$
		~508	<ul style="list-style-type: none"> • $p_1 > p_{1s}$ • $p_1 = 106$ • $V_{PR} = 66.67\%$ 	<ul style="list-style-type: none"> • $p_1 > p_{1s}$ • $p_1 = 109$ • $V_{PR} = 66.67\%$
		~200	<ul style="list-style-type: none"> • $p_1 = p_{1s}$ 	<ul style="list-style-type: none"> • $p_1 = p_{1s}$

Table 4.1.5.1 The results of the investigations with the lid with the Ø1.5 mm orifice, p_{1s} - set pressure of the pre-reactor nozzle [mbar], p_1 - obtained pressure in pre-reactor nozzle [mbar], Q_r - set flow through the reactor [ml/min], Q_i - obtained flow in the channel 1 or 2 [ml/min], p_2 - chamber pressure [mbar], V_{PR} - position of the pressure regulator valve.

The flow controller (FC) valve is another adjustable orifice in the set-up. It created opposition to the flow when the pre-reactor nozzle was regulated at 100 mbar preventing to obtain 1l/min flow. As the pressure drop between the pre-reactor nozzle and the inlet of the FC is 30 mbar (see Section 4.1.4) the Δp between the inlet and outlet of FC is lower than the required $\Delta p = 100$ mbar (Bronkhorst specifications).

As mentioned in the introduction to this section, wherever possible ¼" Swagelok components were exchanged with their bigger equivalents to reduce the resistance in the set-up. The safety valve in front of the pump was replaced from size ¼" into KF-60 which resulted in a reduction of the opposition to the flow in front of the pump and its more effective performance.

4.2 Investigation of radical losses in the sampling system

The losses of peroxy radicals on the instrument surfaces prior to their conversion into NO_2 , namely in the pre-reactor nozzle and at the reactor entry, is an inevitable process because of their high reactivity. To characterize the removal processes on these elements the experiments with the HALO inlet were conducted. Then the next step of the investigation was determination of the losses of hydroxyl and organic radicals on the reactor walls using the DUALER 2 set-up. In addition, the effect of amorphous silicon as a coating material on the wall losses was investigated. For these series of experiments the radical source described in Section 3.2.2 was implemented.

4.2.1 Sampling orifice of the pre-reactor nozzle

The radicals produced in the radical source ($[\text{HO}_2^0]$) are lost by the wall losses and the radical-radical reactions ($[\text{HO}_2^{\text{loss}}]$) prior to their reaction with CO and NO in a reactor. Therefore, the observed $[\Delta\text{NO}_2]$ corresponds to a radical amount which is lower than the $[\text{HO}_2]$ produced in the source (see Figure 4.2.1.1). However, the chain length is actually calculated with the amount of radicals produced in the source ($[\text{HO}_2^0]$) as though the losses are neglected and is therefore called effective chain length - eCL :

$$eCL = \frac{[\Delta\text{NO}_2(\text{HO}_2^0 - \text{HO}_2^{\text{loss}})]}{[\text{HO}_2^0]} \quad (4.2.1.1).$$

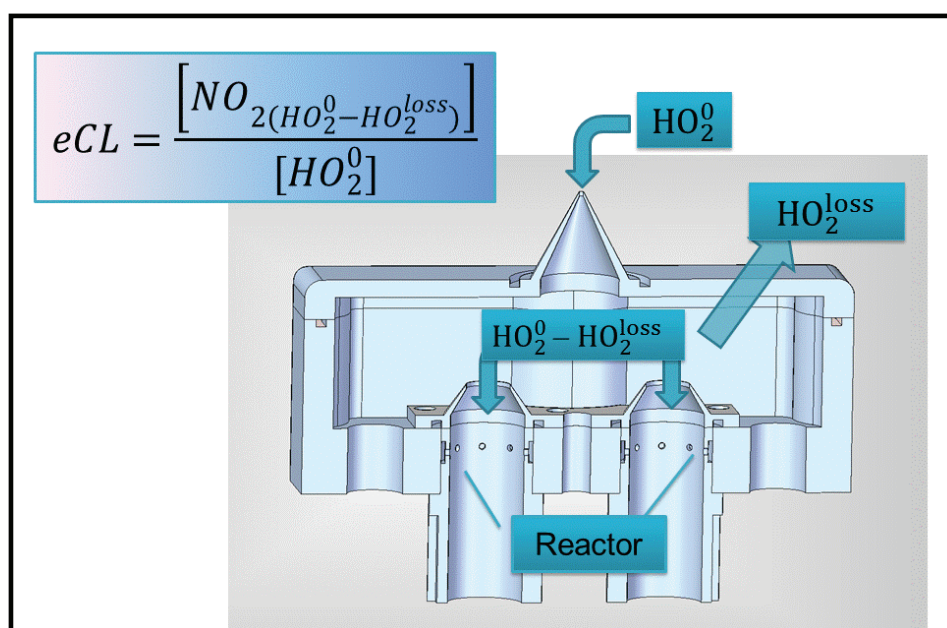


Fig. 4.2.1.1 Schematic representation of the HO_2 losses in the pre-reactor nozzle.

The pre-reactor nozzle of the HALO inlet consists of a conical entry with varied orifice diameter ($\text{\O}1$, $\text{\O}1.2$, $\text{\O}1.5$ mm) and the interior surface shown in Fig. 4.2.1.2.

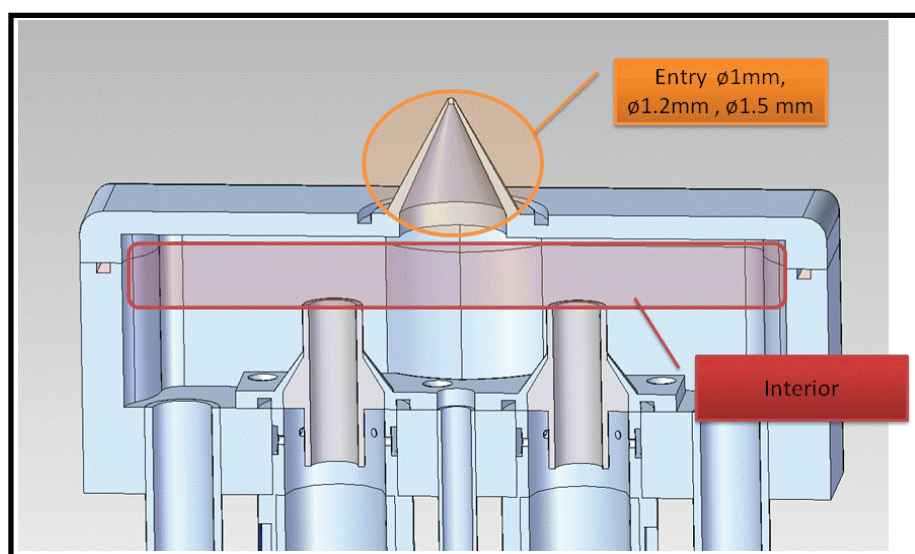


Fig. 4.2.1.2 Schematic representation of the pre-reactor nozzle.

Firstly, the determination of the relative importance of the pre-reactor nozzle parts in the radical losses for the lid $\text{\O}1.2$ mm non-coated and coated by Teflon was carried out. The same magnitude of the radical losses in the interior of the pre-reactor nozzle is expected for both cases. Thus, if the losses on the conical entry are dominating, the eCL for the Teflon coated entry should be higher than for the non-coated. The 4th Teflon insert (see Section 4.2.2.1) as a reactor entry was used and the pressure in the pre-reactor nozzle was regulated at 900, 500 and 300 mbar. The experimental configuration is presented in Fig. 4.2.1.3.

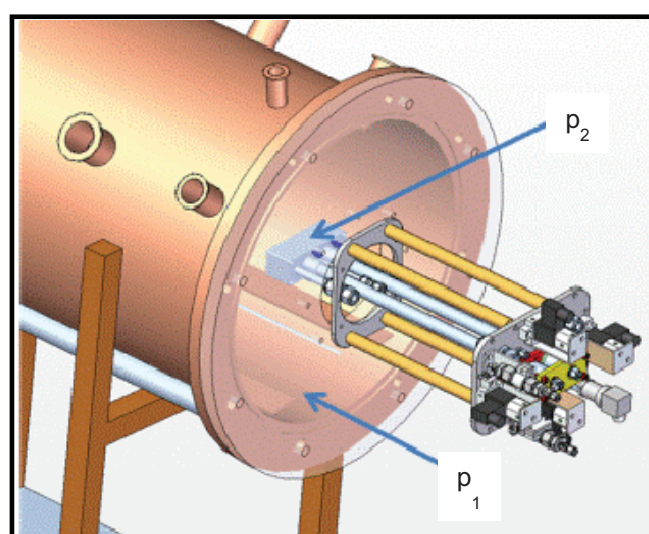
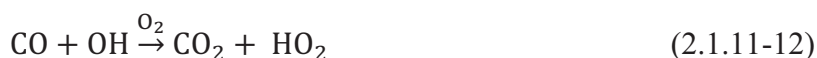


Fig. 4.2.1.3 Schematic representation of the set-up, p_1 – pressure of the pressure chamber, not regulated, p_2 – pressure of the pre-reactor nozzle, variable: 900, 500 and 300 mbar.

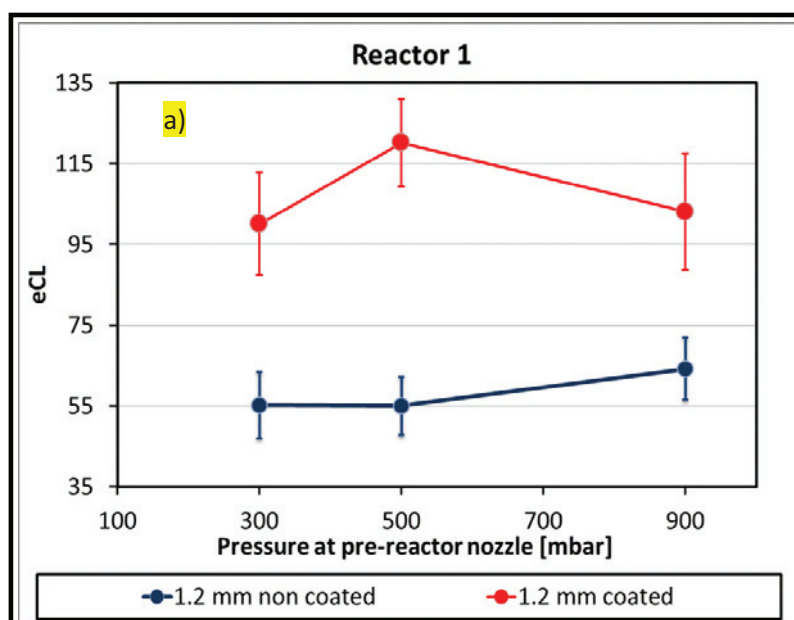
The eCL variations with the pressure are expected as the conditions in the reactor affecting the radical conversion and amplification are changing. Firstly, the amplification reaction:



is pressure dependent, and therefore for lower pressures the reaction rate decreases. In addition, at lower pressures the wall losses are becoming more important, as the molecular collision probability decreases with the decreasing number of the reagent molecules of CO and NO. The chemical reactions terminating the chain reaction which are pressure dependent are slower at lower pressures. As a consequence, the effect of the wall losses in terminating the chain reaction is more dominant.

The outcome of these experiments is presented in Fig. 4.2.1.4, the eCL values are summarized in the Appendix 2.

As expected a decrease of the eCL is observed with a decrease of the pressure except at 500 mbar for the Reactor 1 with the Teflon coated conical entry. The eCL obtained with the non-Teflon coated entry are approximately $50\% \pm 8\%$ lower than with the coated, thereby the radical removal processes are more effective in such an entry. There are observed small differences in the obtained eCL between the reactors but they are within the error bars of the eCL . The results show that the removal processes are favoured in the conical entry.



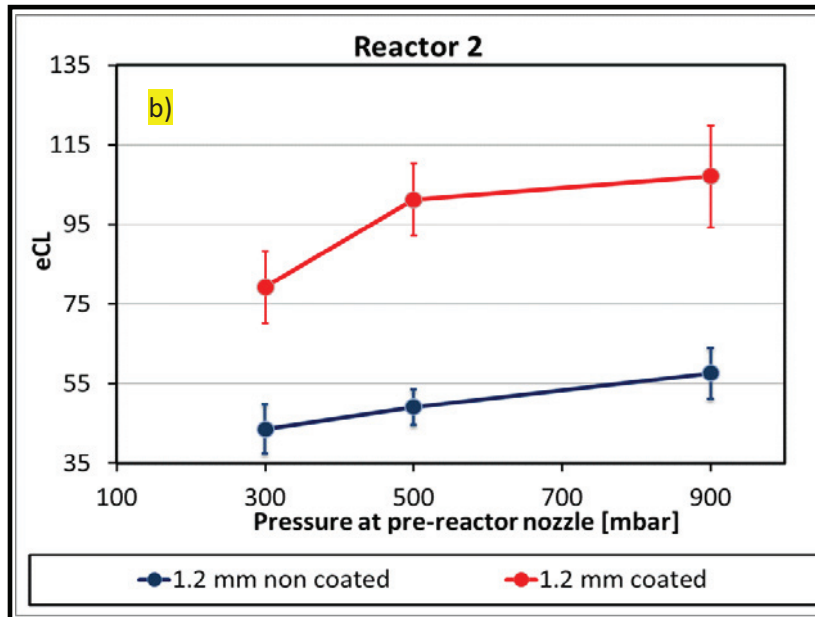


Fig. 4.2.1.4 Determination of the radical losses in pre-reactor nozzle with the Ø1.2 mm non-Teflon and Teflon coated conical entry a) Reactor 1, b) Reactor 2.

Then the effect of the sampling orifice diameter on the radical losses in the pre-reactor nozzle was investigated. Three different Teflon-coated orifices with diameters of Ø1, Ø1.2, Ø1.5 mm were used and based on the obtained eCL the removal processes were compared. Overall wall losses in the pre-reactor nozzle result from the competing processes:

- A higher flow through a wider orifice is expected for the same $\Delta p = p_{external} - p_{inlet}$. A higher flow is related to the corresponding lower residence time in the pre-reactor nozzle, thus the radicals have less time to be removed on the walls.
- On the other hand, a higher flow corresponds to the higher velocity which may lead to the turbulences in the pre-reactor nozzle, and consequently higher losses of the radicals.
- The radical wall loss rate coefficient: k_w is proportional to the ratio S/V (Eq. 2.2.3.15), for a cylindrical entry inversely proportional to a diameter. Thus, k_w is expected to decrease when increasing the diameter, i.e., 33% lower for the Ø1.5 mm entry in comparison to the Ø1 mm. And thereby, a reduction of the losses is expected with the orifices of increasing diameter. As the S/V ratio is 0.36 [mm⁻¹] for the conical part of the entry of all the nozzles, a magnitude of the radical losses is expected to be similar within the conical part for all the nozzles.

Fig. 4.2.1.5 compares the eCL for the Ø1mm entry lid determined within a different series of experiments with the IUP source. Table 4.2.1.1 compares the conditions within these determinations of the eCL .

Experiment set	\varnothing - inner diameter of the quartz tube [mm]	Radical source	SA flow [l/min]
1	15	original shutter	10
2	15	modified shutter	10
3	16	modified shutter	8
4	16	modified shutter	10

Table 4.2.1.1 Comparison of the conditions during the experiments for the $\varnothing 1$ mm entry lid, SA flow synthetic air flow.

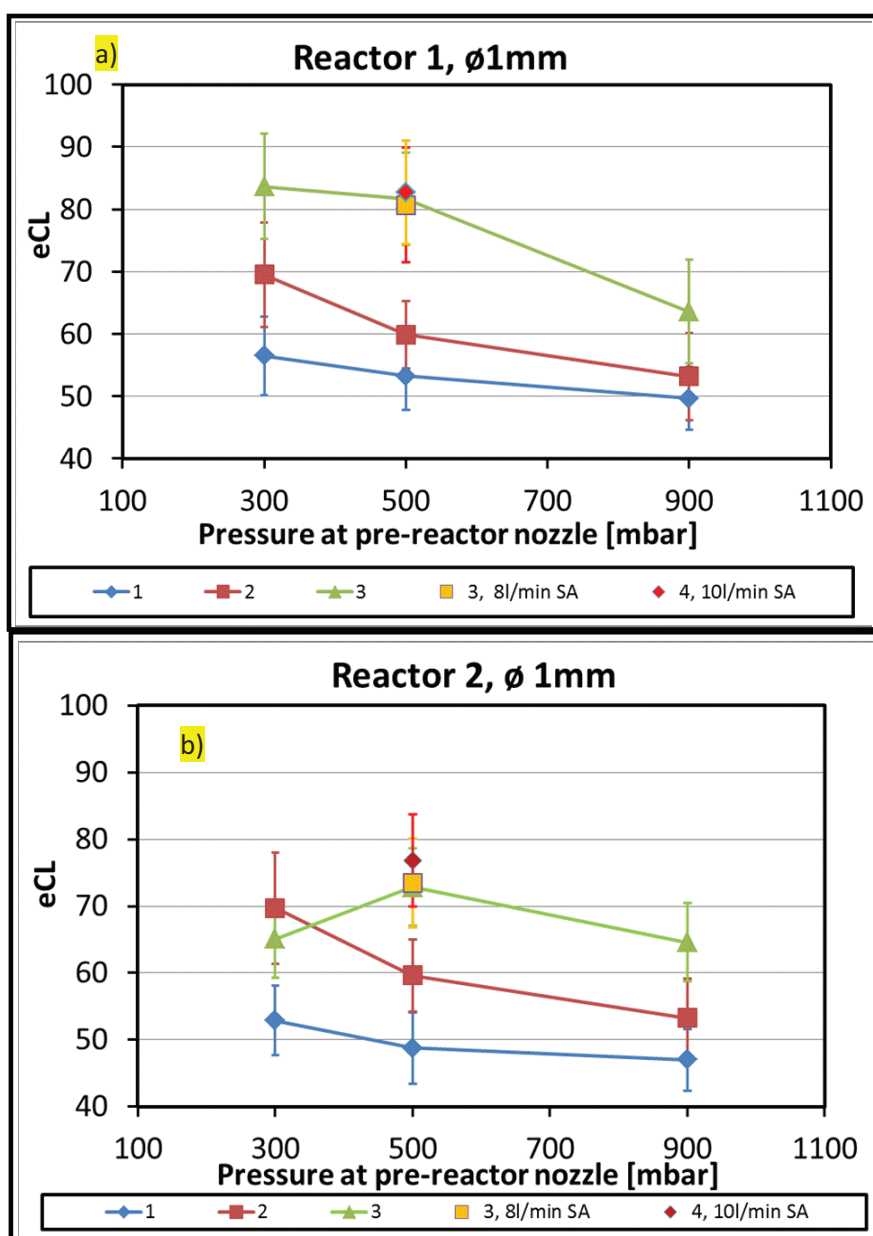


Fig. 4.2.1.5 Variation of the eCL for the orifice $\varnothing 1$ mm a) Reactor 1, b) Reactor 2. Nr. 1-4 refer to a set of the experiments summarized in Table 4.2.1.1.

For the reactor 1 and the quartz tube with diameter of $\varnothing 15$ mm (set of experiments 1 and 2), data points of the obtained eCL value agree within the error bars except at 300 mbar, while for the reactor 2 differences are significantly higher. There is a discrepancy between

the *eCL* determined with different quartz tubes (set of experiments 2, 3, 4), in general higher *eCL* values for Ø16 mm. Thus, within the experiments carried out as the set 3, the *eCL* was repeated: with 8 l/min SA through the quartz source (denoted as 3, 8 l/min SA) and 10 l/min (denoted as 4, 10 l/min SA) at 500 mbar at the pre-reactor nozzle. The *eCL* has been reproducible for both reactors (see Fig. 4.2.1.5). Therefore, change of the flow of the synthetic air through the quartz tube and thus the associated radical losses in the tube did not affect the *eCL* value. The curvature of the *eCL* shows for 1 and 2 set of points a minimum at 500 mbar, a maximum at a set 3 of the experiments. There is no indication of any experimental artefact related to the determination of the *eCL* in sets of 1 and 2.

In Fig. 4.2.1.6 the effect of the sampling orifice diameter on the radical removal in the pre-reactor nozzle is summarized.

The *eCL* for the reactor 1 is higher than for 2 although they are supposed to be identical. This might be attributed to the differences of the geometrical and surface properties of the reactors and/or higher magnitude of the turbulences created in the pre-reactor nozzle in front of the reactor 2 due to asymmetry in the flow sampling resulting in higher radical losses. For the coated Ø1.2 and Ø1.5 mm orifices the *eCL* decreases with the pressure as expected from known chemistry. The *eCL* obtained at different pressures shows a slight curvature with a maximum around 500 mbar for Ø1 mm.

In the case of the pre-reactor nozzle controlled at 900 mbar, the *eCL* obtained with the Ø1 mm orifice for both reactors was ~60% lower in comparison to Ø1.2 and 1.5 mm, what indicates that these orifices are associated with the lowest radical losses. It confirms that higher radical losses are related to the lower flow through the narrower orifice and corresponding higher retention time in the pre-reactor nozzle.

At 500 mbar, the *eCL* with the Ø1.2 mm orifice is significantly higher than with the Ø1 mm, in case of the reactor 1: 47% and the reactor 2: 39 %. The *eCL* values obtained with the orifice Ø1.2 mm and Ø1.5 mm are within the error bars. Thus, for the pressure conditions above 500 mbar the radical losses are the most effective for the orifice Ø1 mm.

In the case of 300 mbar in the pre-reactor nozzle, the obtained *eCL* values for all the orifices are similar within the error bars, except for the orifice Ø1 mm which is 20% lower. The relatively high error bars with Ø1.5 mm are related to the noise of the NO₂ detector signal (3 times higher than for the Ø1 mm). The signal variations might be attributed to high flow and velocity of the sampled air causing pressure disturbances in the pre-reactor nozzle further propagated into the detector.

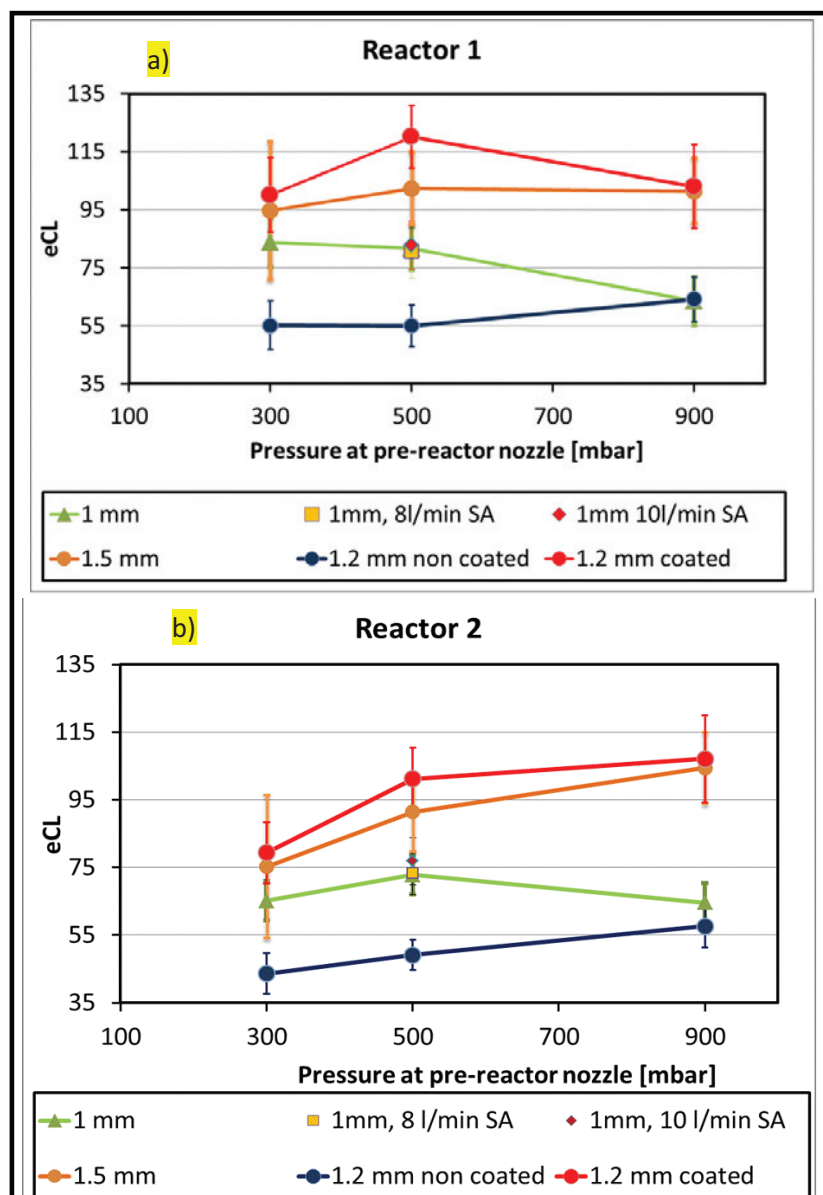


Fig. 4.2.1.6 The eCL determined for different sampling orifice diameters: $\varnothing 1$, $\varnothing 1.2$, $\varnothing 1.5$ mm a) Reactor 1, b) Reactor 2, eCL reproducible for $\varnothing 1$ mm at 500 mbar pre-reactor nozzle with SA through the quartz source 8 l/min (green triangle and yellow rectangle points) and 10 l/min (red diamond point).

4.2.1.1 Pre-reactor nozzle of the DUALER 2 inlet

The radical losses were also investigated within the pre-reactor nozzle of the DUALER 2 inlet comprising the reference and modified reactors and the pre-reactor nozzle. Interference between the reactors, presented in Fig. 4.2.1.7, was observed at 900 mbar. This effect was not detected by the characterization of the single reactors at ambient pressure and without the pre-reactor nozzle. This, therefore, indicates that the pressure regulation enhances the air mixed with CO and NO move backwards to the pre-reactor nozzle.

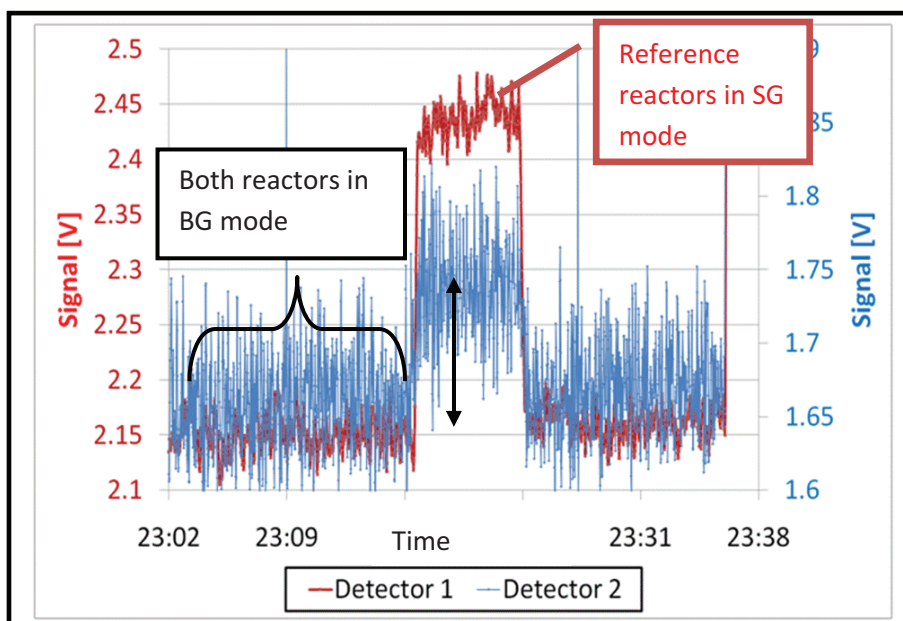


Fig. 4.2.1.7 Interference between the inlet channels. When the channel 2 set in SG mode (modified reactor), an increase of the signal in the channel 1 was observed (reference reactor), denoted as black arrow, the pre-reactor nozzle at 900 mbar.

To suppress the interference the form of the reactor entry was modified. Teflon inserts were added to the reactor entry which had originally a length of 7 mm (see Fig. 4.2.1.8). However, the conical shape of the pre-reactor nozzle constrained the height to only 10 mm, in comparison to the HALO inlet 15 mm.



Fig. 4.2.1.8 A Teflon insert placed on the reactor entry.

Then it was investigated whether the interference occurs. It turned out that for the regulation pressure 900 and 800 mbar it was not the case, see Fig. 4.2.1.9, i.e., the detector signal for the modified reactor set to background mode always remained constant.

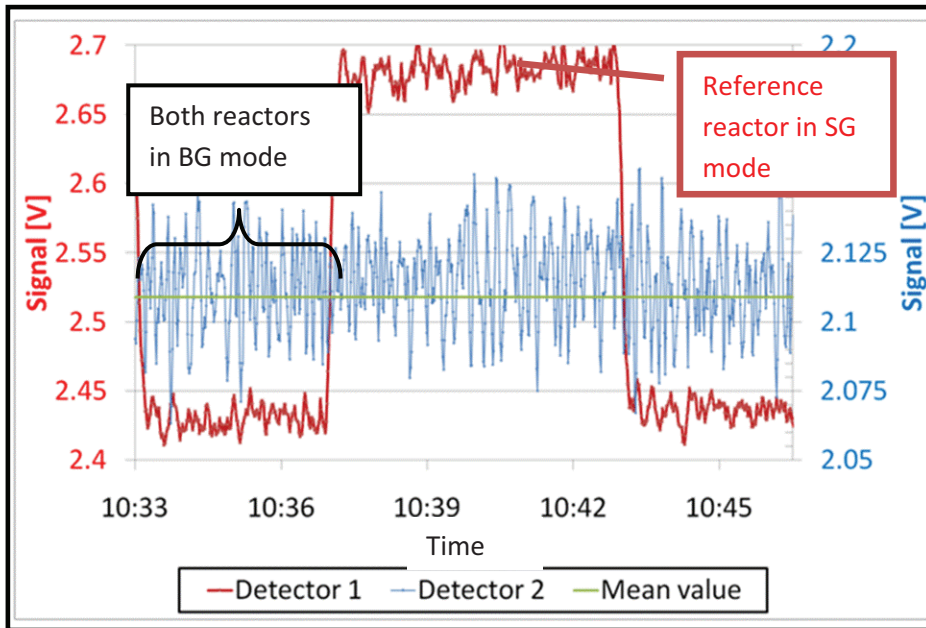


Fig. 4.2.1.9 Example of the successful separation of the reactors, the pre-reactor nozzle at 900 mbar. In red response of the detector 1 used for the reference reactor, in blue response of the detector 2 used for the modified, SG denotes signal and BG background mode.

However, at the regulated pressures below 700 mbar the interference was clearly seen (e.g., at 500 mbar, see Fig. 4.2.1.10). Therefore, the characterization of the inlet was performed only when the pre-reactor nozzle was kept at 900 and 800 mbar.

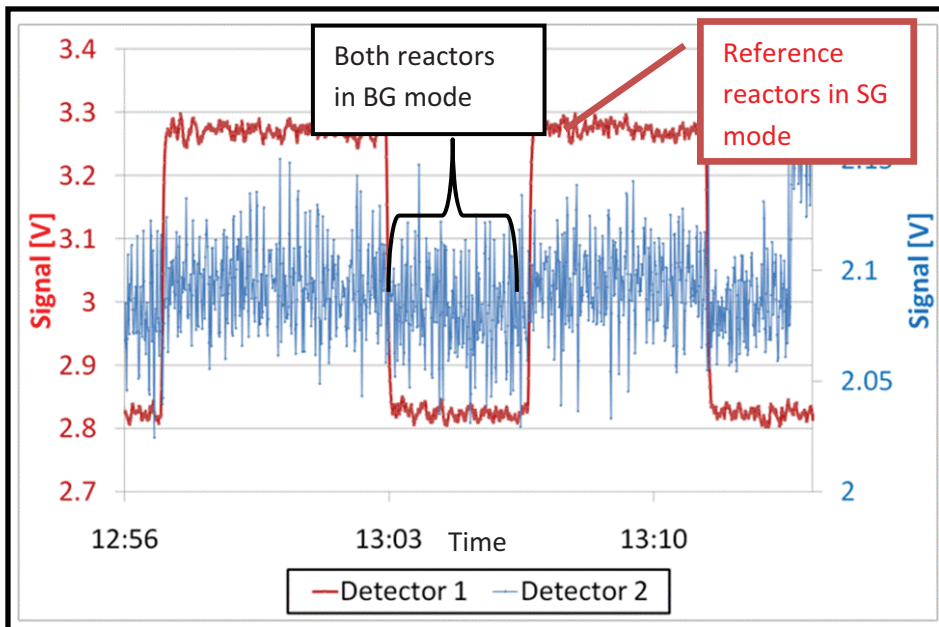


Fig. 4.2.1.10 Observed interference between the reactors, the pre-reactor nozzle at 500mbar. Detector 2 indicates the signal of the modified reactor and detector 1 of the reference reactor, SG and BG denotes and background mode.

In Fig. 4.2.1.11 the obtained *eCL* values are depicted.

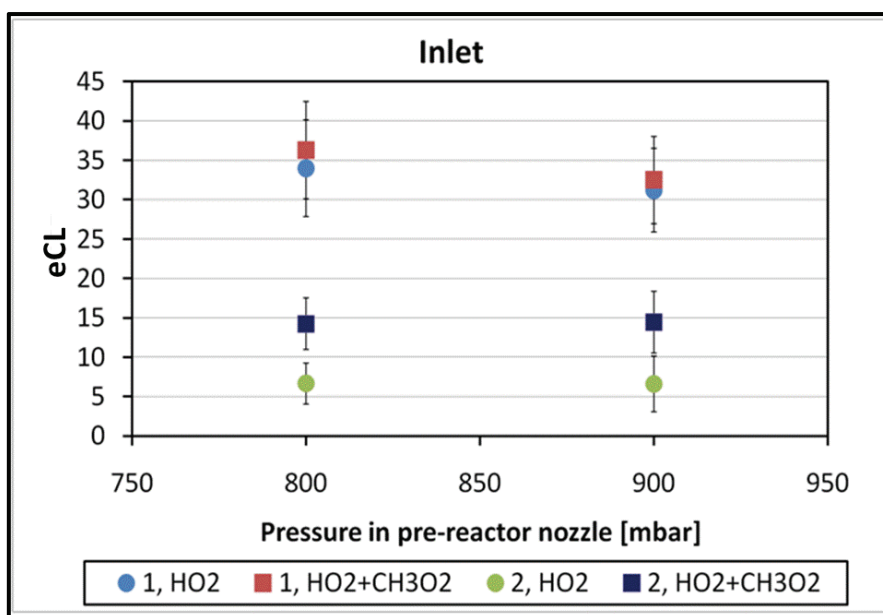


Fig. 4.2.1.11 The obtained eCL for the DUALER 2 inlet, nr 1 the reference reactor, nr 2 the modified reactor.

The eCL is lower than the CL determined for the single reactors (presented in section 4.2.3), i.e., up to 13 times lower for the reference reactor and for the modified reactor 20 times lower. In case of the modified reactor the modulation signal for low mixing ratios of the radicals cannot be clearly seen (Fig. 4.2.1.11), the produced $[ANO_2]$ were close to the detection limit of the detector, therefore relatively high $\frac{\Delta eCL}{eCL}$ up to 54% (see Fig. 4.2.2.12) in comparison to the reference reactor $\frac{\Delta eCL}{eCL} = 17\%$.

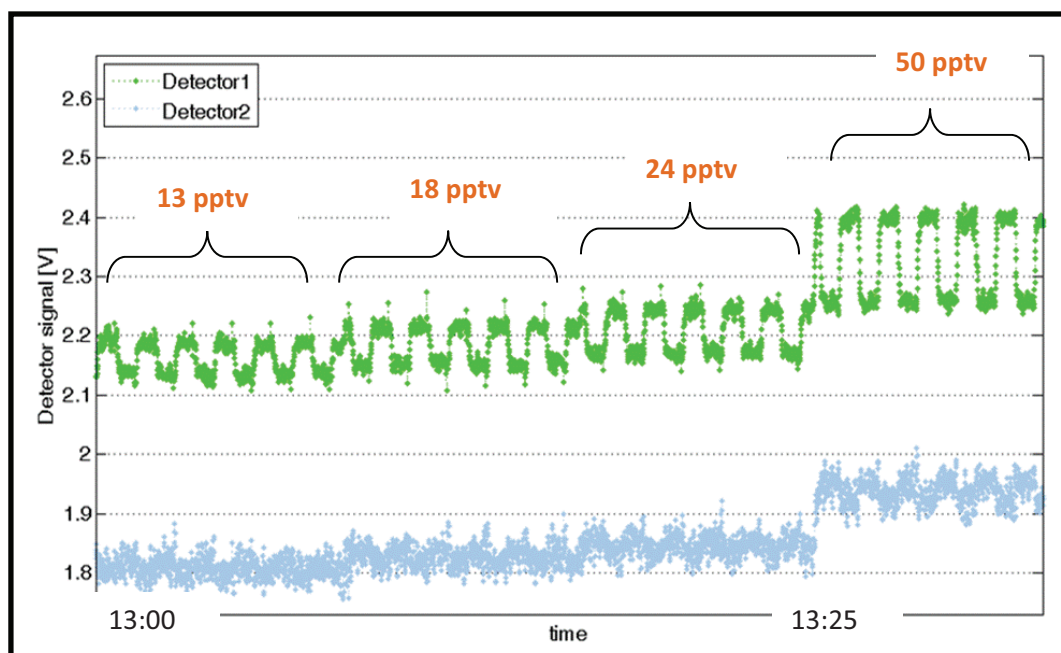


Fig. 4.2.2.12 Comparison of the modulation signal, a signal in green for the reference reactor, a signal in blue for the modified reactor, number in orange the calculated HO₂ mixing ratios.

The significant loss of the radicals (90% of radical removal) is related to the geometry of the pre-reactor nozzle and the reactor entry, with a minimum distance of 1 mm between these components, which act as a trap for the radicals.

4.2.2 Reactor entry

As mentioned in Section 3.1 the reactor entry separates the reactors so that air is sampled only from the pre-reactor nozzle. In addition, the reactor entry should be carefully designed to minimize the radical losses.

4.2.2.1 Interference between reactors, Teflon insert geometry

During the experimental determination of the eCL it was observed that when one of the channels of the HALO inlet was set in signal (SG) mode, the signal of the other channel in the background (BG) mode increased accordingly (see Fig. 4.2.2.1-2). As in the BG mode no radical conversion and therefore no change in the background level are expected, this was a clear indication of the interference between the reactors.

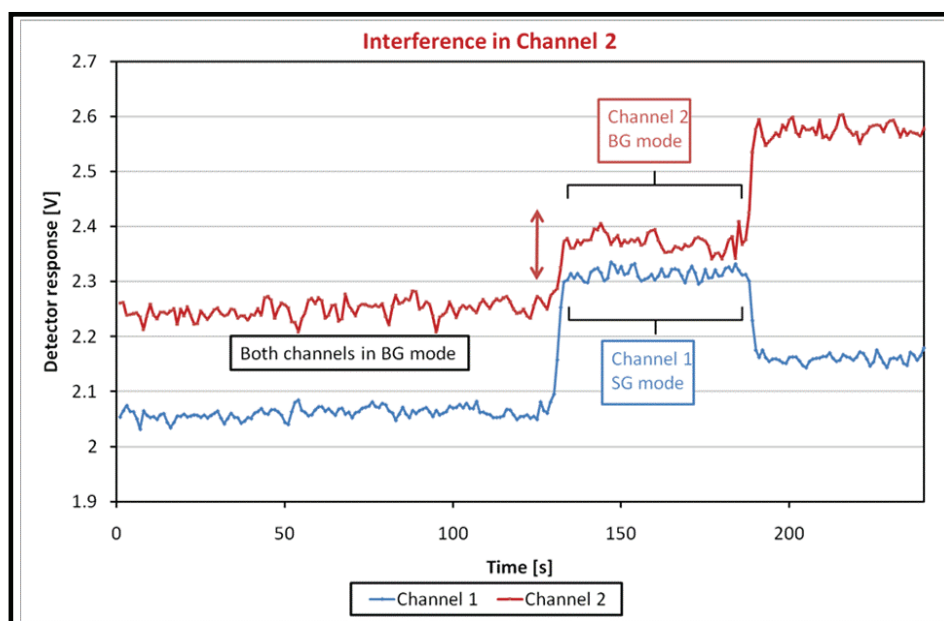


Fig. 4.2.2.1 Interference between the inlet channels. The red arrow denotes the signal increase in the channel 2. P at the pre-reactor nozzle: 600 mbar.

When the channel 1 was set to the SG mode, the signal of the channel 2 also increased (in Fig. 4.2.2.1 marked as a red arrow). This increase is 7% of the background signal, 0.15 V, which taking into account the sensitivity of the detector 0.08ppb/V corresponds to the 1.9 ppb NO₂ interference.

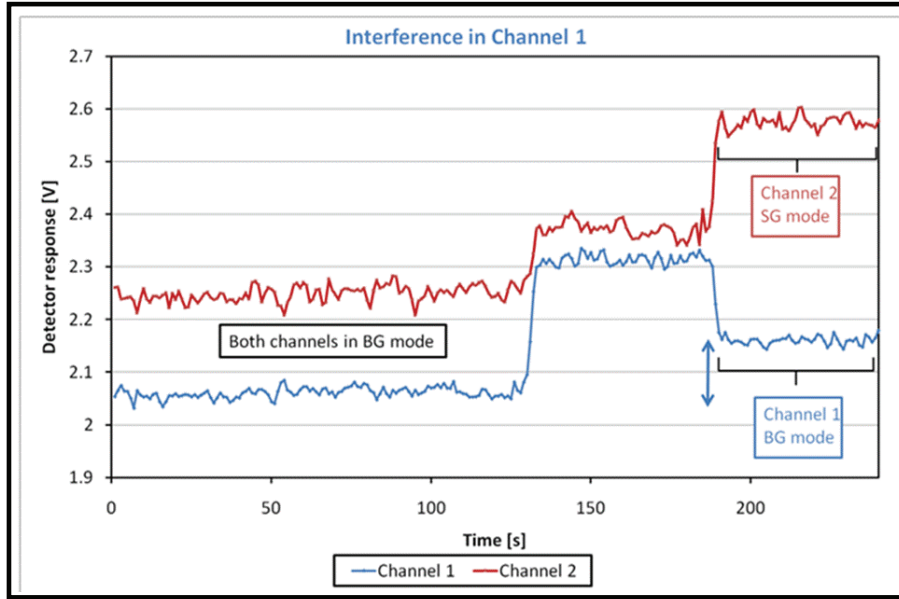


Fig. 4.2.2.2 Interference between the inlet channels. The blue arrow denotes the signal increase in the channel 1. P at the pre-reactor nozzle=600 mbar.

Similarly, the signal increase (in Fig. 4.2.2.2 marked as a blue arrow) is 5% of the background signal, 0.1 V, which taking into account the sensitivity of the detector (0.05ppb/V) corresponds to 2 ppb NO_2 interference of the channel 2 in the channel 1.

This interference results in the underestimation of the eCL by 26%, e.g., when interference occurred for $[HO_2] = 96.9$ pptv, $[\Delta NO_2]_{\text{int}} = 5.6$ ppbv, $eCL_{\text{int}} = 57.8$ and then with the included interference of 2 ppbv $[\Delta NO_2]_{\text{corrected}} = 7.6$ ppbv and $eCL_{\text{corrected}} = 78.4$. Thus, underestimation $26\% = \left(1 - \frac{eCL_{\text{int}}}{eCL_{\text{corrected}}}\right) * 100\%$. As $[RO_2^*]$ is determined from $\frac{[\Delta NO_2]}{eCL}$ with the measured $[\Delta NO_2]$ an error in the eCL will lead to overestimation of $[RO_2^*]$ by 35%, i.e., $35\% = \left(1 - \frac{\frac{[\Delta NO_2]}{eCL_{\text{int}}}}{\frac{[\Delta NO_2]}{eCL_{\text{corrected}}}}\right) * 100\%$, if the interference was not recognized and the reactor entry not modified.

A possible explanation of the interference is schematically presented in Fig. 4.2.2.3. The turbulences resulting from adding of CO and NO into the top part of one reactor through a set of eight small orifices (see Section 3.1.1) are so strong that air with CO and NO leave the reactor through the entry and enter the other reactor and initiates the chain reaction.

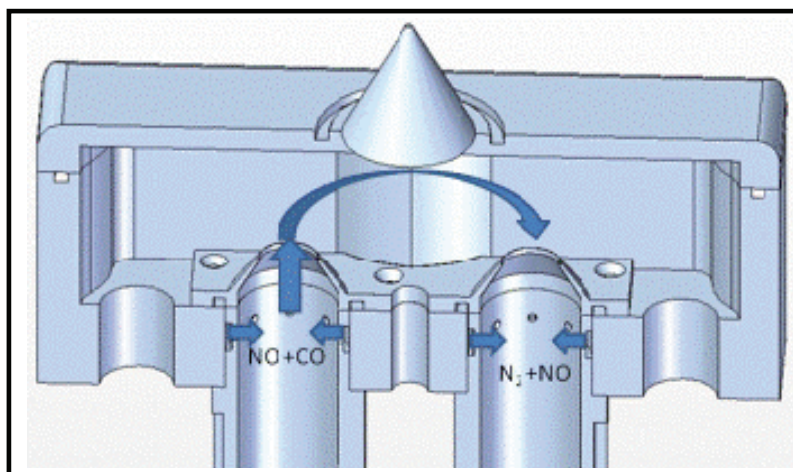


Fig. 4.2.2.3 Schematic representation of the interference between the reactors.

It has been postulated that the geometry of the reactor entry (height, shape) might play an important role in a formation of the interference. The previous work of the TROLAS group at the IUP-Bremen has shown that the height of the reactor entry plays a critical role in preventing the CO+NO losses through the reactor entrance. Therefore, a form of the reactor entry was modified through Teflon inserts to eliminate the interference. Teflon was selected as an inert material to reduce the radical losses on the surfaces. Seven different Teflon elements, summarized in Table 4.2.2.1, were tested whether the interference between the reactors occurs. In addition, the eCL for each reactor was determined to investigate influence of different geometries on the radical wall losses.

Teflon insert	Protrusion (1)	l_1	\varnothing_1	Protrusion (2)	l_2	\varnothing_2	Additional features
1 st	+	9	8	+	10	11	Protrusion (3) conical shape
2 nd	+	6	8	+	10	8	
3 rd	+	12	8	-	0	0	
4 th	+	5.2	4	-	0	0	Protrusion (3) conical shape
5 th	+	6	8	-	0	0	
6 th	-	0	0	-	0	0	$\varnothing=8$ mm of the cross section
7 th	-	0	0	+	10	8	

Table 4.2.2.1 Summary of the Teflon insert features: Protrusion (1) located inside the pre-reactor nozzle, l_1 - protrusion (1) length [mm], \varnothing_1 - protrusion (1) orifice diameter [mm], protrusion (2) inside the reactor, l_2 - protrusion (2) length [mm], \varnothing_2 -protrusion (2) diameter [mm].

Following variables characterize the used Teflon inserts, as highlighted in Fig. 4.2.2.4:

- Presence of a protrusion (1) inside the pre-reactor nozzle whose length and orifice diameter were varied. The protrusion (1) acts an extension of the reactor entry by

increasing the entry height, and the turbulences created by adding NO and CO might be too weak to pass through and consequently the gases will not leave the reactor entry. The diameter was varied, namely all the inserts had $\text{Ø}8$ mm and the 4th insert $\text{Ø}4$ mm.

- Presence of a protrusion (2) inside the reactor of 10 mm constant length and variable orifice diameter. This protrusion plays a role as a shelter for NO and CO leaving the top addition point and thereby turbulences are screened in a direction of the reactor entry.
- Shape of the part inside conical nozzles (3): cylindrical or conical.

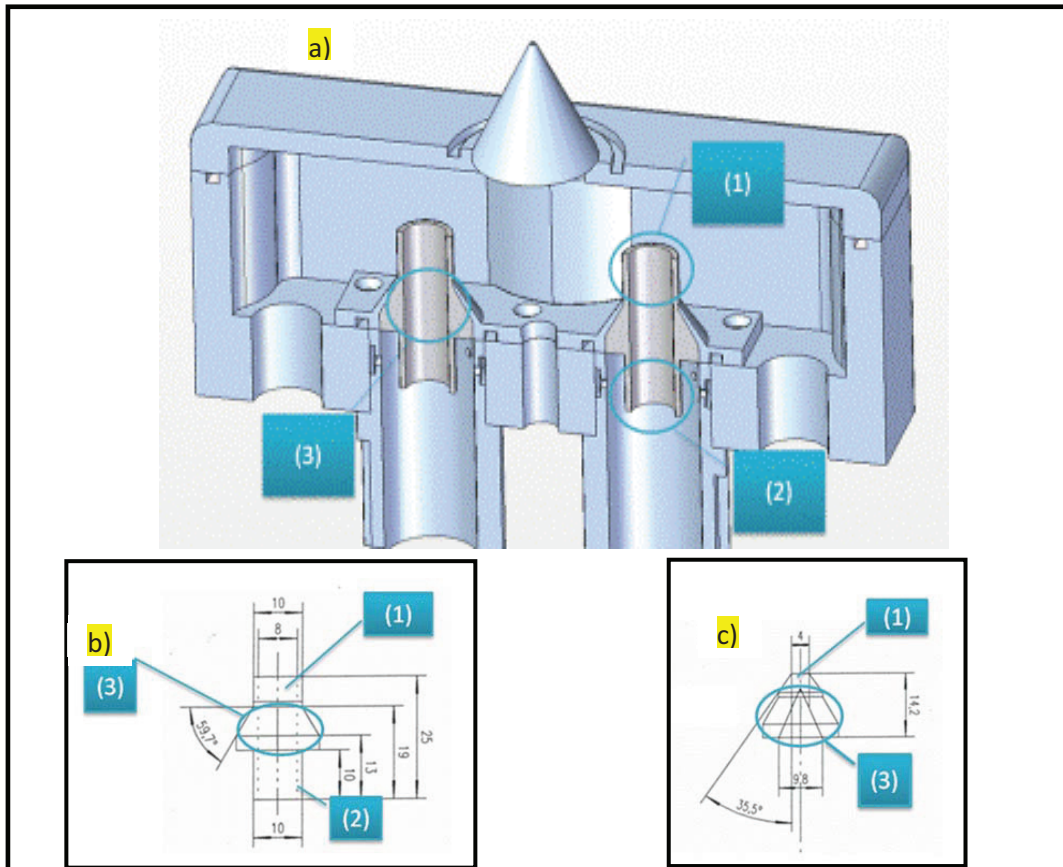


Fig. 4.2.2.4 Main features of the Teflon inserts a) (1) and (2) protrusions, shape of the protrusion inside the conical nozzle of the plate (3), Cut view of b) insert 2nd and c) insert 4th.

The investigation of the radical losses in the reactor entry was conducted with the pressure of the pre-reactor nozzle set at 900, 500 and 300 mbar. The measurements below 300 mbar are rather difficult to perform because of the signal instabilities observed with the luminol detector. The sampled air was kept at a laboratory pressure of around 1013 mbar.

For all the inserts except for the 6th no interference was observed between the reactors, i.e., when one channel was in the SG mode, the detector signal for the other channel did not change, which is illustrated in Fig. 4.2.2.6 with the exemplary results of the 5th insert at 500 mbar.

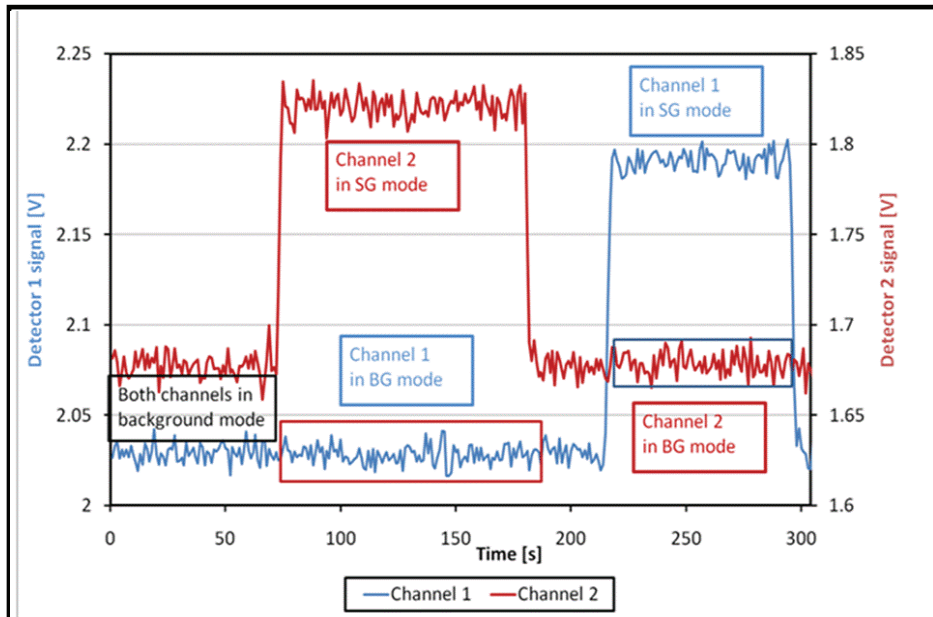


Fig. 4.2.2.6 Example of the successful separation of the reactors with the 5th insert, *P* at the pre-reactor nozzle=500 mbar.

The 6th insert was not sufficient enough to separate the reactors as small interference occurred (see Fig. 4.2.2.7). Thus, it is not advisable to use this insert in the final construction of the HALO inlet.

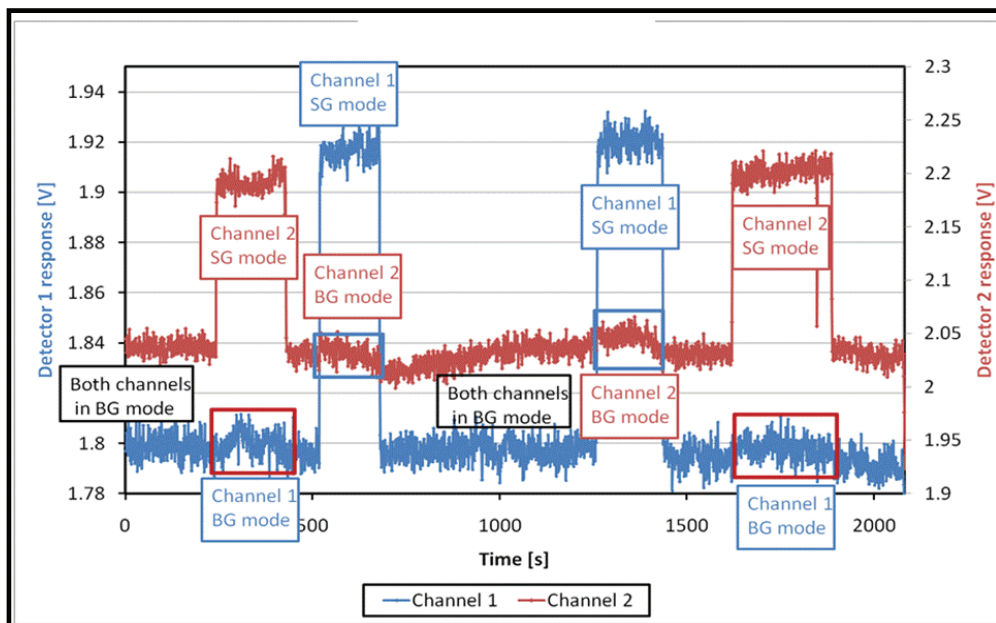


Fig. 4.2.2.7 The results of the tests of the interference between the reactors with the 6th insert, *P* at the pre-reactor nozzle=300 mbar.

4.2.2.2 Teflon inserts

Once the interference between the reactors was sorted out, a series of experiments at the different pressures at the pre-reactor nozzle were carried out to gain insight into the

removal processes in the reactor entry. The pressure in the pre-reactor nozzle was regulated at 900, 500 and 300 mbar. Based on the definition of the eCL (Eq. 4.2.1.1) the radical losses at the reactor entry are related to a reduction in the measured $[\Delta NO_2]$ and consequently in the determined eCL .

In general, the overall radical losses during these experiments which will be reflected in the eCL value depend on:

a) Losses in the pre-reactor nozzle

Two competing processes are taking place in the pre-reactor nozzle. As $\Delta p = p_{external} - p_{inlet}$ varies, the flow through the lid orifice also changes and thereby the entrance velocity of the gas into the pre-reactor nozzle. In case of high Δp , the corresponding velocity is high too, which may lead to the turbulences, and consequently the radical losses in the pre-reactor nozzle. On the other hand, a decrease in Δp leads to lower gas velocity and the corresponding higher retention time in the pre-reactor nozzle. Thus, the probability that the radicals are lost before reaching the amplification point of the reactor is higher.

b) Losses in the reactor entry, i.e., Teflon insert

The role of the insert elements in minimizing interference between the reactors has been detailed in the previous section. The efficiency of the radical losses in the reactor entry depends on the geometry of the insert. In addition, placing the insert in the HALO inlet will also modify the pre-reactor nozzle properties and thus the losses occurring there. The radical removal processes in the insert are expected to occur in the following way:

- The protrusion (1) acts as an extension of the reactor entry. Two competing processes affecting the radical losses are taking place as a function of the length l_1 of the protrusion (1). Residence time in pre-reactor nozzle t_0 and in the protrusion t_1 is varying with a change of l_1 which is illustrated in Fig. 4.2.2.8. With higher l_1 , t_1 is also higher and thereby higher radical losses are also expected according to:

$$[RO_2(t)^*] = [RO_2^0] * \exp(-k_w * t) \quad (2.2.3.14).$$

Concurrently, lower t_0 corresponds to higher t_1 and thus lower radical removal processes in the pre-reactor nozzle.

- The protrusion (2) inside the reactor acts as a shelter for NO and CO leaving the top addition point. However, the radicals will reach the reaction gases later by the time t_2 (see Fig. 4.2.2.8) than in the insert not having this element. Therefore, the radicals

will be lost on the walls through the passage in the protrusion (2) and the eCL is expected to be lower for the reactor with this protrusion (Eq. 4.2.1.1).

- A decrease in the pressure of the sampling air is associated with an increase in the volume flow and a decrease of the retention time through the reactor entry, as the mass flow through the reactor is kept constant during the measurements. Thus, more radicals are expected to be lost at higher pressures and consequently it is expected an increases of the difference in the eCL for different inserts.

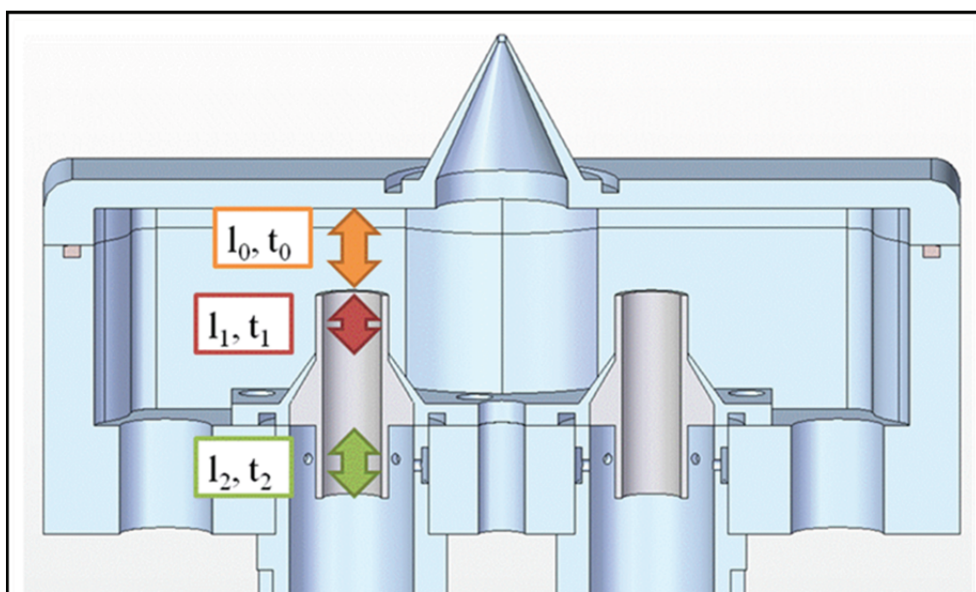


Fig. 4.2.2.8 Schematic diagram of the effect of the Teflon insert geometry on the radical losses: t_0 - residence time in the pre-reactor nozzle, l_0 - distance between the pre-reactor nozzle wall and the insert entrance, t_1 - residence time in the protrusion (1), l_1 - length of the protrusion (1), t_2 - residence time in the protrusion (2), l_2 - length of the protrusion (2).

The experimental eCL values are presented in the Appendix 2.

Effect of protrusion (1) on radical losses

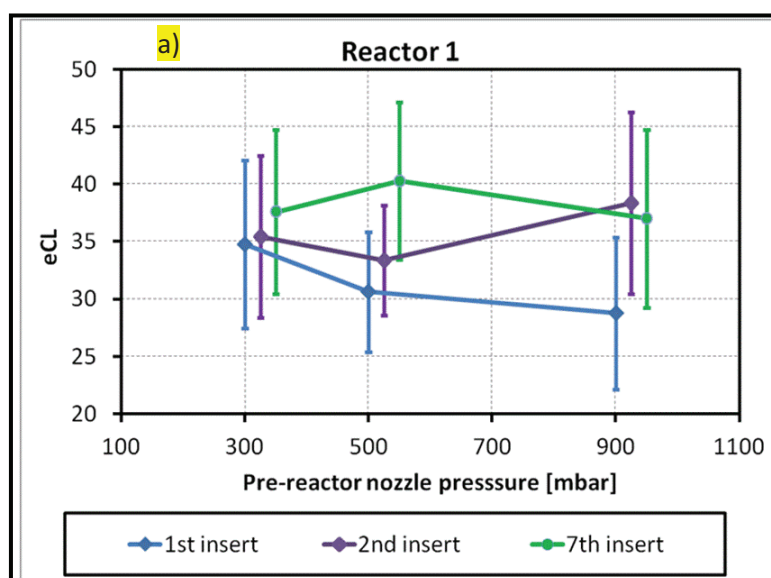
The effect of the protrusion (1) on the radical losses will be compared based on two sets of inserts: 1st, 2nd, 7th and 3rd, 5th, 6th.

The inserts 1st, 2nd, 7th are characterized by different length of the protrusion (1), the highest by the insert 1st. All of them include the protrusion (2), which is wider for the insert 1st is than the other two. The radical losses in the pre-reactor nozzle and the protrusion (1) will define the eCL value. As the insert 7th does not include the protrusion (1), the lowest radical losses are expected and thus the highest eCL value among all these inserts. The main features of the inserts are summarized in Table 4.2.2.2.

Teflon insert	Protrusion (1)	l_1	\varnothing_1	Protrusion (2)	l_2	\varnothing_2	Additional features
1 st	+	9	8	+	10	11	Protrusion (3) conical shape
2 nd	+	6	8	+	10	8	
7 th	-	0	8	+	0	8	

Table 4.2.2.2 Comparison of the inserts 1st, 2nd and 7th. Protrusion (1) located inside the pre-reactor nozzle, l_1 - protrusion (1) length [mm], \varnothing_1 - protrusion (1) orifice diameter [mm], protrusion (2) inside the reactor, l_2 - protrusion (2) length [mm], \varnothing_2 -protrusion (2) diameter [mm].

The obtained eCL values are compared in Fig. 4.2.2.9. The eCL at different pressures present a slight curvature, with a maximum around 500 mbar for the insert 7th without protrusion (1) and a minimum for the inserts 1st and 2nd. It should be noted that the eCL for the HALO reactors is slightly different although they are supposed to be identical. As expected the highest eCL is obtained for the insert 7th for the reactor 1, the lowest for the insert 1st, in case of the reactor 2 this relationship is not clearly observed. This might be due to slight differences in the geometrical and surface properties of the reactors entry, which is made of a soft material from which it might be difficult to manufacture two identical inserts. In addition, during their setting up in the reactor entry the inserts might undergo a deformation. Based on the eCL values obtained for this set of inserts for both reactors, it can be concluded that there is observed a small enhancement of the radical losses with an increase of the length of the protrusion (1).



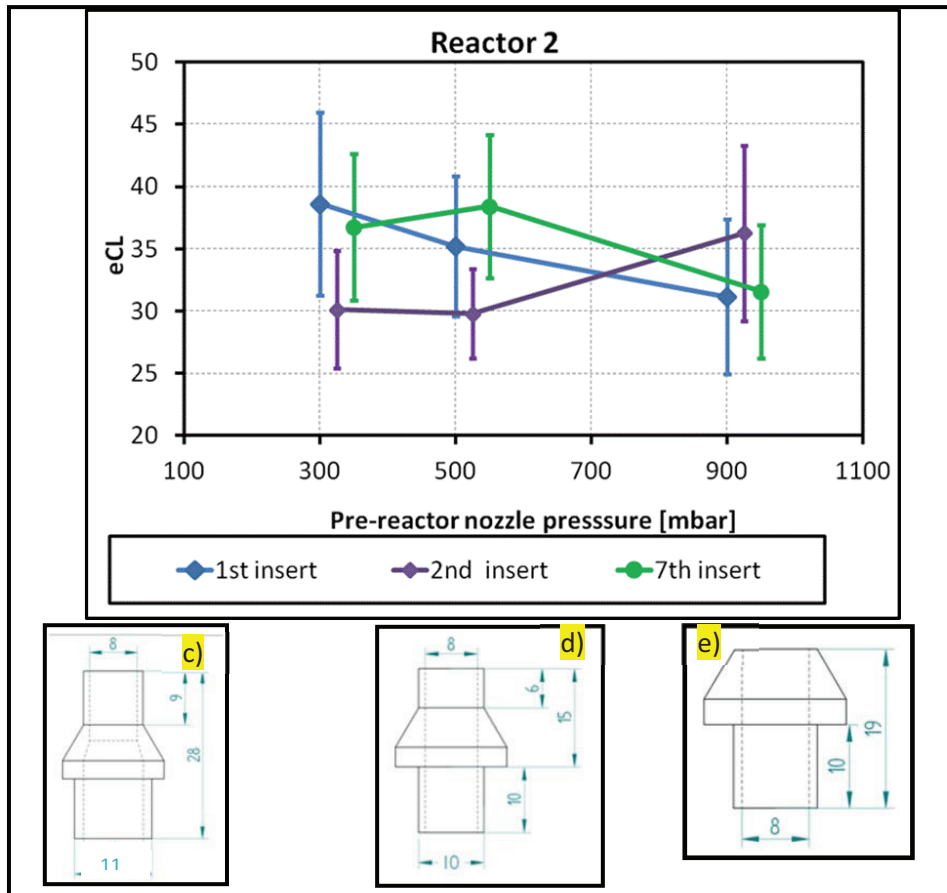


Fig. 4.2.2.9 The eCL comparison for the inserts 1st, 2nd, 7th a) Reactor 1, b) Reactor 2. For clarity the pressure in pre-reactor nozzle is shifted in the figure for different inserts, though all were kept at 300, 500 and 900 mbar. A cut view with the dimensions in mm of the inserts c) 1st, d) 2nd, e) 7th.

The inserts 3rd, 5th, 6th are characterized by different length of the protrusion (1), i.e., 5th has half height of insert 3rd and no protrusion (2). For the insert 3rd with the longest protrusion (1) among the investigated inserts, the highest radical losses are expected within the protrusion (1) and thereby the lowest eCL . The inserts are compared in Table 4.2.2.3.

Teflon insert	Protrusion (1)	l_1	\varnothing_1	Protrusion (2)	l_2	\varnothing_2
3 rd	+	12	8	-	0	0
5 th	+	6	8	-	0	0
6 th	-	0	8 ^(a)	-	0	0

Table 4.2.2.3 Comparison of the inserts 3rd, 5th and 6th. Protrusion (1) located inside the pre-reactor nozzle, l_1 -protrusion (1) length [mm], \varnothing_1 - protrusion (1) orifice diameter [mm], protrusion (2) inside the reactor, l_2 - protrusion (2) length [mm], \varnothing_2 -protrusion (2) diameter [mm]. (a) $\varnothing=8$ mm of the cross section.

The obtained eCL values presented in Fig. 4.2.2.10. The eCL for different pressures shows a slight curvature, with a minimum around 500 mbar for the inserts with the protrusion (1). Following the expectations the eCL for the insert 6th in general is characterized by the highest eCL among the analysed inserts. There is observed an increase of the eCL with the

pressure. This indicates an effect compensating of the pressure dependency of the amplification reactions 2.1.11-12.

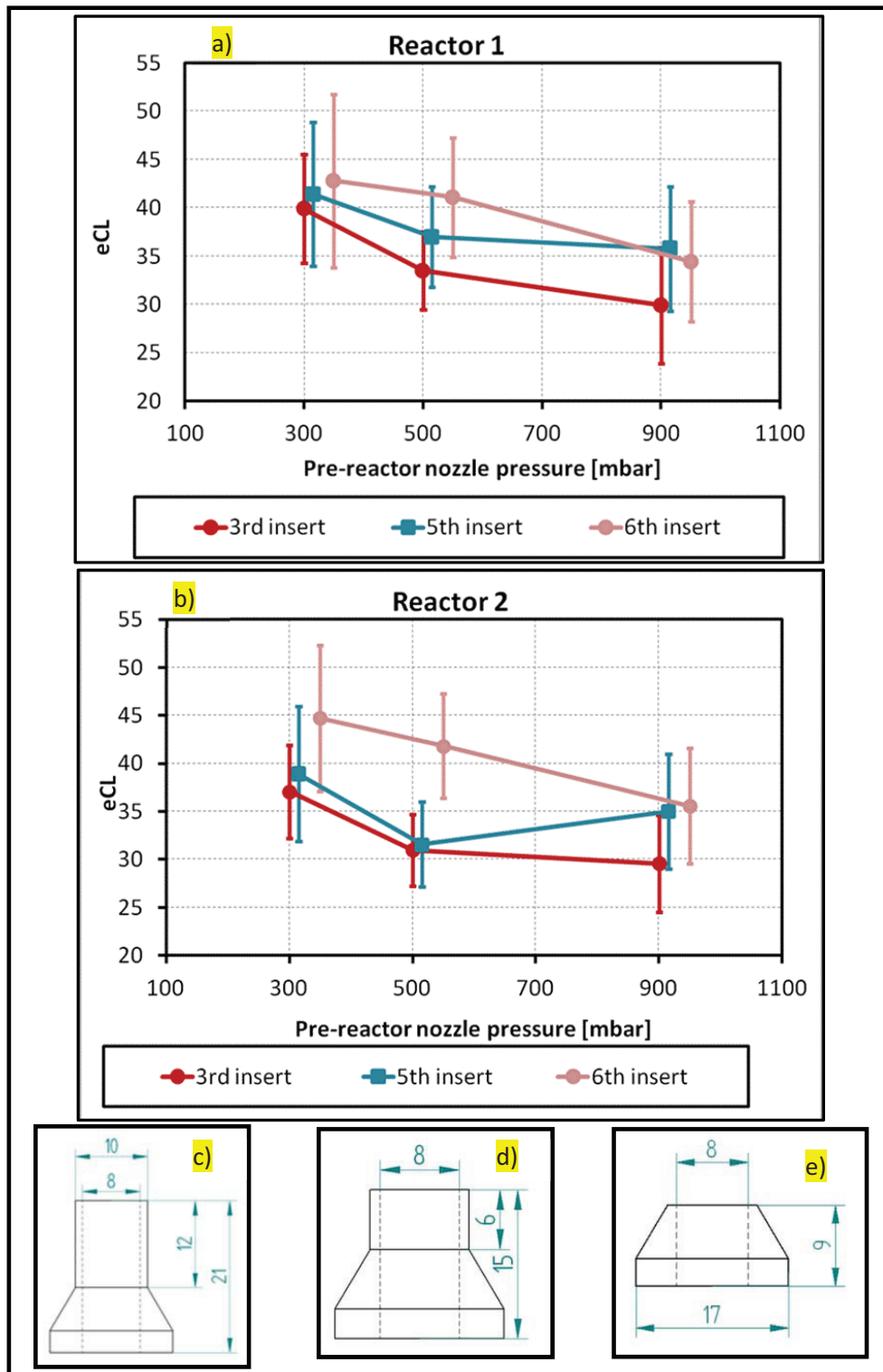


Fig. 4.2.2.10 The eCL comparison for the inserts 3rd, 5th, 6th a) Reactor 1, b) Reactor 2. For clarity the pressure in pre-reactor nozzle is shifted in the figure for different inserts, though all were kept at 300, 500 and 900 mbar. A cut view with the dimensions in mm of the inserts c) 3rd, d) 5th, e) 6th.

From these experiments, as predicted, it can be concluded that presence of the protrusion (1) increases the radical losses.

Effect of protrusion (2) on radical losses

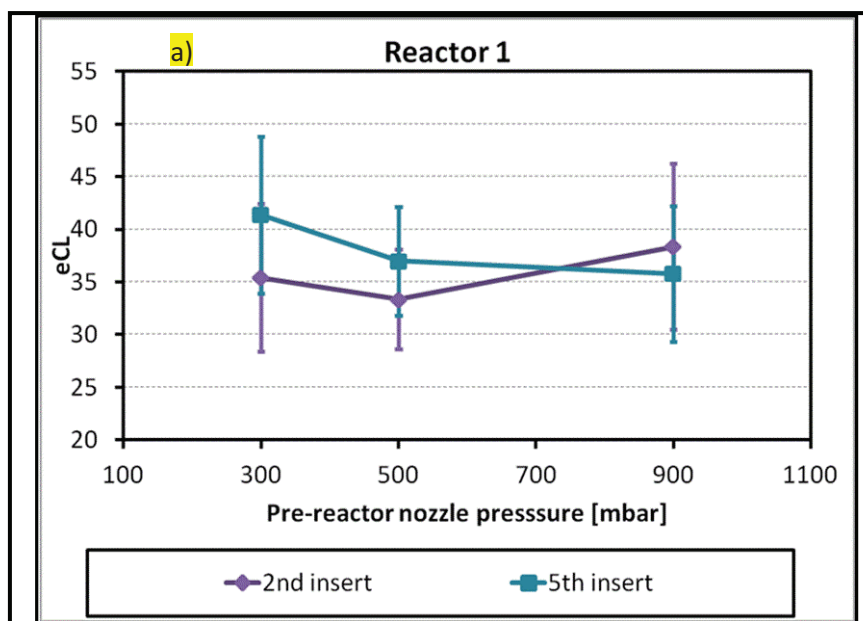
The effect of the protrusion (2) on the radical losses will be compared based on two sets of inserts: 2nd and 5th; 6th and 7th.

The inserts 2nd and 5th (compared in Table 4.2.2.4) have the same length of the protrusion (1) - 6 mm; and thereby the magnitude of the radical losses in the pre-reactor nozzle and this protrusion should be equal. However, the radical removal processes can occur in the protrusion (2) of the insert 2nd before reaching the reaction gases. Therefore, the *eCL* was expected to have lower value for the reactor with the 2nd insert.

Teflon insert	Protrusion (1)	l_1	\varnothing_1	Protrusion (2)	l_2	\varnothing_2
2 nd	+	6	8	+	10	8
5 th	+	6	8	-	0	0

Table 4.2.2.4 Comparison of the inserts 2nd and 5th. Protrusion (1) located inside the pre-reactor nozzle, l_1 -protrusion (1) length [mm], \varnothing_1 - protrusion (1) orifice diameter [mm], protrusion (2) inside the reactor, l_2 - protrusion (2) length [mm], \varnothing_2 -protrusion (2) diameter [mm].

In Fig. 4.2.2.11 the *eCL* for the inserts 2nd and 5th is illustrated.



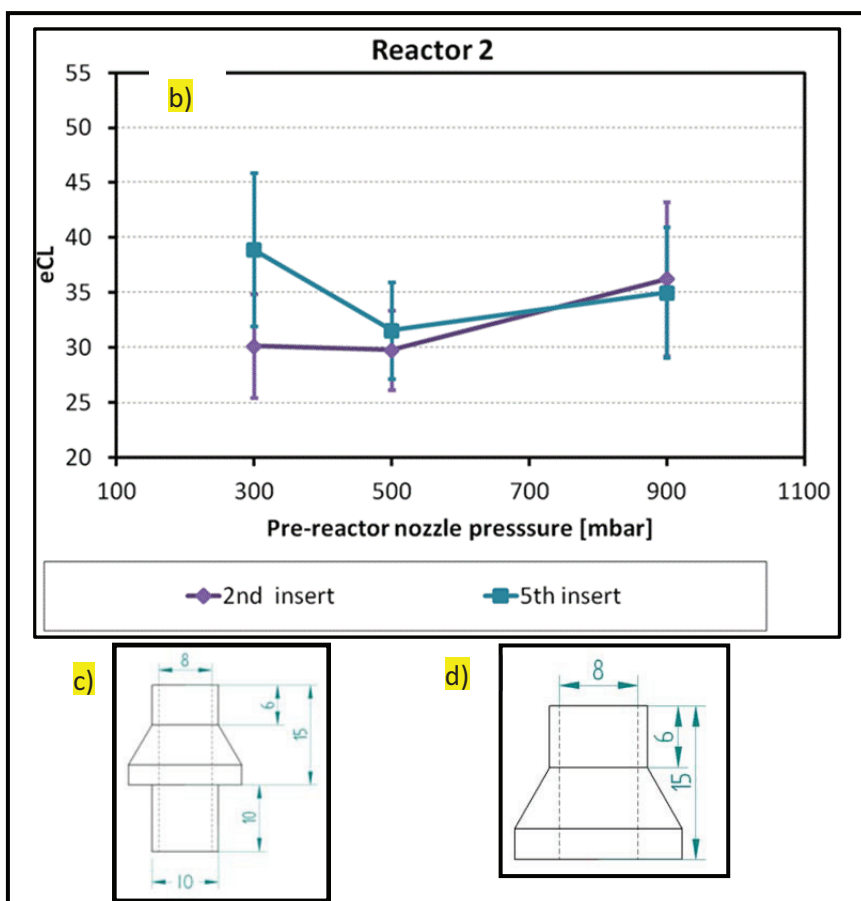


Fig. 4.2.2.11 The eCL comparison for the inserts 2nd and 5th a) Reactor 1, b) Reactor 2. A cut view with the dimensions in mm of the inserts c) 2nd and d) 5th.

As in the previous determination the eCL at different pressures shows a slight curvature, with a minimum around 500 mbar for the inserts with the protrusion (1). The eCL for different inserts seems to be only significantly different at the lowest investigated pressure (300 mbar) what might be related to the higher magnitude of turbulences associated with a higher flow. Thus, the protrusion (2) increases the radical losses at low pressures.

The inserts 6th and 7th are characterized by the absence of the protrusion (1), thus the same radical losses in the pre-reactor nozzle will take place. The 7th insert includes also the protrusion (2) and similarly to the investigation of the entries 2nd and 5th a lower eCL is expected in comparison to the 6th. Table 4.2.2.6 summarizes the features of the inserts.

Teflon insert	Protrusion (1)	l_1	\varnothing_1	Protrusion (2)	l_2	\varnothing_2
6 th	-	0	8 ^(a)	-	10	8
7 th	-	0	0	+	0	0

Table 4.2.2.6 Comparison of the inserts 6th and 7th. Protrusion (1) located inside the pre-reactor nozzle, l_1 -protrusion (1) length [mm], \varnothing_1 - protrusion (1) orifice diameter [mm], protrusion (2) inside the reactor, l_2 - protrusion (2) length [mm], \varnothing_2 -protrusion (2) diameter [mm]. (a) $\varnothing=8$ mm of the cross section.

Fig. 4.2.2.12 presents the obtained eCL values for the inserts 6th and 7th.

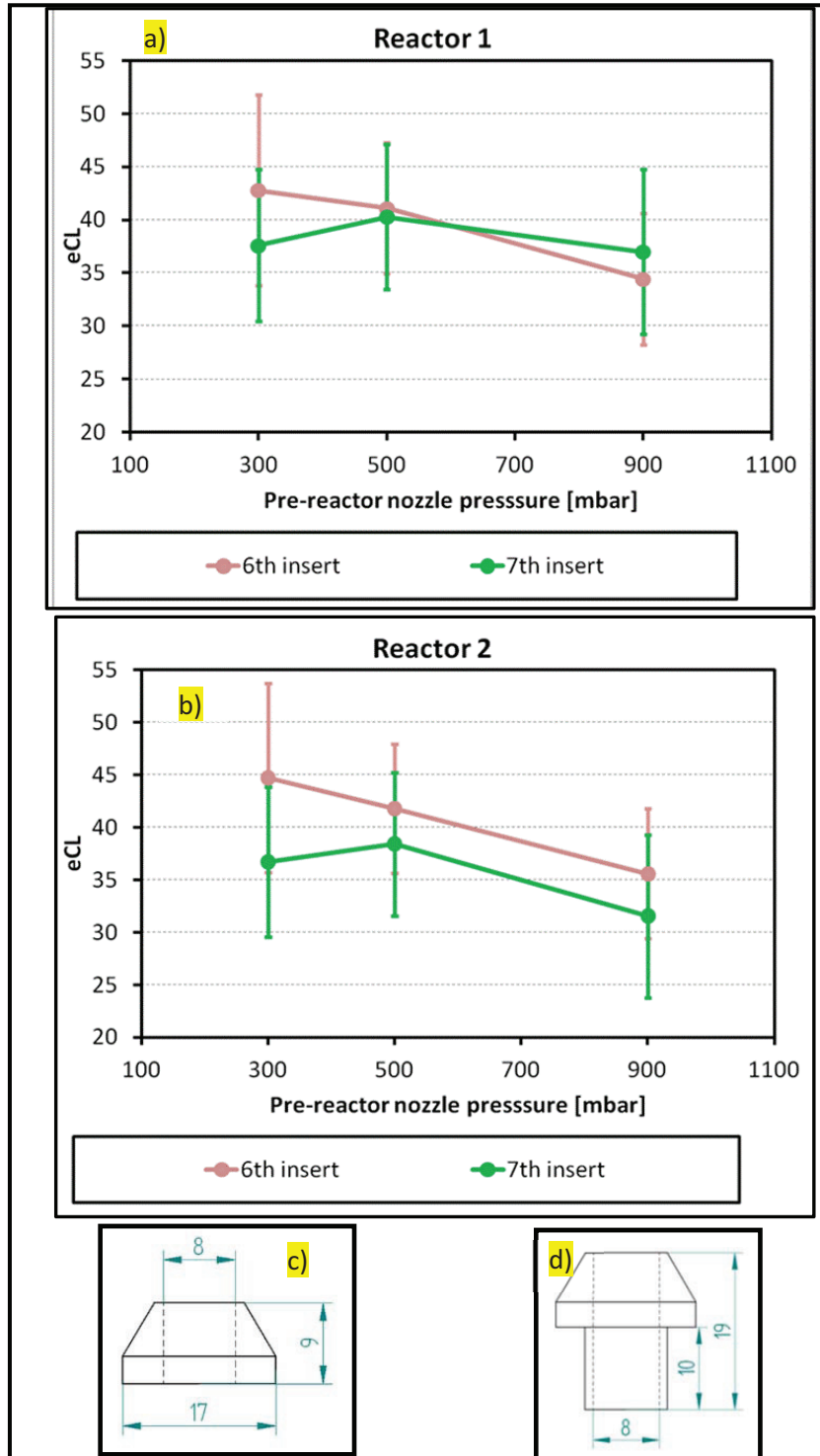


Fig. 4.2.2.12 The e_{CL} comparison for the inserts 6th and 7th a) Reactor 1, b) Reactor 2. A cut view with the dimensions in mm of the inserts c) 6th, d) 7th.

The e_{CL} at different pressures shows a slight curvature, with a maximum around 500 mbar for the insert with the protrusion (2). Similarly to the previously presented set of the inserts (2nd and 5th), there has been observed a slight variation of the e_{CL} for the inserts including the protrusion (2). Likewise only significant difference between the e_{CL} is observed at 300 mbar pressure.

Based on the obtained results it can be interpreted that an increase the radical losses is related to the presence of the protrusion (2), whose effect is clearly lower than the effect of protrusion (1) and only significant at the lowest pressure of 300 mbar.

Effect of entry orifice on radical losses

The inserts 4th and 5th differ by the length of the protrusion (1), i.e., 5.2 and 6 mm, respectively (see Fig. 4.2.2.13). In addition, the orifice (1) diameter is significantly different, i.e., is twice lower for the insert 4th. The radical wall losses depend on the surface/volume ratio (S/V) which for a cylinder is proportional to $1/r$, where r is a radius. Thus, as a first approximation the losses twice lower are expected for wider 5th insert. However, the shape of the insert interior is different: 4th - conical, 5th - cylindrical and the ratio (S/V) for these surfaces differs 19% , the S/V for the 4th is 5.93 cm^{-1} and for the 5th is 5 cm^{-1} , which in comparison to 200% S/V ratio of the orifice (1) is expected not to play a significant role.

On the other hand, as the sampling flow through the reactor entry is constant, based on the Bernoulli equation (2.3.2.1) the velocity of gas through a narrower orifice is higher. Consequently, it is expected a lower retention time within the insert 4th (67% lower), a quicker transport of the radicals to the conversion and amplification area and thus lower probability of the wall losses.

Table 4.2.2.7 summarizes the features of the inserts.

Teflon insert	Protrusion (1)	l_1	\varnothing_1	Protrusion (2)	l_2	\varnothing_2	Shape of protrusion (3)
4 th	+	5.2	4	-	0	0	Conical
5 th	+	6	8	-	0	0	Cylindrical

Table 4.2.2.7 Comparison of the inserts 4th and 5th. Protrusion (1) located inside the pre-reactor nozzle, l_1 - protrusion (1) length [mm], \varnothing_1 - protrusion (1) orifice diameter [mm], protrusion (2) inside the reactor, l_2 - protrusion (2) length [mm], \varnothing_2 -protrusion (2) diameter [mm].

Fig. 4.2.2.13 compares the results of the determination of the eCL for the inserts 4th and 5th.

The eCL for both reactors is higher for the insert 4th than for 5th, in average of 28%. Based on the definition of the eCL (Eq. 4.2.1.1), it is concluded that more radicals are lost in the wider orifice of the insert 5th.

The eCL at different pressures shows a slight curvature with minimum around 500 mbar for 5th insert. This is in agreement for a general tendency for the inserts with the protrusion (1). The highest eCL is observed at lower pressure. It might be attributed to lower

radical losses related to the quicker flow at lower pressures and consequently lower retention time in the pre-reactor nozzle and the reactor entry.

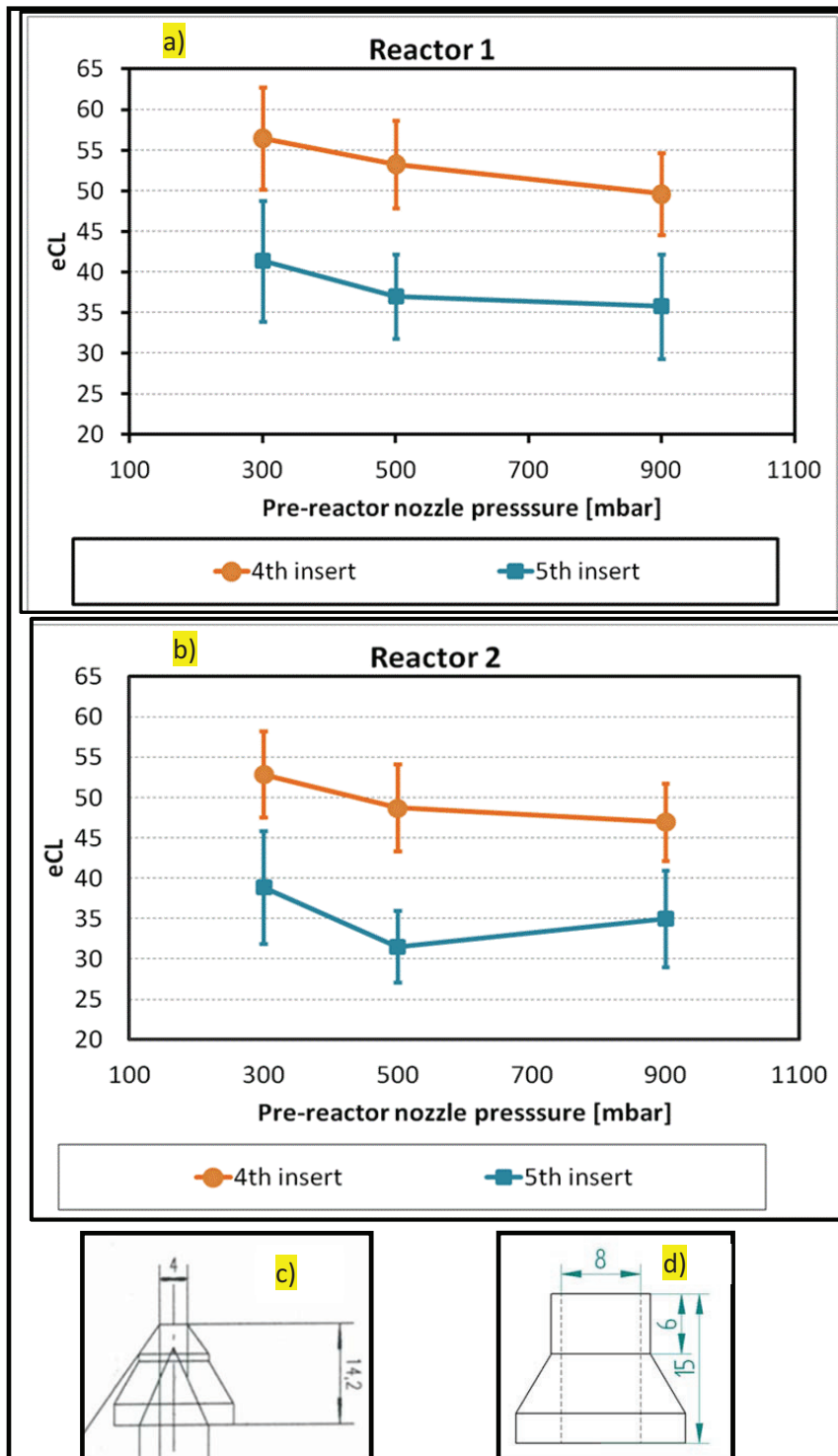


Fig. 4.2.2.13 The eCL comparison for the inserts 4th and 5th a) Reactor 1, b) Reactor 2. A cut view with the dimensions in mm of the inserts c) 4th, d) 5th.

Effect of ozone production on the obtained *eCL*

During the *eCL* determination the radical source was kept at laboratory conditions at the pressure around 1013 mbar and room temperature. Thereby the production of the radicals and ozone as a result of photolysis of water and oxygen remained constant (see Section 3.4.2). However, there have been observed that there were variations of the maximum ozone production depending on the pressure of the pre-reactor nozzle shown in 4.2.2.14, between 1.7-2.6 ppbv. The mass flows of the sampling and addition gases (NO and CO) are kept constant. Thus, the obtained O_{3max} mixing ratio at the same pressure and temperature conditions is expected to be constant.

The observed variations of $[O_{3max}]$ might result from the variable conditions during the air sampling. With higher $\Delta p = p_{external} - p_{inlet}$, the sampling flow through the sampling lid orifice increases. The ozone mixing ratio entering the inlet changes as the velocity profile of the sampled air in the source changes also. As the *eCL* is calculated from Eq. (3.4.2.1) and $[HO_2]$ from Eq. (3.4.2.6) and $[O_3]$ from Eq. (3.4.2.7):

$$eCL = \frac{[\Delta NO_2]}{[HO_2]} = \frac{[\Delta NO_2]}{\frac{\sigma_{H_2O} [H_2O] [O_3]}{\sigma_{O_2} [O_2]}} = \frac{[\Delta NO_2]}{\frac{\sigma_{H_2O} [H_2O]}{\sigma_{O_2} [O_2]} * [O_{3max}] * \frac{I_{detected}}{I_{max}}} \quad (4.2.2.1)$$

for higher $[O_{3max}]$ lower *eCL* will be obtained.

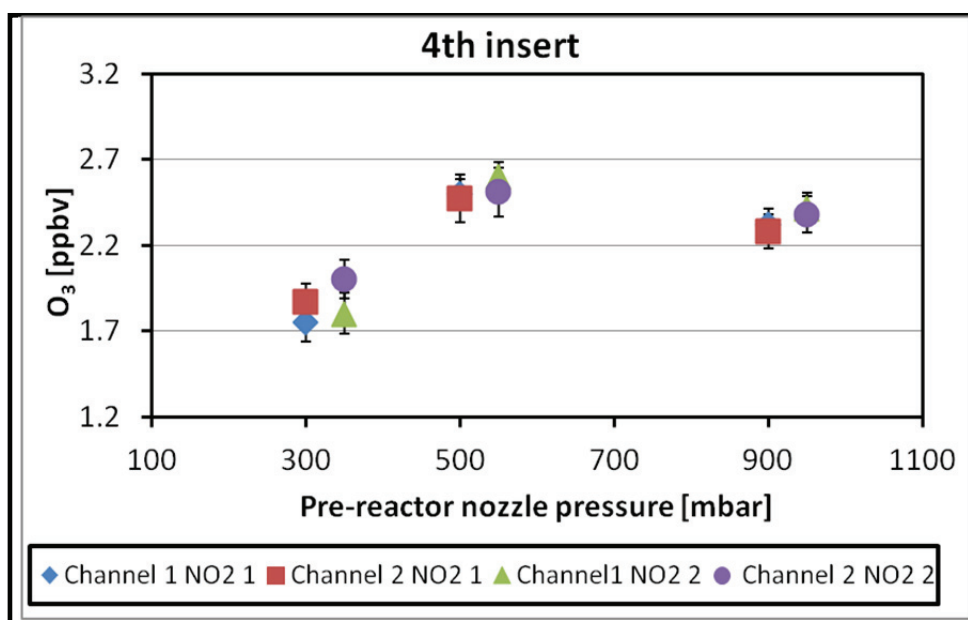


Fig. 4.2.2.14 The observed variations of the maximum ozone production with the pre-reactor nozzle pressure, $NO_{2,1/2}$ refers to NO_2 calibration performed before/after *eCL* determination. For clarity the pressure in pre-reactor nozzle is shifted in the figure for different NO_2 calibrations, though all were kept at 300, 500 and 900 mbar.

Fig. 4.2.1.15 shows the eCL corrected for the variations of O_{3max} , for the insert 4th at certain pressure conditions the eCL was recalculated with O_{3max} obtained for other pressures. Based on this correction, the $eCL_{corrected}$ at 300 mbar is lower than the $eCL_{corrected}$ at 900 mbar as expected.

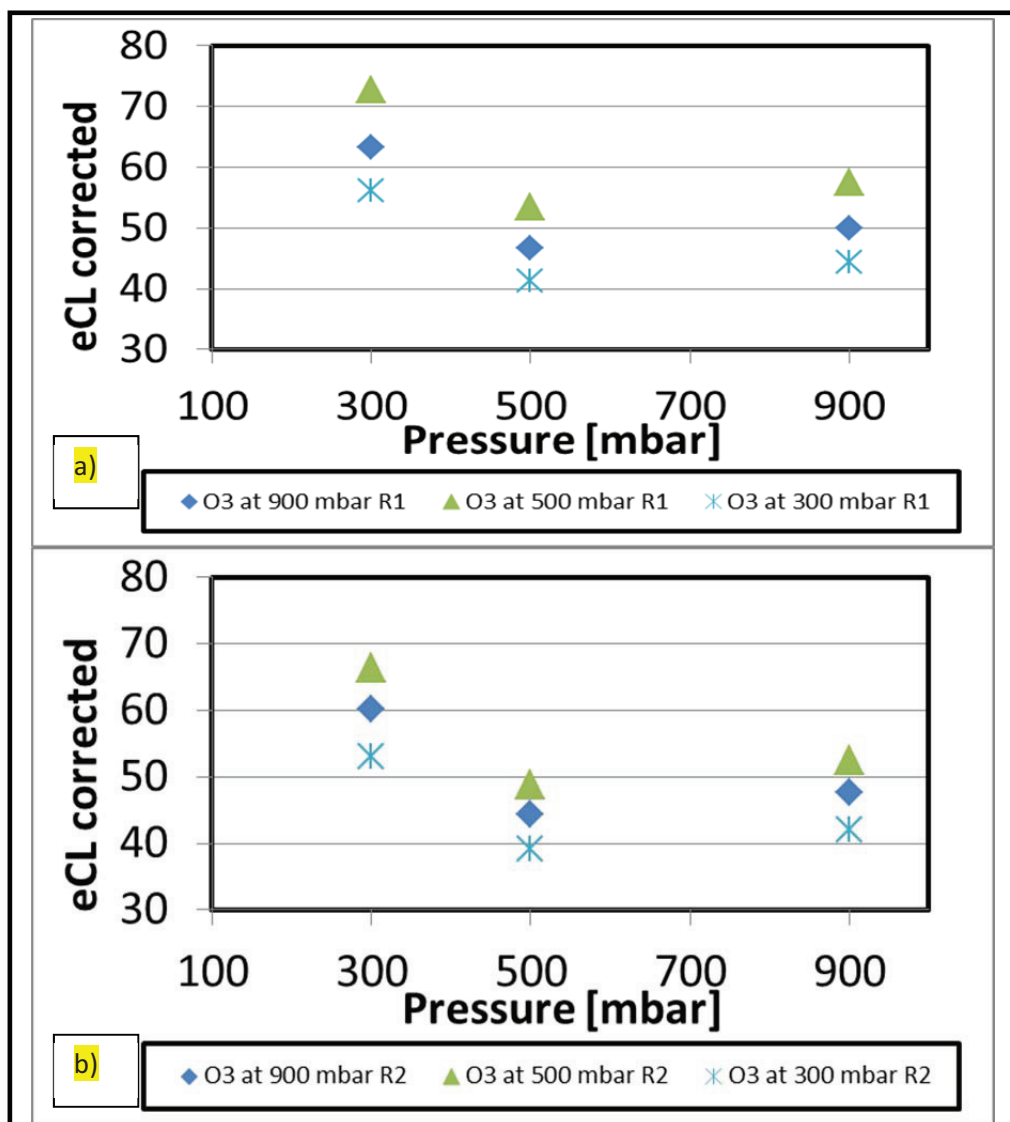


Fig. 4.2.1.15 The eCL corrected by the variations in the ozone production a) Reactor 1, b) Reactor 2.

4.2.3 Reactor walls

Further determination of the radical removal processes in the PeRCA instrument concerned a characterization of the losses of HO_2 and RO_2 radicals in the reactor as a pre-study of the selective measurement of their atmospheric concentrations. For this purpose two reactors, so called reference and modified were designed. The radical source producing HO_2 and a $HO_2+CH_3O_2$ mixture described in Section 3.2.2 was deployed for these experiments performed at the laboratory pressure around 1013 mbar.

Theoretical considerations of the radical removal in the modified reactor

The modified reactor shown in Fig. 4.2.3.1 was designed to eliminate the radicals sampled through the reactor entry with an initial concentration ($[HO_2^0]$) which are then partially lost (HO_2^{loss}) while passing through the reactor walls. Thus, only some portion of the radicals will reach the conversion and amplification point ($HO_2(t)$) then:

$$[HO_2^0] = [HO_2^{loss}] + [HO_2(t)] \quad (4.2.3.1).$$

$[HO_2(t)]$ is determined from:

$$[HO_2(t)] = [HO_2^0] * \exp(-t * k_{wHO_2}) \quad (2.2.3.14).$$

Where: k_{wHO_2} is a wall loss rate coefficient. A retention time t in the radical loss zone of volume V , area A and length l :

$$t = \frac{V}{Q} = \frac{A * l}{Q} \quad (2.2.3.13).$$

Similar calculations are valid for the organic radicals. Considering the difference in the radical losses on the reactor walls, i.e., k_{wHO_2} exceeds k_{wRO_2} (Mihele et. al., 1999), higher removal of HO_2 than of RO_2 is expected. Thus, based on this property, the separation of the organic radicals from the total sum of radicals might be feasible and then determination of solely RO_2 concentration.

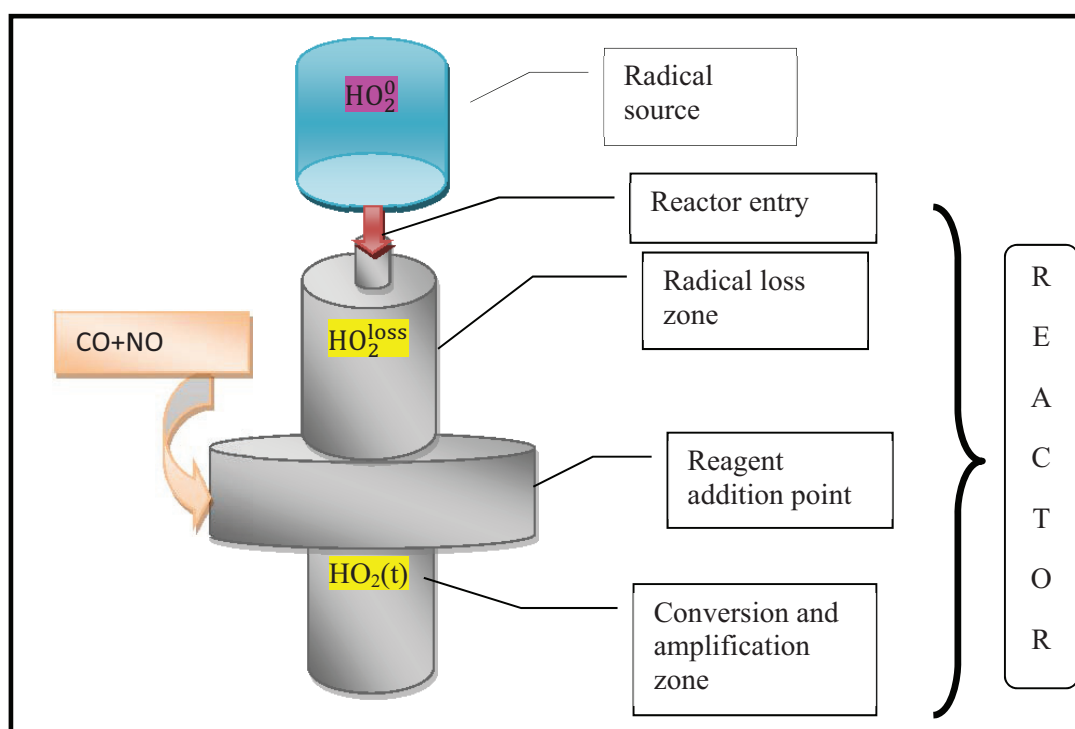


Fig. 4.2.3.1 A scheme of the modified reactor.

The previous work by Kartal D., 2009 has shown that $k_{wHO_2}^{DUALER} = 1.5 \text{ s}^{-1}$ reproduces reasonably the variations of the CL with the pressure for the reactor of the DUALER inlet, for details concerning the inlet see Section 3.1. $k_{wHO_2}^{modified} = 1 \text{ s}^{-1}$ was calculated for the modified reactor based on the comparison of the flow, L length, V volume, S surface area for the DUALER and modified reactors (see Table 4.2.3.1) with Eq. (2.2.3.16) (Hayman, 1997):

$$k_w = 1.85 \left(\frac{v^{1/3} D^{2/3}}{d^{1/3} L^{1/3}} \right) \left(\frac{S}{V} \right) \quad (2.2.3.16).$$

$D_{HO_2} = 0.21, D_{CH_3O_2} = 0.14 \text{ cm}^2/\text{s}$ were calculated from the formula based on the Fuller, Schettler and Giddings (FSG) method taken from Clark M., 2002:

$$D = \frac{10^{-3} T^{1.75} \sqrt{M_r}}{p (V_A^{1/3} + V_B^{1/3})^2} \quad (4.2.3.2).$$

Where: T is temperature [K], p pressure [atm], V_A molar volume of the gas [cm^3/mol], V_B molar volume of air [$20.1 \text{ cm}^3/\text{mol}$]

$$M_r = \frac{m_A + m_B}{m_A * m_B} \quad (4.2.3.3).$$

Where: m_A molar mass of the gas [g/mol], m_B molar mass of air [$28.97 \text{ g}/\text{mol}$].

As $k_{wHO_2}^{modified}$ is lower than $k_{wHO_2}^{DUALER}$, lower magnitude of the losses is expected in the modified reactor comparing to the DUALER reactor. The concentration of HO_2 reaching the amplification zone in the modified reactor was estimated for different pressures on the basis of Eq. (2.2.3.14); assuming k_w does not vary with the pressure. Within 9.5 cm of the modified reactor up to 99% of the radicals is expected to be removed prior to reaching the addition point of CO and NO at 1013 mbar pressure of the sampled air (see Fig. 4.2.3.2 blue squares). As the mass flow through the reactor is kept constant, the volume flow increases with the pressure and the residence time of air decreases and thus fewer radicals are removed. This is an important consideration for the deployment of PeRCA for the radical speciation in airborne measurements. The residence time for the pressure ranging from 100 to 1000 mbar has been calculated with:

$$t = t_{STP} * \frac{1013.25}{p} \quad (4.2.3.4).$$

Where: t_{STP} is residence time calculated at STP conditions and p pressure [mbar].

Similarly, the k_w for the modified reactor was calculated based on the comparison to the PFA reactor used by Mihele et. al., (1999) $k_{wHO_2}^{modified} = 0.11 \text{ s}^{-1}$ and to the quartz reactor used by Clemitshaw et. al., (1997) $k_{wHO_2}^{modified} = 0.49 \text{ s}^{-1}$. With these coefficients a radical

removal efficiency (RE) was estimated in the modified reactor, see Fig. 4.2.3.2, from the following formula:

$$RE = \frac{[HO_2(t)]}{[HO_2^0]} * 100\% = \exp(-t * k_{wHO_2}) * 100\% \quad (4.2.3.5).$$

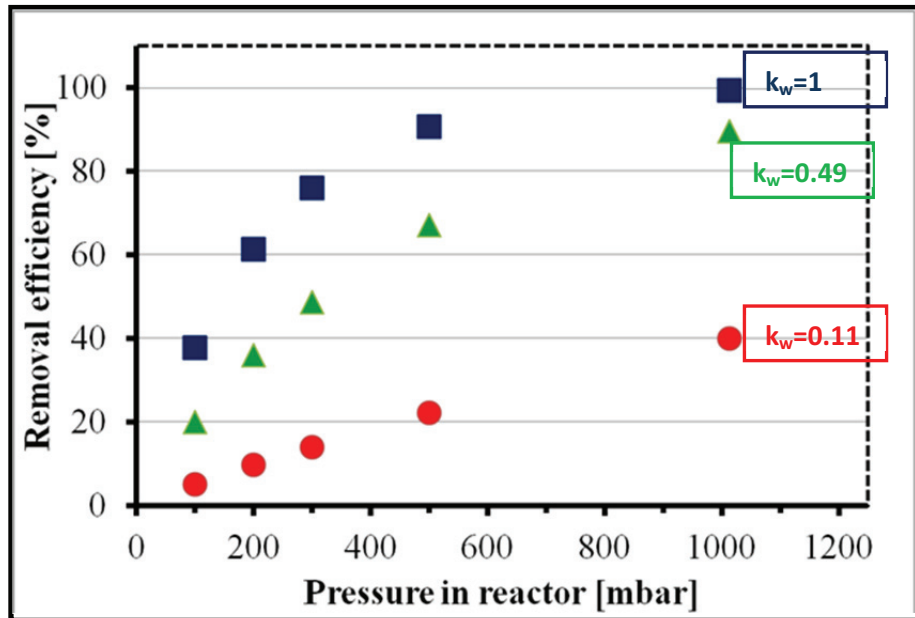


Fig.4.2.3.2 Calculated removal efficiency of HO_2 (RE) in the modified reactor based on the comparison with the reactors used by Mihele et. al., (1999) in red, Clemitchaw et. al., (1997) in green, Kartal (2009) in blue.

Table 4.2.3.1 summarizes properties of the reactors characterized in this work and used for the comparison.

	Modified/Reference reactor (this work)	Reactor by Kartal et al., 2009 DUALER	Reactor by Clemitchaw et al., 1997	Reactor by Mihele et al., 1999
Entry diameter [mm]	10	10	16	-
Entry length (from orifice to the addition point) [mm]	9.5 reference 108 modified	14	90	-
Inner diameter [mm]	29	21	16	4.8
Length [mm]	299	310	165	15000
Volume [cm ³]	197	108	33	27
S/V [1/cm]	1.38	1.90	2.50	8.33
k_w for HO_2 [s ⁻¹]	0.24	1.5	2.5	2.8
Q flow [dm ³ /min]	1	0.5	2	1

	Modified/Reference reactor (this work)	Reactor by Kartal et al., 2009 DUALER	Reactor by Clemitshaw et al., 1997	Reactor by Mihele et al., 1999
t residence time [s]	12.4	15.2	1	1
τ_{diff} for HO ₂ [s]	19.8	10.4	6.0	0.5
τ_{diff} for CH ₃ O ₂ [s]	30.0	15.8	9.1	0.82
CO %	9	7.4	7	4
NO ppm	3	3	3	2
CL	399±40 (reference) 128±30 (modified)	274±31	180	110 ⁽¹⁾
Reactor material	Stainless steel coated with Teflon		Pyrex	¼" PFA tube

Table 4.2.3.1 Comparison of the reactor features. S/V - surface to volume ratio, τ_{diff} - diffusion time, k_w - wall loss rate coefficient [s^{-1}], determined experimentally for the reactors modified/reference and by Mihele et al., (1999), and estimated based on Eq. (2.2.3.2) according to the experimental CL for the reactors by Clemitshaw et al., (1997) and by Kartal et al., (2009) DUALER. (1) The CL obtained for C₂H₅O₂ Mihele et al., (2000).

Diffusion time was calculated from the following expression:

$$\tau_{diff} = \frac{d^2}{2D} \quad (4.2.3.6).$$

Where: D is diffusion coefficient [cm^2/s] from Eq. (4.2.3.2), d is a diameter of the reactor [cm].

Experimental results and discussion

The amplification factor was determined experimentally for the modified and reference reactors without the pre-reactor nozzle. The potential wall losses of the radicals in the reactor entry were assumed to be negligible. In the reference reactor peroxy radicals are amplified and converted immediately behind the reactor entry and therefore the CL for this reactor is assumed to be close to the actual chain length. In the modified reactor HO₂ radicals are partially lost due to the high rate of the wall losses and the radical-radical reactions before reaching the conversion zone, RO₂ radicals are also expected to be removed to some extent. As the CL is calculated according to the known amount of HO₂ entering the reactor, the CL for the modified reactor is an effective chain length (eCL), lower than the CL determined for the reference reactor. The experimental CL obtained with HO₂ for the reference reactor is denoted CL_2 , for the modified reactor eCL_1 , with RO₂* for the reference reactor CL_4 and for the modified reactor eCL_3 . Fig. 4.2.3.3 shows the experimental results.

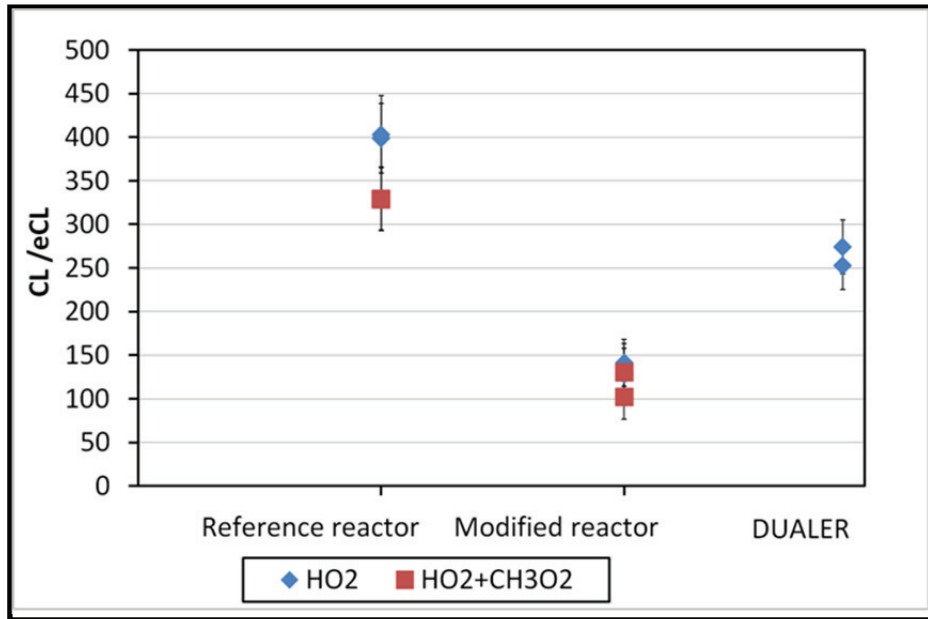


Fig. 4.2.3.3 The chain length obtained experimentally for the reference and the DUALER reactors (CL) and for the modified reactor (eCL).

As expected, the eCL for the modified reactor is lower than the CL of the reference reactor, namely 3 times lower. In addition, the noise of the detector signal was 4.5 times higher than in case of the reference reactor, although the same detector was used for the determination of the chain length. Thus, the relative uncertainty $\frac{\Delta CL_{1,3}}{CL_{1,3}}$ is 23% (the modified reactor), in comparison to $\frac{\Delta CL_{2,4}}{CL_{2,4}}=12\%$ (the reference reactor). This higher level of the noise for the modified reactor might be the result of shorter distance between the addition points (20 cm) in contrast to the reference reactor: 30 cm, which can cause pressure disturbances in the tube which are propagated further into the detector.

For the reference reactor the obtained ratio $\frac{CL_{50\%HO_2+50\%CH_3O_2}}{CL_{HO_2}}$ is 0.84 ± 0.20 . This is related to the fact that CH_3O_2 is firstly converted into HO_2 via the reactions (2.1.2, 2.2.3.7-8) which is then amplified and converted into NO_2 . Clemitshaw et al., 1997 reported that the theoretical fractional yield of this conversion for 3 ppmv NO is 0.85. Therefore, for the calibration mixture of the radicals consisting of equal amount of HO_2 and CH_3O_2 , only 0.925 of HO_2 will participate in the chain reaction and the theoretical ratio $\frac{CL_{50\%HO_2+50\%CH_3O_2}}{CL_{HO_2}}$ should also be equal to 0.925. The ratio determined in this study is 10% lower and this discrepancy is within the measurement uncertainty.

In Fig. 4.2.3.3 the comparison of the CL determined for the DUALER and reference reactors is shown. For both reactors the residence time of the sampled air in the reactor is sufficient to complete the chain reaction, which is around 3s (Clemitshaw et al., 1997; Kartal

et al., 2009). The obtained CL for the reference reactor is 1.5 higher than in case of the DUALER (see Table 4.2.3.1) and a number of factors contribute to this difference:

- Different conditions for the concentration of the CO reagent: DUALER 7.4%, reference 9%. Based on the results of a modelling study of the reactor chemistry by Kartal et al., (2009), around 7% increase of the CL is expected between CO 7% and 9% (see Fig. 4.2.3.4).
- The reactor surface/volume ratio (S/V) (see Eq. 2.2.3.15) is 38% lower for the reference reactor than for the DUALER, thus lower radical removal and higher CL are expected for the reference reactor. The ratio between the value obtained as $\frac{v^{1/3}}{d^{1/3}L^{1/3}}$ from Eq. (2.2.3.16) for the DUALER and for the reference reactor is 0.92. Therefore, 8% enhancement of the radical losses would be expected in the reference reactor with respect to the DUALER reactor. As $CL_{REFERENCE} > CL_{DUALER}$, the properties as sampled air velocity, reactor length seem to play a minor role comparing to (S/V).

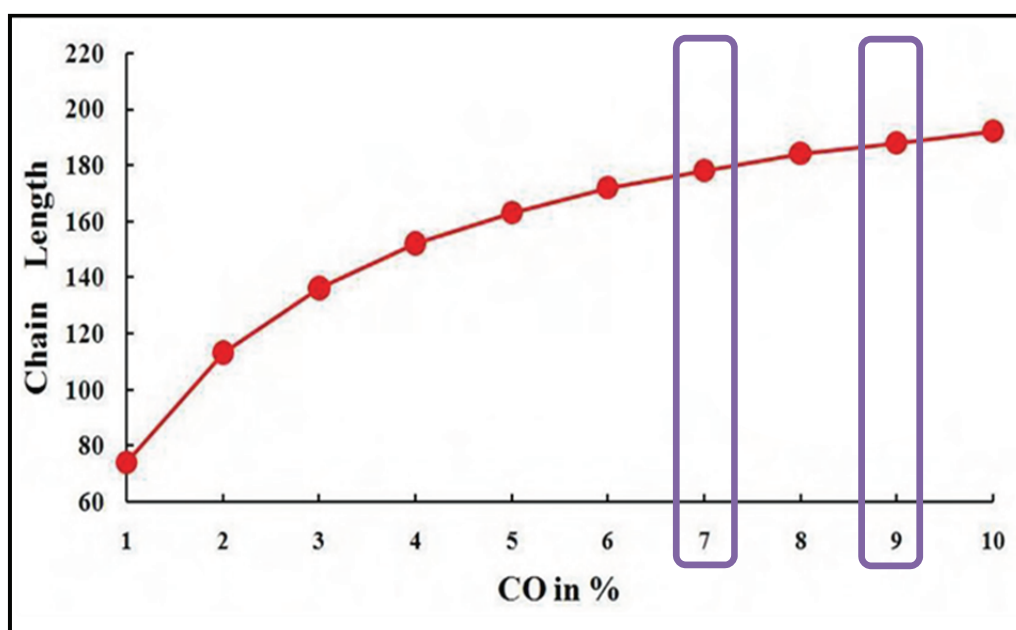


Fig. 4.2.3.4 Variations of the CL with CO mixing ratio at 3 ppmv NO and with 50 pptv CH_3O_2 initial mixing ratio (Kartal D., PhD thesis, 2009). In violet marked CL for CO 7% and 9%.

To quantify the radical losses in the modified reactor, the removal coefficients ‘ a ’ for HO_2 and ‘ b ’ for RO_2 are introduced. If the losses occurring in the first 9.5 cm of the reactor are known, i.e., ‘ a ’ and ‘ b ’, the CL of the modified and the reference reactors should be the same as the conditions affecting the chain reaction for both reactors are identical:

- pressure of the sampled air - the experiments are performed at the same laboratory pressure around 1013 mbar with 1l/min of the total sampled air flow,

- geometry of the reactors: length, volume to surface ratio are equivalent,
- surface properties of both reactors are the same, both Teflon coated.

Therefore:

$$CL_{\text{REFERENCE}} = CL_{\text{MODIFIED}} \quad (4.2.3.7).$$

From the definition of the CL in case of HO_2 radicals:

$$\frac{[\Delta\text{NO}_{2,\text{REFERENCE}}]}{[\text{HO}_2]} = \frac{[\Delta\text{NO}_{2,\text{MODIFIED}}]}{[\text{HO}_2 - \text{HO}_2^{\text{LOSS}}]} = \frac{[\Delta\text{NO}_{2,\text{MODIFIED}}]}{(1-a)*[\text{HO}_2]} \quad (4.2.3.8).$$

Where: $[\Delta\text{NO}_{2,\text{REFERENCE}}]$ is the $[\Delta\text{NO}_2]$ produced in the reference reactor and $[\Delta\text{NO}_{2,\text{MODIFIED}}]$ is the $[\Delta\text{NO}_2]$ produced in the modified reactor.

Then:

$$a = 1 - \frac{eCL_1}{CL_2} = \frac{[\Delta\text{NO}_{2,\text{MODIFIED}}]}{[\text{HO}_2]} / \frac{[\Delta\text{NO}_{2,\text{REFERENCE}}]}{[\text{HO}_2]} \quad (4.2.3.9).$$

Followed by:

$$a = 1 - \frac{[\Delta\text{NO}_{2,\text{MODIFIED}}]}{[\Delta\text{NO}_{2,\text{REFERENCE}}]} \quad (4.2.3.10).$$

Similar calculations are valid for a mixture of radicals $\text{RO}_2^* = \text{HO}_2 + \text{RO}_2$:

$$\frac{[\Delta\text{NO}_{2,\text{REFERENCE}}]}{[\text{RO}_2^*]} = \frac{[\Delta\text{NO}_{2,\text{MODIFIED}}]}{[\text{RO}_2^* - \text{RO}_2^{\text{LOSS}}]} = \frac{[\Delta\text{NO}_{2,\text{MODIFIED}}]}{(1-c)*[\text{RO}_2^*]} \quad (4.2.3.11).$$

Where: 'c' is the total removal coefficient for RO_2^* radicals:

$$c = 1 - \frac{eCL_3}{CL_4} \quad (4.2.3.12).$$

In case of the radical mixture to the radicals removal the losses of HO_2 and RO_2 contribute equally, which can be expressed as follows:

$$c = 50\% * a + 50\% * b \quad (4.2.3.13).$$

Then the removal coefficient 'b' for organic radicals can be calculated as:

$$b = \frac{c - 50\% * a}{50\%} \quad (4.2.3.14).$$

The chain length was determined twice for the reference and the modified reactors. Thus, four calculated values of the removal coefficients are presented in Fig. 4.2.3.5 and in Table 4.2.3.2 the obtained averaged values are summarized.

a	c	b
0.66±0.17	0.65±0.19	0.63±0.21

Table 4.2.3.2 Averaged removal coefficients: a for HO_2 , b for RO_2 , c for RO_2^* .

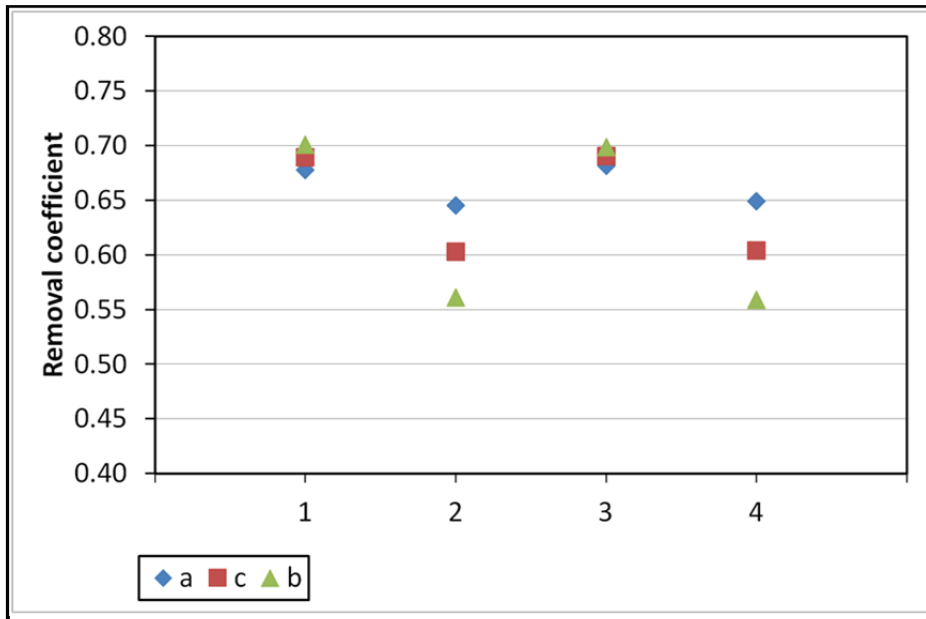


Fig. 4.2.3.5 The calculated removal coefficients.

The removal coefficients 'a' and 'b' can also be expressed as:

$$a = \frac{[\text{HO}_2^{\text{loss}}]}{[\text{HO}_2^{\text{source}}]} \quad (4.2.3.15)$$

$$b = \frac{[\text{RO}_2^{\text{loss}}]}{[\text{RO}_2^{\text{source}}]} \quad (4.2.3.16).$$

Thus, combining Eq. (2.2.3.17), (4.2.3.15-16) k_w :

$$k_{w\text{HO}_2} = -\frac{\ln(1-a)}{t} \quad (4.2.3.17)$$

$$k_{w\text{RHO}_2} = -\frac{\ln(1-b)}{t} \quad (4.2.3.18).$$

The calculated k_{HO_2} and $k_{\text{CH}_3\text{O}_2}$ coefficients are presented in Table 4.2.3.3.

	Radical	
	HO ₂	CH ₃ O ₂
Removal efficiency	a=0.66±0.17	b=0.63±0.21
k_w rate coefficient [s ⁻¹]	0.24±0.11	0.22±0.12

Table 4.2.3.3 The results of determination of the wall loss rate coefficients for HO₂ and CH₃O₂.

As can be seen from the results, $k_{w\text{HO}_2}$ and $k_{w\text{CH}_3\text{O}_2}$ do not differ significantly for the modified reactor and thus the separation of HO₂ and CH₃O₂ based on differences in the wall losses cannot be performed with this set-up. However, these findings do not corroborate the previous results, e.g., by Mihele et al., (1999) which showed differences depending on the radical composition, (1/4" PFA tube $k_{w\text{HO}_2} = 2.8 \pm 0.2 \text{ s}^{-1}$ and $k_{w\text{CH}_3\text{O}_2 + \text{C}_2\text{H}_5\text{O}_2} = 0.8 \pm 0.1 \text{ s}^{-1}$). The surfaces of both reactors are made from the inert material - Teflon; hence no differences in

the radical reaction on the reactor walls are expected. To the similarity of the obtained k_{wHO_2} and $k_{wCH_3O_2}$ for the modified reactor might contribute:

- The surface to volume ratio (S/V) of the reactor (see Eq. 2.2.3.15), in case of the PFA reactor 6 times higher than the modified reactor. On materials with large surface area to volume ratio, e.g., with very small diameter, reactions proceed at much faster rates because of more surface available to react.
- The $\frac{\tau_d}{\tau_r}$ ratio of diffusion time to air residence time of the radicals in the reactor: the reactor by Mihele et al., (1999) $\frac{\tau_d}{\tau_r}=1.6$, in contrast to 0.5 for the modified reactor. Thus, for the reactor by Mihele diffusion of the radicals to the walls is more effective as ($\tau_d < \tau_r$), in case of the modified reactor the radicals pass through the removal zone with a sampled air flow before they can reach the reactor walls ($\tau_d > \tau_r$), and could be lost on them.

The experimental ratio for the modified and DUALER reactors $\frac{k_{HO_2}^{modified}}{k_{HO_2}^{DUALER}} = \frac{0.24}{1.50} = 0.16$ is 4 times lower than the theoretical ratio of 0.70 obtained with the k_w calculated according to Eq. (2.2.3.16) $\frac{k_{HO_2}^{modified}}{k_{HO_2}^{DUALER}} = \frac{0.77}{1.11} = 0.70$. Based on the properties of the modified reactor (dimensions and sampled air flow), the experimental $k_{HO_2}^{modified}$ cannot be explained. Therefore, the radical losses in the reactor entry were estimated as k'_w with parameters summarized in Table 4.2.3.4:

$$k'_w = \left(\frac{v^{1/3}}{d^{1/3} L^{1/3}} \right) \left(\frac{S}{V} \right) \quad (4.2.3.19).$$

Air residence time in the reactor entry was calculated from air flow and area of the entry by Eq. (2.2.3.13). Based on these calculations, the radical losses in the entry of the modified reactor are expected to be 50% lower than in the DUALER. This difference is mainly attributed to the residence time of air which is 3 times lower in the modified reactor entry in comparison to the DUALER.

Reactor entry	Reactor by Kartal et al., 2009 DUALER	Reactor Modified (this work)
\varnothing diameter [cm]	1	1
L length [cm]	1	0.7
S/V surface/volume [1/cm]	4	4

Reactor entry	Reactor by Kartal et al., 2009 DUALER	Reactor Modified (this work)
a cross section area [cm ²]	0.79	0.79
V volume [cm ³]	0.79	0.55
Q flow [cm ³ /s]	6.76	13.52
v air velocity [cm/s]	8.60	17.21
t residence time [s]	0.12	0.04
k'_w	15.16	21.52
$\exp(-k'_w * t)$	1.8	0.9

Table 4.2.3.4 Parameters used to estimate the radical losses in the reactor entry.

Another approach to estimate the wall loss rate coefficient from the obtained chain length of the reference reactor is based on the formula provided by Hastie et al., 1991:

$$\frac{1}{CL} \approx \frac{k_{wHO_2} * [HO_2]}{k_{HO_2+NO} * [NO] * [HO_2]} + \frac{k_{HONO} * [NO] * [OH]}{k_{CO+OH} * [CO] * [OH]} \quad (2.2.3.12).$$

The corresponding reaction rate coefficients were taken from the Data Base (JPL 10-6) Chemical Kinetics and Photochemical Data for Use in Atmospheric Studies (Sander et. al, 2011). Therefore, for $CL=401 \pm 44$ k_{wHO_2} should be 0.87, which is 3.6 times higher than the calculated from Eq. (4.2.3.17) $k_{wHO_2}=0.24 \text{ s}^{-1}$. On the other hand, the calculated CL for $k_{wHO_2}=0.24 \text{ s}^{-1}$ should be 697; the obtained CL_I is 57% of this value. This calculus is also confirmed by the simulations with the Kintecus model.

One possible explanation of this discrepancy might be an overestimation of the time during which the radicals are in contact with the reactor walls. It is assumed that the radicals reach the addition point 9.5 cm below the reactor entry and there start to react with NO and CO and are converted into NO₂. It might be the case that the addition gases move also towards the entrance of the reactor due to turbulent mixing with the sampled air, against the assumed direction, and the radicals get in contact with the reactant gases before they reach the real addition point. Table 4.2.3.5 presents the estimation of k_{HO_2} the radical loss rate coefficient when the radical loss zone length varies between 1.6 and 8 cm determined with the formulas (4.2.3.14) and (2.2.3.13). Therefore, the radicals should pass through the loss zone with a length of 3 cm to match the k_{wHO_2} obtained from the chemistry equation (2.2.3.12).

L [cm]	k_{wHO_2} [s ⁻¹]
8	0.31
7	0.36
6	0.41

L [cm]	k_{wHO_2} [s^{-1}]
5	0.50
4	0.62
3	0.83
2	1.24
1.6	1.56

Table 4.2.3.5 Calculated k_{HO_2} radical loss rate with varying radical loss zone length L between 1.6 and 8 cm.

In summary, the results of this study indicate that the concept of the modified reactor has to be altered to be used for the selective measurements of concentrations of HO_2 and RO_2 radicals. For further development of the reactor, it is advised to construct a reactor with higher k_w and thus the ratio S/V as high as 8, with a small diameter 5 mm (as in case of the reactor by Mihele et. al., 1999) to increase available surface to react upon. In this concept a separation of the radicals is based on different removal probability on the walls rather than the diffusive transport, similarly to the findings of Mihele et al., (1999). To prevent from low CL value due to high k_w (see Eq. 2.2.3.12) NO mixing ratio could be increased to 5-6 ppmv and CO to 11% (below explosive level). In addition, to keep the diffusion time lower than the air residence time of the radicals in the reactor $\tau_d < \tau_r$ (for a 5mm diameter τ_d below 0.7s) so that the radicals can reach the reacting surface before leaving the removal zone with a air flow ($Q=1l/min$), the length of the removing zone is recommended to be 50 cm. However, such a solution might be difficult to implement in the aircraft where the physical constraints play a role in designing an instrument.

An increase of the available surface to remove the radicals might be achieved by using a concept of an annular denuder (see Fig. 4.2.3.6) which comprises two coaxial cylinders so that the sampled air is forced to pass through the annular space. However, the annulus should be carefully designed to reduce the flow resistance created by such a barrier inside the reactor. Therefore, there has been compared the theoretical flow resistance for two annuluses with an inner diameter d_1 between 2.2 and 1.8 cm and a length of $L=3$ cm, the outer diameter $d_2=2.9$ cm according to the formula:

$$R = \frac{2\eta L}{\Pi} * \frac{1}{\frac{a^4}{4} - \frac{r^2 a^2}{2} + \frac{r^4}{4}} \quad (2.3.1.3).$$

Where: $a=d_1/2$, $r=d_2/2$. A reduction of 4 mm in the inner diameter results in twice higher resistance for $d_1=1.8$ cm in comparison to $d_1=2.2$ cm.

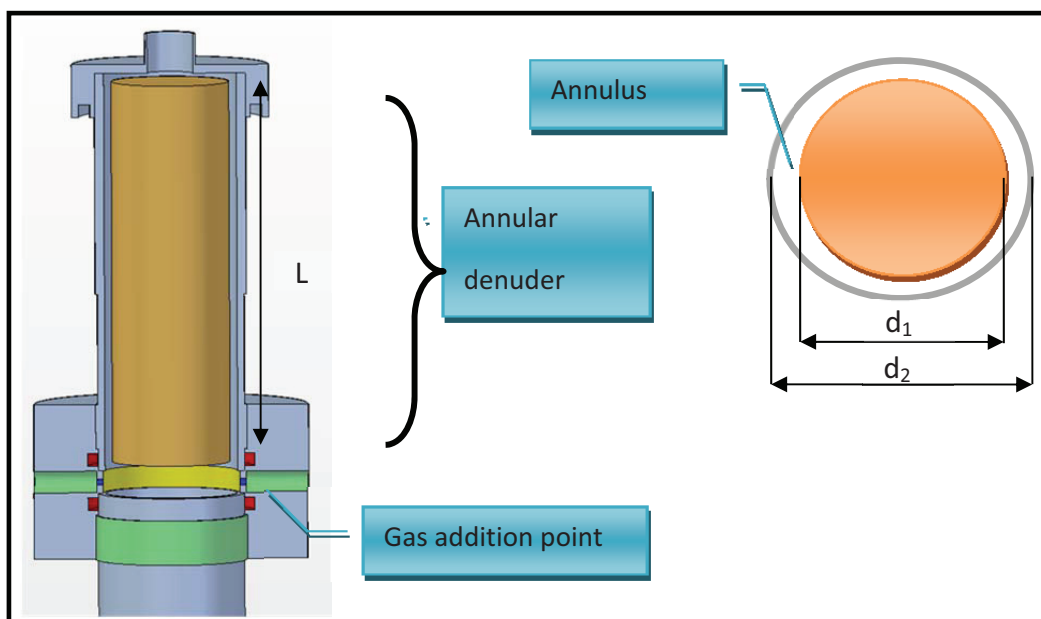


Fig. 4.2.3.6 A scheme of an annular denuder in the modified PeRCA reactor for the radical speciation, d_1 - inner diameter, d_2 - outer diameter and L - length of the annulus.

Table 4.2.3.6 compares parameters: $\frac{\tau_d}{\tau_r}$ and $\frac{S}{V}$ ratios playing important role in the radical losses.

d_1	τ_d	τ_r	$\frac{\tau_d}{\tau_r}$	S/V
2.2	1.0	1.2	0.81	5.7
1.8	1.6	1.8	0.88	3.6
0.5	0.66	1	0.66	8

Table 4.2.3.6 Comparison of $\frac{\tau_d}{\tau_r}$ and $\frac{S}{V}$ [1/cm] ratios for the denuder, for comparison values in bold for the reactor by Mihele et. al., (1999), τ_d - diffusion time [s], τ_r - residence time [s], d_1 - inner diameter of the annulus [cm].

From the analysis above it can be concluded that by a modification of the reactor by an introduction of the annular denuder to increase the available surface to eliminate the radicals can be achieved without decreasing a diameter of the reactor and increasing its length. Such a solution can be easily employment for airborne measurement. In addition, the precondition $\frac{\tau_d}{\tau_r} < 1$ is be fulfilled so the radicals will reach the reactor walls and be lost on them with a different efficiency.

Effect of coating materials on the CL

The radical wall losses depend on the surface properties (Mihele et al., 1999). Therefore, inert materials as Pyrex glass or Teflon coated stainless steel are selected for the sampling system of the radicals. For two identical reactors with different coating: quartz (amorphous silicon) and Teflon, the CL was determined to compare effect of the surfaces on

the radical losses for HO₂ and HO₂+CH₃O₂ (50%:50%). In contrast to the Teflon coating used by the TROLAS group (a 50 μm layer provided by the company HST GmbH) which is black, the quartz coated surfaces are characterized by a colourful hue (see Fig. 3.1.3.1). Therefore, the reactor with the quartz coating will be referred henceforth as a rainbow reactor.

Similarly to the experiments described in the previous section, at first HO₂ radicals were sampled and the CL_{HO_2} was calculated for the rainbow reactor. Then the $CL_{HO_2+CH_3O_2}$ was determined for the radical mixture HO₂+CH₃O₂. The obtained results were compared with the chain length of the reference reactor, see Fig. 4.2.3.7.

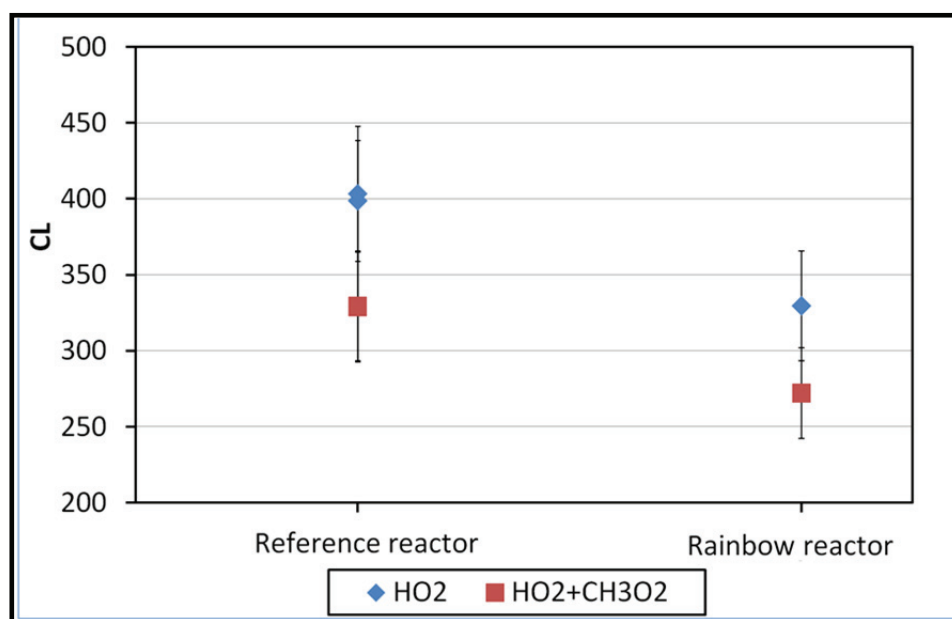


Fig. 4.2.3.9 A Comparison of the CL obtained experimentally for the reference and rainbow reactors.

The CL for the rainbow reactor is lower 17% in comparison to the reference reactor. The results of these experiments indicate that, compared to Teflon, the silicon coating does not lead to an improvement in reducing the radical wall losses. The ratio $\frac{CL_{50\%HO_2+50\%CH_3O_2}}{CL_{HO_2}}$ is 0.83 ± 0.13 and within the measurement uncertainty it is in agreement with the theoretical value 0.925.

The wall loss rate coefficient $k_{wHO_2} \approx 1.3 \text{ s}^{-1}$ for the reactor coated with quartz was estimated from Eq. (2.2.3.16), which is comparable to the Teflon coating. However, quartz coated elements can be welded safely which offers a quick and easy solution for a modification of the components after being coated. In contrast, welding of Teflon the coated components is not possible owing to an emission of the toxic vapours at high temperature.

4.3 Application of the laboratory results to aircraft measurements: OMO (Oxidation Mechanism Observations) mission

The results obtained within the laboratory characterization and theoretical considerations of the HALO inlet have been re-analyzed in this section focusing on the particular requirements of the airborne measurements planned in the frame of the OMO measurement campaign onboard the HALO aircraft (see Section 2.4). This analysis refers to the chemical and physical constraints identified in the previous sections.

Chemical characterization of the HALO inlet

- The chemical characterization pointed out that the eCL decreases with the pressure in the pre-reactor nozzle.
- An increase of the inlet sampling orifice leads to a decrease of the radical removal processes which is shown in the obtained eCL .
- An increase of the noise of the NO_2 detector signal is related to an increase of the inlet orifice. It leads further to an increase of the eCL uncertainty (ΔeCL) and consequently to a decrease of the accuracy of determination of the RO_2^* mixing ratio. Based on the obtained eCL and ΔeCL , the $\text{Ø}1.2$ mm orifice is the most appropriate for the final HALO inlet construction.
- The radical losses are reduced by decreasing the diameter of the reactor entry which is reflected in the obtained eCL . A 4 mm diameter orifice is recommended for the final PerCEAS set-up.

Physical characterization of the HALO inlet

During the OMO campaign the pressure of the pre-reactor nozzle will be kept constant and below the pressure of the sampled air, i.e., below 200 mbar. High sampling flows are generally suitable to minimize the radical losses in the pre-reactor nozzle, such as 1000 ml/min.

- The $\text{Ø}1.2$ mm sampling orifice shows the best hydraulic characteristics for the OMO campaign which is reflected in sufficient air to be sampled through the channel and a control of the pressure in the pre-reactor nozzle.
- The CEAS detector is characterized by lower hydraulic resistance than the luminol detector, therefore it can be introduced in the HALO set-up and the hydraulic properties of the instrument will be kept.

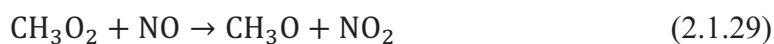
- A reduction of the resistance against the flow of the CO ½” scrubber was achieved by using tube (KF-25). The adaptation of the new scrubber and its fixing elements is related to series of constraints required for airborne measurement such as heating power demand and weight limitations and has to be carefully optimized.

The performance of the PeRCEAS instrument was extensively tested in the field campaign PARADE. In general, the flow of $Q=1000$ ml/min could be sampled and the pressure was successfully regulated at 300 mbar in the pre-reactor nozzle. Difficulties in the pressure regulation and flow sampling occurred at special conditions, e.g., insect in the sampling orifice of the lid.

4.4 Radical speciation

The discrimination of the HO₂ concentrations in the total sum of peroxy radicals is of great interest for the investigation of some of the processes affecting the oxidative capacity of the atmosphere. Therefore, the most important step in the radical speciation consists of the separation of HO₂ and RO₂ in the total sum of peroxy radicals RO₂^{*}.

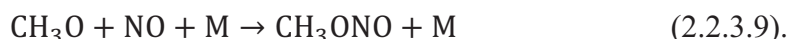
In contrast to HO₂, the reaction of RO₂ with NO generally leads in different extension to a stable nitrite, e.g., for the most abundant in the atmosphere organic radical CH₃O₂ the reaction:



followed by:



competes with:



If the reaction with NO is favoured, the branching ratio $\frac{k_{\text{CH}_3\text{O}+\text{NO}}[\text{NO}][\text{CH}_3\text{O}]}{k_{\text{CH}_3\text{O}+\text{NO}}[\text{NO}][\text{CH}_3\text{O}] + k_{\text{CH}_3\text{O}+\text{O}_2}[\text{O}_2][\text{CH}_3\text{O}]}$ increases. Consequently, CH₃O is not further converted into HO₂ and the transformation into CH₃ONO is favoured. In the present work, this is proposed to be used to measure separately HO₂ from RO₂ in the PeRCA reactor.

The reaction



is also possible, but under the atmospheric conditions the product yield for CH₃ONO₂ is very small <0.5% (Tyndall et al., 2001). And thus, the reaction (2.2.3.7) was not included in the numerical simulations.

Supposing there is a sampling mixture of the radicals $RO_2^* = HO_2 + RO_2$. At a certain NO mixing ratio in the reactor to a total measured $[\Delta NO_2]_{tot}$ contributes the NO_2 created as a result of HO_2 conversion and amplification with the amplification factor CL_1 and similarly for RO_2 with the CL_2 :

$$[\Delta NO_2]_{tot1} = [\Delta NO_2]_1 + [\Delta NO_2]_2 = [HO_2] * CL_1 + [RO_2] * CL_2 \quad (4.4.1)$$

This is also valid for another NO mixing ratio with the CL_3 for HO_2 and in case of RO_2 the CL_4 :

$$[\Delta NO_2]_{tot2} = [\Delta NO_2]_3 + [\Delta NO_2]_4 = [HO_2] * CL_3 + [RO_2] * CL_4 \quad (4.4.2)$$

Solving the set of equations (4.4.1) and (4.4.2), $[HO_2]$ and $[RO_2]$ abundances can be calculated:

$$[HO_2] = \frac{[\Delta NO_2]_{tot1} * CL_4 - [\Delta NO_2]_{tot2} * CL_2}{CL_1 * CL_4 - CL_2 * CL_3} \quad (4.4.3)$$

$$[RO_2] = \frac{[\Delta NO_2]_{tot2} * CL_1 - [\Delta NO_2]_{tot1} * CL_3}{CL_1 * CL_4 - CL_2 * CL_3} \quad (4.4.4)$$

if CL_1 , CL_2 , CL_3 and CL_4 are known and the corresponding NO_2 deltas are measured.

In the following sections a new technique allowing partial speciation of HO_2 from RO_2 employing the reaction of oxy radical with NO to partially remove organic radicals from the radical mixture in the PerCA reactor will be described.

The separation can also be based on a significant removal of RO_2 from RO_2^* via the reaction



and thus $\frac{k_{CH_3O+NO} * [NO]}{k_{CH_3O+NO} * [NO] + k_{CH_3O+O_2} * [O_2]} \approx 1$. Hornbook et al., 2011, Edwards et al., 2003 successfully used the same concept to separate the radicals in the improved Peroxy radical Chemical Ionization Mass Spectrometry (PerCIMS.) $[HO_2]$ abundance in the mixture can be determined at high NO levels (so called 'HO₂ mode') when to a total measured $[\Delta NO_2]_{tot}$ contributes the NO_2 which stems solely from the HO_2 conversion and amplification with the amplification factor CL_5 :

$$[\Delta NO_2]_5 = [HO_2] * CL_5 \quad (4.4.5)$$

At low NO levels (so called 'RO₂^{*} mode') to a total $[\Delta NO_2]_{tot}$ contributes the NO_2 produced as a result of the HO_2 conversion and amplification with the amplification factor CL_1 and similarly for RO_2 with the CL_2 :

$$[\Delta NO_2]_{tot1} = [\Delta NO_2]_1 + [\Delta NO_2]_2 = [HO_2] * CL_1 + [RO_2] * CL_2 \quad (4.4.1)$$

Then $[RO_2]$ abundance can be determined from:

$$[RO_2] = \frac{[\Delta NO_2]_{tot1} - \frac{CL_3 * [\Delta NO_2]_5}{CL_5}}{CL_2} \quad (4.4.6).$$

A series of numerical simulations was made to verify these new approaches to measure $[HO_2]$ and $[RO_2]$ selectively (described in Section 4.4.1). The results are compared with the laboratory data available at the TROLAS group (described in Section 4.4.2). The implications of the simulation results for the standard PerCA measurements are provided. In the end, applications for airborne measurements are discussed (section 4.4.3).

4.4.1 Modeling studies for ground based measurements

A series of simulation with the Kintecus based on the model described in Section 2.5 was conducted for the following purposes:

- To investigate the variations of the CL with NO at 298 K and 1013 mbar,
- To characterize the inlet chemistry,
- To establish the conditions for the optimal sensitivity and the separation between HO_2 and different RO_2 .

CO was kept at 9% as it is proposed for the flight measurements. The HO_2 wall losses rate coefficient k_{wHO_2} was set 0.83 s^{-1} , as it was adjusted according to the experimental CL of 403 ± 44 obtained at 1013 mbar for the reference reactor of the DUALER 2 inlet (see section 4.2.3), as a first approach the RO_2 losses were neglected and thus $k_{wRO_2} = 0 \text{ s}^{-1}$. Firstly, a mix of the radicals with only the two most abundant species, i.e., HO_2 and CH_3O_2 , was investigated (described in section 4.4.1.1). Then the investigation was extended to other two organic peroxy radicals which are also likely to be present in significant concentrations in the troposphere (described in section 4.4.1.2).

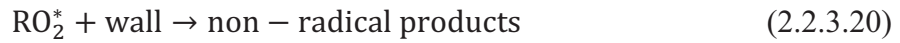
4.4.1.1 CH_3O_2 as an example of organic peroxy radical

50 pptv HO_2 , 50 pptv CH_3O_2 , mixture with equal radical mixing ratios 25 pptv HO_2 and 25 pptv CH_3O_2 were given as an input data in the model. The results of the CL simulations are presented in Fig. 4.4.1.1 and summarised in Appendix 3 in Table 4.4.1.1.

The CL initially increases with $[NO]$ concentration and then reaches a maximum at 3 ppmv NO. At low $[NO]$ a raise of the CL is observed because $[NO]$ increase favours the reaction



relatively to the reactions



At much higher levels of [NO] the reaction



becomes important for the radical removal and therefore a decrease of the *CL* is observed.

Similar *CL* variations with NO were determined by Clemitshaw et al., 1997.

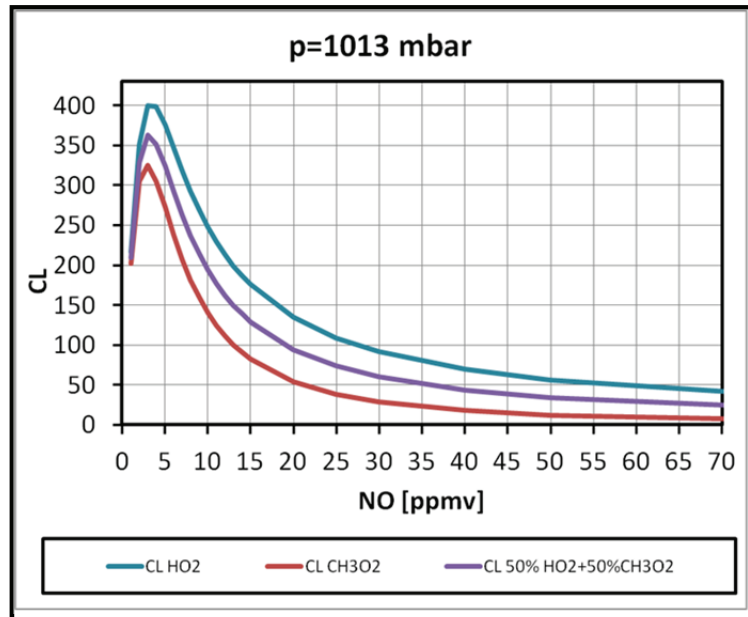


Fig. 4.4.1.1 The *CL* variations with NO for HO₂, CH₃O₂ and 50%HO₂+50%CH₃O₂ mixture.

According to the simulations at 1013 mbar the retention time *t* in the stainless steel reactor of DUALER 2 (12.4 s) is sufficient for completing the chain reaction at all selected NO levels, shown in Fig. 4.4.1.2.

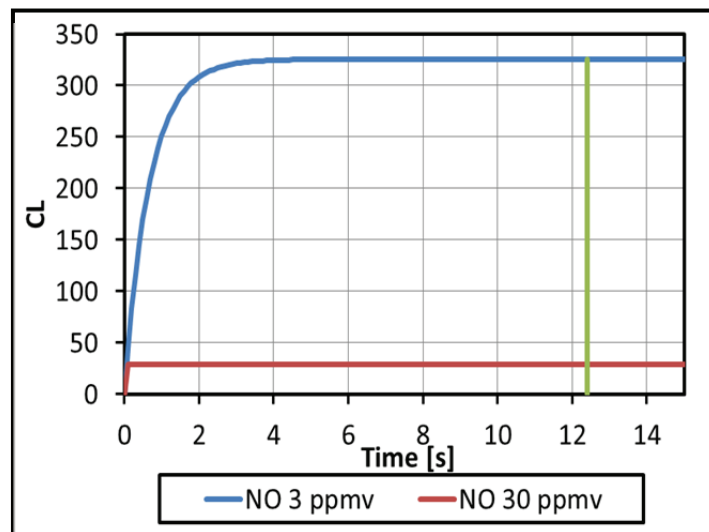


Fig. 4.4.1.2 A temporal evolution of the $CL_{\text{CH}_3\text{O}_2}$ for NO 3 and 30 ppmv, as a green line indicated the residence time of air in the reactor (12.4 s).

As a first approach, the CH_3O_2 heterogeneous losses were neglected in the numerical simulations. In order to investigate the potential effect of $k_{w\text{CH}_3\text{O}_2}$ on the CL values presented above, a sensitivity study was made. The following $k_{w\text{CH}_3\text{O}_2}$ values were used:

- 0 s^{-1} (no losses),
- 0.12 s^{-1} , based on the $k_{w\text{CH}_3\text{O}_2}/k_{w\text{HO}_2}$ ratio obtained by Mihele et al., 1997,
- 0.83 s^{-1} equal to $k_{w\text{HO}_2}$,
- 8.3 s^{-1} , i.e., $10 \cdot 0.83$,
- 83 s^{-1} , i.e., $100 \cdot 0.83$.

CO was kept at 9% and $k_{w\text{HO}_2} = 0.83 \text{ s}^{-1}$, as input data 50 pptv CH_3O_2 was given. The results of these simulations are presented in Fig. 4.4.1.3 and compared with the CL obtained at 3 ppmv NO for 6 different $k_{w\text{HO}_2} = 0.5; 0.83; 1.5; 2; 2.5; 3 \text{ s}^{-1}$.

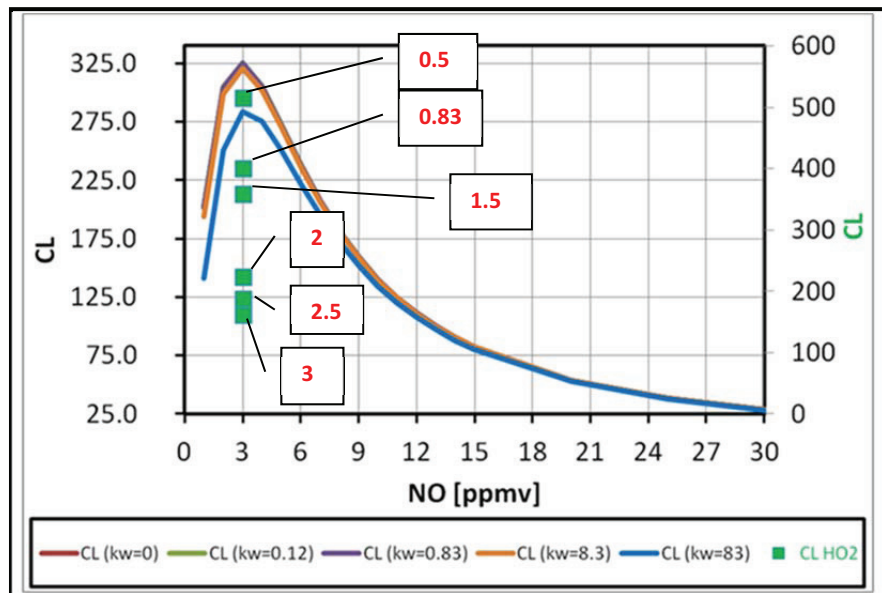


Fig. 4.4.1.3 The $CL_{\text{CH}_3\text{O}_2}$ with different $k_{w\text{CH}_3\text{O}_2} = 0; 0.12; 0.83; 8.3 \text{ s}^{-1}$ as solid lines. The CL as points in green obtained for HO_2 with different $k_{w\text{HO}_2}$ indicated as number in red

Fig. 4.4.1.4 compares the $CL_{k_{w\text{CH}_3\text{O}_2} \neq 0}$ and $CL_{k_{w\text{CH}_3\text{O}_2} = 0}$ as $(100\% * \frac{CL_{k_{w\text{CH}_3\text{O}_2} = 0} - CL_{k_{w\text{CH}_3\text{O}_2} \neq 0}}{CL_{k_{w\text{CH}_3\text{O}_2} = 0}})$.

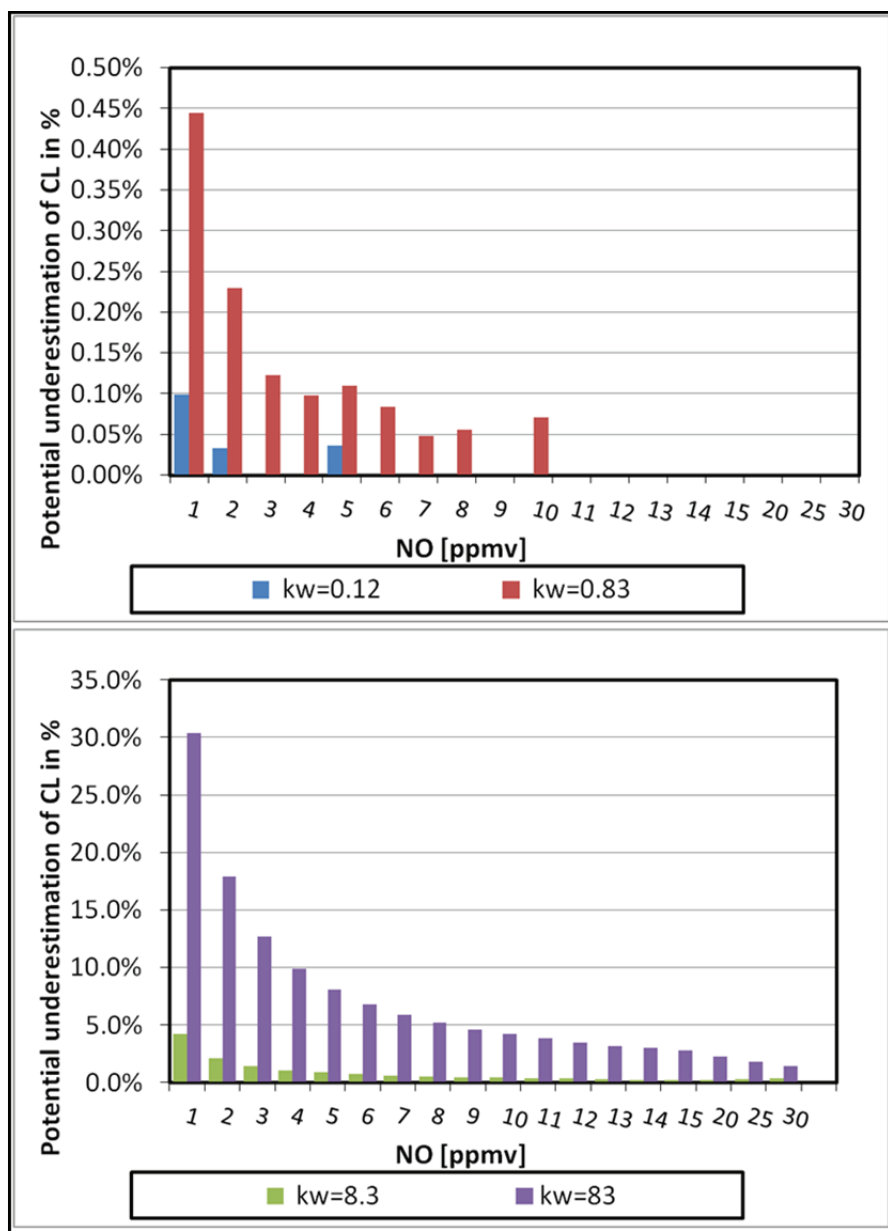


Fig. 4.4.1.4 Comparison of the *CL* obtained with $k_{wCH_3O_2} \neq 0$ relatively to the *CL* with $k_{wCH_3O_2} = 0 \text{ s}^{-1}$ for CH_3O_2 .

The relative difference between the *CL* obtained with $k_{wCH_3O_2} \leq 0.83 \text{ s}^{-1}$ and $k_{wCH_3O_2} = 0 \text{ s}^{-1}$ is below 0.45%. The highest difference between the *CL* determined with $k_{wCH_3O_2} = 8.3 \text{ s}^{-1}$ and $k_{wCH_3O_2} = 0 \text{ s}^{-1}$ is 4% for 1 ppmv NO. The relative difference between the *CL* obtained with $k_w \neq 0$ the *CL* with $k_w = 0 \text{ s}^{-1}$ decreases at higher NO mixing ratios. This can be attributed to that at higher [NO] the radical losses gain less importance in comparison to the reaction of CH_3O_2 with NO



i.e., a decrease of the branching ratio $\frac{k_{wCH_3O_2}}{k_{CH_3O_2+NO}*[NO]+k_{wCH_3O_2}}$.

In summary, the simulation results indicate that the CH_3O_2 losses on the reactor walls after adding $\text{NO}+\text{CO}$ and prior to their conversion into HO_2 are negligible because CH_3O_2 radicals are rapidly transformed into HO_2 in the reaction with NO (reaction 2.1.29). As the reaction is not pressure dependent this is also the case for other pressure conditions.

Entire removal of CH_3O_2 at $\text{NO}>300$ ppmv leads to a significant reduction of the CL value owing to the terminating reaction:



Thus, the NO mixing ratio shall be optimized to remove significantly CH_3O_2 , e.g., below 70%, and to obtain the measureable CL , e.g., $CL=29$ at 30 ppmv NO .

The simulation results of the CL presented in this section demonstrate that different CL values are obtained for HO_2 and CH_3O_2 at the certain NO mixing ratio. Thus, using different NO mixing ratios allows determination of the HO_2 and CH_3O_2 mixing ratios from the measured deltas NO_2 according to the formulas (4.4.3) and (4.4.4) if the CL_{1-4} are known. Based on these simulations, 3 ppmv NO with the maximum CL_{HO_2} and 10 ppmv were selected for HO_2 and CH_3O_2 speciation.

4.4.1.2 Other organic peroxy radicals

The modeling studies were also made for other organic radicals $t\text{-C}_4\text{H}_9\text{O}_2$ (having an industrial source) and originating from isoprene (having a biogenic source) showing different chemical pattern of the conversion into HO_2 from CH_3O_2 .

In case of $t\text{-C}_4\text{H}_9\text{O}_2$, firstly it is converted into CH_3O_2 via reactions (4.4.1.1-5) and followed by the conversion of CH_3O_2 into HO_2 via the reactions (2.1.2) and (2.2.3.8) which is further converted and amplified into NO_2 via the reactions (2.1.5, 2.1.11-12), (see Table 4.4.1.2). The yield of HO_2 from $t\text{-C}_4\text{H}_9\text{O}_2$ is expected to decrease significantly as $[\text{NO}]$ increases because of several reasons:

- the intermediate oxy radical, $t\text{-C}_4\text{H}_9\text{O}$ (i.e., $(\text{CH}_3)_3\text{CO}$), cannot react with O_2 owing to the absence of a hydrogen atom in the position α to the radical centre,
- the only chain propagating reaction available is its slow thermal decomposition (4.4.1.3).

As a result, the alternative reaction with NO (4.4.1.4) is predicted to compete effectively with the reaction (4.4.1.3).

The chemical reactions and the reaction rate coefficients for the reactions (4.4.1.1-5) are adapted from Ashbourn et al., 1998 and for others taken from the Data Base (JPL 10-6)

Chemical Kinetics and Photochemical Data for Use in Atmospheric Studies (Sander et al., 2011) and are summarized in Table 4.4.1.2.

Reaction	Rate constants for bimolecular reactions at 298 K	No.
$(\text{CH}_3)_3\text{CO}_2 + \text{NO} \rightarrow (\text{CH}_3)_3\text{CO} + \text{NO}_2$	$4.5\text{E-}12 * 0.82^{(a)}$	4.4.1.1
$(\text{CH}_3)_3\text{CO}_2 + \text{NO} \rightarrow (\text{CH}_3)_3\text{CONO}_2$	$4.5\text{E-}12 * 0.18^{(a)}$	4.4.1.2
$(\text{CH}_3)_3\text{CO} \rightarrow \text{CH}_3 + \text{CH}_3\text{COCH}_3$	1490	4.4.1.3
$(\text{CH}_3)_3\text{CO} + \text{NO} \rightarrow (\text{CH}_3)_3\text{CONO}$	$4.10\text{E-}11$	4.4.1.4
$\text{CH}_3 + \text{O}_2 \rightarrow \text{CH}_3\text{O}_2$	instantaneous	4.4.1.5
$\text{CH}_3\text{O}_2 + \text{NO} \rightarrow \text{CH}_3\text{O} + \text{NO}_2$	$7.7\text{E-}12$	2.1.2
$\text{CH}_3\text{O} + \text{O}_2 \rightarrow \text{CH}_2\text{O} + \text{HO}_2$	$1.9\text{E-}15$	2.2.3.8
$\text{CH}_3\text{O} + \text{NO} + \text{M} \rightarrow \text{CH}_3\text{ONO} + \text{M}$	$2.89\text{E-}11$	2.2.3.7
$\text{HO}_2 + \text{NO} \rightarrow \text{NO}_2 + \text{OH}$	$8\text{E-}12$	2.1.5
$\text{CO} + \text{OH} \xrightarrow{\text{O}_2} \text{CO}_2 + \text{HO}_2$	$2.4\text{E-}13$	2.1.11-12

Table 4.4.1.2 The mechanism of converting t-C₄H₉O₂ into HO₂, (a) is branching ratio.

As an input data in the model 50 pptv HO₂, 50 pptv t-C₄H₉O₂, a mixture with equal radical mixing ratios 25 pptv HO₂ and 25 pptv t-C₄H₉O₂ were given. Fig. 4.4.1.5 shows the simulation results and in Appendix 3 Table 4.4.1.3 summarizes the obtained *CL*.

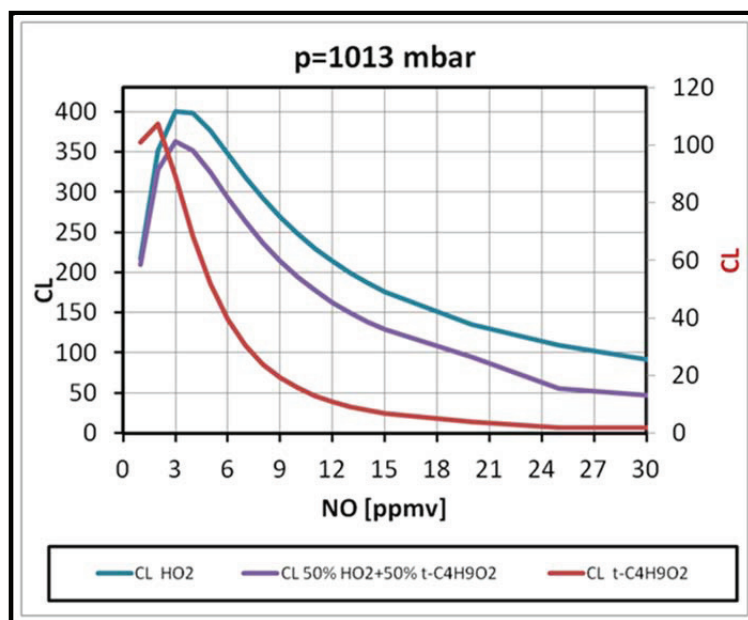


Fig. 4.4.1.5 The *CL* variations with NO for HO₂, t-C₄H₉O₂ and 50%HO₂+50% t-C₄H₉O₂ mixture.

As predicted, much stronger decrease of the *CL* with [NO] for t-C₄H₉O₂ in comparison to HO₂ is observed. For example at 3 ppmv NO the $CL_{t-C_4H_9O_2}$ is 80% lower than the CL_{HO_2} . Therefore, the NO condition for CH₃O₂ separation from HO₂ (3 ppmv and 10 ppmv) are not optimal for t-C₄H₉O₂ as its NO₂ contribution ($[\Delta\text{NO}_2]_{t-C_4H_9O_2} =$

$[t - C_4H_9O_2] * CL_{t-C_4H_9O_2}$) to the total $[NO_{2tot}]$ might be at the detection limit of the detector. Thus, it is proposed 2 and 6 ppmv NO mixing ratios for the determination of $[t - C_4H_9O_2]$ from the mixture $t-C_4H_9O_2 + HO_2$. The results of these simulations have additional importance for the standard PeRCA technique for which the CL for all sampled peroxy radicals is assumed to be equal to the CL_{HO_2} . Therefore, underestimation of RO_2^* abundance comprising $t-C_4H_9O_2$ is predicted resulting from a much lower $CL_{t-C_4H_9O_2}$ than the CL_{HO_2} .

The radicals initiated by a degradation of isoprene via OH leads to the rapid formation of six types of isomeric peroxy radical: $C_5H_8(OH)O_2$ (Jenkin et al., 1998), called $R1O_2$, e.g., $HOCH_2C(CH_3)=CHCH_2O_2$. A simplified model was developed for the $R1O_2$ conversion into HO_2 via the reactions (4.4.1.6-8), excluding the radical-radical reactions, as summarized in Table 4.4.1.4. The reaction rate coefficients are adapted from Jenkin et al., 1998.

Reaction	Rate constants for bimolecular reactions at 298 K	No.
$R1O_2 + NO \rightarrow R1O + NO_2$	$3.9E-12 * 0.9^{(a)}$	4.4.1.6
$R1O_2 + NO \rightarrow R1ONO_2$	$3.9E-12 * 0.1^{(a)}$	4.4.1.7
$R1O + O_2 \rightarrow \text{products} + HO_2$	instantaneous	4.4.1.8

Table 4.4.1.4 Simplified mechanism of converting $R1O_2$ into HO_2 , (a) is a branching ratio.

The yield of $R1O_2$ conversion into HO_2 is constant and equals 0.9 and is independent of the NO mixing ratio as $\frac{k_{4.4.1.6} * [NO] * [R1O_2]}{k_{4.4.1.6} * [NO] * [R1O_2] + k_{4.4.1.7} * [NO] * [R1O_2]} = \frac{k_{4.4.6}}{k_{4.4.6} + k_{4.4.7}} = 0.9$. The CL variations with NO for these radicals are the same as for HO_2 , however the obtained CL is 10% lower than for HO_2 . In contrast, the yield of the CH_3O_2 conversion into HO_2 is NO dependent and shows more complex dependence from NO: $\frac{k_{CH_3O+NO+M} * [NO]}{k_{CH_3O+NO+M} * [NO] + k_{CH_3O+O_2} * [O_2]}$. Therefore, for CH_3O_2 the $CL_{CH_3O_2}/CL_{HO_2}$ ratio varies with NO, in contrast to the isoprene originated radicals $CL_{R1O_2}/CL_{HO_2} = 0.9$. Fig. 4.4.1.6 shows the simulation results and in Appendix 3 Table 4.4.1.5 summarizes the obtained CL .

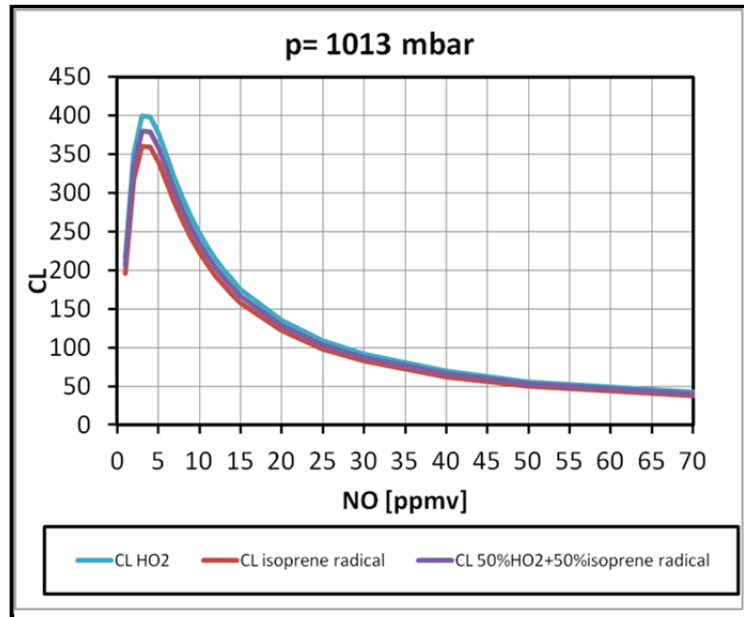


Fig. 4.4.1.6 The CL variations with NO for HO_2 , isoprene radicals, 50% HO_2 +50% CH_3O_2 isoprene radicals.

The following conditions has to be fulfilled to calculate $[HO_2]$ and $[RO_2]$ from Eq. (4.4.3-4): $CL_1 * CL_4 - CL_2 * CL_3 \neq 0$. As $\frac{CL_2}{CL_1} = 0.9$ and $\frac{CL_4}{CL_3} = 0.9$ for isoprene and HO_2 radicals, then $CL_1 * 0.9 * CL_3 = 0.9 * CL_1 * CL_3$ and as a result $[HO_2]$ and $[RO_2]$ cannot be determined. Therefore, the radicals for which $\frac{CL_2}{CL_1} = \frac{CL_4}{CL_3} = \text{const}$ and independent on NO, RO_2 cannot be discriminated from HO_2 with employment of varying the NO mixing ratios.

As $\left(\frac{k_{1R1O_2+NO} * [NO] * [R1O_2]}{k_{1R1O_2+NO} * [NO] * [R1O_2] + k_{2R1O_2+NO} * [NO] * [R1O_2]} = 0.9 \right)$ only 10% of isoprene radicals is removed from RO_2^* and the removal efficiency does not depend on the NO mixing ratio. Thus, HO_2 cannot be isolated from the radical mixture and solely its abundance cannot be determined.

The CL was simulated for different kinds of typical air masses containing radical mixtures with different proportions of HO_2 , CH_3O_2 , $t-C_4H_9O_2$ and radicals originating from isoprene:

- remote, unpolluted mix₁: 70% HO_2 +30% CH_3O_2 (Wayne, 2000),
- urban mix₂: 64% HO_2 +18% CH_3O_2 +18% $t-C_4H_9O_2$,
- forest mix₃: 54% HO_2 +23% CH_3O_2 +23%isoprene radical.

The results are summarized in Appendix 3 in Table 4.4.1.6. This enables to estimate an error in RO_2^* determination for ambient measurements, which is associated with the assumption in the standard PerCA technique that the CL for all sampled peroxy radicals equals to the CL_{HO_2} (see Fig. 4.4.1.7a) or proposed $CL_{50\%HO_2+50\%CH_3O_2}$ (see Fig. 4.4.1.7b).

The error for the first approach has been calculated (similarly for the $CL_{50\%HO_2+50\%CH_3O_2}$) as:

$$\begin{aligned} \left(\frac{[RO_2^*]_{CL_{mix}} - [RO_2^*]_{CL_{HO_2}}}{[RO_2^*]_{CL_{mix}}} \right) * 100\% &= \left(\frac{\frac{[\Delta NO_2]}{CL_{mix}} - \frac{[\Delta NO_2]}{CL_{HO_2}}}{\frac{[\Delta NO_2]}{CL_{mix}}}} \right) * 100\% \\ &= \left(\frac{CL_{HO_2} - CL_{mix}}{CL_{HO_2}} \right) * 100\% \end{aligned} \quad (4.4.1.1).$$

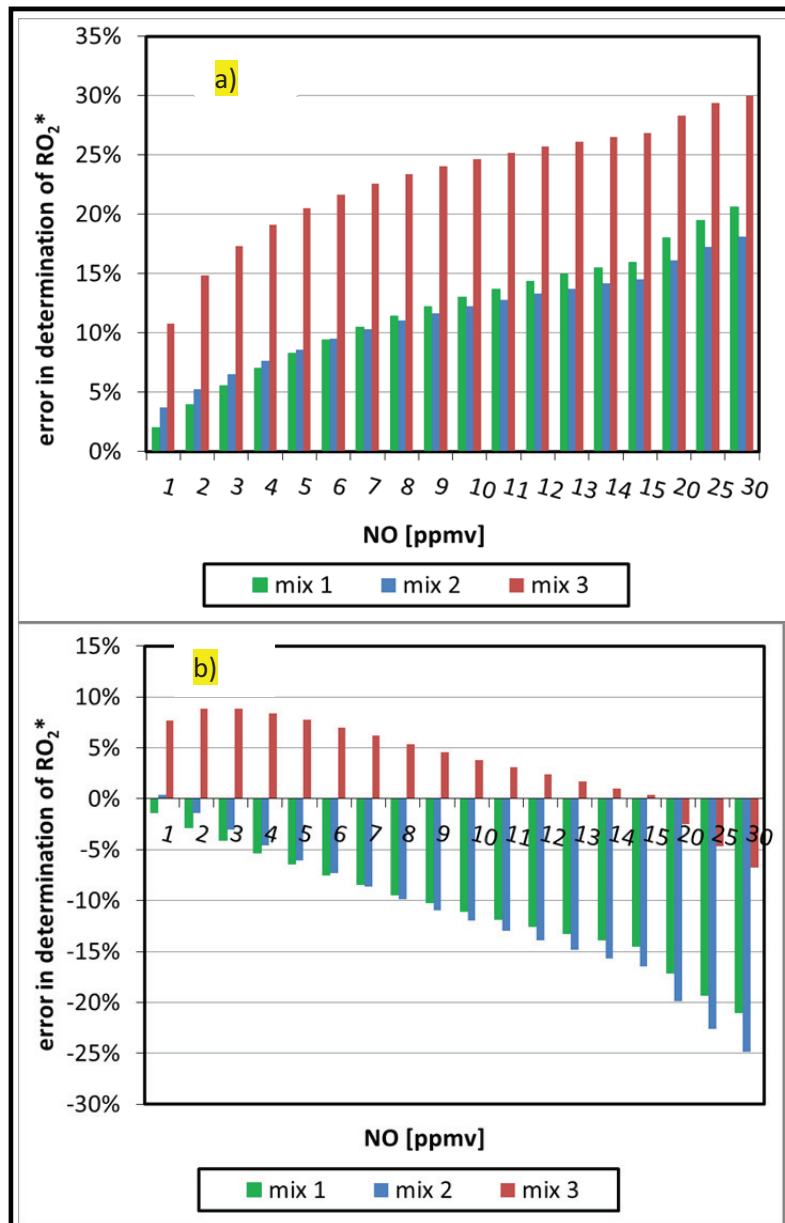


Fig. 4.4.1.7 Error in the determination of RO_2^* a) $\left(100\% * \frac{CL_{HO_2} - CL_{mix}}{CL_{HO_2}} \right)$ with the assumption $CL_{mix} = CL_{HO_2}$,
 b) $\left(100\% * \frac{CL_{50\%HO_2+50\%CH_3O_2} - CL_{mix}}{CL_{50\%HO_2+50\%CH_3O_2}} \right)$ with the assumption $CL_{mix} = CL_{50\%HO_2+50\%CH_3O_2}$,
 mix₁: 70% HO_2 +30% CH_3O_2 , mix₂: 64% HO_2 +18% CH_3O_2 +18% t- $C_4H_9O_2$,
 mix₃: 54% HO_2 +23% CH_3O_2 +23%isoprene radical.

As can be seen in Fig. 4.4.1.7a using the CL_{HO_2} instead of the CL_{mix} leads to underestimation of RO_2^* at 3 ppmv NO (used for the measurements during the campaigns (Kartal et. al., 2009)):

- 6% in the remote, unpolluted areas,
- 7% in the urban areas,
- 17% in the forest areas.

Thus, a presence of organic radicals in the sampled air increases the uncertainty of the RO_2^* determination for the standard PerCA.

According to these simulations using the $CL_{50\%HO_2+50\%CH_3O_2}$ at 3 ppmv NO instead of the CL_{HO_2} leads to decrease of the uncertainty of the RO_2^* abundance:

- 4% overestimation in the remote unpolluted areas,
- 3% overestimation in the urban areas,
- 9% underestimation in the forest areas.

Thus, it is advisable to decrease the uncertainty of RO_2^* determination to use the $CL_{50\%HO_2+50\%CH_3O_2}$ to determine the RO_2^* abundance instead of the standard CL_{HO_2} .

4.4.2 Comparison with the experimental results

The Kintecus model was applied to simulate the available laboratory results obtained with the glass reactor (described in section 3.1.2.1) for HO_2 and a $HO_2+CH_3O_2$ mixture (50%:50%) and the NO mixing ratio between 3 and 24 ppmv. CO was kept at 9% in the reactor. The radical source producing HO_2 and $HO_2+CH_3O_2$ mixture as described in section 3.2.2 was deployed for these experiments performed at the laboratory pressure around 1013 mbar. The obtained eCL_{exp} is presented in Fig. 4.4.2.1, the error bars (ΔeCL_{exp}) were calculated from the error propagation law (Eq. 3.4.3.2).

The experimental CL is called experimental effective chain length (eCL_{exp}) because it is obtained with the amount of radicals produced in the source under assumption that the losses in the reactor entry are neglected. The eCL_{exp} errors bars at NO amount exceeding 12 ppmv are up to 2.5 higher than for the eCL at 3 ppmv which can be attributed to the sensitivity decrease of the NO_2 detector at higher NO mixing ratios.

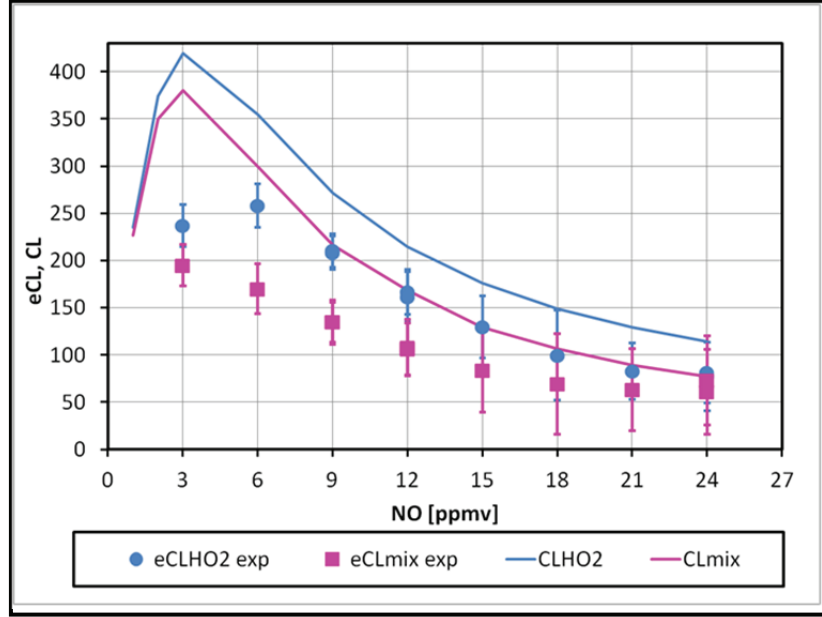


Fig. 4.4.2.1 The determined experimentally eCL_{exp} variations with NO for HO_2 and a $HO_2+CH_3O_2$ mixture (50%:50%) and the CL simulated with $k_{wHO_2}=0.76 \text{ s}^{-1}$ and $k_{wCH_3O_2}=0.58 \text{ s}^{-1}$.

On the basis of Eq. (2.2.3.16): $k_w = 1.85 \left(\frac{v^{1/3} D^{2/3}}{d^{1/3} L^{1/3}} \right) \left(\frac{S}{V} \right)$, the wall losses rate coefficient was calculated for the glass reactor: $k_{wHO_2}=0.79 \text{ s}^{-1}$ and $k_{wCH_3O_2}=0.60 \text{ s}^{-1}$, the diffusion coefficient D was estimated with the formula (4.2.3.7) (Clark M., 2002): $D_{HO_2} = 0.21, D_{CH_3O_2} = 0.14 \text{ [cm}^2/\text{s]}$. The CL simulated by the numerical model with these k_w is presented in Fig. 4.4.2.1 by lines, whereas the obtained experimentally eCL_{exp} by symbols. The modeled CL significantly deviates from the experimental one, e.g., the eCL_{exp} is twice higher than the $CL_{simulated}$ at $NO=3 \text{ ppmv}$. In addition, a maximum CL differs between the $CL_{simulated}$ at 3 ppmv NO and the eCL_{exp} at 6 ppmv. A better agreement for the maximum between the $CL_{simulated}$ and the eCL_{exp} was achieved by adjusting of the wall loss rate coefficient k_{wHO_2} to 1.7 s^{-1} (see Fig. 4.4.2.2), $k_{wCH_3O_2} = 0 \text{ s}^{-1}$ as the previous simulation results showed that organic radicals are not lost in the reactor. Considering this $k_{wHO_2} = 1.7 \text{ s}^{-1}$ and based on Eq. (2.2.3.16) a diffusion coefficient $D_{HO_2}=0.67 \text{ cm}^2/\text{s}$ was calculated, which is approximately a factor of 3 bigger than the $D_{HO_2} = 0.21 \text{ cm}^2/\text{s}$ obtained with the formula (4.2.3.2) from Clark M., 2002.

The numerical model only considers the chemistry in the reactor. The CL and the eCL are connected in the following way:

$$CL = \frac{[\Delta NO_2]}{[HO_2(t)]} = \frac{[\Delta NO_2]}{[HO_2 - HO_2^{loss}]} = \frac{[\Delta NO_2]}{[HO_2] * \exp(-t * k_{wHO_2}^e)} = \frac{eCL}{\exp(-t * k_{wHO_2}^e)} \quad (4.4.2.1).$$

Where: $[HO_2]$ is the initial radical concentration, $k_{wHO_2}^e$ wall loss rate coefficient in the reactor entry, $t = \frac{V}{Q} = \frac{A \cdot l}{Q}$ the retention time in the nozzle calculated from formula (2.2.3.13), $Q=2$ l/min, $l=2.5$ cm, $\varnothing=0.4$ cm. The same calculations are valid for organic radicals.

The $CL_{CH_3O_2}$ and the uncertainty $\Delta CL_{CH_3O_2}$ were determined from the experimental CL_{mix} , ΔCL_{mix} for $HO_2+CH_3O_2$ mixture (50%:50%) and CL_{HO_2} , ΔCL_{HO_2} :

$$CL_{CH_3O_2} = 2 * CL_{mix} - CL_{HO_2} \quad (4.4.2.2)$$

$$\Delta CL_{CH_3O_2} = \sqrt{(2 * \Delta CL_{mix})^2 + (\Delta CL_{HO_2})^2} \quad (4.4.2.3).$$

- In the first approach the diffusion coefficient was calculated with Eq. (4.2.3.7): $D_{HO_2}=0.21$, $D_{CH_3O_2}=0.14$ cm²/s. With these D the coefficients $k_{wHO_2}^e = 39.1$ and $k_{wCH_3O_2}^e = 29.8$ s⁻¹ were estimated by Eq. 2.2.3.17, which corresponds to 37% HO_2 and 29% CH_3O_2 loss in the reactor entry determined from:

$$RE = \frac{[HO_2(t)]}{[HO_2^0]} * 100\% = \exp(-t * k_{wHO_2}^e) * 100\% \quad (4.2.3.5).$$

The CL experimental (blue dots and pink rectangles) and the CL simulated (pink and blue line) are compared in Fig. 4.4.2.3.

- In the second approach with Eq. (2.2.3.1) $k_{wHO_2}^e = 84$ s⁻¹ for the reactor entry was estimated with $D_{HO_2}=0.67$ cm²/s, calculated from the reactor $k_{wHO_2} = 1.7$ s⁻¹. This $k_{wHO_2}^e = 84$ s⁻¹ corresponds to 63% HO_2 loss in the reactor entry according to Eq. (4.2.3.5). $D_{CH_3O_2}=0.45$ cm²/s was estimated considering $D_{HO_2}=0.67$ cm²/s and the determined previously ratio $D_{HO_2}/D_{CH_3O_2}= 0.21/0.14$. With $D_{CH_3O_2}=0.45$ cm²/s $k_{wCH_3O_2}^e = 64$ s⁻¹ was obtained which corresponds to 53% loss of CH_3O_2 . As in the previous case the measured (blue dots and pink rectangles) deviates significantly from the modeled CL (in Fig. 4.4.2.2 violet and red line).
- In the third approach k wall loss rate coefficient of the entry was determined from:

$$k = \frac{\gamma \bar{c} A}{4V} = \frac{\gamma \bar{c}}{d} \quad (4.4.2.4).$$

Where: γ is uptake coefficient (ratio of the number of molecules lost to the surface to the number that strike the surface), \bar{c} mean thermal velocity of the gas-phase reactant, d is a diameter of the entry. Material of the entry and the reactor is identical: glass. The conditions during air sampling were similar, i.e., pressure, and as \bar{c} is directly proportional to temperature which was constant during the experiments, $\gamma * \bar{c}$ is constant

for the reactor and the entry. The wall loss rate coefficient of the entry $k_{wHO_2}^e = 8.5 \text{ s}^{-1}$ based on $k_{wHO_2}^{reactor} = 1.7 \text{ s}^{-1}$ was calculated from:

$$k_{wHO_2}^e = k_{wHO_2}^{reactor} * \frac{d_{reactor}}{d_{entry}} \quad (4.4.2.5).$$

Where: $d_{reactor} = 2 \text{ cm}$ diameter of the reactor, $d_{entry} = 0.4 \text{ cm}$ diameter of the entry. $k_{wHO_2}^e = 8.5 \text{ s}^{-1}$ corresponds to 9.4% HO_2 loss in the reactor entry according to Eq. (4.2.3.5). As in the previous cases the model output (green line in Fig. 4.4.2.2) is not in accordance with the results obtained experimentally (blue dots and pink rectangles).

In conclusion, k_w^e loss rate in the reactor entry cannot be estimated from $k_w^{reactor}$ within the reactor, as the consideration of the competition with the chemical amplification and terminating reactions in the reactor is necessary.

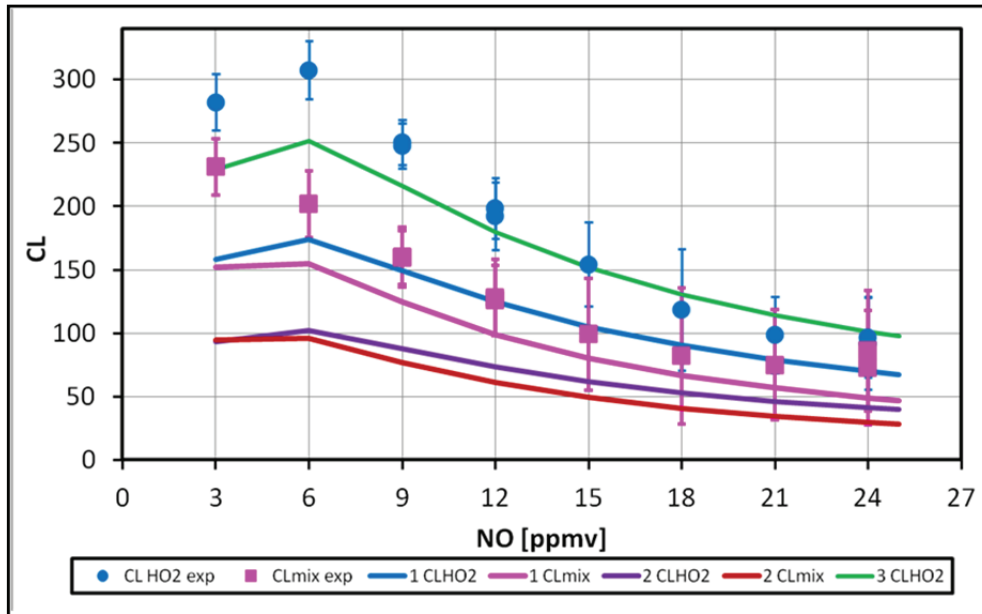


Fig. 4.4.2.2 Comparison of the simulated CL variations with NO and the obtained experimentally for HO_2 and $HO_2+CH_3O_2$ mixture (50%:50%) corrected for the radical losses in the entry: 1 HO_2 37% (blue line) and 29% (pink line) CH_3O_2 loss, 2 HO_2 63% (violet line) and 53% CH_3O_2 loss (red line), 3 HO_2 9% loss (green line). Error bars for the experimental CL are equal to uncertainty ΔeCL .

- In the fourth approach the radical losses were estimated from the difference between the experimental eCL_{exp} and simulated CL . Considering the ratio $CL_{simulated}/eCL_{exp}$ ratio the losses in the entry were calculated: 16% for HO_2 and 15% for CH_3O_2 . Then with Eq. (4.4.2.1) $k_{wHO_2}^e = 19.9 \text{ s}^{-1}$ and $k_{wCH_3O_2}^e = 14.9 \text{ s}^{-1}$ were determined. The similar order of the losses is in agreement with the previous determination with the DUALER 2 reactor (see section 4.2.3). Fig. 4.4.2.3 compares the experimental CL_{exp} variations with NO with the results of the simulations.

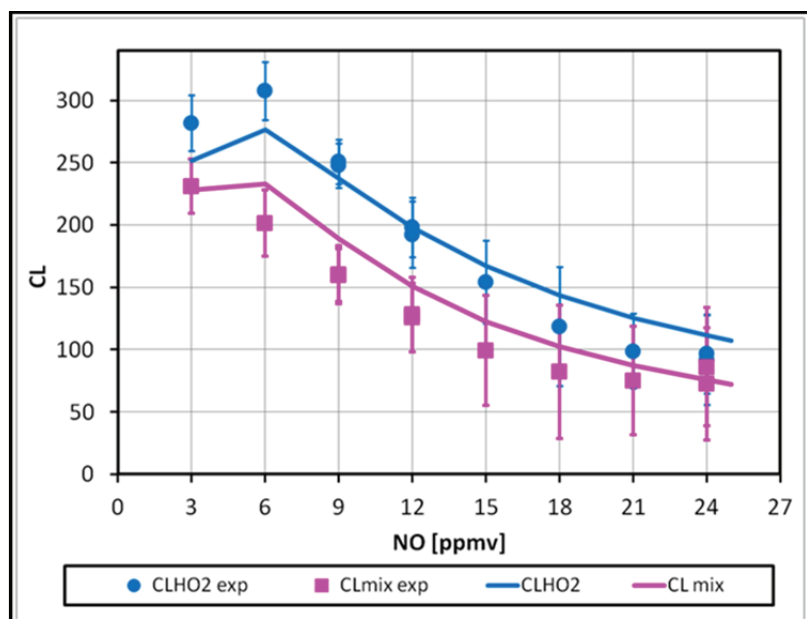


Fig. 4.4.2.3 Comparison of simulated CL variations with NO and obtained experimentally for HO_2 and $HO_2+CH_3O_2$ mixture (50%:50%) corrected for radical losses in the nozzle 16% for HO_2 and 15% for CH_3O_2 . Error bars for the experimental CL are equal to uncertainty ΔeCL .

The simulated CL in Fig. 4.4.2.3 agrees very well with the experimental results above 12 ppmv NO for HO_2 and a $HO_2+CH_3O_2$ mixture (50%:50%). For HO_2 below 6 ppmv NO the experimental values of the CL are approximately 8% higher than the simulated CL and for the radical mixture between 6-9 ppmv NO the experimental values are 17% lower than the simulated CL . These differences can result from the instrumental noise and instability, the uncertainties of the rate coefficient of the reactions, possibly incomplete mechanism of the conversion and amplification. Thus, in general the model is able to reproduce reasonably the experimental results. In summary, the following parameters describe the glass reactor: wall loss rate coefficient of the reactor $k_{wHO_2}^{reactor}=1.7\text{ s}^{-1}$, $k_{wCH_3O_2}^{reactor}=0\text{ s}^{-1}$, wall loss rate coefficient of the reactor entry $k_{wHO_2}^e = 19.9\text{ s}^{-1}$ and $k_{wCH_3O_2}^e = 14.9\text{ s}^{-1}$ corresponding to the loss of 16% for HO_2 and 15% for CH_3O_2 , respectively.

Based on the experimental results, α - conversion efficiency of CH_3O_2 into HO_2 and the uncertainty $\Delta\alpha$ were calculated as:

$$\alpha = \frac{CL_{CH_3O_2}}{CL_{HO_2}} \quad (4.4.2.6)$$

$$\Delta\alpha = \alpha * \sqrt{\left(\frac{\Delta CL_{CH_3O_2}}{CL_{CH_3O_2}}\right)^2 + \left(\frac{\Delta CL_{HO_2}}{CL_{HO_2}}\right)^2} \quad (4.4.2.7).$$

Fig. 4.4.2.4 compares the experimental and simulated conversion efficiency.

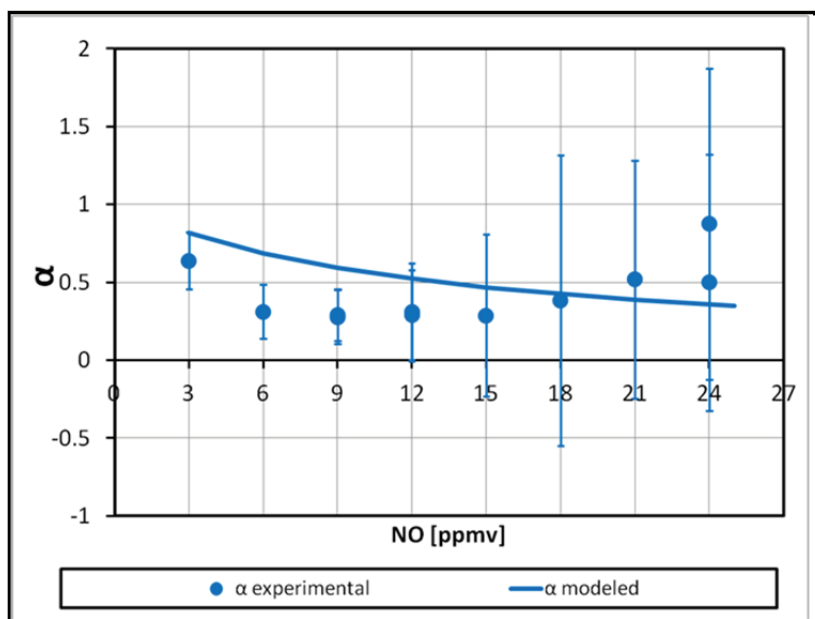


Fig. 4.4.2.4 Variations of the conversion efficiency CH_3O_2 into HO_2 with NO .

In conclusion, the experimental results demonstrated that the conversion efficiency of CH_3O_2 into HO_2 decreases with NO and a partial separation between CH_3O_2 and HO_2 occurs in the PeRCA reactor which is reflected in the obtained CL .

Based on the simulation results and the experimental research in a laboratory, the PeRCA instrument consisting of 2 glass reactors for the separated measurement of RO_2 and HO_2 for ground based measurement with the modes switched between signal and background (see section 2.2.3) is proposed. The measurements will be run simultaneously at two different NO mixing ratios (6 ppmv NO and 12 ppmv NO) so that RO_2 will be partially removed from RO_2^* . This technique is not sensitive to all RO_2 species equally. As the CL_{RO_2} CL for CH_3O_2 , the most abundant organic radicals, is assumed and this methodology will lead to:

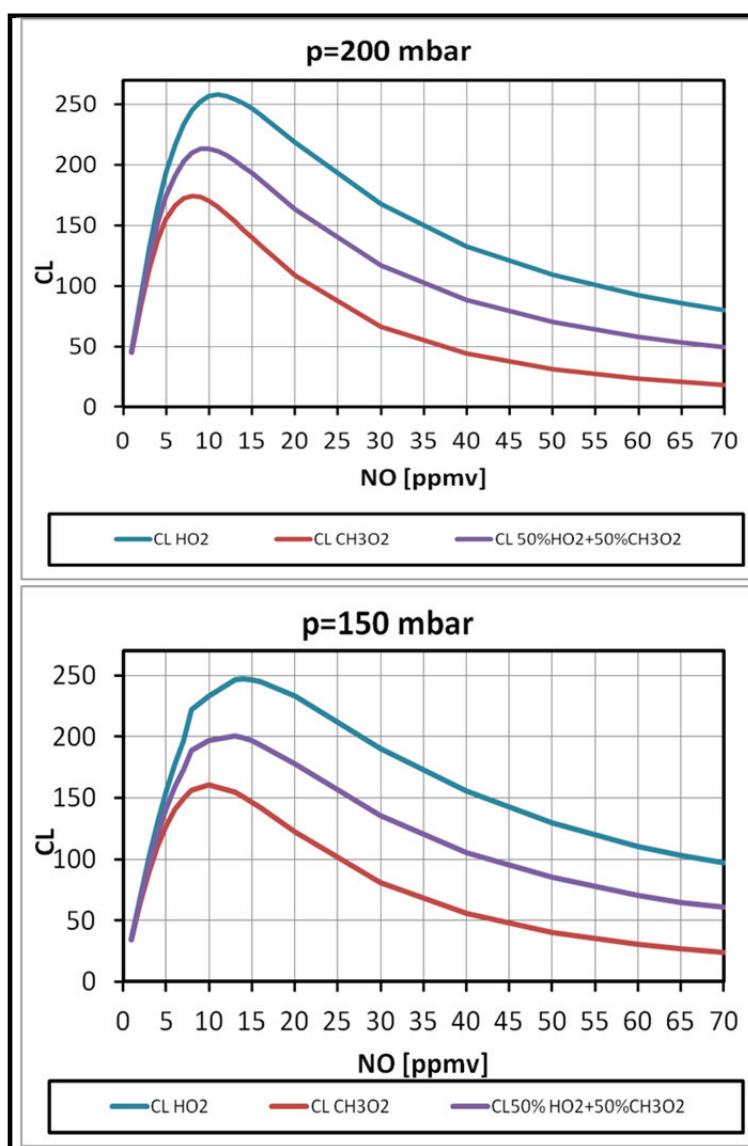
- 3% underestimation of HO_2 and 9% underestimation of RO_2 in the urban environment with the radical mixture: 64% HO_2 +18% CH_3O_2 +18% t- $\text{C}_4\text{H}_9\text{O}_2$,
- 21% overestimation of HO_2 and 23% underestimation of RO_2 in the forest environment with the radical mixture: 54% HO_2 +23% CH_3O_2 +23%isoprene radical.

4.4.3 Applications for airborne measurements

For airborne measurement of peroxy radicals the inlet is kept at constant pressure below the ambient pressure to obtain the stable sampling and detection conditions independently to ambient pressure. To investigate the effect of the pressure on the CL a series

of simulations was made with the following pressure conditions: 100 mbar, 150 mbar, 200 mbar and considering the pressure dependency of the reactions (see section 2.2.3).

Isoprene and other VOC that have local sources close to the ground are short lived species (residence time around 30 minutes) and are removed from the atmosphere via the chemical reactions. Therefore, the organic radicals originating from them are not expected at the flight altitudes and HO₂ and CH₃O₂ and their mixture (50%:50%) were used as representatives of the radicals present for the airborne measurements. The reactor wall losses rate coefficient k_{wHO_2} was set as 0.83 s⁻¹ and assumed pressure independent, the CH₃O₂ losses were neglected: $k_{wCH_3O_2} = 0$ s⁻¹. The results of the simulations are presented in Fig 4.4.3.1 and summarized in Appendix 3 in Tables 4.4.3.1-3.



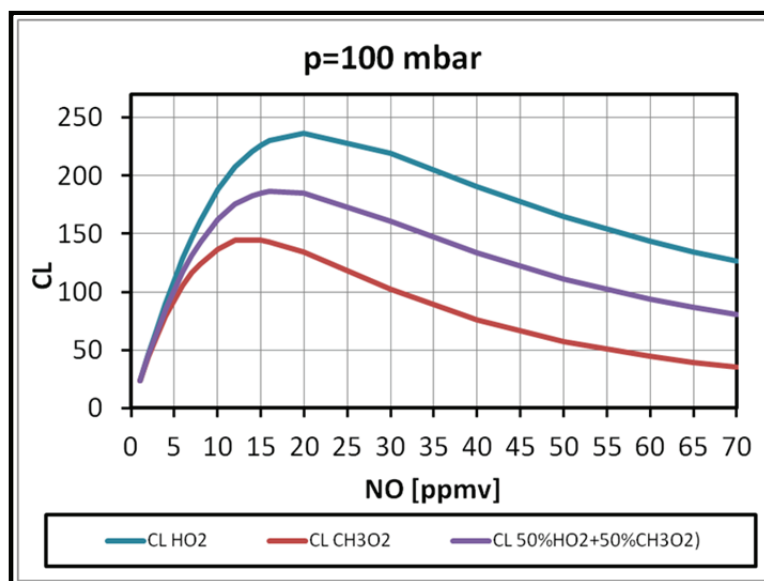


Fig. 4.4.3.1 The CL variations with NO for HO_2 , CH_3O_2 and $50\%HO_2+50\%CH_3O_2$ at different pressure conditions.

As expected from the known chemistry a decrease of the pressure leads to a decrease in the CL . It results mainly from the pressure dependence of the reactions (2.1.11-12) in the amplification cycle; the reaction rate decreases with the pressure. The NO mixing ratio for which the highest value of the CL is obtained changes with the pressure, e.g., for the mixture of radicals $50\%HO_2+50\%CH_3O_2$ at 200 mbar at 10 ppmv, at 100 mbar at 16 ppmv. This result demonstrates the advantage to increase NO in the reactor when measuring at low pressures to increase the CL value.

The CL was simulated at 100 mbar for the radical mixtures containing different proportions of CH_3O_2 and HO_2 . This enables to estimate an error in RO_2^* determination for the standard PerCA measurements, shown in Fig. 4.4.3.2, similarly as in Section 4.4.1.2. According to the results CH_3O_2 in the sampled air may increase the uncertainty of the RO_2^* determination and leads to up to 10% underestimation of $[RO_2^*]$ and most likely between 3-5%. Using the $CL_{50\%HO_2+50\%CH_3O_2}$ instead of the CL_{HO_2} does not lead to a significant reduction of the $[RO_2^*]$ uncertainty.

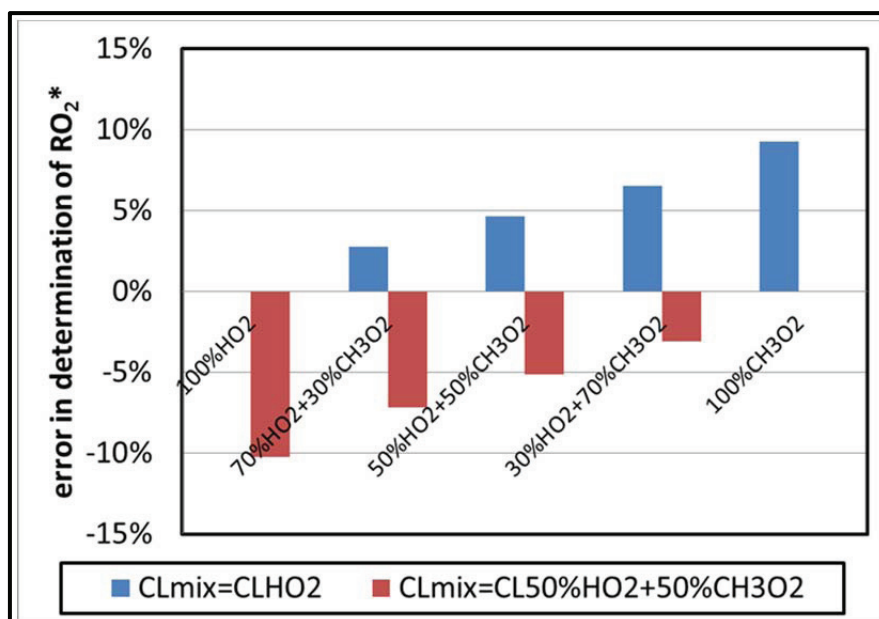


Fig. 4.4.3.2 Error in determination of RO_2^* $\left(100\% * \frac{CL_{HO_2} - CL_{mix}}{CL_{HO_2}}\right)$ with the assumption $CL_{mix} = CL_{HO_2}$, and $CL_{mix} = CL_{50\%HO_2+50\%CH_3O_2}$.

Similarly to the results obtained in 4.4.4.1 Section, the modeled output presented in this section confirmed that the CL obtained for HO_2 and CH_3O_2 differ at similar NO mixing ratio in the reactor. Thus, it is possible to determine the HO_2 and CH_3O_2 mixing ratios from measured deltas NO_2 according to formulas (4.4.3) and (4.4.4) provided the CL_{1-4} are known.

A complete removal of RO_2 from RO_2^* at NO exceeding 250 ppmv results in a significant reduction of the CL owing to the terminating reaction 2.2.2.2: $OH + NO + M \rightarrow HONO + M$. Therefore, the NO mixing ratio in the reactor should be optimized to remove considerably RO_2 , e.g., below 71%, and to obtain the measureable $CL_{CH_3O_2}$, e.g., 39, at 65 ppmv NO at 100 mbar. For airborne measurements the control of the pressure in the sampling system is essential and the regulation can be obtained by implementation of the common pre-reactor nozzle kept at constant pressure from where the air is sampled to the reactors (Kartal et. al., 2009). For the reactor in such a set-up, the CL is an effective CL (eCL) that is lower than the CL measured for the single reactor at the same pressure, as only the radicals that are not lost at the pre-reactor nozzle surface can be converted and amplified into NO_2 in the reactor. The losses in the pre-reactor nozzle prior to the addition of CO and NO are significant even up to 90% (Kartal et. al., 2009). Based on this loss, the estimated eCL obtained from $CL_{CH_3O_2}=39$ will be insufficient to measure the radicals and thus significant removal of CH_3O_2 as an approach to speciate radicals is unsuitable.

The simulated $CL_{CH_3O_2}$ evolution with time at 100 mbar is presented in Fig. 4.4.3.3.

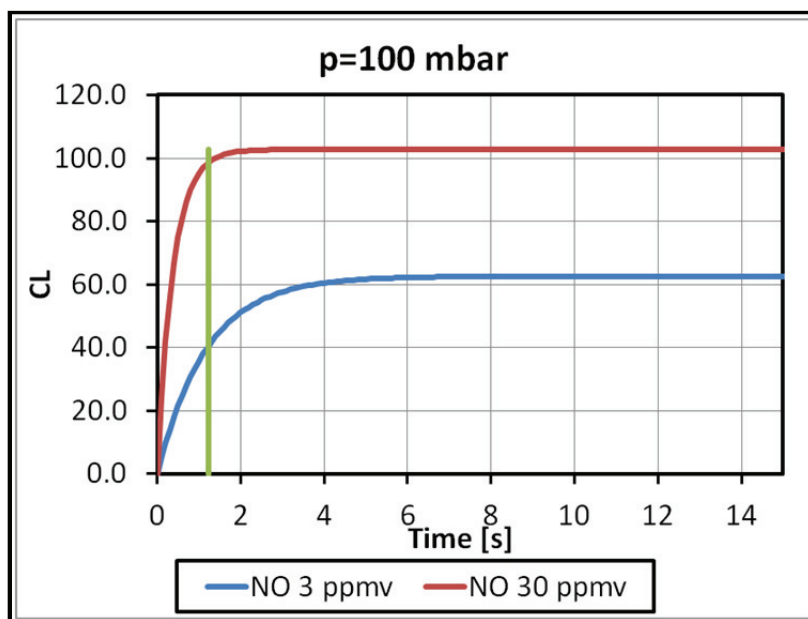


Fig. 4.4.3.3 The temporal evolution of the $CL_{CH_3O_2}$ at 100 mbar, as a green line indicated the residence time of air in the reactor (1.2 s)

For the k_{wHO_2} considered to be constant all over the pressure ranges, at 100 mbar the chain reaction is not completed in the reactor. At NO 3 ppmv the CL could be increased by around 23% if the retention time were 1.8 instead of 1.2 sec. However, to obtain the maximum CL 6s is required. This result demonstrates the advantage to increase the retention time in the reactor when measuring at low pressures to optimize the CL value.

For airborne measurements peroxy radicals, a three-channel instrument is proposed consisting of three separated reactors coupled with three detectors which concurrently work out of phase: two measuring simultaneously at two different NO mixing ratios at the signal mode, e.g., at 100 mbar 10 and 16 ppmv, while the third remains in the background mode at 10 ppmv of NO. Such measurements will allow observations of quickly changing background signal during airborne sampling and thus an increase of the sensitivity and accuracy of the radical determination will be obtained (Kartal, D., et al., 2010; Green, T. J, 2006; Brookes, D., 2009). An additional importance is development of new NO_2 detector suitable for such measurements. Commonly used luminol detector cannot be operated at pressures below 200 mbar due to luminol flow instabilities and at the NO mixing ratio as high as 10 ppmv owing the sensitivity decrease with NO.

5. Summary and conclusions

This chapter brings together the results and conclusions drawn from it. The goal is to provide the link between the various threads of work, propose more general conclusions and identify the areas requiring further research and development.

In this work I fulfilled the aim to design an optimum sampling system for the airborne measurement of peroxy radicals based on the PeRCA technique. For this purpose the HALO and DUALER 2 inlets, comprising the reactors and the pre-reactor nozzle, were developed and characterized in the laboratory experiments. Two important features were included based on the previous experience of the TROLAS group with PeRCA on different platforms:

- The concurrent measurements of the radical and background signal in two identical separated reactor-detector channels, to eliminate an effect of sudden variations in the background air during the airborne measurements.
- The pressure stabilisation of the instrument achieved by an introduction of a common pre-reactor nozzle where the pressure is controlled and kept constant to account for the changes in the radical sampling and detecting conditions.

The inlets, HALO and DUALER 2, were designed within this work and manufactured at the mechanical workshop of the University of Bremen.

The first focus was the laboratory characterization of the flow resistance in the PeRCA set-up. The activities carried out to fulfill this aim were as follows:

- Development of the software in Labview to operate the pressure regulator and the flow controllers.
- Investigation of the performance of the set-up at the pressure under the expected flight conditions, by using a pressure chamber whose pressure was regulated between 200-1013 mbar.
- Identification and quantification of the contribution of the main elements in the set-up imposing a restriction against the sampling flow. The Hagen-Poiseuille law was used for the interpretation of the experimental results.

For 1 l/min set sampling flow through the reactor and 100-200 mbar set pressure in the pre-reactor nozzle and kept below the external pressure the following results were obtained:

- The resistance of the inlet sampling orifice with a diameter of $\varnothing 1$ mm is 3 times higher than the $\varnothing 1.5$ mm orifice. The diameter of the sampling orifice is not the factor limiting

the amount of air to be sampled through the reactor but the overall resistance of the components of the measurement set-up (i.e., tubes, flow controllers, gas scrubbers). Thus, increasing of the orifice diameter will not increment significantly the sampling flow but will lead to difficulties in the pressure regulation in the pre-reactor nozzle.

- The CO scrubber was identified as a critical resistance element in the set-up which prevents effective sampling because of the resistance created by the material inside and the grid.
- The CEAS (Cavity Enhanced Absorption Spectroscopy) detector shows similar hydraulic resistance to the luminol detector and its implementation will not change the main hydraulic properties of the instrument.
- The relative resistances of the components were quantified on the basis of the relation between the pressure drop within the set-up and the total pressure difference between the pre-reactor nozzle and the pump inlet ($\Delta p=145$ mbar):
 - Reactor, detector, tubes, luminol trap: 21%,
 - Flow controller: 69%,
 - Scrubbers: 10%.

The 10% contribution of the scrubbers is however crucial concerning the specification by Bronkhorst that the flow controllers can regulate flow if the pressure difference between the inlet and outlet of the flow controller is $\Delta p=100$ mbar.

- The flow and the pressure conditions in the set-up are optimized when:
 - Diameter of the sampling orifice = 1.2 mm,
 - Length of the reactor entry = 14 mm,
 - Diameter of the orifice of the reactor entry = 4 mm,
 - Diameter of the tube used as a CO scrubber = 25 mm.

The second focus was a comprehensive study of the removal processes of peroxy radicals by using different inlet surfaces, and geometries, and radical composition.

The activities carried out to fulfill these objectives were following:

- Identification of the parameters in the inlet geometry playing a role in radical removal processes. For this purpose calibrations were performed and the interpretation was based on the obtained experimentally effective chain length (eCL) for different geometries of the inlet sampling orifice, pre-reactor nozzle, and reactor entry.

- Comparison of the losses of different radicals: HO₂ and CH₃O₂, the main peroxy radicals to be expected in the ambient measurements, on the reactor walls. For this purpose HO₂ and a mixture of HO₂ and CH₃O₂ (50%:50%) were generated.
- Investigation of the losses of HO₂ and CH₃O₂ on different surfaces: reactor walls coated by Teflon and amorphous silicon.

Concluding remarks of this part of the work are:

- Reduction of the radical losses is related to
 - a) An increase of the inlet sampling orifice which can be attributed to the corresponding decrease of the S/V ratio (surface to volume) and to the corresponding decrease of the retention time related to higher flow through the orifice with bigger diameter.
 - b) A decrease of the reactor entry orifice which can be caused by the corresponding decrease of the retention time as a consequence of the corresponding higher velocity of gas through smaller orifice and quicker transport of the radicals to the conversion and amplification area.
- Removal processes are more effective
 - a) In the conical entry than in the interior of the pre-reactor nozzle by 50%±8%.
 - b) When increasing the length of the reactor entry.
- The obtained radical losses coefficients for HO₂ and CH₃O₂ are not significantly different in the modified reactor (0.24±0.10 and 0.22±0.12 s⁻¹, respectively). It can be attributed to higher diffusion time of the radicals to the reactor walls than the retention time ($\tau_d > \tau_r$). Therefore, the radicals pass through the removal zone before they can reach the reactor walls and could be lost on them with different efficiency.
- The difference in the wall loss rate coefficient k_{wHO_2} determined for the DUALER and DUALER 2 reactors ($k_{HO_2}^{DUALER} = 1.5 \text{ s}^{-1}$ and $k_{HO_2}^{DUALER 2} = 0.24 \pm 0.1 \text{ s}^{-1}$) cannot be explained on the basis of their dimensions and retention times. The discrepancy can be attributed to overestimation of the retention time and/or losses in the reactor entry.
- The radical removal on quartz and Teflon coated surfaces is similar.

The third focus was the investigation of the effect of the wall losses and the pressure conditions on the conversion of peroxy radicals in the PerCA reactor via numerical simulations. The activities carried out to fulfill this aim were as follows:

- Development of a box model in Kintecus V4 compiler to simulate the main chemical reactions and physical processes (wall losses) in the PerCA reactor.

- Simulation of the chain length CL variations with NO concentration at different pressures for different radicals (HO_2 and organic: CH_3O_2 , $t-C_4H_9O_2$ and isoprene originating radicals and their mixtures). Analysis of these results for the standard PerCA measurements at 3 ppmv NO used during the campaigns (Kartal et. al., 2009).
- Comparison of the simulated CL ($CL_{simulated}$) with the experimental data (CL_{exp}) obtained with the glass reactor.

Concluding remarks based on the simulation results are the following:

- CH_3O_2 losses on the reactors walls after the addition of NO+CO and prior to their conversion into HO_2 are insignificant as CH_3O_2 is rapidly transformed into HO_2 in the reaction with NO. As this reaction is pressure independent this is also the case for all pressure conditions.
- The model developed in Kintecus V4 is able to reproduce reasonably the experimental results of the CL variations of HO_2 and a mixture of $HO_2+CH_3O_2$ (50%:50%) for the glass reactor when the losses in the reactor entry are included in the model (16% for HO_2 and 15% for CH_3O_2). The simulated CL values agree very well with the experimental output above 12 ppmv NO. For HO_2 below 6 ppmv NO the CL_{exp} is approximately 8% higher than the $CL_{simulated}$ and for a mixture of radicals between 3-6 ppmv NO the CL_{exp} is 17% lower than the $CL_{simulated}$. These differences can be related to the instrumental noise and instability, the uncertainties of the reaction rate coefficient, possibly incomplete mechanism of the conversion and amplification.
- In the case of the radicals such as $t-C_4H_9O_2$ (converted into CH_3O_2 and then into HO_2) the CL value decreases strongly with an increase of the NO mixing ratio in comparison to HO_2 , as the intermediate oxy radical, $t-C_4H_9O$, cannot react with O_2 because it does not possess a hydrogen atom in the position α to the radical centre. Therefore, at the standard measurement conditions, i.e., 3 ppmv NO, underestimation of RO_2^* abundance comprising $t-C_4H_9O_2$ is predicted resulting from the $CL_{t-C_4H_9O_2}$ being 80% lower than the CL_{HO_2} used to calculate the RO_2^* abundance ($[RO_2^*]$).
- Presence of organic radicals in the sampled air increases the uncertainty of the RO_2^* determination for the standard PerCA at 3 ppmv NO. Therefore, using the CL_{HO_2} to calculate RO_2^* abundance leads to the following underestimation of $[RO_2^*]$ for ground based measurements:
 - 6% in the remote, unpolluted areas,

- 7% in the urban areas,
- 17% in the forest areas.

For airborne measurement it leads to up to 10% underestimation of $[RO_2^*]$ and most likely between 3-5%.

It is proposed for ground based measurements using the $CL_{50\%HO_2+50\%CH_3O_2}$ to determine RO_2^* abundance instead of the standard CL_{HO_2} to decrease the uncertainty of RO_2^* determination. It will lead to the following decrease of the uncertainty of $[RO_2^*]$:

- 4% overestimation in the remote, unpolluted areas,
 - 3% overestimation in the urban areas,
 - 9% underestimation in the forest areas.
- The CL value depends on the NO mixing ratio and the pressure conditions as expected from known chemistry. The CL value increases with the NO mixing ratio and reaches a maximum at 3 ppmv NO at 1013 mbar; above 3 ppmv NO it is observed that there is a reduction of the CL . Lower values of the CL with a pressure decrease are obtained as amplification reactions are pressure dependent. The NO mixing ratio at which the CL reaches a maximum value is pressure dependent, e.g., for a mixture of radicals $HO_2+CH_3O_2$ (50%:50%) at 200 mbar at 10 ppmv, at 100 mbar at 16 ppmv.

The fourth focus was the design and characterization of an inlet for the airborne measurement of peroxy radicals on board the HALO aircraft on the basis of existing experience and the information obtained in the investigation above:

- A three channel prototype of the inlet was developed for measurements of the radicals (two for total sum and organic radicals) and one for the background signal, which can be disassembled into the basic components. However, such an inlet could not be certified. The safety regulations, such as a reduction of the bird strike effect, related to the physical constraints like shape, size, orientation and position, defined the shape and size of the HALO inlet.
- Based on the HALO constraints, the final dimensions of the HALO inlet were settled comprising a rectangular pre-reactor nozzle of dimensions 126x44mm welded to two reactors with an inner diameter of ID=17mm.
- For the pressure regulation in the pre-reactor nozzle two lines ($\frac{1}{2}$ " tubes) were symmetrically placed. The pressure sensor was installed nearby the pre-reactor nozzle to determine accurately the pressure in the sampling system.

- A minimum height of the reactor entry to suppress interference between the reactors is 14 mm. This interference occurs because the sampled air mixed with the reagents CO and NO move backwards to the pre-reactor nozzle through the reactor entry and this process is enhanced by the pressure regulation. Separation of the reactors can also be achieved by an introduction of a 10 mm long cylindrical protrusion inside the reactor.
- The *eCL* value decreases with a reduction of the pressure in the inlet. It can be related to a decrease of efficiency of the radical conversion owing to pressure dependence of the amplification reactions. The chemical losses, competing with the amplification reactions, show also pressure dependence and are slower with decreasing pressure. Therefore, the effect of the wall losses in termination of the chain reaction is expected to be more significant at lower pressure.
- An increase of the noise of the NO₂ luminol detector signal is related to an increase of the inlet sampling orifice. It leads further to an increase of the *eCL* uncertainty (ΔeCL) and consequently to a decrease of the accuracy of determination of the RO₂^{*} mixing ratio.
- The radical losses are reduced by decreasing the diameter of the reactor entry which is reflected in the obtained *eCL* value.

In the fifth focus the capability of the PerCA technique to speciate HO₂ and RO₂ from the total sum of radicals RO₂^{*} was investigated. Two approaches were proposed:

- a) Removal of HO₂ by the heterogeneous losses on the surface prior to an introduction of the radicals to the amplification and conversion area in the reactor.
- b) Partial removal of organic peroxy radicals by the chemical reaction with NO.

For the approach a) the following activities were carried out:

- Construction of a modified reactor to measure solely RO₂ by varying a position of the addition point of NO and CO. HO₂ radicals were expected to be partially eliminated while passing through the reactor walls.
- Determination of the removal efficiency of the radicals based on the *CL* values determined for the modified and the reference reactors for HO₂ and a mixture of HO₂+CH₃O₂ (50%:50%).

The related conclusions are:

- No differences in removal efficiency on the reactor walls were observed for HO₂ and CH₃O₂. It can be caused by higher diffusion time of the radicals to the reactor walls than

the retention time ($\tau_d > \tau_r$) and therefore the radicals pass through the removal zone before they can reach the reactor walls and could be lost on them with a different efficiency. Therefore, this set-up does not allow separating HO₂ from RO₂. New concepts for a novel reactor with a diameter of Ø5 mm and a length of L=50 cm or a reactor with an annular denuder for which $\tau_d < \tau_r$ are proposed for the selective measurements of concentrations of HO₂ and RO₂.

In the approach b) the following activities were carried out:

- Investigation of the effect of NO concentration on a removal of different organic radicals (CH₃O₂, t-C₄H₉O₂, isoprene originating radicals) by numerical simulations with the chemical box model developed in Kintecus V4 as already investigated within the third focus described above.
- Comparison with the existing results from the laboratory experiments with the glass reactor for HO₂ and a mixture of HO₂+CH₃O₂ (50%:50%) and for the NO mixing ratios between 3 and 24 ppmv.

The related conclusions are as follows:

- Bases on the results of simulations and experiments, for the identical NO mixing ratios in the reactor the CL_{HO_2} and $CL_{CH_3O_2}$ are different, and the ratio $\frac{CL_{CH_3O_2}}{CL_{HO_2}}$ varies with the NO mixing ratio as expected from the known chemistry. Thus, by using different NO mixing ratios the radicals like methyl peroxy radical can be determined separately from HO₂ in a radical mixture when the CL_{HO_2} and CL_{RO_2} are known. This is also valid for the radicals originating from the precursors C₂-C₅ alkanes, i.e., NMHC having between two and five carbon atoms for which oxy radical (RO) reacts with O₂.
- For isoprene-like radicals (having isoprene and unsaturated hydrocarbons as organic precursors) with the constant ratio $\frac{CL_{RO_2}}{CL_{HO_2}}$ at different NO mixing ratios, RO₂ cannot be separated from HO₂ by varying the NO mixing ratios in the reactor.
- A PeRCA instrument consisting of 2 glass reactors for the selective measurement of RO₂ and HO₂ for ground based measurement is suggested. The measurements will be run concurrently with switching between signal and background mode at two different NO mixing ratios (6 and 12 ppmv NO). The technique is not sensitive to all RO₂ species equally. As CL_{RO_2} the CL for CH₃O₂, the most abundant organic radicals, is assumed and this methodology will lead to:

- 3% underestimation of HO₂ and 9% underestimation of RO₂ in an urban environment,
- 21% overestimation of HO₂ and 23% underestimation of RO₂ in a forest environment.
- Using different NO mixing ratios is a potential improvement for the deployment of PeRCA for airborne measurements in the upper troposphere where CH₃O₂ is the main RO₂ expected. For airborne selective measurements of HO₂ and CH₃O₂, a three-channel instrument is proposed consisting of three separated reactors coupled with three detectors which concurrently work out of phase: two measuring simultaneously at two different NO mixing ratios at the signal mode (e.g., at 100 mbar 10 and 16 ppmv), while the third remains in the background mode (e.g., 10 ppmv).

Clearly, the laboratory studies are required to generalise these results to non-methane radicals together with the development of the instrument and testing its performance in the field campaigns.

In the sixth focus the optimal set-up and the measurement conditions for the deployment on board of the HALO aircraft are recommended on the basis of the interpretation of the results obtained. These are the following:

- Geometry and dimensions of all the components should be designed to fit to the pylon:
 - Shape of the pre-reactor nozzle: rectangular,
 - Size of the pre-reactor nozzle: 126x44 mm,
 - Diameter of two reactors: 17 mm,
 - Length of the reactors within the pylon: 430 mm,
 - Shape of the sampling entry: conical,
 - Height of the sampling entry: 20 mm.
- In order to reduce the hydraulic resistance within the set-up and to enable to keep the pressure in the pre-reactor nozzle at 100 mbar and to sample the flow 1l/min the following points shall be taken into account:
 - Diameter of the sampling orifice: 1.2 mm.
 - Sufficient size of the flow controller valve (FC valve) so that the flow can be controlled at the pressure difference between the inlet and the outlet of the FC below 100 mbar.
 - Diameter of the tube of the CO scrubber: 25 mm. The adaptation of the new scrubber and its fixing elements has to be carefully optimized which is related to a series of constraints required for the airborne measurement such as the limitations of heating power demand and weight.

- With the components of the set-up available at present the following pressure (p) can be kept in the pre-reactor nozzle and the corresponding flow (Q) through the reactor can be obtained at external pressures under the expected flight conditions:
 - $p=150$ mbar and $Q=1000$ ml/min,
 - $p=120$ mbar and $Q=700$ ml/min,
 - $p=100$ mbar and $Q=600$ ml/min.
- In order to minimize the radical losses on the inlet surfaces and to optimize the eCL value and the uncertainty ΔeCL , the following features of the inlet are recommended:
 - Diameter of the inlet sampling orifice: 1.2 mm,
 - Diameter of the reactor entry: 4 mm,
 - Length of the reactor entry: 15 mm,
 - Quartz coating of the surfaces. In contrast to Teflon, quartz coated components can be conveniently modified by welding.
- In order to optimize the CL value when measuring at low pressures the following points shall be taken into account:
 - An increase of the retention time in the reactor by a decrease of the sampling flow or an increase of the reactor length.
 - An increase of the NO mixing ratio above the standard 3 ppmv. However, it will lead to a decrease in the luminol detector sensitivity. Therefore, the implementation of another type of NO₂ detector is recommended for such measurements.

This work contributed to the development, optimization and characterization of the sampling system for peroxy radicals based on the PerCA technique for the airborne platforms. The main scientific output of the present work is planned to be summarised in a scientific publication.

Appendix 1

FLOW-BUS

During installation of the FLOW-BUS the device (flow controller, pressure regulator) is obtaining a node number in the FLOW-BUS which is kept in the memory of the device and the FLOW-BUS system is established. After disconnecting, the devices can be connected via cables in a random way but with the rules according to the scheme by Bronkhorst (i.e., first module on the bus needs the bus begin-terminator and the last instrument needs bus-end terminator). Then the power is switched on and the FLOW-BUS still is established.

The communication of the FLOW-BUS system with the computer was performed by the FLOW-BUS DDE server allowing data exchange with Microsoft Windows applications. Reading/changing parameter values via FLOWDDE is performed by a different interface to the instrument e.g., application in LabView and there is only need of:

- topic, used for channel number of the device: 'C(X)', equivalent to node number obtained during the installation to the FLOW-BUS (see Fig. 1 and 2),
- item, used for parameter number: 'P(Y)', e.g., P(8) for reading the measured value as the amount of mass flow or pressure (see Fig. 1).

The digital output measured values are presented as an unsigned integer in the range of 0-32000 and for signal 0-100% where 100% corresponds to the maximum range of the device. Thus, the measured value can be calculated:

$$\text{Measured value} = \frac{\text{digital output} \cdot \text{max. range}}{32000} \quad (1).$$

- P(9) for setting the value as the amount of mass flow or pressure and setpoint is limited between 0-100% (see Fig. 2). Thus, the setpoint value is given as:

$$\text{Digital setpoint} = \frac{\text{Setpoint} \cdot 32000}{\text{max. range}} \quad (2).$$

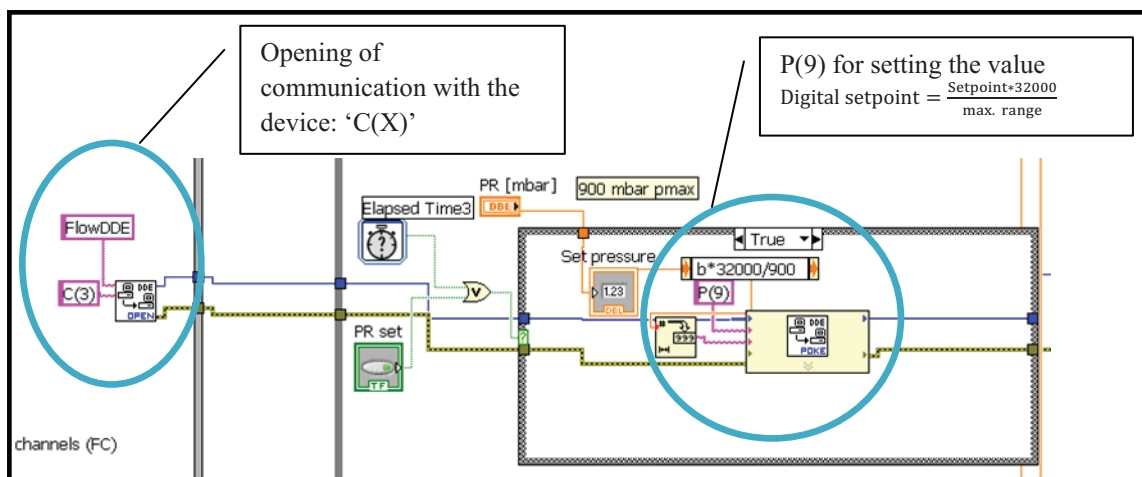


Fig. 1 View of Labview Block Diagram for setting the value of device.

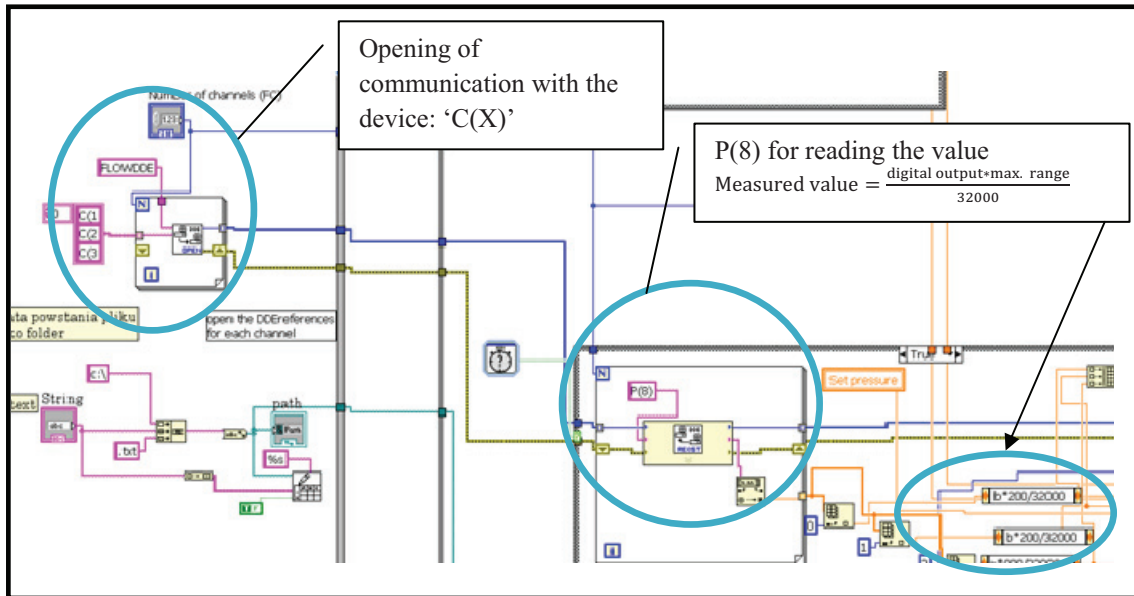


Fig. 2 View of Labview Block Diagram for reading the value of device.

Appendix 2

The eCL for the HALO inlet

1.5 mm						
Pressure at pre-reactor nozzle [mbar]	Reactor 1			Reactor 2		
	CL	$\Delta CL/CL$ [%]	$\Delta CL/CL$	CL	$\Delta CL/CL$ [%]	$\Delta CL/CL$
900	101.4	11%	11.2	104.4	10%	10.5
500	102.4	12%	12.3	91.4	13%	11.7
300	94.7	25%	23.8	75.2	28%	21.1
1.2 mm non-coated						
Pressure at pre-reactor nozzle [mbar]	Reactor 1			Reactor 2		
	CL	$\Delta CL/CL$ [%]	$\Delta CL/CL$	CL	$\Delta CL/CL$ [%]	$\Delta CL/CL$
900	64.2	12%	7.7	57.6	11%	6.3
500	55.0	13%	7.2	49.1	9%	4.4
300	55.2	15%	8.3	43.6	14%	6.1
1.2 mm coated						
Pressure at pre-reactor nozzle [mbar]	Reactor 1			Reactor 2		
	CL	$\Delta CL/CL$ [%]	$\Delta CL/CL$	CL	$\Delta CL/CL$ [%]	$\Delta CL/CL$
900	103.1	14%	14.4	107.1	12%	12.9
500	120.1	9%	10.8	101.2	9%	9.1
300	100.1	12%	12.7	79.3	11%	9.0
1 mm						
Pressure at pre-reactor nozzle [mbar]	Reactor 1			Reactor 2		
	CL	$\Delta CL/CL$ [%]	$\Delta CL/CL$	CL	$\Delta CL/CL$ [%]	$\Delta CL/CL$
900	63.6	13%	8.3	64.6	9%	5.8
500	81.7	9%	7.4	72.8	9%	5.8
300	83.6	10%	8.4	65.1	9%	5.8
500 8L/min	80.7	10%	8.3	73.5	9%	6.3
500 10L/min	82.7	11%	9.2	76.8	9%	6.6

Table 1. The eCL obtained with different inlet sampling orifices: Ø1.5 and Ø1.2, Ø1 mm.

Insert number Pre-reactor nozzle pressure	Reactor 1		Reactor 2	
	CL	$\Delta CL/CL$	CL	$\Delta CL/CL$
First teflon insert 900 mbar	28.8	6.6	31.2	6.2
First teflon insert 500 mbar	30.6	5.2	35.2	5.6
First teflon insert 300 mbar	34.8	7.3	38.6	7.3
Second teflon insert 900 mbar	38.4	7.9	36.3	7.0
Second teflon insert 500 mbar	33.4	4.8	29.8	3.6
Second teflon insert 300 mbar	35.4	7.0	30.1	4.7
Third teflon insert 900 mbar	29.9	6.0	29.6	5.0
Third teflon insert 500 mbar	33.5	4.0	31.0	3.7
Third teflon insert 300 mbar	39.9	5.6	37.1	4.8
Fourth teflon insert 900 mbar	49.7	5.0	47.0	4.8
Fourth teflon insert 500 mbar	53.3	5.4	48.8	5.4
Fourth teflon insert 300 mbar	56.5	6.3	52.9	5.3
Fifth teflon insert 900 mbar	35.8	6.4	35.0	6.0
Fifth teflon insert 500 mbar	37.0	5.2	31.6	4.4
Fifth teflon insert 300 mbar	41.4	7.4	38.9	7.0
Sixth teflon insert 900 mbar	34.4	6.2	35.6	6.0
Sixth teflon insert 500 mbar	41.1	6.2	41.8	5.4
Sixth teflon insert 300 mbar	42.8	9.0	44.7	7.6
Seventh teflon insert 900 mbar	37.0	7.8	31.6	5.4
Seventh teflon insert 500 mbar	40.3	6.8	38.4	5.8
Seventh teflon insert 300 mbar	37.6	7.1	36.7	5.9

Table 2. The eCL obtained with different reactor entries. Description in Table 4.2.2.1.

Appendix 3 The speciation

NO [ppmv]	CL_{HO_2}	$CL_{CH_3O_2}$	Ratio $\frac{CL_{RO_2}}{CL_{HO_2}}$	$CL_{50\%HO_2+50\%CH_3O_2}$
1	217	202	0.93	210
2	351	305	0.87	328
3	400	325	0.81	363
4	399	305	0.77	352
5	376	272	0.72	324
6	347	238	0.69	293
7	319	208	0.65	263
8	293	181	0.62	237
9	269	159	0.59	214
10	248	141	0.57	194
11	229	125	0.54	177
12	213	112	0.52	163
13	199	100	0.50	150
14	187	91	0.48	139
15	176	82	0.47	129
20	135	54	0.40	94
25	109	38	0.35	74
30	92	29	0.31	60
40	69	18	0.26	44
50	56	13	0.22	34
80	35	6	0.17	21
90	32	5	0.16	18
150	19	3	0.13	11
250	12	2	0.13	7
321	10	1	0.15	6
400	8	1	0.15	5

Table 4.4.1.1 Simulation results at $p=1013$ mbar of the CL variations with NO for HO_2 , CH_3O_2 and $50\%HO_2+50\%CH_3O_2$ mixture.

NO [ppmv]	CL _{HO2}	CL _{t-C4H9O2}	Ratio $\frac{CL_{RO_2}}{CL_{HO_2}}$	CL _{50% HO2+50%t-C4H9O2}
1	217	101	0.47	210
2	351	107	0.31	328
3	400	89	0.22	363
4	399	68	0.17	352
5	376	52	0.14	324
6	347	39	0.11	293
7	319	31	0.10	263
8	293	24	0.08	237
9	269	19	0.07	214
10	248	16	0.06	194
11	229	13	0.06	177
12	213	11	0.05	163
13	199	9	0.05	150
14	187	8	0.04	139
15	176	7	0.04	129
20	135	4	0.03	94
25	109	2	0.02	56
30	92	2	0.02	47

Table 4.4.1.3 Simulation results at p=1013 mbar of the CL variations with NO for HO₂, t-C₄H₉O₂ and 50%HO₂+50% t-C₄H₉O₂ mixture.

NO [ppmv]	CL _{HO2}	CL _{R1O2}	Ratio $\frac{CL_{RO_2}}{CL_{HO_2}}$	CL _{50% HO2+50%R1O2}
1	217	196	0.90	206
2	351	317	0.90	334
3	400	361	0.90	380
4	399	360	0.90	379
5	376	340	0.90	358
6	347	313	0.90	330
7	319	287	0.90	303
8	293	263	0.90	278
9	269	242	0.90	255
10	248	223	0.90	235
11	229	206	0.90	218
12	213	192	0.90	203
13	199	179	0.90	189
14	187	168	0.90	177
15	176	158	0.90	167
20	135	121	0.90	128
25	109	98	0.90	104
30	92	83	0.90	87
40	69	62	0.90	66
50	56	50	0.90	53
80	35	32	0.90	34
90	32	28	0.90	30
150	19	17	0.90	18
250	12	11	0.90	11

Table 4.4.1.5 Simulation results at p=1013 mbar of the CL variations with NO for HO₂, isoprene radicals, 50%HO₂+50% isoprene radicals

NO [ppmv]	CL _{HO2}	CL _{CH3O2}	CL _{isoprene radical}	CL _{t-C4H9O2}	CL _{50% HO2+50% CH3O2}	CL _{70% HO2+30% CH3O2}	CL _{70%*0.77HO2+30%*0.77CH3O2+0.3*0.77isoprene}	CL _{64% HO2+18%CH3O2+18*t-C4H9O2}
1	217	202	196	101	210	212	209	193
3	400	325	361	89	363	377	374	330
4	399	305	360	68	352	371	368	322
5	376	272	340	52	324	345	344	299
6	347	238	313	39	293	315	314	272
7	319	208	287	31	263	285	286	247
8	293	181	263	24	237	259	260	224
9	269	159	242	19	214	236	237	204
10	248	141	223	16	194	216	217	187
11	229	125	206	13	177	198	200	172
12	213	112	192	11	162	183	185	159
13	199	100	179	9	150	170	172	147
14	187	91	168	8	139	158	160	137
15	176	82	158	7	129	148	150	128
20	135	54	121	4	94	111	113	97
25	109	38	98	2	74	88	90	77
30	92	29	83	2	60	73	75	64
40	69	18	62	2	44	54	56	48
50	56	13	50	2	34	43	45	38
80	35	6	32	2	21	27	28	24
90	32	5	28	2	18	24	25	21

Table 4.4.1.6 Simulation results at p=1013 mbar of the CL variations with NO for radical mixtures 1-3.

NO [ppmv]	CL _{HO2}	CL _{CH3O2}	Ratio $\frac{CL_{RO_2}}{CL_{HO_2}}$	CL _{50% HO2+50%CH3O2}
1	46	45	0.97	46
2	91	83	0.92	87
3	131	114	0.87	122
4	165	138	0.83	152
5	194	155	0.80	174
6	216	166	0.77	191
7	233	172	0.74	203
8	245	174	0.71	210
9	252	173	0.69	213
10	256	170	0.66	213
11	258	165	0.64	212
12	257	159	0.62	208
13	254	153	0.60	204
14	251	146	0.58	199
15	246	140	0.57	193
16	241	133	0.55	187
20	218	108	0.50	163
30	167	67	0.40	117
40	133	44	0.33	88
50	109	31	0.29	70
60	92	24	0.25	58

NO [ppmv]	CL _{HO2}	CL _{CH3O2}	Ratio $\frac{CL_{RO2}}{CL_{HO2}}$	CL _{50%HO2+50%CH3O2}
65	86	21	0.24	53
70	80	18	0.23	49
80	71	15	0.21	43
90	63	12	0.19	38
150	39	5	0.14	22

Table 4.4.3.1 Simulation results at p=200 mbar of the CL variations with NO for HO₂, CH₃O₂ and 50%HO₂+50%CH₃O₂ mixture.

NO [ppmv]	CL _{HO2}	CL _{CH3O2}	Ratio $\frac{CL_{RO2}}{CL_{HO2}}$	CL _{50%HO2+50%CH3O2}
1	35	34	0.98	35
2	69	64	0.93	66
3	101	89	0.89	95
4	130	111	0.85	120
5	156	128	0.82	142
6	178	141	0.79	159
7	197	150	0.76	173
8	222	156	0.70	189
10	233	161	0.69	197
13	246	155	0.63	201
14	247	151	0.61	199
15	247	147	0.60	197
16	245	142	0.58	194
20	233	122	0.52	178
30	191	81	0.42	136
40	156	56	0.36	106
50	130	40	0.31	85
60	111	30	0.27	71
65	103	27	0.26	65
70	97	24	0.24	61
80	85	19	0.23	52
90	76	16	0.21	46
150	47	7	0.15	27
250	29	3	0.11	16
320	20	2	0.12	11
400	18	2	0.10	10

Table 4.4.3.2 Simulation results at p=150 mbar of the CL variations with NO for HO₂, CH₃O₂ and 50%HO₂+50%CH₃O₂ mixture.

NO [ppmv]	CL _{HO2}	CL _{CH3O2}	Ratio $\frac{CL_{RO2}}{CL_{HO2}}$	CL _{50%HO2+50%CH3O2}
1	23	24	1.01	23
2	46	44	0.95	45
3	69	63	0.91	66
4	90	79	0.88	85
5	110	93	0.85	102
6	129	106	0.82	117
7	146	117	0.80	131
8	162	125	0.77	143

NO [ppmv]	CL _{HO2}	CL _{CH3O2}	Ratio $\frac{CL_{RO_2}}{CL_{HO_2}}$	CL _{50% HO2+50%CH3O2}
10	188	137	0.73	162
12	207	144	0.70	176
14	221	145	0.65	183
15	226	144	0.64	185
16	230	143	0.62	187
20	236	135	0.57	185
30	219	103	0.47	161
40	191	76	0.40	133
50	165	57	0.35	111
60	144	44	0.31	94
65	135	39	0.29	87
70	127	35	0.28	81
80	113	28	0.25	71
90	102	24	0.23	63
150	63	10	0.16	37
250	39	5	0.12	22
320	31	3	0.11	17
400	25	3	0.10	14

Table 4.4.3.3 Simulation results at p=100 mbar of CL variations with NO for HO₂, CH₃O₂ and 50%HO₂+50%CH₃O₂ mixture.

Bibliography

A

Ashbourn, S. F. M., Jenkin, M. E., Clemitshaw K. C.: Laboratory Studies of the Response of a Peroxy Radical Chemical Amplifier to HO₂ and a Series of Organic Peroxy Radicals, *Journal of Atmospheric Chemistry*, Volume 29, Issue 3, pp. 233-266, 1998.

Andrés-Hernández, M. D., Burkert, J., Reichert, L., Stöbener, D., Meyer-Arnek J., Burrows, J. P., Dickerson, R. R., and Doddridge, B.: Marine boundary layer peroxy radical chemistry during the AEROSOLS99 campaign: measurements and analysis, *J. Geophys. Res.*, 106, 20833–5 20846, doi:10.1029/2001JD900113, 2001.

Andrés-Hernández, M. D., Kartal, D., Reichert, L., Burrows, J. P., Meyer Arnek, J., Lichtenstern, M., Stock, P., and Schlager, H.: Peroxy radical observations over West Africa during AMMA 2006: photochemical activity in the outflow of convective systems, *Atmos. Chem. Phys.*, 9, 3681-3695, doi:10.5194/acp-9-3681-2009, 2009.

B

Bader G., Deuflhard P.: A Semi-Implicit Mid-Point Rule for Stiff Systems of Ordinary Differential Equations, *Numer. Math.*, 41,373-398, 1983.

Boeker E., and Van Grondelle R.: *Environmental Physics*, John Wiley & Sons, 2000, ISBN: 0471997803.

Brookes, D.: Characterisation of a PERCA instrument and measurements of peroxy radicals during the West African Monsoon 2006, Ph.D. thesis, University of Leicester, U.K., 2009.

Bruus H, *Theoretical microfluidics*, Oxford Master Series in Physics, 2008.

Burkert, J., Andrés-Hernández, M.D., Stöbener, D., Burrows, J.P., Weissenmayer, M., Kraus, A.: Peroxy radical and related trace gas measurements in the boundary layer above the Atlantic Ocean, *J. Geophys. Res.*, 106 , 6, p. 5457, 2001a.

Burkert, J., Behmann, T., Andrés Hernández, M.D., Weißenmayer, M., Perner, D., and Burrows, J.P.: Measurements of peroxy radicals in a forested area in Portugal. *Chemosphere-Global change science*, 3327-3338, 2001b.

C

Cantrell, C. A., Shetter, R. E., Lind, J.A., et al., An Improved Chemical Amplifier Technique for Peroxy Radical Measurements, *J. Geophys. Res.*, 98, 2897-28909, 1993.

Cantrell, C. A., Shetter, R. E., Gilpin, T. M., Calvert, J. G., Eisele, F. L, and Tanner, D. J.: Peroxy radical concentrations measured and calculated from trace gas measurements in the Mauna Loa Photochemistry Experiment 2, *J. Geophys. Res.*, 101, 14653-14664, 1996.

Cantrell, C.A., Edwards, G.D., Stephens, S., Mauldin, L., Kosciuch , E., Zondlo, M., and Eisele, F.: Peroxy radical observations using chemical ionization mass spectrometry during

TOPSE, *Journal of Geophysical Research*, Vol. 108, No. D6, 8371, doi: 10.1029/2002JD002715, 2003.

Clemmishaw, K., Carpenter, L., Penkett, S., and Jenkin, M.: A calibrated peroxy radical chemical amplifier for ground-based tropospheric measurements, *J. Geophys. Res.*, 102, D21, 25405-25416, 1997.

D

DeMore, W. B., Golden, D. M., Hampson, R. F., Howard, C. J., Kolb, C. E., Kurylo, M. J., Molina, M. J., Ravishankara, A. R., and Sander, S. P.: Chemical kinetics and photochemical data for use in stratospheric modeling: Evaluation number 11, JPL Publ., 94-26, 1994.

E

Edwards, G. D., C. A. Cantrell, S. Stephens, B. Hill, O. Goyea, R. E., Shetter, R. L. Mauldin III, E. Kosciuch, D. J. Tanner, and F. L. Eisele: Chemical ionization mass spectrometer instrument for the measurement of tropospheric HO₂ and RO₂, *Anal. Chem.*, 2003.

Emmerson, K. M. & Carslaw: Night-time radical chemistry during the TORCH campaign, *N. Atmospheric Environment*, 43(20), 3220-3226, 1352-2310, DOI: 10.1016/j.atmosenv.2009.03.042, 2009.

F

Fuchs, H., Hofzumahaus, A., and Holland, F.: Measurement of tropospheric RO₂ and HO₂ radicals by a laser-induced fluorescence instrument, *Rev. Sci. Instrum.*, 79, 084104, doi:10.1063/1.2968712, 2008.

Fuchs, H., Bohn, B., Hofzumahaus, A., Holland, F., Lu, K. D., Nehr, S., Rohrer, F., and Wahner A.: Detection of HO₂ by laser-induced fluorescence: calibration and interferences from RO₂ radicals, *Atmos. Meas. Tech.*, 4, 1209–1225, doi:10.5194/amt-4-1209-2011, 2011.

G

Geyer, A., Hofzumahaus, A., Holland, F., Konrad, S., Klüfel, T., Pätz, H.-W., Perner, D., Schäfer, H.-J., Volz-Thomas, A., and Platt, U.: Nighttime production of peroxy and hydroxyl radicals during the BERLIOZ campaign. Observations and modeling studies, *J. Geophys. Res.* 108(D4), 8249, doi:10.1029/2001JD000656, (PHOEBE: BERLIOZ special section), 2003.

Geyer, A., and Stutz, J.: The Vertical structure of OH-HO₂-RO₂ Chemistry in the nocturnal boundary layer: A one-dimensional study. *J. Geophys. Res.* 109, D16301, doi: 10.1029/2003JD004425, 2004.

Green, T. J., Reeves C. E., Fleming Z. L., Brough N., Rickard A. R., Bandy B. J., Monks P. S. and Penkett S. A: An improved dual channel PERCA instrument for atmospheric measurements of peroxy radicals, *J. Environ. Monit.*, 8, 530-536, DOI: 10.1039/B514630E, 2006.

Green, D. W. and Perry, R. H.: Perry's Chemical Engineers' Handbook, 8th Edition, McGraw-Hill, United States, 2400 pp., 2007.

H

Hanke, M., Uecker, J., Reiner, T., and Arnold, F., Atmospheric peroxy radicals: ROXMAS, a new mass-spectrometric methodology for speciated measurements of HO₂ and RO₂ and first results, *Int. J. Mass Spec.*, 213, 91, 2002.

Hard, T. M., O'Brien, R.J., Chan, C. Y., and Merhrabzadeh, A. A.: Tropospheric free radical determination by FAGE, *Environ. Sci. Technol.*, 18, 768, 1984.

Hastie, D.R., Weißenmayer, M., Burrows, J.P., and Harris, G.W.: Calibrated chemical amplifier for atmospheric ROx measurements, *Anal. Chem.* 63, 2048-2057, 1991.

Hayman, G.D.: Numerical Model of the Calibration Source of a PERCA Instrument, AEAT-24737/20410001/001, 1997.

Hofzumahaus, A., et al., Reply [to "Comment on 'The measurement of tropospheric OH radicals by laser-induced fluorescence spectroscopy during the POPCORN field campaign' by Hofzumahaus et al. and 'Intercomparison of tropospheric OH radical measurements by multiple folded long-path laser absorption and laser induced fluorescence' by Brauers et al."], *Geophys. Res. Lett.*, 24(23), 3039–3040, doi:10.1029/97GL02947, 1997.

Hofzumahaus, A., U. Aschmutat, M. Heßling, F. Holland, and D. H. Ehhalt, The measurement of tropospheric OH radicals by laser-induced fluorescence spectroscopy during the POPCORN Field Campaign: *Geophys. Res. Lett.*, 23(18), 2541–2544, doi:10.1029/96GL02205, 1996.

Hofzumahaus et al., 'Intercomparison of tropospheric OH radical measurements by multiple folded long-path laser absorption and laser induced fluorescence' by Brauers et al."], *Geophys. Res. Lett.*, 24(23), 3039–3040, doi:10.1029/97GL02947, 1997.

Hornbrook R. S., Crawford J. H., Edwards G. D., Goyea1 O., Mauldin R. L., Olson J. S., and Cantrell C. A.,: Measurements of tropospheric HO₂ and RO₂ by oxygen dilution modulation and chemical ionization mass spectrometry, *Atmos. Meas. Tech.*, 4, 735–756, 2011.

Kinetic measurements using flow tubes

Howard C. J.: Kinetic measurements using flow tubes, *J. Phys. Chem.*, 1979, 83 (1), pp 3–9
DOI: 10.1021/j100464a001

I

Ianni, J. C.: A Comparison of the Bader-Deuflhard and the Cash-Karp Runge-Kutta Integrators for the GRI-MECH 3.0 Model Based on the Chemical Kinetics Code Kintecus, pg.1368-1372, *Computational Fluid and Solid Mechanics 2003*, K.J. Bathe editor, Elsevier Science Ltd., Oxford, UK., 2003.

J

Jenkin, M. E., Saunder, S.M., Pilling, M.J., The tropospheric degradation of volatile organic compounds: A protocol Mechanism Development, *Atmos. Environ.*, 31, 81-104, 1997.

K

Kartal, D.: Characterization and optimization optimisation of a dual channel PERCA for the investigation of the chemistry of peroxy radicals in the upper troposphere, PhD thesis, University of Bremen, Germany, 2009.

Kartal, D., Andrés-Hernández, M. D., Reichert, L., Schlager, H., and Burrows, J. P.: Technical Note: Characterisation of a DUALER instrument for the airborne measurement of peroxy radicals during AMMA 2006, *Atmos. Chem. Phys.*, 10, 3047-3062, doi:10.5194/acp-10-3047-2010, 2010.

L

Lee, J.D., Development and deployment of the FAGE instrument for measurement of HO_x in the troposphere. PhD Thesis, University of Leeds, UK, 2000.

Levy, H.: Normal atmosphere: large radical and formaldehyde concentrations predicted, *Science*, 173, 141-143, 1971.

Lightfoot, P. D., et al., Organic Peroxy-Radicals - Kinetics, Spectroscopy and Tropospheric Chemistry, *Atmospheric Environment Part a-General Topics*, 26, 1805-196, 1992.

M

Mihele, C.M., and Hastie, D.R.: The sensitivity of the radical amplifier to ambient water vapour, *Geophys. Res. Letters* 25, 1911-1913, 1998.

Mihele, C.M., M. Mozurkewich, and Hastie, D.R.: Radical loss in a chain reaction of CO and NO in the presence of water: Implications for the radical amplifier and atmospheric chemistry, *Intern. J. Chem. Kinetics*, 31, 145-152, 1999.

Miyazaki, K., Parker, A. E., Fittschen, C., Monks, P. S., and Kajii, Y.: A new technique for the selective measurement of atmospheric peroxy radical concentrations of HO₂ and RO₂ using a denuding method, *Atmos. Meas. Tech.*, 3, 1547-1554, doi:10.5194/amt-3-1547-2010, 2010.

Mozurkewich, M., P. H. McMurry, A. Gupta, and J. G. Calvert (1987): Mass accommodation coefficient for HO₂ radicals on aqueous particles, *J. Geophys. Res.*, 92(D4), 4163-4170, doi:10.1029/JD092iD04p04163.

Murphy D. M., Fahey D. W.: Mathematical treatment of the wall loss of a trace species in denuder and catalytic converter tubes, *Anal. Chem.*, 1987, 59 (23), pp 2753-2759, DOI: 10.1021/ac00150a006, 1987

P

Parker, A. E., Monks, P. S., Wyche, K. P., Balzani-Loov, J. M., Staehelin, J., Reimann, S., Legreid, G., Vollmer, M. K. & Steinbacher, Peroxy radicals in the summer free troposphere: seasonality and potential for heterogeneous loss, *M. Atmos. Chem. Phys.*, 9(6), 1989-2006, ACP 1680-7316, 2009.

Finlayson-Pitts B. J., and Pitts, Jr J. N.: Chemistry of the Upper and Lower Atmosphere Theory, Experiments, and Applications, Elsevier Inc., 2000, ISBN: 978-0-12-257060-5.

Platt, U., LeBras, G., Poulet, G., Burrows, J.P., and Moortgat, G.: Peroxy radicals from nighttime reaction of NO₃ with organic compounds, *Nature* 348, 147-149, 1990.

Platt, U., Alicke, B., Dubois, R., Geyer, A., Hofzumahaus, A., Holland, F., Mihelcic, D., Klüpfel, T., Lohrmann, B., Pätz, W., Perner, D., Rohrer, F., Schäfer, J., and Stutz, J.: Free radicals and fast photochemistry during BERLIOZ, *J. Atmos. Chem.*, 42, 359-394, 2002.

Q

Qi, B., Takami, A., and Hatakeyama, S.: A Calibration Method for Measurement of Small Alkyl Organic Peroxy Radicals by Chemical Amplifier Analytical Sciences, 22(8), 1091, DOI: 10.2116/analsci.22.1091, 2006.

R

Reichert, L., Andrés Hernández, M.D., Stöbener, D., Burkert, J., and Burrows, J.P.: Investigation of the effect of water complexes in the determination of peroxy radical ambient concentrations: implications for the atmosphere, *Journal of Geophys. Res.*, 108, D1, 4017-4032, 2003.

Reiner, T., Hanke, M., and Arnold, F., Atmospheric peroxy radical measurements by ion molecule reaction-mass spectrometry: A novel analytical method using amplifying chemical conversion to sulfuric acid, *J. Geophys. Res.*, 102, 1311, 1997.

Reiner, T., Hanke, M., and Arnold, F., Aircraft-borne measurements of peroxy radicals in the middle troposphere, *Geophys. Res. Letts.*, 25, 47, 1998.

Reiner, T., Hanke, M., and Arnold, F., Aircraft-borne measurements of peroxy radicals by chemical conversion/ion molecule reaction mass spectrometry: Calibration, diagnostics and results, *J. Geophys. Res.*, 104, 18,647, 1999.

S

Sadanaga, Y., Matsumoto, J., Sakurai, K., Isozaki, R., Kato, S., Nomaguchi, T., Bandow, H., Kajii, Y.: Development of a measurement system of peroxy radicals using a chemical amplification/laser-induced fluorescence technique, *Review of Scientific Instruments*, Volume: 75, Issue: 4, Pages: 864-872, DOI: 10.1063/1.1666985, 2004.

Sander, S. P., J. Abbatt, J. R. Barker, J. B. Burkholder, R. R. Friedl, D. M. Golden, R. E. Huie, C. E. Kolb, M. J. Kurylo, G. K. Moortgat, V. L. Orkin and P. H. Wine: "Chemical Kinetics and Photochemical Data for Use in Atmospheric Studies, Evaluation No. 17," JPL Publication 10-6, Jet Propulsion Laboratory, Pasadena, 2011, <http://jpldataeval.jpl.nasa.gov>."

Seinfeld H. J., and Pandis, S.N.: Atmospheric Chemistry and Physics, Wiley&Sons, 1997. ISBN:0-471-17816-0.

Selman et al., *Adv. in Chem. Eng.*, Vol 10, p.211, 1978.

Sommariva, R., S. S. Brown, J. M. Roberts, D. M. Brookes, A. E. Parker, P. S. Monks, T. S. Bates, D. Bon, J. A. de Gouw, G. J. Frost, J. B. Gilman, P. D. Goldan, S. C. Herndon, W. C. Kuster, B. M. Lerner, H. D. Osthoff, S. C. Tucker, C. Warneke, E. J. Williams, and M. S. Zahniser, Ozone production in remote oceanic and industrial areas derived from ship based measurements of peroxy radicals during TexAQS 2006, *Atmos. Chem. Phys.*, 11, 2471-2485, 2011

Stöbener, D., Weiterentwicklung einer peroxyradikalquelle für die Kalibration von RO₂-Messungen in Außenluft, Diplomarbeit, Universität Bremen, 1999.

W

Wayne P. R.: *Atmospheric Chemistry*, Oxford University Press, 2000. ISBN: 0-19-855571-7.

Weinstock, B.: Carbon monoxide: residence time in the atmosphere, *Science*, 166, 224-225, 1969.

Wendisch, M., Brenguier, J.-L.: *Airborne Measurements for Environmental Research Methods and Instruments Wiley Series in Atmospheric Physics and Remote Sensing*, ISBN 978-3-527-40996-9 - Wiley-VCH, Berlin, in preparation, 2013.

Whalley, L. K.; P. M. Edwards, K. L. Furneaux, A. Goddard, T. Ingham, M. J. Evans, D. Stone, J. R. Hopkins, C. E. Jones, A. Karunaharan, J. D. Lee, A. C. Lewis, P. S. Monks, S. J. Moller, and D. E. Heard *Atmos. Chem. Phys.*, 11, 7223-7233, 2011

ACKNOWLEDGEMENTS

I would like to thank...

...my professor J. P. Burrows for being always ready to assist and encourage me especially during times I get lost in the research.

...my supervisor, Dr. Maria Dolores Andrés Hernández, for providing reminders, encouragements and “pushes” especially when I get out of line, distracted or slow in my work.

... PROUB for organizing interesting workshops for PhD students and overall assistance.

... Dr. Annette Ladstätter-Weißenmayer and PIP for the encouragements, advice.

...my colleagues of the TROLAS group, Dr. Markus Horstjann, Vladyslav Nenakhov, Dr. Deniz Kartal, Viktor Schmidt, for providing encouraging comments during our meetings and support in laboratory experiments.

.... my colleagues Victor Gorshelev and Dr. Anna Serdyuchenko for discussions during long lab experiments and Alexandra Cherkasheva and Dr. Larisa Istomina for enjoyable moments.

...my best friends Aum, Dilsen, Jingwen and Guang, Kamila, Faiza, Chiara, Neung, Ronald, Vicky for all the enjoyments and the “listening ears” and encouragements especially during moments of frustration.

...my friends all over the globe Marcela, Ola, Ania for always being there for me.

...my parents for their prayers, encouragements and understanding and for always lifting me up when I was homesick or frustrated.

...mechanical workshop of the Institute of Environmental Physics: Elke Sorgenicht, Andre Brünkers and Simone Eilers and all other members.

...most especially, to the “Great Designer” up there, keeping watch over us.

...and to all the people that have made an impact to this study and to me during my PhD in Germany.

MANY THANKS.

Erklärung

Hiermit erkläre ich, dass ich die Arbeit ohne unerlaubte fremde Hilfe angefertigt habe, dass ich weiterhin keine anderen als die angegebenen Quellen und Hilfsmittel benutze und die den benutzten Werken wörtlich oder inhaltlich entnommenen Stellen als solche kenntlich gemacht habe.

Bremen, 14.03.2013

Anna Chrobry